ЕЛЕКТРОТЕХНИЧКИ ФАКУЛТЕТ
УНИВЕРЗИТЕТА У БАЊАЛУЦИ

FACULTY OF ELECTRICAL ENGINEERING
UNIVERSITY OF BANJALUKA

ЕЛЕКТРОНИКА
ELECTRONICS

YU ISSN 1450-5843

ГОДИШТЕ 5, БРОЈ 1-2, ДЕЦЕМБАР 2001. ● *VOLUME 5, NUMBER 1-2, DECEMBER 2001*

F A C U L T Y O F E L E C T R I C A L E N G I N E E R I N G
U N I V E R S I T Y O F B A N J A L U K A

Address: Patre 5, 78000 Banjaluka, Republic of Srpska, Bosnia and Herzegovina
Phone: + 387 51 211-408, + 387 51 212-820
Fax: + 387 51 211-408

E L E C T R O N I C S

Editor: Prof. Branko L. Dokić, Ph. D.
Faculty of Electrical Engineering
University of Banjaluka, Republic of Srpska
e-mail: bdokic@etfbl.net

Program Committee:

- Nikolaos Uzunoglu, National Technical University of Athens, Greece
- Barry Jefferies, University of Hertfordshire, UK
- Vojin Oklobd`ija, University of California, Davis, USA
- Bratislav Milovanovi}, Faculty of Electronics Niš, FR Yugoslavia
- Mili} Stoji}, Faculty of Electrical Engineering Beograd, FR Yugoslavia
- Vojislav Aranlelovi}, Institute "Vinča" Beograd, FR Yugoslavia
- Veljko Milutinovi}, Faculty of Electrical Engineering Beograd, FR Yugoslavia
- Ilija Stojanovi}, SANU Beograd, FR Yugoslavia
- Vladimir Kati}, Faculty of Technical Sciences Novi Sad, FR Yugoslavia
- Aleksandar Ili{kovi}, Faculty of Electrical Engineering Banjaluka, RS
- Milorad Bo`i}, Faculty of Electrical Engineering Banjaluka, RS

Secretary: Petar Matić, B.Sc.
e-mail: pero@etfbl.net,
http://www.etfbl.net/pero
Faculty of Electrical Engineering
University of Banjaluka, Republic of Srpska

Publisher: Faculty of Electrical Engineering
University of Banjaluka, Republic of Srpska
Address: Patre 5, 78000 Banjaluka, Republic of Srpska, Bosnia and Herzegovina
Phone: + 387 51 211-408, + 387 51 212-820
Fax: + 387 51 211-408
http://www.etfbl.net

Number of printed copies: 150

PREFACE

The International journal “Electronics”, published by University of Banja Luka, is devoting its special issue to the 11th International Symposium on Power Electronics – Ee2001. The editor of the journal Prof. Dr. Branko Dokić has invited us, as guest-editors, to present the most interesting papers from the symposium. This is a part of very successful collaboration between the Faculty of Electrical Engineering in Banja Luka and the Faculty of Technical Sciences in Novi Sad (Yugoslavia) in several fields and particularly in organization of two related international conferences – International Conference on Industrial Electronics - INDEL, and International Symposium on Power Electronics – Ee.

The 11th Symposium on **Power Electronics – Ee 2001** (**Energetska elektronika – Ee 2001)** was held in Novi Sad since October 31 to November 2, 2001. It was co-organized by Power Electronic Society sited in Novi Sad, Faculty of Technical Sciences – Institute for Power, Electronics and Communication Engineering from Novi Sad, Institute "Nikola Tesla" from Belgrade and Novi Sad Fair. Ministry of Science, Technologies and Development of Republic of Serbia, Serbian Academy of Science and Art (SANU) and Institute of Electrical and Electronic Engineers (IEEE) -YU Section, sponsored it.

The symposium presented 107 papers from various institutions in 16 countries (Austria, Belgium, Bosnia & Herzegovina – Republic of Srpska, Canada, P.R. China – Hong Kong, Germany, Hungary, Italia, Republic of Macedonia, Malaysia, Poland, Romania, Switzerland, United Kingdom, U.S.A. and Yugoslavia) and gathered around 200 participants (scientist, engineers, manufacturers, students…). All papers were published in proceedings - both in hard copy form (521 pages) and in electronic form (CD-ROM). CD-ROM also contains multimedia presentations of the organizers and commercial sponsors, facts about Power Electronic Society, as well as complete list of papers from all symposiums on Power Electronics (1973-2001).

Besides, annual meeting of the Power Electronic Society and meeting of the IEEE Industrial Electronics, Industry Application & Power Electronics Joint Chapter were held. Parallel to the symposium, the 10th International Fair »Electronics« enabled the participants to meet the latest design and realizations of devices, systems, hardware and software in the field of electronics, telecommunications and computer industry.

The symposium highlighted the problems and practical or virtual solution from many fields. Five topics were put forward: Power Converters, Electrical Drives, Electrical Machines, Control & Measurement in Power Engineering and Power Electronics in Telecommunications. The most interesting contribution were in the areas of power electronics application in automobiles, industrial motor drives, distributed power generation, fundamental definitions of electrical quantities, modeling of power electronics components, new or improved power electronic converters, power quality (harmonics, filters…), vector controlled induction machines, sensor less AC motor drives, new concepts of electrical machine modeling, electrical machines construction and maintenance, measurement in power engineering, new control methods (neural networks and fuzzy logic for control of drives), education in power electronics etc.

The symposium brought some new items. The first one was a new topic – Power Electronics in Telecommunications, as a consequence of professional's great interest. Then, there were new Proceedings size (A4) and printing papers in two columns. Student’s contest papers were also the new item.

The selection of the papers presented in this issue is only one of several possible to represent the 11th Symposium on Power Electronics – Ee 2001. We would like to emphasize our thanks to the authors who have accepted our request for prompt respond and fast adaptation of the papers to journal requirements. More details about the symposium can be found at Internet address: www.ns.ac.yu/prez.

We would also like to invite all readers of the »Electronics« journal to take active participation by submitting the papers or attending the next **12th International Symposium on Power Electronics – Ee2003**, which will be organized in NOVI SAD, YUGOSLAVIA in October or November, 2003 (www.ns.ac.yu/ee2003).

Guest Editors:
Prof. Dr. Vladan Vučković
Prof. Dr. Vladimir Katić

BIOGRAPHY OF Prof.Dr. VLADAN VUČKOVIĆ

Vladan Vučković (Vladdan Vuchkovich), born 1928 in Kragujevac (Serbia, Yugoslavia), holds a Ph.D. degree from University of Belgrade, Department of Electrical Engineering (1964). Now retired, he was full professor in University of Belgrade (Department of Electrical Engineering), in University of Novi Sad (Department of Technical Sciences) and in Electronic Faculty in Niš. During his 40-years university career he has established and taught numerous fundamental courses, as for example, Magnetic Amplifiers, Transient Phenomena in Electrical Machines, Power Electronics, Theory of Electrical Machines, Electrical Drives, Control of Electrical Drives, Microcomputers in Power Electronics.

Parallel to this assignment, he was about 30 years Manager of Control Department in Electrical Engineering Institute "Nikola Tesla" in Belgrade, where he and his team have developed a series of different devices in the field of power electronics, electrical drives and analog and digital automatic control.

He has published over 80 scientific papers and articles in national and international professional publications and conference proceedings, as well as two monographs ("Generalized Theory of Electrical Machines" and "Electrical Drives").

BIOGRAPHY OF Prof.Dr. VLADIMIR KATIĆ

Prof. Vladimir A. Katić was born in Novi Sad, Yugoslavia in 1954. He received B.Sc. degree from University of Novi Sad in 1978, and M.Sc. and Ph.D. degrees from University of Belgrade in 1981 and 1991, respectively, all in electrical engineering. From 1978 he is with Institute for Power, Electronics & Communication Engineering of Faculty of Technical Sciences, University of Novi Sad, where he is currently Associated Professor. From 1991 he is the Head of Power Electronics and Converters Group. He was Director of the Institute for Power, Electronics & Communication Engineering (1993-98) and from 1998 he is the Vice-Dean of the Faculty of Technical Sciences.

The main areas of scientific interest and research of Prof. Katić are power quality, modelling of power electronics converters and standardization in electrical engineering. He is the author or co-author of more than 160 scientific papers published in international and national monographs, journals or conferences proceedings. He is also reviewer, member of international programme committees and session chairmen of many international or national journals and conferences. Prof. Katić has been the head, main researcher or researcher of 2 international and 26 national scientific projects or studies.

He is the author of the "Power Electronics - Worked Problems" and "Power Electronics – Practicum of Laboratory Exercises", books, which are used in teaching at University of Novi Sad.

From 1994 he is the president of Organizing Committee of scientific gatherings “Developments Trends - TREND” on different topics, while from 1995, Co-Chairman of International Symposium on Power Electronics – Ee, together with Prof. Vučković.

He is founder and acting president of the Power Electronics Society, which has the aim of promoting, organizing symposiums and publishing publications in area of power electronics and adjacent fields.

Prof. Katić is the Senior Member of IEEE – Power Electronic Society, IEEE - Induatrial Electronics Society, IEEE - Industrial Application Society and Chairman of IEEE Joint Chapter on Industry Applications, Industrial Electronics and Power Electronics Societies at Novi Sad. He is observer Member at CIGRE SC36 (Paris), Member of International and National Committees of CIGRE and National Committee of CIRED.

AN INTEGRATED AUTOMOTIVE STARTER-GENERATOR WITH A WIDE SPEED RANGE

John Miller, Vojislav Stefanović, John Kelly***
Research Lab.Ford Motor CoDearborn, MI, USA
** Consultant V-S Drives Afton, Virginia, USA*
*** Ph.D Student Michigan State University, Lansing, MI, USA*

Abstract: - *Automotive manufacturers worldwide are exploring new methods to reduce fuel consumption and emissions. The new proposed 42V standard for passenger automobiles makes an integrated starter-generator both a possibility and a necessity. This paper first examines the required properties of this new system and then goes on to define what we believe to be the most appropriate system configuration. A need for an extended speed range of an induction machine is defined and a new method for an efficient pole changing technique, called Pole- Phase Modulation (PPM), is described*[1]. *The control of such a novel drive is given, for both motoring and generating operations, including transition from one to the other mode. Experimental results, obtained on the actual machine are also given.*

1. INTRODUCTION

The importance of auxiliary drives in passenger cars is sharply increasing as various methods for improved fuel economy and reducing pollution are implemented. Most of these methods, for both conventional and HEV, involve engine shutdown during idle or rest periods. However, such start/stop strategies would inconvenience the user by rendering power assist steering and cabin climate control inoperative during engine shutdown. Therefore, in this case electric drives for power assist steering, air conditioning as well as transmission oil pump become mandatory, while the existing starter and generator functions need to be optimized.

At the same time, if these auxiliary drives were to be electrified, their power density, starting characteristics and cost have to be significantly improved. In preparation for the changeover to electric auxiliary drives, the industry adopted in 1998 the new voltage standard for conventional passenger cars, the 42V PowerNet.

Considering the power rating and the efficiency impact, the most important of all future auxiliary drives is the drive combining the integrated starter generator (ISG) functions, a single machine which replaces the DC starter and the AC Lundell alternator. The ISG on 42V PowerNet supply is expected to have the rated power between 5 and 10 kW. In order to be successfully implemented, an ISG has to meet the following requirements:

- High starting torque at most unfavorable operating conditions;
- Wide speed range in generator mode, typically from 600 to 8000 rpm;
- High efficiency in 600 – 4000 rpm speed range. (Covering I4 to V8 engines).
- Acceptable cost

The most important reasons for combining starter and alternator in a single machine of increased power rating are:

- A desire to eliminate the present car starter, the only passive component during engine operation, which is used less than 1% of the total driving time and which, by its weight, lowers fuel efficiency and takes precious space under the hood.
- Need to replace the present belt and pulley coupling between the alternator and the crankshaft. As the alternator power rating increases, to accommodate additional electric loads, the side-pull on the bearings and the problem of belt slipping will be pushed to the limit or require yet larger and more costly components.
- Need to provide a fast control of the generator output voltage during load dumps in order to improve the distributed power quality and thus be able to reduce the voltage margins of all other electric components, thereby reducing their cost.
- A desire to eliminate the slip-rings and the brushes in the present, wound rotor, alternators. Beside the obvious reliability issue with 10-years/150,000 miles car life, slip-rings present a problem of getting the required excitation to the rotor. The reason is that at high speeds (currently above approximately 8,000 rpm or 2,900 rpm engine speed) the brushes tend to lose contact with the slip-rings, due to slip-ring eccentricity.

While attractive, the concept of combining two electrical machines into a single one carries a substantial technical challenge: the ISG has to be designed and optimized for two, widely different modes of operation. The starter needs to develop a high motoring torque, at low temperatures, with decreased battery capacity (40% - 60% of +25^{o}C capacity is lost below -25^{o}C) and increased viscous friction in engine. This naturally leads to a machine with a large number of poles. The generator, on the other hand, has to provide high efficiency over a very wide speed range, leading to a machine with a low-pole number. Other motor manufacturers have arrived at the same conclusion [1]. Thus, ideally, starter and alternator need to operate with a different pole-number.

The next Section describes a new method for changing a pole number in an induction machine and

[1] Several patent applications covering the PPM technique and various control strategies have been filed.

shows the stator winding connections for high and low pole number. Section 3 presents starter and generator control while Section 4 gives the experimental results, with the conclusions outlined in Section 5

2. PRINCIPLES OF POLE- PHASE MODULATION OF AN AC MACHINE WINDING

The new method, called Pole- Phase Modulation (PPM) is the most general way of discrete speed control of an AC machine fed from a constant frequency source. As opposed to conventional methods of discrete speed control, such as Dahlander, or pole- amplitude modulation (PAM), where the number of phases at both speeds is constant, in PPM the number of phases can also be varied. With this additional degree of freedom practically all speed ratios in a two speed machine can be achieved, as long as the number of slots is correctly selected. Only the PPM method allows for a lower speed in a two speed AC machine operating at constant frequency to be less than 50% of the higher speed. In addition, a PPM winding can, under certain circumstances, be reconnected to have more than two synchronous speeds.

PPM can be implemented in machines with conventional windings, as well as in toroidally wound machines. A toroidal winding offers more flexibility in pole number selection, has shorter overhangs and can be better cooled than a conventional one.

Denoting by p_1 the number of pole pairs and by m_1 the number of phases at one synchronous speed, and by p_2 and m_2 the same parameters at another speed, one can represent the relationship of PPM to other discrete speed control methods as shown in Fig. 1.

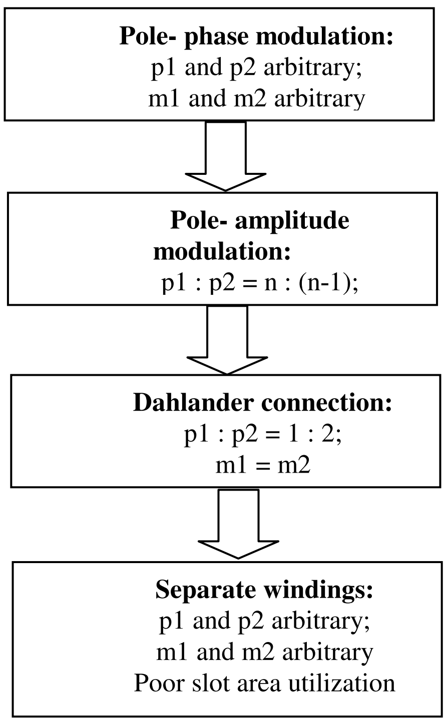

Fig. 1. *Hierarchy of discrete speed control methods for an AC machine*

2.1. PPM with conventional winding

Both sides of each coil in a conventional AC winding are placed in the slots. The coil pitch is equal for all coils and is constant – it cannot be changed during pole-changing winding reconnection. When PPM is implemented with a conventional winding, an access to basically each coil, or a group of coils, is necessary. The coils have a pitch equal to, or slightly smaller than a full pitch for lower number of poles.

When the ratio of two speeds is 1:3, 1:5, 1:7 etc. (1: odd number), the coils usually have full pitch at lower polarity. When the ratio of two speeds is 1:2, 1:4, 1:6, etc. (1: even number), the coils must have shortened pitch at lower polarity. A special case of PPM winding with speed ratio 1:2 is Dahlander connection, in which the coil pitch at lower polarity is 50% shortened in order to give a full pitch at higher polarity.

The conventional winding connections for (1: odd number) and (1: even number) combinations will be illustrated by the following two examples.

Speed ratio (1: odd number) - full pitch winding at lower polarity: Consider an AC winding which has to operate in 4-pole, and in 20-pole connection. For PPM implementation the winding will be double layered and will have five phases at four poles (m_4 = 5) and two phases at twenty poles (m_{20} = 2). Phase belt at four poles is q_4 = 2, and at twenty poles q_{20} = 1.

Coil pitch expressed in a number of teeth is y = $\tau_{p,4}$ = 10, and the winding is placed in 40 slots.

Winding configuration at two polarities is shown in Fig. 2. For purpose of clarity only coils belonging to one phase, i.e. carrying the same current, are shown in this figure. Current direction in the coils is given by the arrows.

For the four pole connection, Fig. 2, the adjacent two coils belong to the same phase (q_4 = 2). The pole areas are denoted by N_4 and S_4. For the twenty pole connection, Fig. 2 below, the phase belt is equal to one and the pole pitch is equal to two. Pole areas in this connection are denoted by N_{20} and S_{20}.

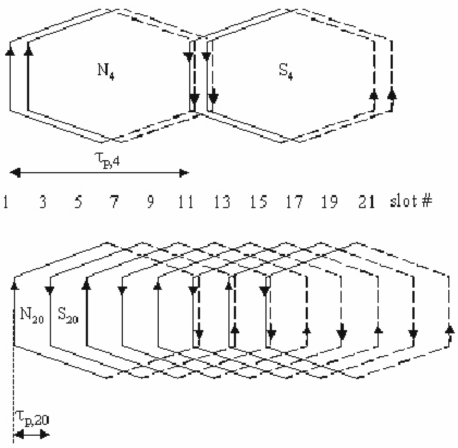

Fig. 2. *PPM winding connection for 4- pole (above) and 20- pole (below) operation*

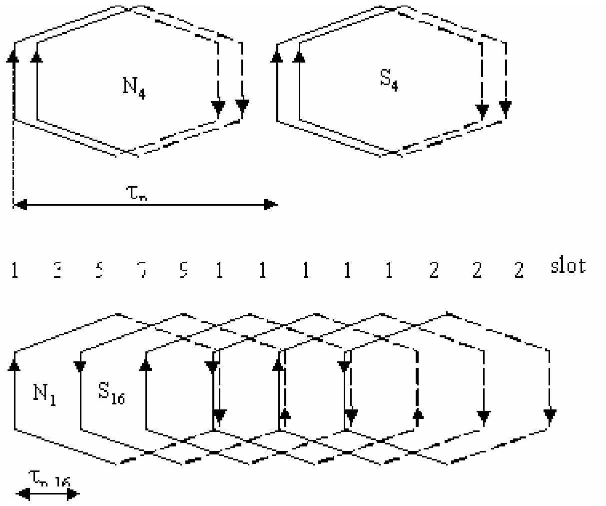

Fig. 3. *PPM winding connection for 4- pole (above) and 16- pole (below) operation*

Speed ratio (1: even number) - shortened winding pitch at lower polarity: Assume that an AC machine has to operate in 4- pole, and in 16- pole connection (Fig. 3).

The double layer winding for PPM in this case will have six phases at four poles ($m_4 = 6$) and three phases at sixteen poles ($m_{16} = 3$). Phase belt at four poles is $q_4 = 2$, and at sixteen poles $q_{16} = 1$. Coil pitch expressed in a number of teeth is $y = 9$, and the winding is placed in 48 slots.

Again, as in Fig. 2, only the coils belonging to the same phase are shown in Fig. 3.

2.2 PPM with toroidal winding

The full power of PPM can be reached only with toroidal winding, due to its unique capability to realize any coil pitch. The basic difference between toroidal and conventional windings is that coil pitch in a conventional winding is hardware defined, whereas in a toroidal winding it is software defined. In other words, a conventional winding is built of coils whose geometric dimensions determine winding pitch – the distance between the left side and right side of a coil is firmly defined, Fig. 4.

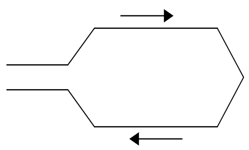

Fig. 4. *Schematic representation of a conventional coil. The current flows in both directions – compare with toroidal coil connection, Fig.5.*

In a toroidal winding, a coil alone cannot push the flux from the stator to the rotor yoke, since each coil side in the airgap conducts the current only in one direction, Fig. 5. To obtain the same effect as in a standard induction machine, two appropriately selected elementary coils are connected in series. Thus, a coil known from conventional machines is created in toroidal machines by defining directions of currents in any two elementary coils, Fig. 5. The geometry of toroidal coils allows for a flexible current control in each half of a complete coil, consisting of two elementary coils.

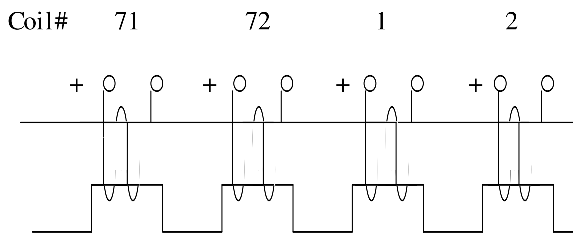

Fig. 5. *Schematic representation of elementary coils in a toroidally wound machine. All coils are wound in the same directions; the front end of the coil is designated as (+); the back end is (-). Each winding is obtained by connecting appropriate coils in series.*

A toroidal machine creating 2-pole flux distribution is shown in Fig. 6. The coil currents in each phase are chosen in such a manner that they have the same amplitude and phase shift in one half of adjacent coils.

A new number of poles in a toroidally wound machine is achieved simply by changing the phase angle between currents in the coils. For example, by changing the phase shift between the currents in the coils, the 2-pole stator winding of machine in Fig. 6 is reconfigured as a 12-pole machine, Fig. 7.

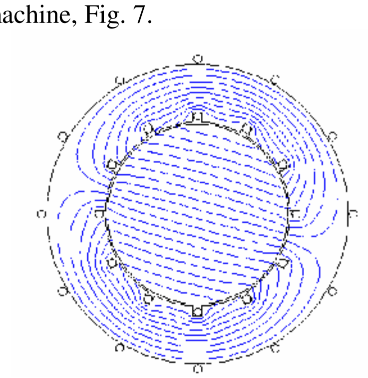

Fig. 6. *Toroidal winding connection for 2-pole operation*

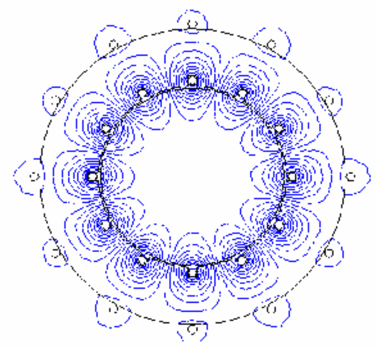

Fig. 7. *Toroidal winding connection for 12- pole operation*

2.3 PPM applied to starter-generator

To evaluate the PPM method and to gain experience in integrated starter alternator design, a toroidal induction machine was built, using existing 72-slot stator laminations. In general, the number of pole pairs P is a function of the total number of stator slots N, the phase belt q, and the number of phases m according to the equation

$$P = \frac{N}{2*q*m} \tag{1}$$

where P and m must be integers, and q is usually an integer. This means that an m-phase machine with N slots can be built having several pole pairs, the number of which depends on the value of q. In this application, it was selected to have 12 poles for the starter and 4 poles for the generator.

The toroidal machine phase belts for 12-pole and 4-pole configurations are first defined as:

$$q_{12} = 72/(12m_{12}) = 6/m_{12} \tag{2}$$
$$q_4 = 72/(4m_4) = 18/ m_4 \tag{3}$$

where m is the number of phases, 72 is the number of stator slots and q is the corresponding phase belt, expressed in a number of slots. An additional constraint is that:

$q_{12} = n\, q_4$

where n is an integer. Finally, the last condition is that the sum of all line currents is zero.

Eq. (2) shows that with a 72-slot machine, the maximum number of phases (neglecting all other considerations) can be 6 for a 12-pole connection and 18 for 4-pole connection. Having a different number of phases for these two configurations would lead to an inefficient use of current sensors. In order to minimize the number of current sensors, a three-phase winding was selected for both configurations, that is:

$m_{12} = m_4 = 3$

The phase belts for 12-pole and 4-pole configurations are consequently:

$q_{12} = 2$ $q_4 = 6$

One possible winding connection, for a 3-phase toroidal machine, which satisfies all requirements is shown in Fig. 8. Coils #1 & #2, #19 & #20, #55 & #56, form one branch, etc. The top point of each branch (+1, +21, +5, +25, +9, +29, +13, +33 and +17) is connected to a corresponding inverter totem pole mid-point, Figures 9 and 10. A (-) phase sign for the 4-pole connection means that the current entering the connection point of the corresponding branch (+21 for –A, +9 for –B and +33 for –C) has the opposite direction from the currents entering the other two branches belonging to the same phase.

Pole changing is performed by inverter control, by re-assigning coil strings to different phases without a need for any mechanical contactors as shown in Fig. 8, 9 and 10.

3. CONTROL

For rather obvious reasons of fast regulation of the generator output voltage, it was decided to use field oriented (vector) control. While sensorless control is very attractive and entirely feasible for generator mode, the very high starting torque required at standstill in starter mode and the cumulative novelties in this design pointed to a more conservative, sensor based approach. Also, the plan is to make use of the already available VR (variable reluctance) encoder, currently used for the engine firing control. With these decisions, the choice of Indirect Vector Control became obvious.

In a starter mode, the control has to pre-flux the motor in a 12-pole configuration and then to accelerate it to 600 rpm, at which point the engine develops its own torque. The starter accelerates entirely under torque control which is better suited for this application. The torque profile may be adjusted in a function of battery voltage, temperature, etc.

At approximately 600 rpm, the control reduces the commanded torque to zero, disconnects the machine from the supply and re-connects it in a 4-pole configuration. At the same time, the control switches to a generator mode – the controlled variable becomes the DC voltage.

Thus, the changeover from starter to generator mode has to be with the machine disconnected from the supply. The time to reduce and then to re-establish the flux is in the order of 1-2 sec. That precludes fast and frequent pole change, so that all auxiliary functions, such as torque boost and crankshaft torque damping need to be performed with the 4-pole configuration.

The control is presented schematically in Fig. 11. A well known, standard indirect vector control is used and only the most salient aspects are explained here.

In a starter mode, the input is the torque command, which defines the commanded q-axis current, eq. (4). The commanded flux, appearing in eq.(4) is calculated from eq.(5), where T_r is the rotor time constant.

$$i^*_{qs} = \mathrm{K1}\ T^* = \frac{2}{3}\frac{1}{PP}\cdot\frac{L_r}{L_m}\cdot\frac{T^*}{\Psi^*_{dr}} \tag{4}$$

$$\Psi^*_{dr} = \int\left(\frac{L_m}{T_r}i^*_{ds} - \frac{\Psi^*_{dr}}{T_r}\right)dt \tag{5}$$

The only addition in the generator mode to the q-axis control is that the output from the voltage regulator, divided by the measured speed defines the commanded torque, Fig. 12. The d-axis control, same for both modes, regulates the machine flux, which is at the rated value for the starter and is reduced in a generator mode, as the speed is increased. The estimated flux is obtained from eq. (5), when commanded quantities are replaced with feedback values.

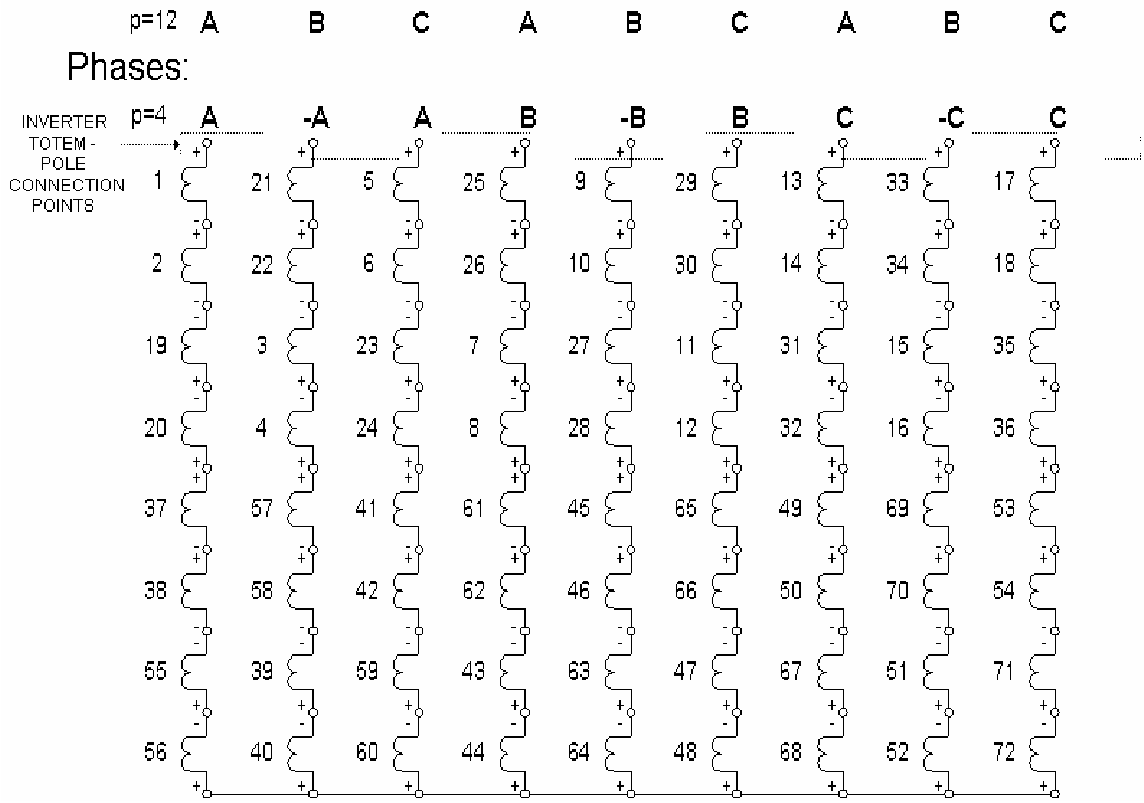

Fig. 8. *Winding connection for 4-pole and 12-pole configurations. The coil polarity is shown in Fig. 5. The coil connections and the inverter connection points (indicated above) are fixed. Pole change is performed by assigning coil strings to the appropriate phases, through inverter control, Figures 9 & 10.*

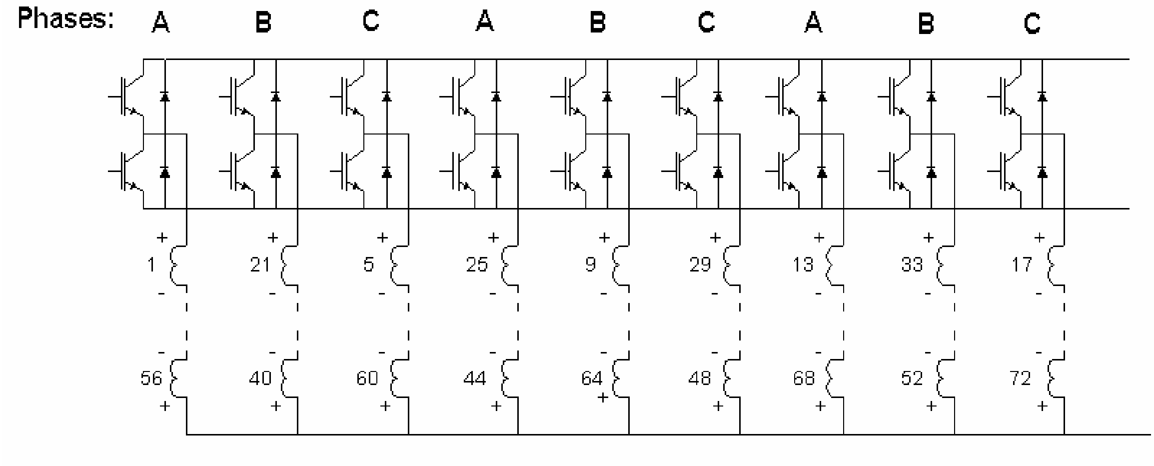

Fig. 9. *12-pole inverter connections and control. The elementary coils are connected in series, as shown in Fig.8. All nine inverter totem poles are used.*

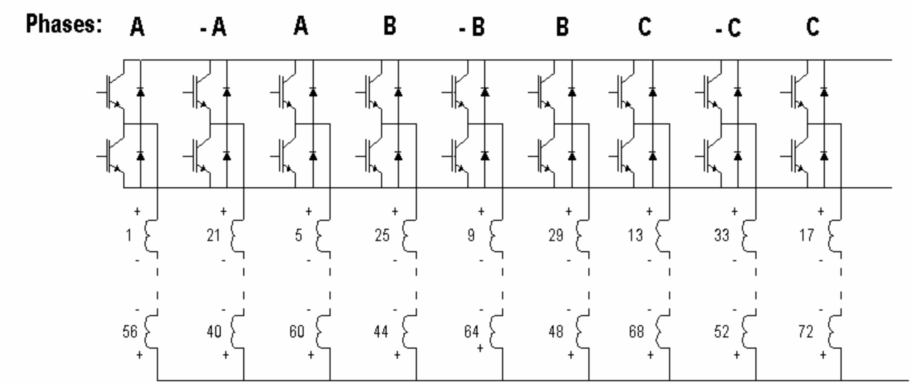

Fig. 10.*4-pole inverter connections and control. The elementary coils are connected in series, as shown in Fig.8.*

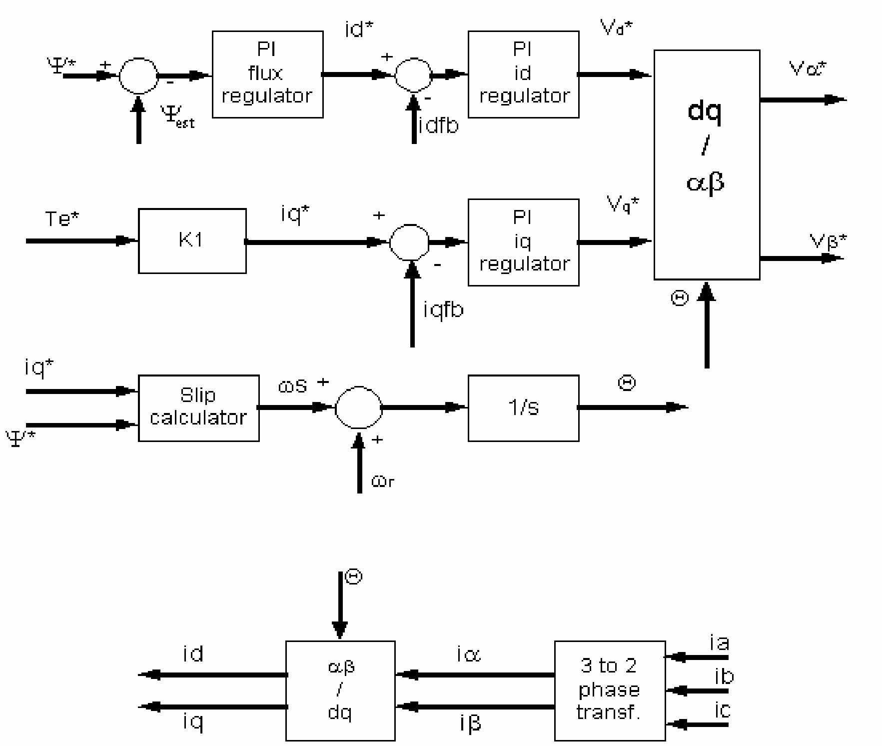

Fig.11. *Schematic diagram of indirect vector control, in synchronous reference frame. The slip calculator defines the specific slip value, eq.(14), which gives de-coupled control of the machine torque and flux. The flux position Θ defines the reference frame transformations.*

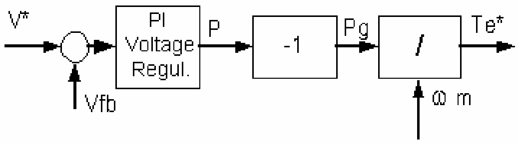

Fig. 12. *The output from the voltage PI regulator represents the induction machine power P, which needs to be multiplied by (-1) to account for generating action [3-4]. The so obtained generator power P_g is divided by the motor speed ω_m to obtain the generator commanded torque $T^*_e{}^*$. That torque is then used to define the commanded current i_q^*, eq. (4)*

The commanded currents, i_d^* and i_q^*, Fig. 11, are compared with measured currents, transformed to d-q reference frame. The current errors in d and q axis are processed through their respective anti-windup PI regulators, the output of which represent the commanded voltages, V_d^* and V_q^*. These voltages, transformed to a stationary reference frame, determine the PWM duty cycle.

Transformation to and from a synchronous reference frame is performed using the rotor flux position angle, Fig. 11.

In a course of this project, extensive simulation was performed to evaluate various control aspects, as well as to asses the effect of sensor imperfections (DC offset, non-linearity, scale error and limited resolution) on the system performance. These results are too extensive to be reported here. In summary, it was found that the current sensors need to have low DC offset and good linearity, while the voltage sensor was not critical. The position sensor, evaluated with respect to resolution, requires a minimum of 1024 encoder pulses per revolution (10-bit resolution).

4. EXPERIMENTAL RESULTS

The experimental results were obtained at the Michigan State University. In setting to obtain the experimental verification of all design and simulation that was done, usual practical problems were encountered. While they were real and took significant time to be resolved, if at all, they have negligible scientific value and are not reported here. One problem worth mentioning is the difficulty in balancing the currents in three parallel branches, belonging to each phase, 4-pole configuration, Figures 8 & 10. The cause of the problem was identified; the remedy would required a different machine design. As a result, the machine was operated in a generator (4-pole) mode with nine rather than 3 phases. While that temporary solution eliminated the un-balance, the number of current sensors became impractical. That problem is the subject of continuous work.

The laboratory set-up, used in obtaining the experimental results is shown in Fig. 13. The TMS320C DSP collects current, position and torque data. This information is passed via the FPGA to the PC. The PC is operating under real-time Linux, RTLinux 3.0. RTLinux allows the PC to handle time-critical tasks. Upon receiving the data, the PC begins the control program and any desired data acquisition.

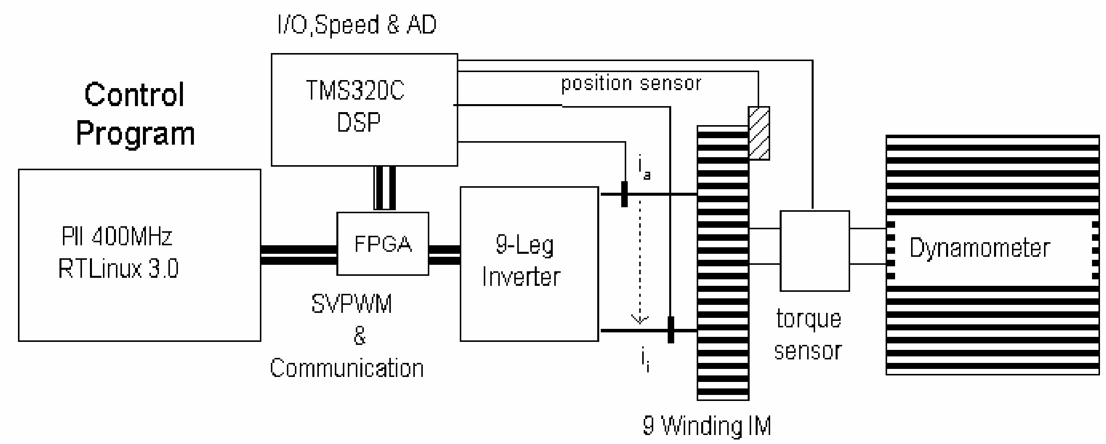

Fig. 13. *Laboratory set-up, used to obtain experimental results.*

The outputs of the control program are voltage commands, which are sent from the PC to the FPGA. In addition to handling the communication, the FPGA is tasked with executing space vector pulse width modulation, SVPWM. It is computationally faster to perform the 9-phase SVPWM on the FPGA than on the DSP. The resulting pulses from the FPGA are sent to the nine-leg inverter. The combination of PC and DSP, allows for convenient code development and implementation.

The open loop torque-speed characteristic for 12-pole and 4-pole configurations is shown in Fig. 14.

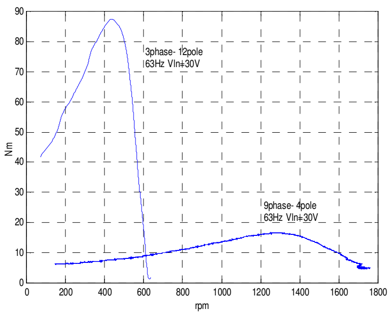

Fig. 14. *Open-loop torque speed curves for 4-pole and 12-pole configurations.*

5. CONCLUSION

Increasing electrical loads are favoring new alternator technology in passenger cars. Presently, there is an intensive search for the best configurations of integrated starter-generators (ISGs). Because of a very wide speed range in a generator mode, it is believed that an induction machine, with a flux weakening capability holds advantage over the other machine types. Even then, the starter and generator operating requirements are so different, that pole changing would be preferred. This paper presented an original method for pole changing in an induction machine, called Pole-Phase Modulation. The method was described in a detail and was then used to provide 12-pole (starter) to 4-pole (generator) change in an ISG. The winding diagram for both configurations is given, as well as the corresponding inverter connections. A standard indirect vector control is used in both starter and generator modes. A variable reluctance encoder, used for engine firing is to be used also as a rotor position sensor. Preliminary operating experience is reported, together with some experimental results. One of the key problems was a successful current balancing in a 4-pole, 3-phase configuration, which is the subject of a continuing research.

6. REFERENCES

[1] H. Schaefer: "Starter/Alternator with Vector-Controlled Induction Machine", Automotive Electronics, Jan. 2000, pp. 44 – 46

[2] 2. J. Miller and V. Ostovic: "Pole-Phase Modulated Toroidal Winding for an Induction Machine", US Patent 5,977,679.

[3] E. Levy: "Variable Speed Induction Generator as a Source of Constant DC Voltage", Proceedings of Universities Power Engineering Conference (UPEC), Edinburgh, Sept. 8-10, 1998.

[4] S.R Silva and R.O.C. Lyra: "Pulse Width Modulation Exciter for Flux Control of an Isolated Induction Generator", Proceedings of 1995 EPE Conference, Seville, pp. 3.233 – 3.238

CONTROLLED MULTI DRIVES

Borislav I. Jeftenić
Faculty of Electrical Engineering, Belgrade, Yugoslavia

Abstract: *Controlled multi drives are used in a great number of industrial plants. The functioning of large and complex systems such as ironworks, paper mills, excavators, etc. depends on the performance of the controlled multi drives. A systematic survey of multi drives based on the method of coupling and mutual influence is presented in the paper. Following that, an overview of the appropriate control algorithms, sorted by the principle of operation and the means of realization, is given. The paper is illustrated with selected applications of controlled multi drives from the author's practice.*
Key words: *Controlled drive, speed synchronization, load distribution*

1. INTRODUCTION

The phrase multi drive is used to describe all the drives in a technological process. If the controlled operation is of the drives is required by the process, based on the controlled speed of the individual drives, the expression controlled multi drives is adequate. For the great deal of such drives, the mechanical coupling on the load side is typical. The load torque component, that is the consequence of the coupling between the drives with indexes i and i+1, is, in general, represented by the following:

$$m_{s,i,i+1} = K_p(\omega_i - \omega_{i+1}) + K_e(\theta_i - \theta_{i+1}) \quad (1)$$

K_p is the viscous damping coefficient, K_e is the torsional stiffness of the coupling material, and ω and θ are the corresponding speed and position of the motor shafts. The practical values of the coefficients vary in a very broad range, starting from zero; therefore, diverse cases of coupling exist. In general, the practical cases may be characterized as follows:

a) Drives with rigid coupling $K_p \approx 0$ $K_e \to \infty$;

b) Drives with resilient coupling, $K_p \approx 0$ $K_e \neq 0$;

c) Drives with viscous damping coupling, $K_p \neq 0$ $K_e \approx 0$;

d) Mech. uncoupled drives. $K_p \approx 0$ i $K_e \approx 0$.

The coupling of the multi drives in the process, dictates the coordinated control. The necessity for such control is imposed for two reasons; the first comes from the fact that the drives are mechanically coupled, and the second is the consequence of the process / technological requirements for the multi drive.

The structure of the control algorithm for the multi drive is determined by the above reasons, e.g. by the dominant component of the coupling load torque, or by the reasons given by the process. Sometimes, the features of the selected equipment can significantly influence the implementation of the control algorithm.

2. MULTIMOTOR DRIVES STRUCTURES

According to the former classification of the multi drives, this section presents a survey of the typical drive configurations, accompanied with the requirements that need to be fulfilled by the control subsystem, to successfully realize the multi drive.
type

2.1. Drives with rigid coupling

With this type of drives, the coupling of the individual motors is done by the mechanical transmission devices, and is usually unbreakable. The coupled motors have the same speed, or the speeds may be different, but in a fixed ratio, settled by the mechanical gear-box. The configuration may be found in the very high power drives, where, given the technical or economic circumstances, it was not possible to use the single motor drive. The examples are the big rolling mills, where the limited space for the motor rules out the single big motor, therefore, a pair of two smaller motors is used. Another reason for selection of this configuration is the planned increase in the capacity of the plant. In the first phase of construction a single motor is placed, after what, in the second phase, the second drive motor is added [1]. The typical configuration of such drive is shown in Fig. 1.

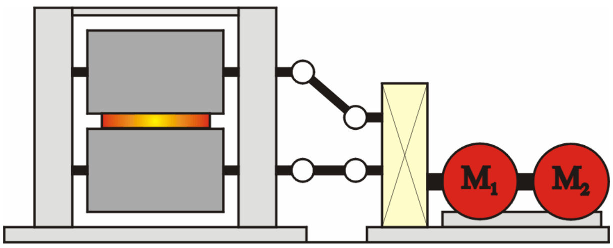

Fig. 1. *The layout of the motors in the rolling mill.*

The second distinctive example for the drives with rigid coupling is the drive for rotational movement of the bucket-wheel excavator platform, used in the opencast mines. The platform is supported by the base of the excavator, over the horizontal axial ball bearing, with the radius of 10 to 20m, depending on the size of the excavator. The rotation of the platform over the vertical axis is provided over the system of gears. The big gear-wheel (with the diameter similar to the diameter of the bearing) is located on the platform and the small gear -wheel is fitted on the shaft of the drive motor, or the shaft of the appropriate reductor. The concept of the rotational movement is illustrated in Fig. 2. In order to keep the platform of the rotational excavator vertical, the drive must be realized with two or three drive motors, positioned evenly on the circumference of the bigger gear wheel [2].

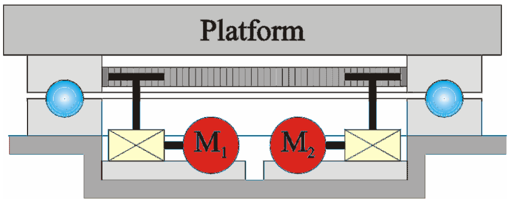

Fig. 2. *The bucket-wheel excavator platform drive*

The belt drives, web and felt drives in the paper machines, also belong to this group, if the length demands the use of more then one drive motors.

In the above or similar drives, only one speed regulator is sufficient, and only one speed sensor is needed to fulfill the speed control. However, special care must be taken to coordinate the load distribution between the coupled drives. The technique used is determined by the type of the motor and the converter used.

2.2. Drives with resilient coupling

The drives in resilient connection are the drives coupled by extremely long shafts, chains or belts, where twisting and elongation becomes noticeable / significant. On the other hand, from the practical point of view, much more interesting are the drives where the mechanical coupling is formed over the material being processed, tapes, pipes, tubes, stripes elongated in hot rolling mills, slabs in ironworks, steel plates in cold rolling mills, paper or board in paper machines. All this drives require the accurate speed control. The coupling in the former group is unbreakable in the technological sense. In the later group, while in normal operation, the drives are coupled, if the material being processed is “loaded”. The cooling dos not exist if the material is “not loaded”. In any case, the drives must keep the set speed ratio. In the first case, with the material loaded, the processing of the material determines the ratio, and in the second case, the drive must be ready for the loading of the material, during which the deformation of the material is unwanted. The basic layout of the drives in the vertical foundry for outpouring of slabs in the steel works is presented in Fig. 3. [3] In the finishing sections of the paper machine, with the paper already dry and firm, the drives are in resilient coupling by the sheet. The principal layout of the drives in this phase of the paper making is displayed in Fig. 4 [4, 5, and 7].

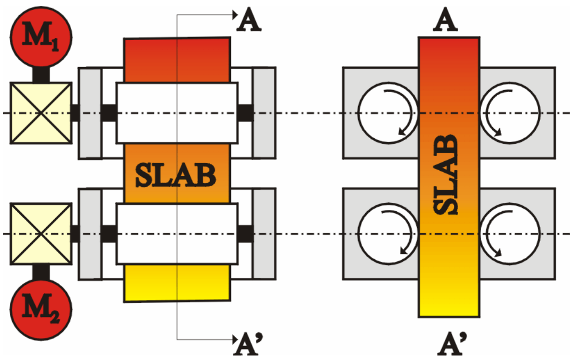

Fig.3. *The foundry drive*

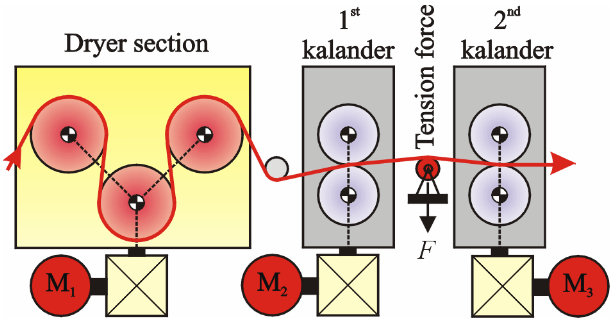

Fig. 4. *The drives in the paper machine in the dry section.*

All the drives in resilient coupling have individual speed closed loop, controller and a speed sensor. The drives coupled by the material, have an additional reason for the separate speed regulator, namely the synchronized operation before and after the “loading” of the material. It should be emphasized that these drives, due to the elasticity of the coupling material, have a cross-coupling, forces, torques in the material, given by Equation (1). The presence of this cross-coupling gives rise to the problems of load distribution [3, 7], hence one drive usually takes over the load of the other, sending it to breaking region, making the load distribution drastically violated. The force F in the material is given by (2):

$$F = K\left[(m_{e1} - m_{m1}) - (m_{e2} - m_{m2})\right] \qquad (2)$$

In equation (2), m_e is the motor torque, m_m is the load torque of the drive in uncoupled state, and K is the correlation coefficient.

This phenomenon is especially significant in the drives coupled by the material being processed, namely, if the force F exceeds the required, permitted values, a plastic deformation, or in extreme cases, rupture of the material occurs. To overcome this problem, an additional regulation of the force is necessary, either with the measurement of the force magnitude, or indirectly, by the regulator of the load distribution [3, 7].

2.3. Drives with viscous damping coupling

The drives with viscous damping coupling are connected by the material being processed, which is plastically deformed during processing. The examples are rolling drives in hot rolling mills, where the processing is done by pressing, as opposed to stretching, or the drives in the paper machine in the early sections where the sheet is still wet. To avoid the longitudinal strain of the material, with drives in the mentioned technological processes, the speeds of the drives should be in the exact predetermined ratios, that is, the line speed of the material should be equal, or slightly different, to compensate for the stretching of the material due to the pressing. If the configuration permits, to totally avoid longitudinal strain, the material may form the loop between the drives, a well known solution in engineering practice. Figure 5 shows the configuration of the hot rolling mill drive, with two rolling sections. An early, forming section of the paper machine, where the drying is accomplished by pressing is shown in Fig. 6. In the early phase the sheet is very wet and soft, having no tolerance for longitudinal strain, therefore, the synchronization of the drives deserves great attention. Motors M_1 and M_2 are in rigid connection over the colander that forms the web, but, this two drive is with the next, and all the others between each other are in viscous damping coupling [4, 5, 6, 7].

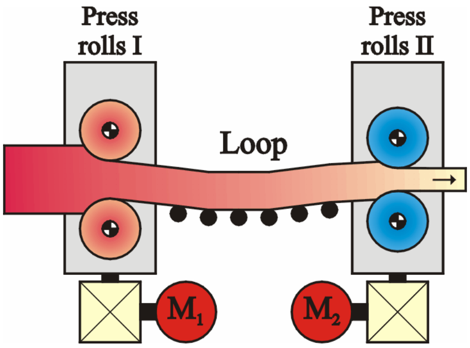

Fig.5. *The drives in press-roll mill, without stretching.*

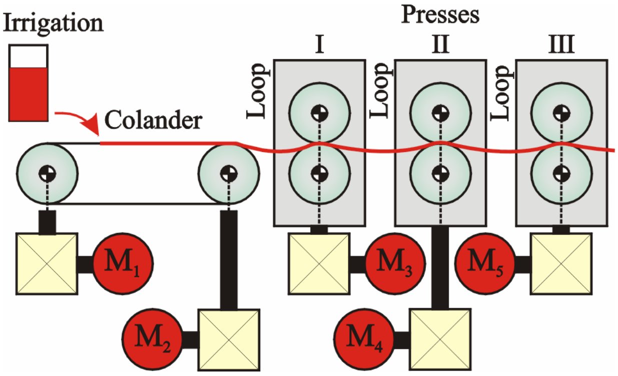

Fig.6. *The drives of a paper machine in the early phase of web forming.*

The drives with viscous damping coupling must have individual speed regulation, consequently, the converter and the controller must provide it. The longitudinal strain is eliminated by cascading the reference and by forming the loop between the drives.

2.4. Uncoupled drives

This group is formed, as mentioned earlier, the drives without the mechanical connection, but with the technological coupling, i.e. the technological process is possible by the synchronization of the drives. The typical example is the plant for continuous lateral sheet cutting, known as the flying shear. The principle of operation is shown in Fig 7. [8, 9, 10].

The first in the line of the flying shear plant is the press drive. It unwinds the sheet from the roll, and feeds it between the cylinders that carry the blades of the shear. Strictly speaking, the two drives are mechanically coupled only during the short cutting period, while the blades cut the material, however this may be neglected from the practical point of view, so the drives are mechanically uncoupled. The drive for the knives must be precisely coordinated with the press drive, since this determines the accuracy of the length being cut. To get the high quality of the cut, with no rupture or crumpling, the peripheral velocity of the sheet and the knives during the cut must be equal. During one round, the blades travel the distance of $L_k=\pi D_k$, which is, in general, different from the selected length to be cut (L). This is why the blades must have the variable speed between the two consecutive cuts. There are two possible solutions for this problem. In one case, the motor itself provides the variable speed, but, due to the low bandwidth of the mechanical system, this method can be used only where the sheet speed is low, with the relatively long lengths to be cut. With the higher sheet speed, the mechanical variator is used to provide the variable speed of the knives during the single revolution. The variation of the speed is provided by the mechanical mechanism, i.e. the flying shear mechanism, with the drive motor kept at the constant speed. The ratio of the speed of the press motor, and of the shear drive is proportional to the ratio L/L_k. The accuracy of the cut length depends on the possibility to keep the ratio constant; the usual required accuracy is at 0.1%, for example, in the paper industry, the tolerated error is at the most 1mm, for the cut of the length 1000mm. It is obvious that the two drives need independent, extremely accurate speed regulation.

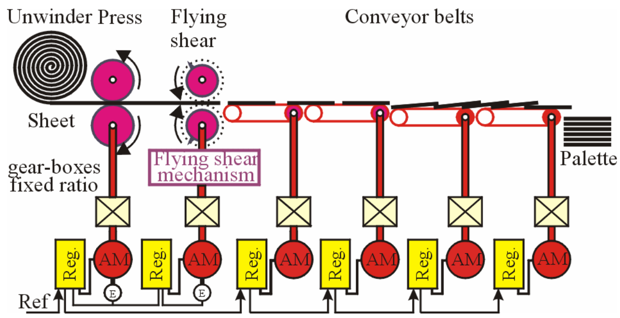

Fig. 7. The flying shear drive

The remaining drives shown in Fig. 7, the belt drives should also have synchronized speed, to properly align the parts, however the required accuracy is not very high, therefore the slip compensation as a function of the load, is adequate.

3. THE CONVERTER AND THE CONTROLLER FOR THE CONTROLLED MULTI DRIVES

Controlled drives are usually fed from the power converter, which is also true for controlled multi drives. The kind, the type and the number of converters used depend on the type of motors, their power ratings, and of the kind of the multi drive. The control and regulation also depend on the type of the multi drive, but on the type of the converter selected too, then the selection of the converter and the controller for these drives must be analyzed together.

3.1. Drives with rigid coupling

The drives with rigid coupling require only one speed controller, therefore for the drives with lower power ratings, only one power converter of the adequate size, can feed all the motors in the drive. The method for proper distribution of the load among the motors depends on the type of the motors used. With DC drives with separate excitation, with the armatures connected in parallel, the load distribution may be adjusted through the field, Fig. 8. For the motors with the same power ratings, the proper load distribution is achieved with the series connection of the armature windings.

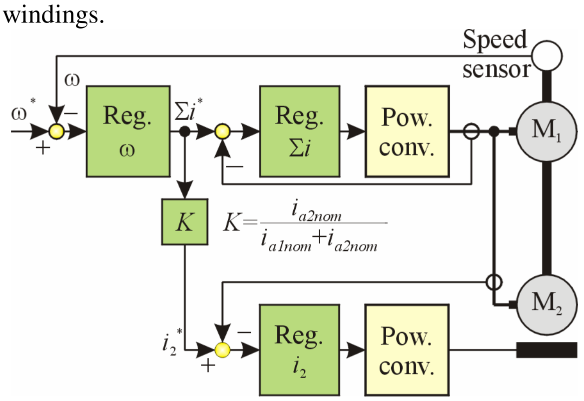

Fig. 8. *Converter and the controller for the two rigidly coupled drives with the low power ratings.*

With induction motors connected in parallel, the load distribution is influenced only by the correct selection of the torque-speed characteristic. For the squirrel-cage induction motors there exist no economical method for adjustment of the mechanical characteristic of the readymade motors, it has to be done during the selection. For the slip-ring induction motor, the mechanical characteristic can be adjusted afterwards, with the inclusion of the rotor resistors. This too is not an economical solution, so it is seldom found in the industry

Drives with medium and high power ratings require the use of separate converter for each motor; therefore, the load distribution is accomplished at the control level, such that every motor takes a part of the total load, proportionate to its ratings. The common speed controller determines the needed value of the total torque reference. The block diagram of such a drive with DC motors is given in Fig. 9.

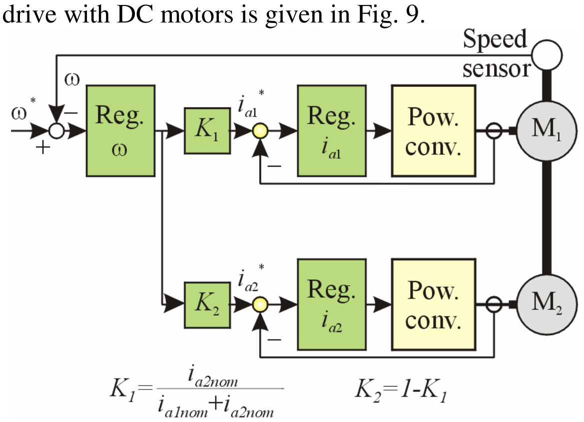

Fig.9. The converter and the controller for the two rigidly coupled drives, with separate power converters

In the drives with induction motors, with separate converters, the principle from Fig. 9 can be used, but the field oriented control of the motors is necessary.

The present question from the engineering practice deserves special attention: how can we realize such a drive with standard power converters for induction motors? The standard converters are designed for single drives, and the practical reasons determine their frequent use, availability, price, etc. The converters have a built-in speed controller, which can not be disabled, without the change of the control algorithm software. The manufacturers of the drives do not give us such an option. The solution may is found with the use of the standard options of the converters, namely one of the drives is configured in the speed closed loop mode, and the others in the torque control mode. With the reference torque for the first drive usually not known, the torque reference for the other drives may be the actual torque of the first drive, which is readily available information. If the torque information is not available, it can be determined based on the information of the actual and the synchronous speed [7]. In this way, each motor develops the torque proportionate to the torque of the first motor, and the coefficient of proportionality is determined based on the ratings of the motors. To enable the torque control mode, the value of the actual torque magnitude should be determined. Modern power converters determine the torque indirectly, without the torque sensor, but they require the speed measurement. This presents no problem in the given application. The block diagram of the proposed solution is given in Fig. 10. The figure shows that the speed information is introduced in both converters, but in the first it represents the speed feedback, and in the other it is used for the torque calculation.

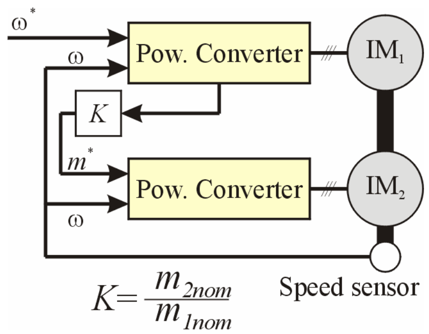

Fig.10. *The load distribution in the rigidly coupled induction motor drives, with single speed sensor*

3.2. The drives with resilient coupling

Every one of the drives in the resilient coupling must be in the speed closed loop, that is, it must have its own controller, speed sensor, and the separate converter .Each speed controller, should receive its own reference value. There exist two basic methods for the speed reference distribution, the parallel and the series (cascade) method. The reference distribution in parallel is used in drives that have the predetermined speed ratios, Fig. 11. The constants K_1 to K_3, in Fig. 11 depend on the individual drive's required speed ratio to the main reference, and are the function of the gear-ratio of the mechanical transmission, and the other mechanical parameters of the system. The cascade distribution, shown in Fig. 12 is used with drives that need to transmit the change of the speed, called the draw, of one drive to the other drives later in the technological line. The examples are rolling mills and paper industries. Constants K1 to K3 in Fig. 12 are determined as in the above, while z1, z2 ... are the selected draw settings.

The problem of load distribution that is possible in these drives is solved with the additional correction of the referent speed, based on the measured strain in the material that couples the drives, Fig. 13. The strain sensor or the force sensor can be measurement tapes, or the sensor in the bearing, or in the support for the roll carrying the sheet, as shown in Fig 4. Force measurement sensors are susceptible and expensive; however, they are required only between every other drive in the line.

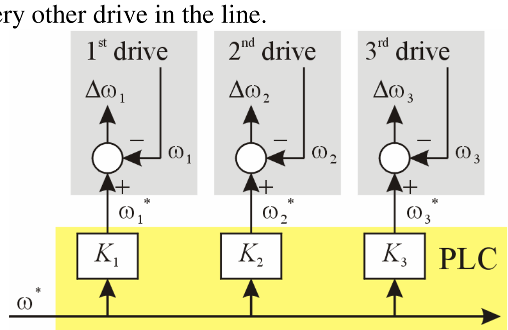

Fig.11. *Parallel method of reference distribution*

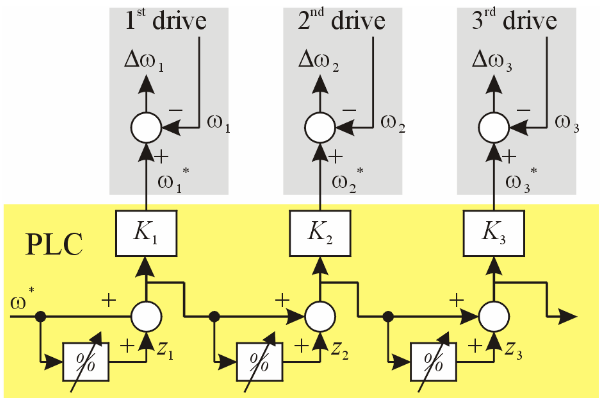

Fig.12. *Series (cascaded) speed reference distribution*

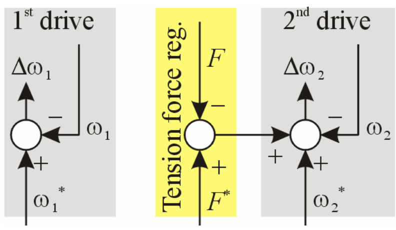

Sl.13. *Control of the strain in the material.*

In many cases, an adequate solution, that is more robust and is cost effective, is the control of the load distribution, among subsequent drives [3, 11], shown in Fig 14. The use of the load distribution regulator gives the system the required stability, and provides the satisfactory control over the strain in the material, for most of the practical applications. The desired load ratio for the drives m_1 and m_2 can be adjusted through the reference value of the load difference Δm^*.

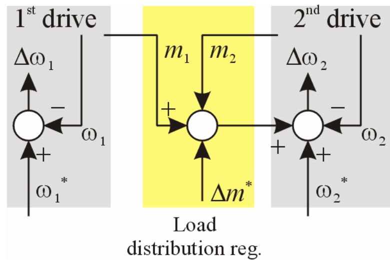

Fig.14. *The load distribution regulator.*

3.3. Drives with viscous damping coupling

The requirements for the controller with this type of drives are similar to the previous case; the separate speed closed loop control is necessary, which requires the separate power converters. The viscous damping of the material establishes the increase of the speed along the technological line, but the increase is relatively higher than with the drives with the resilient coupling. Instead of the draw, in this case, the correction is for the compensation of the elongation of the material. Since the correction should be transferred to the subsequent drives, the selection of cascaded reference distribution is obvious, shown on Fig 12. The problems of the load distribution do not affect these drives, and even if it does, it gives the unwanted strain in the material, and must be eliminated. The problem of the unwanted strain in the material can be effectively overcome by the use of the "loop" between the drives. To ensure the function of the loop, an additional control of the loop depth is used. The measured depth of the loop d is compared to the reference depth d^* and the difference is added to the reference speed of the drive subsequent to the loop, Fig. 15.

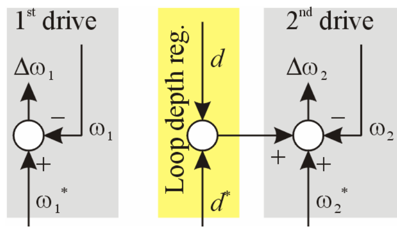

Fig.15. *The control of the loop depth.*

3.4. Uncoupled drives

All the uncoupled drives require separate speed feedback control and a separate power converter. The coordinated work is obtained over the reference. The drive type determines the method of reference distribution, parallel as well as cascaded distribution is possible. The principle of the reference distribution in the form of the master-slave drive is also possible, and has been applied in the aforementioned case of the flying shear. The measured speed of the press motor is used as a reference speed for the shear drive. Given the continuous demand for the precise control of the speed ratio of the two drives, the great attention is given to the selection and the tuning of the shear drive speed controller. PID controller, with the speed and acceleration feed-forward action was selected. The speed of the press drive may be used as a reference for the first conveyor belt drive. The sensor-less speed control is selected for this drive. Due to the fact that no measured speed exists in this drive, motor frequency proceeds as a reference for the second conveyor belt drive, while the speed of the motor is estimated in the controller. The same principle is used for all the subsequent belt drives. The difference between the frequency and the speed signal, and its variation for different loads was practically insignificant, since there were no need for exact synchronization of the belt drives. The method avoids the use of speed sensors on the conveyor belt drives. On the other hand, the estimated speed was not available in the selected drive controller, so this was the only solution. The block diagram showing the reference distribution is shown in Fig 16. The measured speed of the drive is labeled ω, while $\hat{\omega}$ labels the estimated speed of the drive; f in figure 16 denotes the motor frequency.

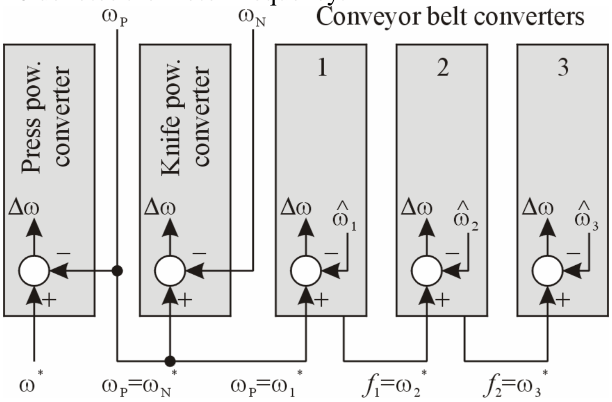

Fig.16. *The reference distribution in the flying shear drive.*

3. LOAD SHARING

The consideration of rational energy consumption is important with multi drives, especially if the high power ratings are used. The right choice of drive's components, undoubtedly contributes to the rational energy consumption. However, a few multi drives are able to save energy, based on the converter side load sharing. To be able to use load sharing, it is necessary that the drives have instantaneous electric power with the opposite signs, only if the algebraic sum of the energy consumed, for the complete drive can be performed.

The necessary condition for load sharing is fulfilled with the drives where some of the motors operate in the recuperative breaking. The adequate condition is fulfilled by the drives where it is possible to share the energy among the drives operating in motoring regime, and the ones operating in recuperative breaking, a form of the load bus. The fulfillment of both conditions is associated with the increase in investment cost, but if the increase in cost is lower than the savings in energy realized, then the investment is justified.

None of the drives analyzed previously does not satisfy the necessary condition, the motors were always in the same operating regime. Some of the drives used the control algorithm to disable the potential operation in the opposite regimes, e.g. the load distribution regulator. The breaking regime in these drives exists during the decrease of speed, when all the drives are in breaking. The rational use of this energy is possible only if it can be fed back to the source/grid. The two conditions must be met, first, the drive components should be capable to do so, and the second, the source should be able to receive the energy.

The typical examples of the drives with the ability to use the breaking energy are the ones with the unwinder drive. One of such plants is the reversible cold rolling mill, where the rolling process is accomplished by the multiple winding of the tin foil during which the foil is wriggled through the press rolls in both directions. At the both ends of the plant, the winder and unwinder drives are placed. The motor in the unwinder provides the constant tension force during the unwinding process, operating in the breaking regime. If the breaking is recuperative, than the produced energy can be placed for use by the other drives in the system. In the aforementioned flying shear drive, the existing unwinder drive could share the energy with the other drives. In the example cited [8], the tension force is obtained by the pneumatic mechanical breaks. The characteristic example with the ability for considerable energy savings, based on the load sharing principle is the rewinder drive, found in the paper industry. During the rewinding process of the completed rolls of paper, the longitudinal cutting is performed along the sides and to the desired width. The same tension force is needed throughout the rewinding of the roll, over the entire diameter, for the storage and transportation purposes.

The load sharing option, among the drives, depends on the type and the concept of the drive. The first controlled drives, in the present sense, have been realized with the Vard-Leonard groups. The generators feeding the individual drives were placed on the shaft of the main drive motor. During the breaking of an individual motors, the energy would be transferred to the other drives through the main drive's shaft. In the DC drives with thyristor converters, internal load sharing is performed over the main bus bars, feeding all the drives, under the assumption that multi-quadrant converters were used. In both cases, there was no need for additional investment to enable the internal load sharing in the drive.

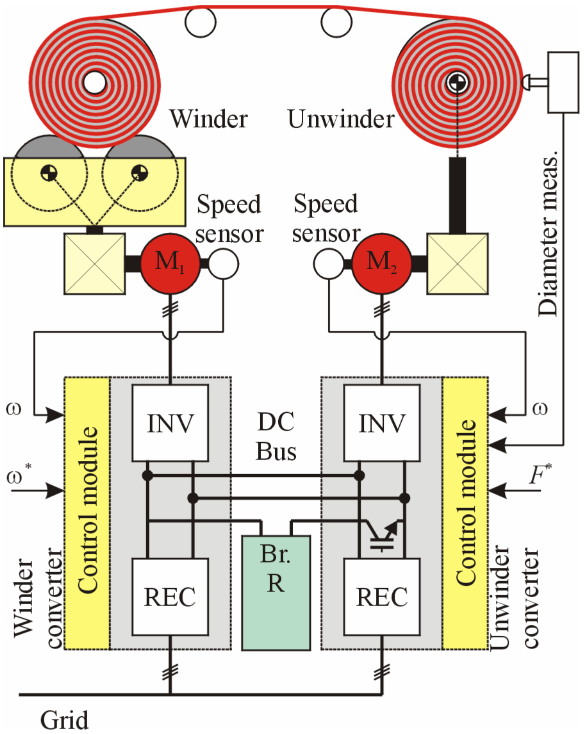

Fig.17. *The rewinder drive.*

Today, the controlled drives are most often realized with the frequency converters (AC-DC-AC). The converters usually utilize the diode rectifier units; that is the reason why the breaking resistors exist in the DC link. The principle reason is the price, in particular, the difference in the price for a 90kW recuperative power converter, and the converter with the breaking resistor is about 60%. This simple, but convincing reason is why the internal load sharing between the frequency converters is accomplished over the DC load bus. Fig 17 shows the basic block diagram of the rewinder drive, with the frequency converters and induction motors [11].

The converter for the unwinder drive is configured in the torque control loop, with the torque reference adapted to the change of the roll diameter, giving the tension force constant and equal to the reference value F^*. The winder drive converter is configured in the speed closed loop, to follow the speed reference ω^*. The DC links of the converters are connected to establish the load sharing. Besides that, the breaking resistor in the DC link is necessary, to consume the energy generated during the stop, when both drives break, producing the electric energy. The described concept of the drive assures the operation with minimum power requirements, equal to the losses in the system only.

5. REALIZATION AND APPLICATION EXAMPLES

The practical realizations of the controlled multimotor drive are very complex, considering the fact that the geometric layout for the drives and the converters, power supply, controll algorithm, the user interface, distribution of the reference, supervison and protection, must all be designed and planned ahead.

In a multi drive, the drive motors may be very distant form each other, but sometimes a number of motors, together with gear-boxes, should be packed in a small place, as is shown in Fig. 18.

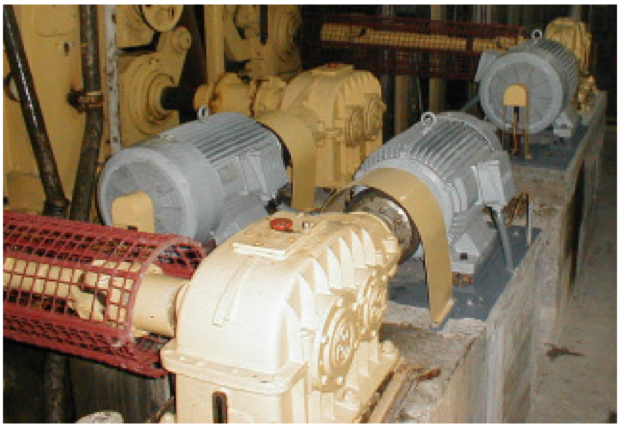

Fig.18. *Drive motors of the three presses in a board factory.*

Power distribution, together with the power converters can be placed a few tens of meters from the motors, requiring the placement of a few kilometers of power cables. Long cable lines can cause a number of difficulties, such as voltage drop, electromagnetic interference, considerable capacitive currents may occur in the drives with high carrier frequencies, etc.

The power converters of newer generation, used today, are very compact, enabling the packing of a great number of converters with high power ratings in a small space. Figure 19 shows the converters of a drive with 12 motors, with the total installed power of 460kW.

The distribution of control signals, references, measurement signals, requires the use of numerous signal cables. In the analog realization, the total length of the signal cables were several tens of kilometers, producing the serious problems. For example, the voltage drop on the reference speed signal may be above 10%, but the draw signal sometimes smaller than 1% of the total reference should be added. Similar problems exist in the protection system, a great number of contacts, tasters, relays, long cables, etc. make the maintenance and the repairs very difficult.

Fig.19. *The frequency converters in a multi drive.*

In modern controlled multi drives, the control and the protection system can be realized in many ways, but in all cases the use of a digital computer is mandatory. In the simple drives, the integrated resources of the power converter control system, with the modest support of a single computer can satisfy the requirements for the control and the protection system [8, 9]. Bigger drives require the support of powerful computer systems, e.g. the programmable logic controllers. Fig. 20 shows the rack with the complete system of control and the protection for the mentioned drive with 12 motors. The core of the system features the PLC that communicates with the power converters over the PROFIBUS protocol and with the total of 13 control panels over the MPI protocol. One panel controls the operation of each drive, while the 13th supervisory control panel incorporates all the information about the system state. The performance of the PLC enabled the load distribution controller to be implemented in the controller, over the profi-bus. However, basic protective functions, all-stop, and the trip of all the drives, is realized in the classical way, with relays, mainly because of the reaction speed. Fig. 20 shows the complete supply and control equipments placed in a standard double-sized rack. The upper part shows the supply components, and the lower, consisting of the PLC and the required relays. With the thyristor drive from the seventies, of the 20th century, this double rack was filled with the equipment for the single drive.

6. CONCLUSION

Analyzing and writing about the broad and complex subject, permits the authors to forget an issue, but it also permits the author to deliberately omit something. The author intended to consider the typical examples of the drives with high power ratings, but also the drives about he is entitled to consider. The drives that are very well known to him, studied both theoretically and practically, during the design, realization and finally successful commissioning.

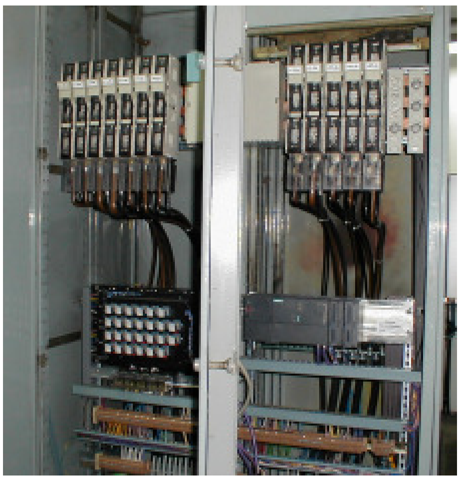

Fig.20. *The control and power equipments placed in a rack.*

7. REFERENCES

[1] Z. Stojiljković, B. Jeftenić, “The reconstruction and commisioning of the drive for the first press roll 2x4.5MW, during the reconstruction of the hot rolling mill”, in Serbian, SARTID, Smederevo, 1995.

[2] B.Jeftenić, “Electric drive for rotational excavator SRs1200”, in Serbian, MSEE thesis, ETF Beograd, 1977.

[3] B. Jeftenić, M. Gvozdenović, "Synchronized work of two controlled DC drives with resilient mechanical connection", Publications of the Faculty of Electrical, Belgrade, 1989.

[4] M.Bebić, B.Jeftenić, M.Belinčević, “Electric drive for a paper machine”, in Serbian, Ee'2001, Novi Sad, Nov. 2001.

[5] B. Jeftenić, M. Bebić, M. Krgović, “The Selection of Sectional Drives for Replacement of the Line Shaft Drive in A Paper Machine”, 7th Meeting of Pulp and Paper Industry of Balkan Countries, Novi Sad, 8-10 November, 2000.

[6] B.Jeftenić, M.Bebić, D.Jevtić, M.Belinčević, “The replacement of the line shaft drive in a paper machine with the sectional induction motor drives”, (in Serbian), *VII Jugoslav simpozium of celulose, paper, packaging and printing*, Zlatibor, 20-22. June 2001.

[7] B.Jeftenić, M.Bebić, D.Jevtić, “The load distribution with mechanically coupled drives”, (in Serbian), Ee'2001, Novi Sad, Nov. 2001.

[8] B. Jeftenić, M.Bebić, M. Milojević, “The reconstruction of the flying shear drive based on the frequency converters”, in Serbian, VI Jugoslav simpozium of celulose, paper, packaging and printing, Zlatibor, 14-16. June 2000.

[9] M. Bebić, B. Jeftenić, M. Belinčević, “The syncronization accuracy testing of the flying shear drive in the no-load conditions”, in Serbian, XLV ETRAN, Aranđelovac, 4-7 June 2001.

[10] M.Belinčević, M.Bebić, B. Jeftenić, “The control algorithm for synchronization of the flying shear drive”, in Serbian, Ee'2001, Novi Sad, Nov. 2001.

[11] B.Jeftenić, “The Rewinder Drive - the project for the paper mill Komuna Skopje”, in Serbian, Beograd, 2001

DEFINITIONS OF THE AVERAGE AND RMS VALUES SUITABLE FOR THE MEASUREMENT AND DESCRIPTIONS OF QUASI STEADY STATE

Petar N.Miljanic, Puskinova 9, Belgrade

Abstract: *Thanks to the development of fast, high precision and accurate analog-to digital converters and fast data processing facilities, it became possible to better define rms and average values and implement the asynchronous sampling when quasi-periodic quantities are measured. The adoption of the suggested definitions would contribute to the precision of the measurement at nearly steady state, as one has in the laboratory, and make possible meaningful measurements of rms and average values when steady state is partly established, as is the case in the industry. The soundness of the proposal is supported by theoretical and simulation investigations and actual measurements.*

Keywords: *average, root mean square, definitions, precision measurements, quasi steady state, asynchronous sampling.*

INTRODUCTION

Often, when high precision measurements are performed, the definition of a measured quantity had to be redefined. For example, the error of a current transformer is usually defined as the difference between the nominal ratio times the secondary current and the primary current, divided by the primary current. In this definition the notion of a current is related to the windings, presuming that the current which enters one terminal is equal to the current which exits the other terminal. However, this is not exactly true. Due to the capacitive currents between the windings they are not equal. So the definition of the error of a current transformer is redefined by stating that primary and secondary currents are those at the marked terminals when marked terminals are at the same potential. Even now the definition lacks precision. If the currents are distorted it must be said that the error is a phasor related to the fundamental harmonic. Of course the influencing quantities must be given, - like the value of a complex burden.

In a similar manner, when a high precision ac wattmeter is calibrated, one should not overlook the possible ambiguity regarding the connections of voltage and current terminals and their potential difference.

From these examples and many similar ones, one realizes that the precision in metrology very much depends on definitions, which must be easily understandable and in the same time without ambiguities. A loose definition is not a problem when the accuracy of the measurement is low, but such definition is inadequate in a high precision measurement. The precision of the measurement depends on the precision of the definition of the quantity, and vice versa, the requirement of the strict definition depends on the accuracy of the measurement.

A metrologist faces an another problem: is it possible to measure a quantity according to its definition? It is well known that a law is good if it can be enforced and applied. Likewise, a definition of a quantity is good if that quantity can be appropriately measured. A very strict definition is of no use if the measurement environment is such that a quantity cannot be measured according to that definition. Therefore, a compromise between the strictness and applicability must be obtained. In the following text an important question concerning ac measurement and definitions will be pointed out.

In Physics and Engineering the notion of rms (root mean square) and average values are often used and at the first glance everything seems to be very clear. Those notions are related to the periodic function. It is presumed that the alternating waves are in the condition called steady state. Although one knows that steady state is never completely established in reality, most measurements and investigations are successfully performed, even not mentioning how stable was the state. The minor changes of amplitude and frequency, unavoidable in the real circumstances, do not jeopardize the measurements. But if the high precision measurement is needed or the changes of frequency and amplitude are larger, the usual definitions of rms and average are not adequate.

Working on the establishment of the national standards for alternating voltage, current and power, at power frequency, the author was faced with the scattering of the results. It has been found that large standard deviations of results are due to the sampling method used. After the redefinition of rms and average values the standard deviations were reduced several dozen times. The remaining standard deviation, of the order of several ppm (parts per million), as it has been found, came mainly from the unstability of the power supplies and instruments used. Actually, with the redefined values of rms and average it became possible to see the instability of the measuring set up.

ASYNCHRONOUS VERSUS SYNCHRONOUS OR RANDOM SAMPLING

The synchronous and random digital sampling of periodic voltage and current waves have been extensively analyzed and instruments based on these methods have been made. Many papers describing these subjects were published [1] to [4]. On the other hand, the asynchronous sampling of waves, for establishing rms voltage, rms current and average power, was considered less precise. The fairly large errors were noticed due to the fact that asynchronously taken samples, used for the calculation of rms and average, do not belong exactly to one or several periods of the measured wave.

This paper will reveal that the measurement using the asynchronous sampling could be very precise if the interval of sampling ("window") is chosen using the new proposed method. And also, that the measurement of newly defined rms and average values with asynchronous sampling is applicable also at quasi-periodic cases, when amplitude and frequency vary during the measurement. The advantages of asynchronous versus synchronous or random sampling could be summarized as:

First, the measurement of ac quantities with asynchronous sampling is much simpler, avoiding the problems related to the synchronization of the instrument with the quantity to be measured. It is very well known that it is difficult to make adequately stable the multiplicators of frequency and the phase-lock-loops (PLL) and that they may introduce errors.

Secondly, the notions of root-mean-square and average quantities are expanded to quasi steady-state of periodic phenomena, a significant contribution to real measurement practice. The voltage or current source in the best laboratories, as is known, may vary for at least several parts per million, and in the industrial environment the variations may be much larger.

Essential facts:

When a sample of a group, close to the mean, is added or taken away, the mean does not change much. In the past, the interval of sampling, called "window", was usually chosen according to the crossing of the wave trough zero. With asynchronous sampling, if the "window" is selected in that way, one extra sample could cause the error equal to 1/n, n being the number of the samples taken during the measurement in that window. Obviously, this error could be very large, for example if n=500, the error could be 0.2%. But if the "window" is selected according to the passages of the wave trough its average values, the error is smaller more than two orders of magnitude.

New definitions:

The average value of a quasi periodic function at time t(m), when the function is equal to its average value, is the average of instantaneous values in the interval t(n)-t(m), where t(n) is the time when, approximately one or several periods before, the function was also equal to its average values.

The rms value of a quasi periodic function at time t(m), when the function is equal to its rms value, is equal to the square root of the average of the squared instantaneous values in the interval t(n)-t(m), where t(n) is the time when, approximately one or several period before, the function was also equal to its rms values.

The averages and rms are discrete quantities in time. The average and rms values, as well as the period, used in the above definitions, may be obtained by the recursive method.

Using the mathematics, for example the rms of an ac voltage at the distinct instant t_m, when the voltage approach its rms value, may be defined as

$$U_{rms(p)}(t_m) = \sqrt{\frac{1}{t_m - t_n} \int_{tn}^{tm} u(t)^2 dt}$$

where t_n is the instant when one or several (p) periods before the voltage approached the rms value.

Practical definitions or instruction for the measurement when asynchronous sampling is used:

The rms value is equal to the square root of the average of the squared samples taken in the interval which starts when the sample becomes larger (alternatively smaller) than the rms and ends when it becomes, after one or several periods, again larger (alternatively smaller) than the rms, omitting the last sample.

The average value is equal to the average of samples obtained in the interval which starts when the sample becomes larger (alternatively smaller) than the average and ends when it becomes, after one or several periods, again larger (alternatively smaller) than the average, omitting the last sample.

One period of the measurement is the minimum for a wave function with a dc component. When more periods are used the filtration of the variation of the rms or average values is introduced. The filtration is proportional to the number of periods taken into account.

Using the mathematics the rms value of, for example ac voltage, may be defined as

$$U_{rms(p)}(t^*) = \sqrt{\frac{1}{m-n} \sum_{s=n}^{m-1} u_s{}^2}$$

where t^* are the discrete instants of time for which the rms is calculated after the m^{th} sample has been taken, m being the number of the m^{th} sample when the measured voltage has become larger than its rms value, n being the number of the n^{th} sample when, one or several periods before, the voltage has become larger then the rms value, p being the number of periods used for the rms calculation.

Therefore, the rms value may be reported after each crossing of the wave trough its rms value; it may vary in time and its value depends on the number of periods (p) in which the samples were taken. For the wave with dc component p must be at least equal to 1. As p is a larger integer, the filtration of the wave is stronger.

Using the mathematics the average value of the electric power may be defined as

$$P_{ave(p)}(t^*) = \frac{1}{m-n} \sum_{s=n}^{m-1} u_s i_s$$

where t^* are the discrete instants of time for which the average power is calculated after m^{th} sample has been taken, m being the number of the m^{th} sample when the measured instantaneous power has become larger than the average value, n being the number of the n^{th} sample when, one or several (p) periods before, the instantaneous power has become larger then its average value, p being the number of periods used for the average power calculation.

The instants t^* for which the rms voltage, the rms current and the average power are calculated are not the same for voltage, for current and for power.

Comment:

RMS and average value, ac voltage, ac current and ac power, so defined, are discrete functions of time. Theoretically, they depend on the sampling rate and periods used during the calculation. When asynchronous sampling is implemented the results are also scattered. However, the simulation study and the actual high precision measurements proved that using these definitions and up to date fast and precision AD conversion and data processing, the repeatability and reproducibility of the measurements of voltage, current and power, at power frequencies, are of the order of several ppm.

CONCLUSIONS

The presented paper emphasizes the importance of a clear and strict definition of a quantity in accordance with precision needed and the feasibility of the measurement.

Using the new definitions of root mean square and average values, it was possible to distinguish which part of the standard deviation is due to the instability of the precision instrument under test and which part is due to the instability of the laboratory sources. It is also possible, using the data obtained with asynchronous sampling, to characterize the short-term stability of high precision ac voltage, current, and power calibrators.

The new definitions consider ac voltage, current and power as discrete quantities with the parameter p showing the number of periods during which these values are calculated. They do not require the steady-state. For example, the rms rotor current of a slip ring induction motor may be measured and plotted versus time. That current is an ac current with variable amplitude and frequency.

The applications of these definitions significantly contribute to the high precision measurements in the laboratories in which almost steady state condition is established. The essential investigations and experiments were carried out at the National Laboratory, were the Apparatus for the Yugoslav standards of ac voltage, current and power, at power frequency, was established Fig.1 [5].

It is shown that in spite of the fact that asynchronous sampling is used, by virtue of the novel calculating method, fast and precise evaluation of rms voltage, rms current and average power could be obtained. The measuring apparatus is assembled for the calibration of the instrument MSB [6], recognized high precision converter of ac power to dc voltage. The new measuring apparatus rely on the fast high precision integrating AD conversion and Volt and Ohm standards. The calibration of two MSB instruments were, using the new method, compared with the calibrated data obtained five years ago at PTB, and reproducibility of better than 30 ppm is confirmed.

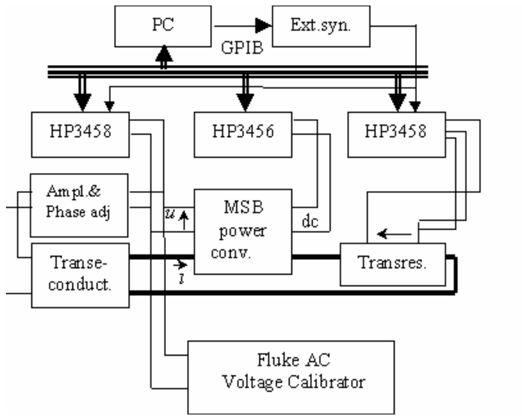

Fig1.

REFERENCES:

[1] Clarke F.J.J. and Stockton J.R.: *"Principles and theory of wattmeters operating on the basis of regulatory spaced sample pairs",* J.Phys.E: Sci.Instrum. 15(1982), pp.645-652.

[2] S.Svensson and K.-E.Rydler: *"A measuring system for the calibration of power analyzers",* IEEE Trans.Instrum.Meas., vol.44,pp.316-317, Apr.1995.

[3] R.Arseneau, p.S.Filipski, and J.J.Zelle: *"An improved three-phase digital recorder system for calibrating power instrumentation"*, IEEE Trans.Instrum.Meas., vol.46, pp.316-317, Apr. 1997.

[4] G.Ramm, H.Moser, and A.Braun: *"A new scheme for generating and measuring active, reactive and apparent power at power frequencies with uncertainties of 5 ppm"*, IEEE Trans.Instrum.Meas., vol.48, pp.422-423, Apr. 1999.

[5] Petar Miljanić, *"Etalon naizmeničnog napona, struje i snage",* Kongres metrologa Jugoslavije 2000, Novi Sad, 15-17 novembar 2000 godine.

[6] P.Miljanić, B.Stojanović, and P.Bošnjaković: *"The development of a high precision power meter",* IEEE Conf. Precision Electromagnetic Measur.Dig., Delft, The Netherlands, 1984, pp.67-68.

FUZZY LOGIC OR PI SPEED CONTROL IN HIGH PERFORMANCE AC DRIVES: WHICH IS PREFERABLE?

*Emil Levi, Zulkifilie Ibrahim **
Liverpool John Moores University, School of Engineering, Liverpool, UK;
** Instrumentation and Electronics Centre, SIRIM Berhad, Shah Alam, Malaysia*

Abstract: *A frequently discussed application of artificial intelligence in motion control is the replacement of a standard PI speed controller with a fuzzy logic (FL) speed controller. Common conclusion that emerges from such studies is that the FL control provides superior performance. However, such a conclusion is usually based on a limited simulation and/or experimental study. It appears that a thorough comparison of the drive behaviour under PI and FL speed control, using simulations and an experimental rig, is still missing. This paper attempts to provide such an in-depth comparison of operation of a vector controlled permanent magnet synchronous motor. Speed responses under PI and FL speed control are at first simulated and then measured on the experimental rig for a variety of operating conditions. Two different machines are used in simulation and experimentation. The transients studied include response to large step speed command from standstill with nominal inertia and an increased inertia, response to small step speed reference change, response to step load torque application and reversing transient. The transient behaviour is examined for various initial speed settings, so that a thorough comparison is enabled. It is shown that superiority of the FL speed control is much less pronounced than it is often portrayed in literature on the basis of limited comparisons. Indeed, in a number of cases PI speed control provided a superior speed response. Predictions obtained by simulations and experimental results are found to be in reasonable agreement, considering all the differences between the simulation and experimental study.*

Keywords: *Speed Control, Fuzzy Logic Control, PI Control, Permanent Magnet Synchronous Motor*

1. INTRODUCTION

A standard approach for speed control in industrial drives is to use a PI controller. Recent developments in artificial intelligence based control have brought into focus a possibility of replacing a PI speed controller with a fuzzy logic (FL) equivalent [1]. Fuzzy logic speed control is sometimes seen as the ultimate solution for high performance drives of the next generation [2].

Operation of a drive with speed control by PI and FL techniques has been compared on a number of occasions. Design of a speed controller is always based on the required response for a single operating point (called 'design case' further on). The existing comparisons fall into one of the two categories: speed response with PI and FL speed control for the design case is substantially different [3-9], or the speed response is more or less the same [10-15]. Comparisons related to the first category are meaningless and they only serve the purpose of proving superiority of the FL control. Any valid comparison necessitates such an initial tuning of the two controllers that the speed response for the design case is at least similar, if not identical [16-18].

Even when tuning of the controllers is appropriate so that a fair comparison is enabled, comparison is usually based on a very limited selection of transients [10,12-15]. These typically include one reference speed setting and application/removal of the load torque at one reference speed. Robustness testing is sometimes included as well, again for a single operating point. Comparison is usually based on the controller design for aperiodic speed response, in which case PI control is known to exhibit sluggish disturbance rejection properties [11]. However, provided that the controller tuning is appropriate, even limited selection of transients for comparison may indicate that FL speed control is not necessarily superior to PI speed control. Improvement of response obtained by FL control in [14] appears to be marginal. The same conclusion is arrived at in [15]. An indication that there are transients in which PI control will yield better response is provided in [10], while [12] shows some transients for which response of PI and FL control is essentially the same. Studies reported in [12,14] are based on simulation only, while [10,13,15] include some experimental results.

A rather thorough experimental study of [11] compares speed responses for load rejection transient, step application of the speed reference, and examines speed tracking capability and robustness to rotor resistance variation. It shows that better overall behaviour is obtainable with FL speed control. However, only a single reference speed setting is again elaborated. The most complete comparative analyses, available at present, are those of [16-18]. Simulation studies [16,17] examine speed response for various values of the speed reference and various controller settings for the design case. They conclude that there are essentially three possible situations, depending on the reference speed setting, transient under consideration, and controller tuning for the design case: better response with PI control, better response with FL control, and more or less the same speed response with both speed controllers. Corresponding experimental study of [18] proceeds along the same lines and compares speed responses obtainable with FL and PI speed control for a variety of transients and operating conditions. The experimental results of [18] confirm that the superiority of FL speed control is largely exaggerated in the existing literature and that there are operating regimes where PI control will yield a better response.

This paper summarises major results presented in [16-18] and therefore provides a detailed comparison of PI and FL speed control performance for a variety of operating conditions. Simulation results, obtained using Matlab/Simulink/Fuzzy Logic Toolbox, and experimental results, related to two different vector controlled permanent magnet synchronous machines (PMSM) are provided. In the experimental rig PI and FL speed controllers are designed and implemented using a PC.

The speed response to rated speed command under no-load conditions, with motor inertia only, is made as similar as possible (aperiodic), so that a fair comparison is enabled. This is regarded as the 'design case' for both simulations and experimental study. Transients considered in the simulation and experimental investigation are the following: application of step speed command other than rated, application of step load torque (disturbance rejection), small step reference speed change, and operation with inertia other than rated. In addition, reversing transient is studied in the experiments as well. The experiments described in the paper could be regarded as a proposal for benchmark tests for comparing the performance of various speed controllers [18].

It is shown that the only case in which FL control is always superior is the load rejection transient. However, even this superiority holds true only when the initial speed controller design is for the aperiodic speed response. If an overshoot is allowed for the design case, disturbance rejection properties of the two speed controllers can be the same in certain operating region [16]. In a number of transients other than this one, PI speed control provided better speed response. Considering the results of the study and taking into account the difficulties encountered in FL speed control implementation, discussed in [15] and [18], it is concluded that superiority of the FL speed control, claimed by many authors, is a rather relative notion.

Vector control of a three-phase current-fed induction or a permanent magnet synchronous machine converts the machine, from the control point of view, into its dc equivalent. It is therefore irrelevant whether the actual machine is a dc machine or a vector controlled ac machine. The results of the study apply to all high performance drives, provided that the speed control loop is under consideration.

2. DESCRIPTION OF THE DRIVE

A permanent magnet synchronous motor drive with rotor flux oriented control is illustrated in Fig. 1. Data of the machines used in simulations and experiments are given in Appendix. The PWM voltage source inverter is controlled by means of three independent hysteresis current controllers. The hysteresis band is adjusted for simulation purposes to ± 0.5 A (i.e., ± 5.7% of the rated current) and is kept constant. The inverter input dc voltage is set to the constant value of 220 V, so that sufficient voltage reserve is provided for operation with good current control at rated speed and maximum torque. Stator q-axis current is limited in accordance with the maximum allowed stator current rms value. Speed PI controller is provided with an anti wind-up mechanism. In the experimental system dc link voltage is equal to 330 V and the hysteresis band equals ±0.2 A, while the stator q-axis current is limited to 2 A. Hysteresis current control is realised using analogue means.

The FL speed controller, illustrated in Fig. 2, is of standard structure with inputs of speed error and change of speed error. As a FL controller on its own is essentially a PD controller equivalent, output of the speed FL controller is integrated in order to yield PI like behaviour. Also, an equivalent anti wind-up feature is included.

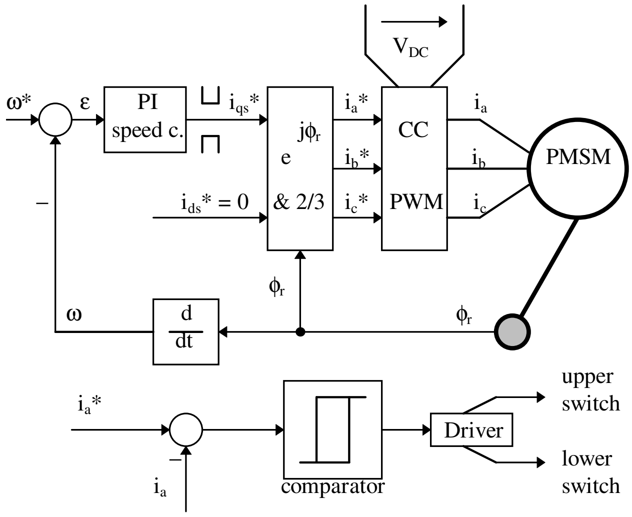

Fig. 1. *Configuration of a rotor flux oriented permanent magnet synchronous motor (PMSM) drive and illustration of a hysteresis current controller.*

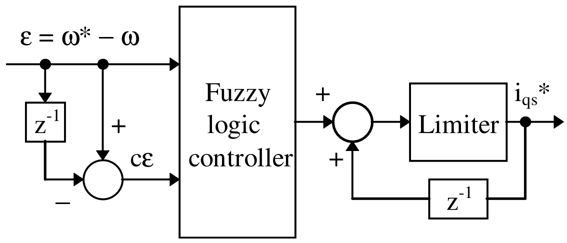

Fig. 2. *Fuzzy logic speed controller.*

The fuzzy logic controller, used in simulations, consists of triangular membership functions with overlap, seven for speed error and seven for the change of speed error, so that a 7x7 rule base is created. The width of the membership functions is reduced in vicinity of zero error, zero change of error and zero stator q-axis current command in order to obtain better steady-state accuracy. Input and output scaling factors are selected, through many simulation runs, in such a way that speed response to the step rated speed command matches as closely as possible the response obtained with PI controller. Initial tuning of the two speed controllers is discussed in the next section.

In the experimental rig fuzzy logic speed controller is implemented using PC and Fuzzy Logic, Simulink and the Real-time Workshop Toolboxes. It should be noted that speed control is the only part of the control algorithm implemented in the 166 MHz Pentium PC. Co-ordinate transformation is realised by means of AD2S100 single processor chip. Position of the drive is measured using a 6-pole resolver. The resolver to digital converter is based on AD2S80A chip. The chip provides a signal proportional to the speed of rotation, that is used to record the actual speed. This signal is, after 12 bit A/D conversion, used as the feedback speed signal for the speed control algorithm as well. Regardless of the fact that only the speed control algorithm calculation takes place in the software, it was found necessary to considerably simplify the FL speed controller since the implementation of the FL speed control in real time was found to be impossible with the minimum prescribed speed control loop sampling frequency of 2.5 kHz. Total number of rules, initially equal to 49, was reduced to 20 rules. This enabled processing time to be reduced to 0.33 ms, so that the required 2.5 kHz frequency could be met (all the subsequent experimental results are obtained with 2.5 kHz sampling frequency). Rule base is modified by removing rules related to medium positive, and medium and large negative speed errors. This modification has a minor impact on all the transients to be considered further on, except for the reversing transient. However, reversing transient is studied only experimentally and the results are not taken into account for comparative purposes. Table 1 illustrates the rule base of the FL speed controller used in the actual implementation. It should be noted as well that the membership functions used in the experimental FL speed controller are of equal widths and with symmetrical peaks, in contrast to the FL speed controller used in simulations.

Table 1. *Implemented FL speed controller rule base.*

ce | e	NL	NM	NS	ZE	PS	PM	PL
NL							
NM			NL	NM	NS		PS
NS			NM	NS	ZE		PM
ZE			NS	ZE	PS		PL
PS			ZE	PS	PM		PL
PM			PS	PM	PL		PL
PL							

3. INITIAL TUNING OF PI AND FL SPEED CONTROLLERS

The PI controller is designed first, on the basis of the speed response to the step rated speed command (180 rad/s) under no-load conditions with rated inertia. The design criteria are set in terms of a speed overshoot less than 0.1 rad/s and minimum rise time considering the limited current capability of the inverter (essentially, aperiodic speed response). Fine tuning to the specification is achieved by trial and error. The FL controller is designed next, using trial and error to achieve as similar response as possible to the one obtained with the PI controller. Figure 3 shows a sample of simulation results and it applies to operation with FL speed controller. Rated step speed command is applied at zero time under no-load conditions. Next, rated load torque is applied at time instant t = 0.025 sec. Finally, speed reference is reduced to 0.9 of the previous setting at time instant t = 0.08 sec. The speed response, d-axis current and reference and actual stator q-axis current are shown.

It is difficult to draw any viable conclusions from traces such as those of Fig. 3, regarding comparison of the drive behaviour under PI and FL speed control. The speed response traces are therefore overlapped and zoomed. The same approach is utilised further in displaying simulation results that apply to other operating conditions and in experimental investigation.

Figure 4 shows zoomed speed responses to the rated speed command application (180 rad/s) at zero time instant, under no-load conditions, obtained using PI and FL speed control. Response of the PI control results in no overshoot, while FL control yields an overshoot of less than 0.1 rad/s. Rise and settling times of the two controllers are effectively the same. The two responses are believed to be close enough, so that a fair comparison is possible for other operating regimes. It should be noted that the bold (blue) trace in Fig. 4 and the subsequent simulation figures corresponds to the PI controller speed response.

The same approach to initial tuning is maintained in the experimental investigation. Experimentally recorded speed responses to rated step speed command of 3000 rpm, under no-load conditions, obtained using PI and FL speed controllers, are illustrated in Fig. 5. Although the two responses are not identical (PI speed control response is somewhat slower), it is believed that the two responses are close enough to enable a good comparison for other transients. Once more, bold (black) trace in Fig. 5 and in all subsequent experimental figures represents PI control speed response, while grey (blue) trace is the one obtained with FL speed control.

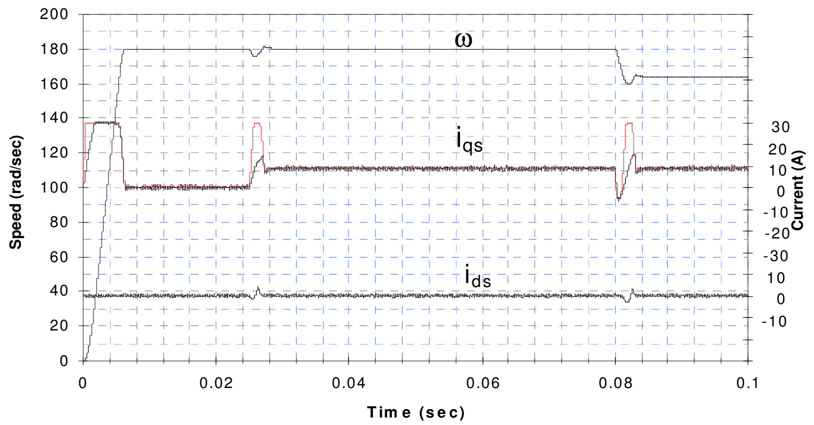

Fig. 3. *Response of the drive to step rated speed command, application of rated load torque and step reduction of the speed reference to 0.9 of the previous setting with FL speed controller*

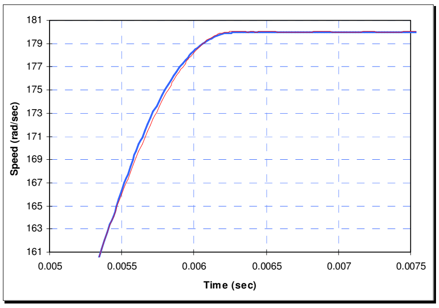

Fig. 4. *Comparison of responses with PI and FL speed control (rated step speed command form standstill, no-load conditions).*

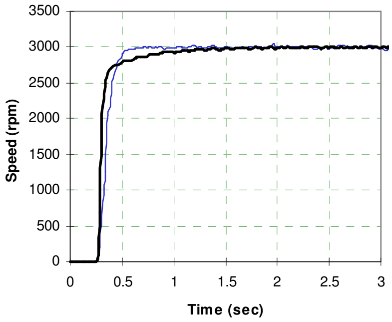

Fig. 5. *Experimentally obtained speed responses with PI and FL speed control (rated step speed command from standstill, no-load conditions).*

4. RESULTS OF THE SIMULATION STUDY

Simulation of the type shown in Fig. 3 is repeated for a number of settings of the initial speed command value. The drive always starts from standstill, the applied load torque always equals rated value, and the speed command is always reduced by 10% of the previous steady-state value. As an example, Fig. 6a compares responses obtained for the initial speed command setting of 40 rad/s. While the disturbance rejection is undoubtedly superior with the FL speed control (Fig. 6b at speed of 90 rad/s), it appears from Fig. 6a that the PI speed control leads to far better response to the step speed command. Response with FL control is very oscillatory and the settling time is much longer, while the overshoot is the same as with PI control. Similarly, response to the small speed reference reduction (Fig. 6c, 10% reduction from initial 60 rad/s value) is better with PI control since the settling time is much shorter. The results reported in Fig. 6 are deliberately selected for the cases when operation with PI control appears to be better than operation with FL control. The only viable conclusion that one could arrive at on the basis of Fig. 6 is that PI control is to be preferred to FL control. Such a conclusion would however be quite erroneous and the previous analysis indicates how misleading improper selection of transients for comparison can be. The overall situation, across the entire speed control range, is much more complex, as shown next.

The same type of study, reported in Fig. 3, is performed over the range of operating speeds from 10 rad/s up to the rated speed (180 rad/s). Overshoot in speed response for large reference speed change, dip due to load torque application and undershoot that follows small reference speed change are measured for PI and FL control, together with the duration of the transient (which is taken as the time needed for the speed error to become smaller than 0.1 rad/s). Results are summarised in Fig. 7. Speed response overshoot/dip/undershoot and settling/restoration time are given. Every attempt was made to provide as accurate readings as possible in compiling data given in Fig. 7. Some errors are however inevitable and these results should be viewed as indicative rather than absolute.

Response to the large step speed reference change is basically the same with PI and FL control for aperiodic design, Fig. 7a, for speed commands between 120 and 180 rad/s. FL control is superior between 40 and 120 rad/s, while PI control is better up to 40 rad/s. Disturbance rejection is better with FL control in all the cases (Fig. 7b). Response to small step speed reference change (Fig. 7c) is better with PI control for initial speeds up to 60 rad/s; from 60 to 180 rad/s response is better with FL control.

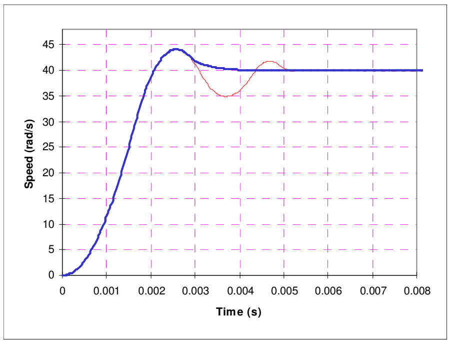

a.

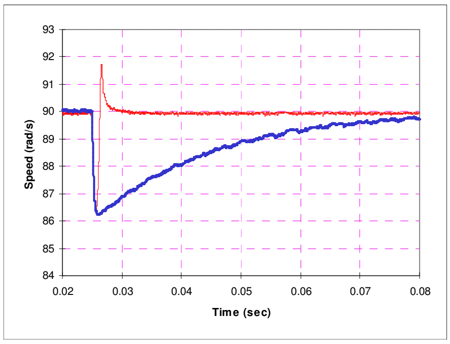

b.

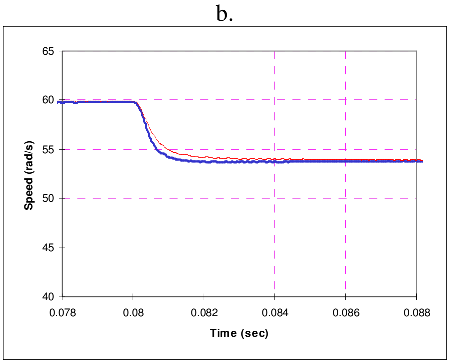

c.

Fig. 6. *Comparison of PI (bold-blue) and FL (grey-red) speed control response for zero overshoot design: a) step change of speed reference from zero to 40 rad/s; b) rated load torque application at 90 rad/s speed; c) change of speed reference from 60 rad/s to 0.9 times previous setting.*

Finally, impact of inertia variation on speed response is examined by simulation. Two tests are conducted. At first, it is assumed that inertia is ten times higher than the one used for controller design. The response to rated speed command and subsequent rated load torque application (at t = 0.2 s) is compared for this case in Fig. 8. As expected, operation of the FL speed controller is in this case superior. This is indeed the situation that is most frequently discussed in the literature and used to underpin the conclusion that operation of the drive with FL speed control is far better than operation with PI control. PI speed controller yields a higher overshoot with much longer settling time for the rated speed command and higher undershoot with longer restoration time for load torque application. The second test is the same, except that now it is assumed that inertia is only 0.3 times the value used in the controller design. Comparison of results for this decrease in system inertia is shown in Fig. 9. It is evident that now both controllers give poor, highly oscillatory response to rated speed command. However, the FL controller takes more time to establish steady-state operation. Undershoot in speed response to rated load torque application is the same for both controllers. PI controller has a long restoration time, while FL controller leads to oscillations in speed response.

5. RESULTS OF THE EXPERIMENTAL STUDY

5.1. Response to step speed command from stand-still, rated inertia

The drive is initially at standstill without any load connected to the shaft. Fig. 10 presents recorded speed responses for speed references equal to 1000, 1500, 2000 and 2500 rpm (3000 rpm case is shown in Fig. 5). FL speed controller provides very good speed response in all the cases, consistent with the one of Fig. 5. The response remains aperiodic for all the speed commands except for 1000 rpm, and the settling time is very much the same for all the speed references. In contrast to this, the response with PI speed control worsens as the speed reference is reduced. Although it remains aperiodic in all the cases, the settling time increases with the decrease in the reference speed setting.

5.2. Response to 10% step reduction of the speed command, rated inertia

Response to large step speed reference represents a transient during which operation in the current limit normally takes place. As the motor was accelerated without the load connected to the shaft, operation in the current limit took place for a very short period of time for transients of Fig. 5 and 10. However, once when the load is connected (Sub-section 5.3), operation in the current limit during prolonged time intervals will take place. In contrast to this, small change in the reference speed setting does not require operation in the current limit regardless of whether the load is connected or not.

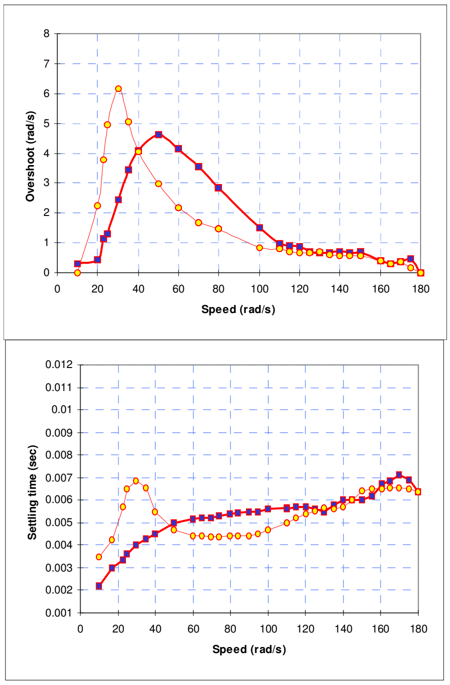

a.

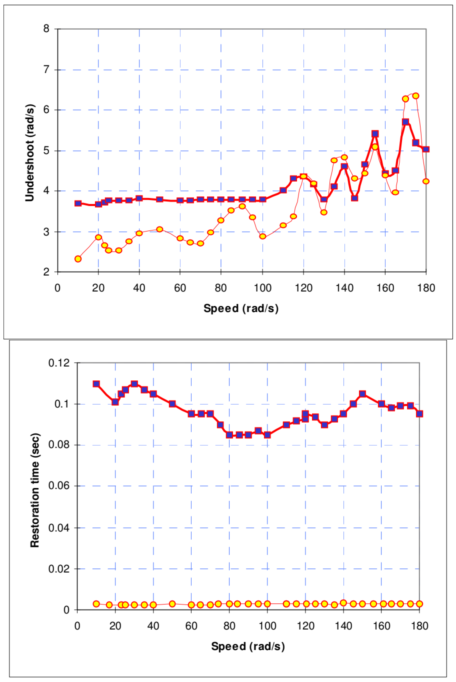

b.

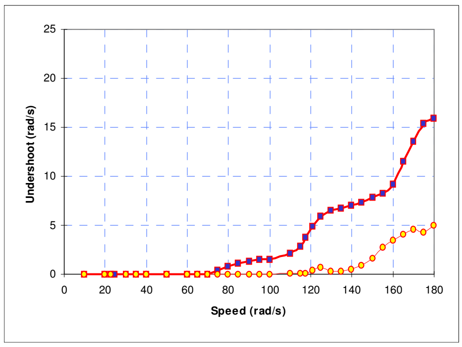

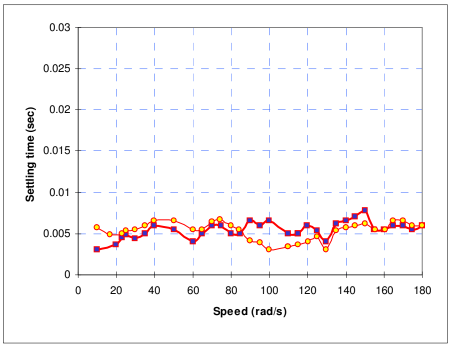

c.

Fig. 7. *Comparison of PI (bold-red) and FL (grey-yellow) speed control over the entire speed region:*
a) speed overshoot and settling time for step application of large speed command;
b) dip in speed and restoration time for rated load torque application;
c) speed undershoot and settling time for small step-wise change in speed command.

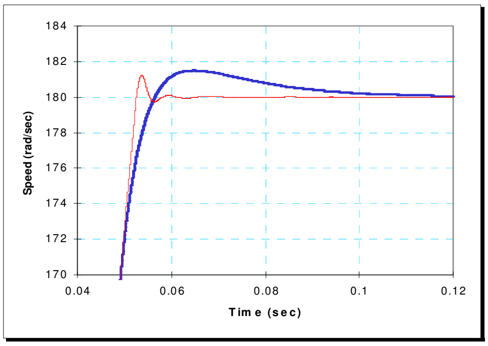

a.

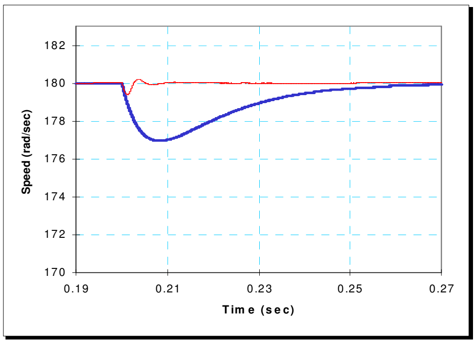

b.

Fig. 8. *Comparison of responses obtained with PI (bold-blue) and FL (grey-red) speed controllers: response to rated step speed command (a.) and response to step rated torque application (b.) (inertia ten times higher than in controller design).*

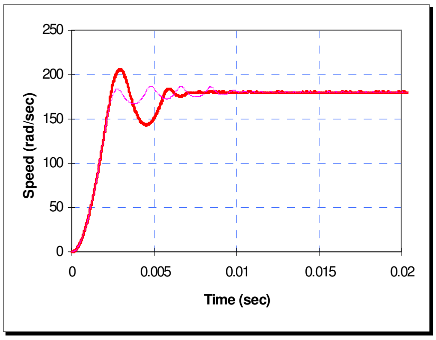

a.

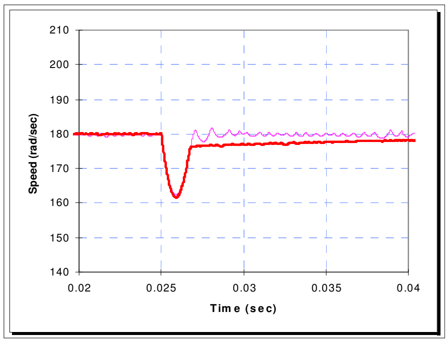

b.

Fig. 9. Comparison of responses obtained with PI (bold-red) and FL (grey-pink) speed controllers: response to rated step speed command (a.) and response to step rated torque application (b.) (inertia 0.3 times the one used in the controller design)

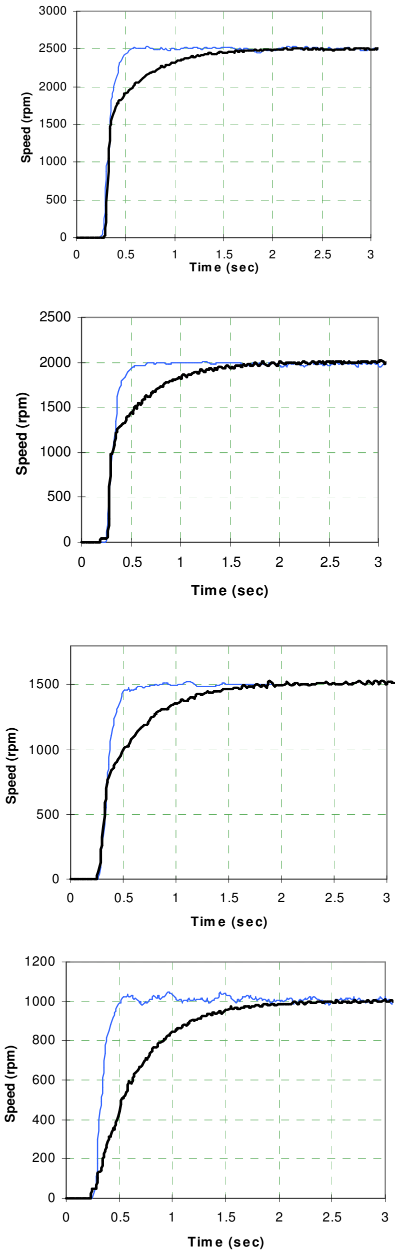

Fig. 10. *Response to 2500, 2000, 1500 and 1000 rpm step speed commands from standstill (rated inertia)*

The machine initially operates in a steady-state arrived at in Figs. 5 and 10. A step speed command reduction, equal to 10% of the previous reference setting, is applied. The results are given in Fig. 11. Response obtained with PI speed controller is much better in terms of both the undershoot and the settling time for all the initial speed settings. This is a consequence of the fact that PI speed controller is characterised with a slightly slower speed response (Fig. 5), which is now beneficial.

5.3. Response to step speed command from stand-still, increased inertia

PMSM is now coupled to a DC motor, whose armature terminals are left open. An effective increase in inertia is therefore achieved, of the order of 3:1. As the DC motor rated speed is 2000 rpm, testing is restricted to at most this speed value. Fig. 12 shows response to application of step speed references equal to 2000, 1500 and 1000 rpm. Operation in the current limit now takes place for a prolonged period of time, as shown by means of current traces for the 2000 rpm acceleration transient.

FL speed controller yields superior response for the 2000 rpm speed reference, with small overshoot and short settling time. Better robustness with respect to inertia variation is one of the most frequently cited advantages of the FL speed control over the PI control. However, decrease in the speed reference setting leads to substantial deterioration of the speed response with FL control. Overshoot for 1500 rpm and 1000 rpm reference settings is around 110 rpm with PI control, while with FL control it is 240 rpm and 340 rpm, respectively. Settling time is approximately the same.

Response to 10% step reduction of the speed command with increased inertia remains very similar to the one with rated inertia (that is, better response is obtained with PI controller) and these results, available in [18], are therefore omitted.

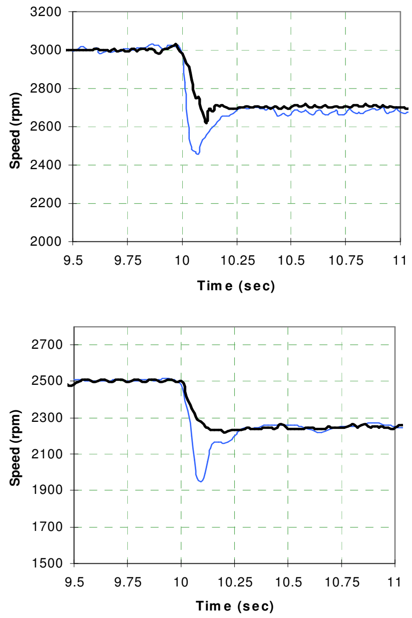

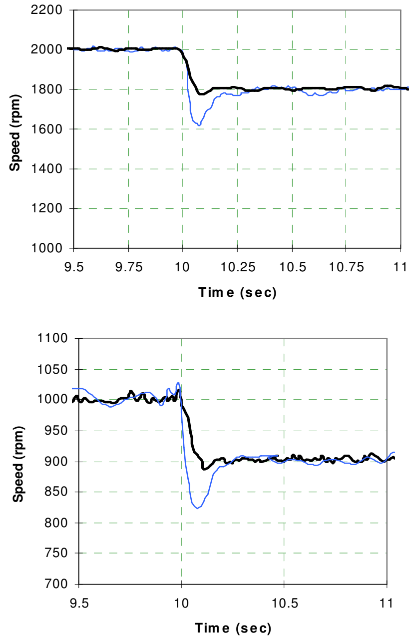

Fig. 11. *Response to step 10% speed reference reduction (rated inertia; previous steady-states in Figs. 5 and 10).*

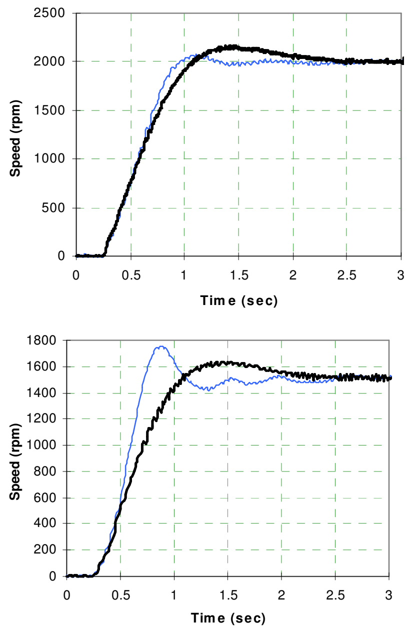

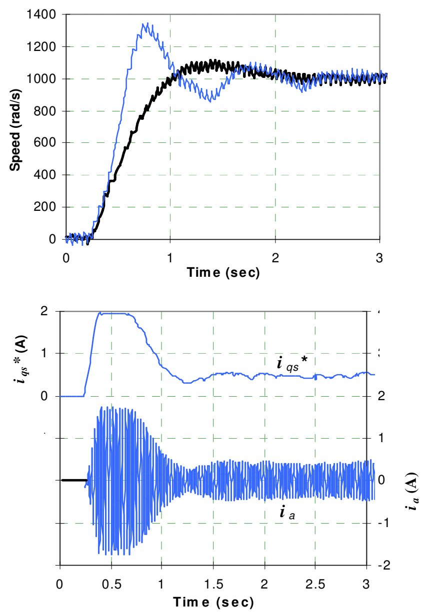

Fig. 12. *Speed response to 2000, 1500 and 1000 rpm step speed commands from standstill and current responses for 2000 rpm transient (increased inertia).*

5.4. Load rejection transients

Load is applied in a step-wise manner in steady-state no-load operation, by connecting the DC motor armature terminals to a resistance bank. If the resistance bank setting is constant, the load torque seen by the PMSM is approximately proportional to the speed of rotation. In order to emulate the constant load torque behaviour at different speeds, the resistance bank setting is changed appropriately for each speed at which testing is performed. Results of the load rejection transient are given in Fig. 13 for 2000, 1500 and 1000 rpm reference speed settings. FL speed control offers superior speed response, with smaller speed dip and shorter recovery time, regardless of the speed reference setting. This is another frequently cited advantage of the FL speed control that is, in contrast to robustness to inertia variation, fully verified by the results of Fig. 13.

5.5. Reversing transient

Speed reversal transient is investigated with the DC motor disconnected, so that rated inertia condition applies. Results are given in Fig. 14 for initial speed settings of 3000 and 1000 rpm. PI speed controller yields a rapid speed reversal with either no overshoot or with very small overshoot. On the other hand, FL speed control is characterised with large speed overshoot. It should be noted that this transient is affected to a great extent by omission of rules in the FL rule base, related to medium and large negative speed errors. The results related to this transient cannot therefore constitute a basis for a valid

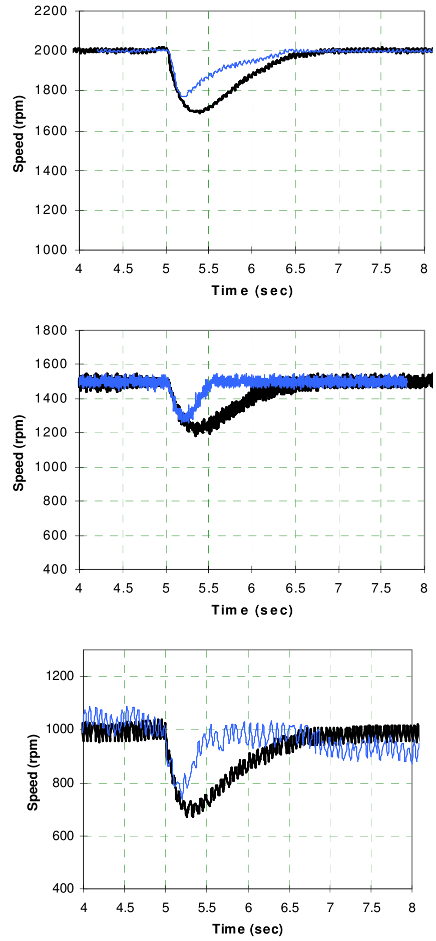

Fig. 13. *Response to step load torque application at 2000, 1500 and 1000 rpm reference speed settings.*

comparison. However, complexity of the FL speed control algorithm has made in this case the implementation of the full FL controller impossible, so that the deterioration in the speed response for the reversing transient represents an unavoidable trade-off between the performance and the acceptable complexity and demands imposed on hardware in implementation.

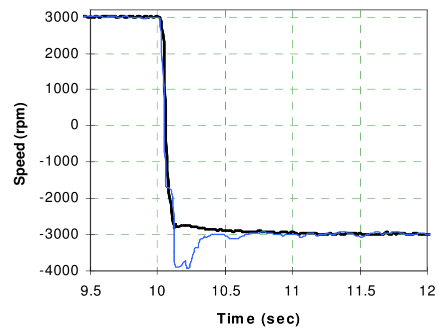

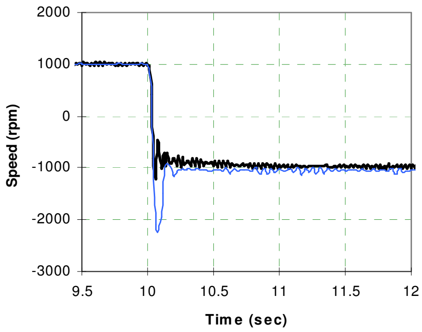

Fig. 14. *Reversing transient, 3000 and 1000 rpm reference speed settings*.

6. CONCLUSION

The paper presents results of an extensive comparative simulation and experimental study, related to PI and FL speed control in high performance drives. Transients encompassed by the study include speed response from standstill to large step speed reference application (with rated and with increased inertia), speed response to small step reference speed change (with rated and with increased inertia), load rejection transient and reversing transient. The transients are examined for a variety of different speed commands, thus enabling a thorough comparison to be made. The main conclusions may be summarised as follows:

- Simulation and experimental results are in full agreement as related to the load rejection properties of the PI and FL speed controller. FL speed controller provides a superior response for all the operating conditions. However, it has to be noted that this is valid only if the controllers are designed for zero overshoot. If a small overshoot is allowed in the design, load rejection capability of the PI speed control may be better than with FL control at some speed settings [16].
- Robustness of the drive to an increase in inertia is universally claimed as one of the main advantages of the FL speed control. While simulation results seem to support this claim (response for only one operating point was studied), the experimental results show that this is not necessarily the case. The robustness depends on the setting of the speed reference. PI control delivered better speed response for two out of three speed settings.
- Speed response to small reference speed change depends on how close the speed responses of the two controllers are for the design point (rated step speed reference with rated inertia here). PI speed controller has demonstrated in the experimental work much better response to all the small reference speed changes, primarily because its response for the design point was slightly slower. Simulation studies suggest that there are speed regions where the two controllers offer at least the same response and in some cases PI speed controller yields better response.
- The paper clearly shows that a detailed comparative analysis of the drive performance should always be performed when a new type of a speed controller is proposed as a substitution for the PI controller. Comparison based on a single operating point or a single transient is more than obviously insufficient.

Considering all the differences between the simulation study and the experimental rig (different motor types, different structure and complexity of the FL controller, inevitable idealisations in the drive modelling, etc.) it seems fair to say that the simulation and experimental results are in good agreement.

The dependence of the speed controller response on the speed set point is usually overlooked. The testing procedure for the speed controller performance, followed here, may be regarded as a proposal for a set of benchmark tests in evaluation of the controller performance. The procedure is detailed in [18].

7. REFERENCES

[1] B.K.Bose, “Expert systems, fuzzy logic, and neural network applications in power electronics and motion control,” Proc. of the IEEE, Vol. 82, No. 8, 1994, pp. 1303-1323.

[2] P.Vas, *“Artificial-intelligence-based electric machines and drives”*, Oxford University Press, New York, 1999.

[3] P.Vas, J.Chen, A.F.Stronach, “Fuzzy control of dc drives,” *25th Int. Power Conv. & Intelligent Motion Conf. PCIM*, Nuremberg, Germany, 1994, pp. 11-31.

[4] G.C.D.Sousa, B.K.Bose, “A fuzzy set theory based control of a phase-controlled converter DC machine drive,” IEEE Trans. on Ind. Appl., Vol. 30, No. 1, 1994, pp. 34-44.

[5] A.Ibaliden, P.Goureau, “Fuzzy robust speed control of induction motor,” *Int. Conf. on Electrical Machines ICEM*, pt. III, Vigo, Spain, 1996, pp. 168-173.

[6] M.Bossak, M.Bauer, “Robust speed and position control of an indirect field oriented controlled induction motor drive using fuzzy logic regulator,” *Int. Conf. on Electrical Machines ICEM*, pt. I, Vigo, Spain, 1996, pp. 219-224.

[7] L.Baghli, H.Razik, A.Rezzoug, “Comparison between fuzzy and classical speed control within a field oriented method for induction motors,” *7th Eur. Conf. Power Elec. & Appl. EPE*, Trondheim, Norway, 1997, pp. 2.444-2.448.

[8] F.Mrad, G.Deeb, “Experimental comparative analysis of conventional, fuzzy logic, and adaptive fuzzy logic controllers,” *IEEE Ind. Appl. Soc. Annu. Meet. IAS’99,* Phoenix, Arizona, 1999, CD-ROM Paper No. 15_6.

[9] D.Hissel, P.Maussian, G.Gateau, J.Faucher, “Fuzzy logic control optimization of electrical systems using experimental designs,” *7th Eur. Conf. Power Elec. & Appl. EPE*, Trondheim, Norway, 1997, pp. 1.090-1.095.

[10] D.Fodor, J.Vass, Z.Katona, “Embedded controller board for field-oriented AC drives,” *IEEE Int. Conf. on Ind. Elec., Control, and Inst. IECON’97,* New Orleans, LA, 1997, pp. 1022-1027.

[11] B.Heber, L.Xu, Y.Tang, "Fuzzy logic enhanced speed control of an indirect field oriented induction motor drive," IEEE Trans. Power Electronics, Vol. 12, No. 5, 1997, pp. 772-778.

[12] V.Donescu, D.O.Neacsu, G.Griva, F.Profumo; "A systematic design method for fuzzy logic speed controller for brushless DC motor drives," *IEEE Power Elec. Spec. Conf. PESC*, Baveno, Italy, 1996, pp. 689-694.

[13] F.Betin, M.Deloizy, C.Goeldel, "Closed loop control of a stepping motor drive: comparison between PID control, self tuning regulation and fuzzy logic control," EPE Journal, Vol. 8, No. 1-2, 1999, pp. 33-39.

[14] W.G. da Silva, P.P.Acarnley, "Fuzzy logic controlled dc motor drive in the presence of load disturbance," *7th Eur. Conf. Power Elec. & Appl. EPE*, Trondheim, Norway, 1997, pp. 2.386.-2.391.

[15] J.Fonseca, J.L.Afonso, J.S.Martins, C.Couto, "Fuzzy logic speed control of an induction motor," Microprocessors and Microsystems, Vol. 22, 1999, pp. 523-534.

[16] Z.Ibrahim, E.Levi, "A detailed comparative analysis of fuzzy logic and PI speed control in high performance drives," *IEE Int. Conf. Power Elec. & Variable Speed Drives PEVD,* London, UK, 1998, pp. 638-643.

[17] Z.Ibrahim, E.Levi, D.Williams, "Fuzzy logic versus PI speed control of servo drives: a comparison," *8th Int. Power Electronics and Motion Control Conf. PEMC,* Prague, Czech Republic, 1998, pp. 4.34-4.39.

[18] Z.Ibrahim, E.Levi, "A comparative analysis of fuzzy logic and PI speed control in high performance AC drives using experimental approach," *IEEE Industry Appl. Society Annual Meeting IAS*, Rome, Italy, 2000, CD-ROM Paper No. 30_03.

8. ACKNOWLEDGEMENT

The work described in the paper has been conducted at the Liverpool John Moores University, where Dr. Ibrahim studied for his PhD degree from 1995 till 1999. The authors gratefully acknowledge financial support provided by the Standards and Industrial Research Institute of Malaysia (SIRIM Berhad) to the first named author, in a form of the PhD studentship. The authors are indebted to

Analog Devices for provision of samples of the resolver-to-digital converter chip AD2S80A and the vector transformation chip AD2S100.

9. APPENDIX: MOTOR DATA

Motor Data	**Simulations**	**Experiments**
Rated torque (Nm)	6.1	1.7
Rated current (A)	6.2	2.7
Peak current (A)	21	10
Rated speed (rpm)	1720	3000
Inertia (kgm^2)	0.00176	0.000256
Rated frequency (Hz)	86	150
Pole pair number	3	3
DC link voltage (V)	220	320

STATE OF THE ART OF VARIABLE SPEED WIND TURBINES

Dejan Schreiber, Application Manager, SEMIKRON International
Sigmundstrasse 200, 90431 Nuremberg, Germany
Phone: +49 911 6559 278 fax: +49 911 6559 293
e-mail: d.schreiber@semikron.com

Abstract: *Variable speed wind turbines are a growing, dominant principle of design for power converters applied in wind power turbines today. Up to 60% of all wind turbines built in the near past are variable speed wind turbines, surely 70% of the ones built in 2001, and up to 80% of these that will be built in 2002. The recent plans for large, high-power, offshore Wind Parks with power of 0.2-2 GW all include variable speed wind turbines.*

Variable speed wind turbines can use more wind, due to the fact that they adapt to the particularity of the wind power itself - the changeable force of the wind. They start at lower wind speeds, and increase the power with speed. The design itself may be more demanding than classic, constant-speed turbine, but the reported energy increase of up to 10% is rewarding.

SEMIKRON has delivered power converters for variable speed wind turbines to various suppliers and wind turbine manufacturers, with different circuit configurations and designs. Most solutions are the so-called IGBT STACKs configurations, IGBT together with heat sink, DC link capacitors, built in protection features, insulation and auxiliary power supply. Power STACKs are delivered for up to 480V grid voltage, with a 1200V IGBT. For the grid voltages of 690V, IGBTs of 1700V are used. All such delivered power systems are 100% tested in application conditions, and ready to use. Proper sizing of converters in the whole operation cycle is possible using SEMIKRON calculation software, SEMISEL, available on Internet, on the www.semikron.com page.

The applied circuit designs, with their benefits and disadvantages, are shown and explained. The existing solutions include solutions for Asynchronous Induction Generator and for Synchronous Generator. All these circuits have been built and delivered, in power ranges from 500 kW up to 2.5 MW. Typical construction designs is shown.

For higher wind turbine power ranges, spatially for the offshore applications, recommended solution would be medium and high voltage drive. That are the wind turbines with the generator voltage in the range of 3.3kV, as well as 4.2kV or 6.3kV, and more. The corresponding semiconductor power converters are completely new constructed.

Key Words: ***Power Electronics, wind power, IGBT, variable drive***

INTRODUCTION

In general, there are two wind power generator principles. An old and very simple one, is with constant, fixed rotor speed. Generator is a simple ac induction motor, with squirrel cage rotor, connected direct, (or via transformer), to the utility grid. Generator mode of operation started when the rotor speed is higher than synchronous speed.

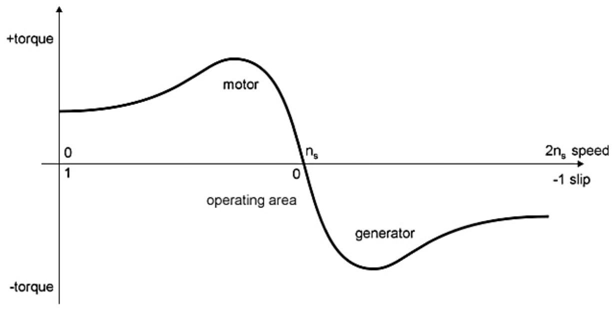

Fig.1. *Torque vs. Speed, (slip)*

The advantage of such construction is that it is very simple. Power electronics part is only W3C, Thyristor circuit, called soft starter, used for starting-up procedure. Wind turbine can produce the power, only if the wind is strong enough, and the rotor speed is higher than the synchronous speed. Control of the produced power, when the wind is stronger, is only possible due to mechanical pitch control of the blades. (In case of weak wind, the rotor blades are in the "full open" position, "catching" the whole wind energy. When the wind is stronger than rated value, (approximately 12m/s), pitch control will take the rotor blades in the position that only a part of wind energy is "caught". Such mechanical control is slow, and the transient overload conditions are very often and large. That produce the mechanical stress and the vibrations of the tower. For the larger wind turbines, 1.5 MW or more, with rotor diameter over 70m, the investment for the stronger towers are very high, comparing to the other wind turbine principles, such as the principle with variable rotor speed.

Variable speed wind turbines are a growing, dominant principle of design for power converters applied in wind power turbines today. Up to 60% of all wind turbines built in the near past are variable speed wind turbines, surely 70% of the ones built in 2000, and up to 75% of these that will be built in 2001. The recent plans for large, high-power, offshore Wind Parks with power of 0.2-2 GW all include variable speed wind turbines.

Variable speed wind turbines can use more wind, due to the fact that they adapt to the particularity of the wind power itself - the changeable force of the wind. They start at lower wind speeds, and increase the power with speed. The design itself may be more demanding than classic, constant-speed turbine, but the reported energy increase of up to 10%, or 15% is rewarding.

The principle is similar to the variable speed as motor 4-qudrant drive. Fig.1 shows torque vs. speed characteristics for the constant motor voltage supply frequency. If the supply frequency is lower, or higher, we will have the family of the characteristics, shown on

Fig.2. We can see that the generator mode of operation is possible to achieve at the different rotor speeds, if the supply frequency is changed.

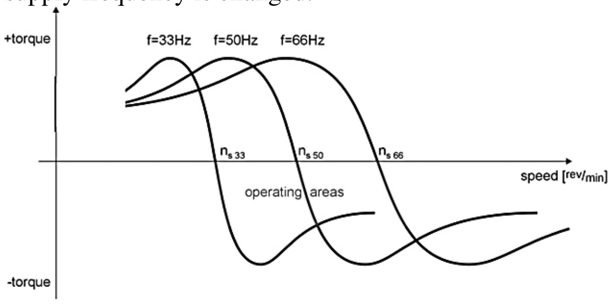

Fig. 2. *Torque vs. speed with the full line-side converter and motor side inverter*

With advancements in power electronics components, especially IGBT-a, such complex solutions became reality, with efficient cost, exploitation, and reliability.

PRINCIPLES OF VARIABLE SPEED WIND TURBINES

For the variable speed wind turbines, several power electronics circuit are in use, with induction or synchronous motor, used as a generator.

The commonly used circuits are:

1. Simple induction, squirrel cage motor

Rare, but using a synchronous motor, with line side converter and motor side inverter, both for full generated power, shown on Fig. 3.

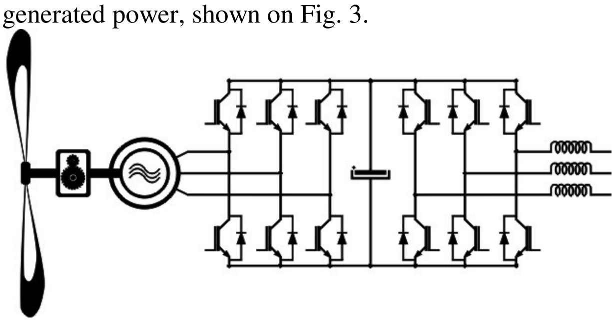

Fig. 3. *4-Q AC Drive*
Induction motor / generator with the full line-side converter and motor side inverter, both for full generated power

Advantages

- Simple AC Induction motor;
- No minimum and maximum turbine speed limits;
- Generated power and voltage increase with the speed;
- Possible VAR-reactive power control;

Disadvantages

- Two full-power converters in series;
- High dv/dt applied at generator windings;
- Power loss of up to 3% of generated power;
- Big DC-link capacitors;
- Line side inductance of 12-15% of generated power

2. Speed control by slip-power recovery

Induction motor with slip rings and wound rotor, as well as the converter and inverter for rotor-power recovery. For that principle circuit, three different mode of operation are possible.

2.1 Stator winding has to be connected to the grid, only when the rotor speed is near synchronous speed. Rotor circuit is always connected to the grid, over inverter and converter. For the lower generator speed (80%), 20% of the generator power will be supplied from the grid to the rotor. For the higher rotor speed (120%), 20% of the generator power will be supplied to the grid via rotor circuit. That circuit is known also as Cascade circuit, and it is shown on Fig. 4.

2.2 Stator and rotor circuit with inverter and converter, are always connected together, and at the beginning disconnected from the grid. Wind start rotation, and for the lower speed than the rated one, the rotor inverter produce the frequency (Frotor), so that frequency corresponding to the speed Frotation + Frotor = 50Hz, (line frequency). For the stronger wind and higher speed, the output frequency is Frotation - Frotor= 50Hz. Stator winding and rotor converter, will be connected to the grid, when the generator voltage is synchronized with grid.

That principle of operation is used for the generator which has to supply constant frequency, and are driven with variable shaft speed.

For both solutions, rotor side inverter operates at lower output frequency, between 10 Hz and near to zero Hz. The connection between rotated rotor and inverter is made via slip rings.

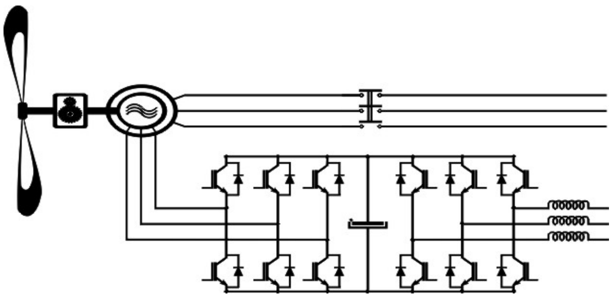

Fig. 4. *Speed control by slip-power recovery*
Induction motor / generator with slip rings, wound rotor, converter and inverter for rotor-power recovery

Advantages

- Two power converters in series for rotor-power exchange (usually 20-30% of the generated power) only
- Maximum power is 120-130% of the motor power
- Semiconductor power losses up to 0,6-0,9% of the generated power
- Line-side inductance is only 3-4.5% (12-15% of the rotor power)
- VAr -reactive power control

Disadvantages

- AC Induction motor with slip rings and rotor windings, non-standard design
- Maintenance problem
- Minimum and maximum turbine-speed limits, (75% - 125%) corresponding to the rotor-power exchange (usually 20-30% of generated power)
- Rotor-side converter operates at low frequency, therefore double size semiconductors needed
- High dv/dt applied at rotor windings
- High frequency current through the rotor bearings

- Non-standard start-up and protection procedure

2.3 Solution with similar circuit but without slip rings is with stator with two three-phase windings. One winding is connected to the grid, and the other is connected to the converter and inverter for rotor-power recovery. Energy transfer from the rotor to the additional stator windings is achieved in inductive way, as in a simple transformer. Rotor power can be taken or given using different directions and frequency of the inverter. Additional advantages of that circuit are: no slip rings, and no need for lower inverter frequency. Disadvantage: additional stator winding,

VARIABLE SPEED WIND TURBINES WITH SYNCHRONOUS MOTOR

When the synchronous motor is in use, there is no need for inverter on the generator side; simple rectifier can be used. Synchronous generator has separate excitation and no reactive power supply, as by induction motor is needed. The output voltage of synchronous generator is lower at lower speed, therefor is one boost chopper built-in, between the rectifier and the DC link capacitors. At the lower speed, boost chopper pump the rectified generator voltage, up to the DC link value necessary for the line side converter operation, (Vdc>Vline-peak).

The circuit is shown on the Fig. 5.

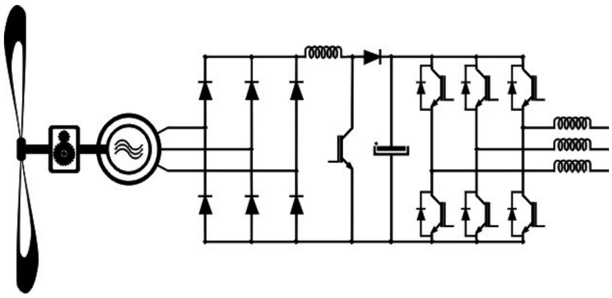

Fig. 5. *Synchronous motor / generator with the rectifier, boost chopper, and line-side converter for the full generated power*

That circuit is often used without gear box, using low speed synchronous generator. In use are the circuits without boost chopper too. DC Link voltage control is achieved due to excitation control of the synchronous generator.

Advantages
- No minimum and maximum turbine-speed limits
- Generated power and voltage increase with speed
- VAR-reactive power control possible
- Simple generator-side converter and control
- No high dv/dt applied to the motor windings

Disadvantages
- Two (three) full-power converters in series
- Power loss of up to 2-3% of the generated power
- Large DC link capacitors
- Line-side inductance of 10-15% of the generated power

POWER ELECTRONICS USED IN VARIABLE SPEED WIND TURBINES

SEMIKRON has delivered power converters, power part, without the controller, for variable speed wind turbines to various suppliers and wind turbine manufacturers, with different circuit configurations and designs. About 70 % of variable speed wind turbines are running using SEMIKRON components. Most solutions are the so-called IGBT STACKs configurations, IGBT switchers, together with heat sink, DC link capacitors, built-in protection features, insulation and auxiliary power supply. Power STACKs are delivered for up to 480V grid voltage, with a 1200V IGBT blocking voltage. For the grid voltages of 690V, IGBTs of 1700V are used. All such delivered power systems are 100% tested in application conditions, and ready to use and delivered, in power ranges from 250kW up to 2.5 MW. Typical construction design, of 400 kVA, at 3 x 690V, is shown on the Fig.6.

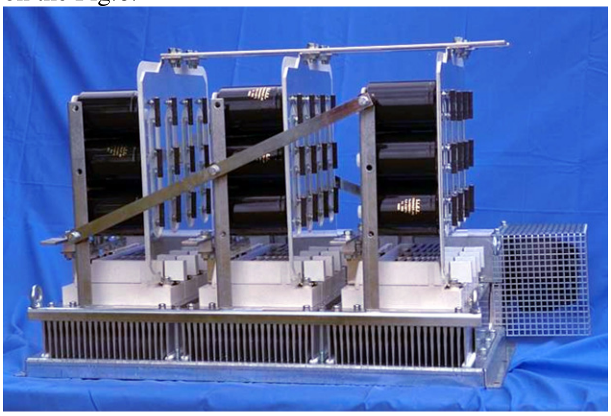

Fig. 6. *IGBT STACK for 400 kVA, at 3 x 690V*

CALCULATATION OF OPERATING JUNCTION TEMPERATURE

Proper sizing of converters in the whole operation cycles is simple possible using calculation software developed for that porpoise. It is available in Internet under http://www.semikron.com and it is simple in use. For any common power electronic application, first the circuit has to be selected. After that the circuit parameters have to be defined:

input voltage
output voltage
cosinusphi
output power
output current
switching frequency
output frequency
load and overload parameter
factor
duration
user defined load cycle
min. output frequency
min. output voltage

After that, you can select your package and device: for example SkiiP1092GB170, and on the next page is to define ambient and heatsink parameters. After pressing the calculate button, calculation results are available. All temperatures vs. time are shown too, as on Fig. 7

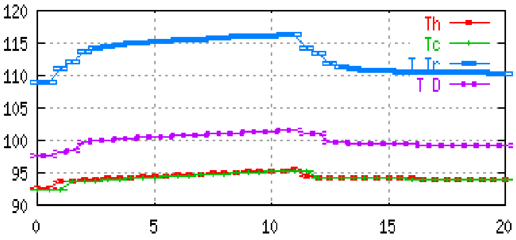

Fig. 7. *Heatsink, Diode and IGBT temperatures vs. time at overload conditions*

CONCLUSION

Power electronics found new application in wind turbines with variable rotation speed. Of all types of motor and generator speed control, the widespread one is the one usually rarely used in four quadrant mode of operation. That is the asynchronous motor with wound rotor and speed control by slip-power recovery. This classical method, started with thyristors in use and mostly used in the '60 and '70, is now finding fresh application.

At the same time, use of synchronous generator is spreading, applying diode rectifier, step-up chopper and line side inverter. This, better, method is allowing full regulation of generator speed, with less power electronics components compared to the asynchronous generator with short-circuited rotor.

It is characteristic that, in both cases, the dominant solutions are the pioneering ones, coming out of the need for pragmatic solutions of the problem, but without participation of famous and successful firms - the manufacturers of the control speed motor drives.

However, as this new industrial branch develops, and is reaching the sum of yearly trade of around ten billion Euro, the pioneering times of wind turbine construction are over. New, powerful forces, equally potent in research and development as they are in investments - the big industrial manufacturers - are progressing into the stage. This will certainly have an impact on the development of power electronics in this field of use.

REFERENCES

[1] SEMIKRON Data Book
[2] www.semikron.com
[3] SEMISEL Calculation Program on http://semisel.semikron.com/semisel/start.asp
[4] D. Srajber, W. Lukasch: “The Calculation of The Power Dissipation for the IGBT and the Inverse Diode in the Circuits with the Sinusoidal Output Voltage” Electronica´92 München
[5] Messe Windtech 2001 Husum September 2001., Data sheets: ENERCON, VESTAS, Neg-Micon, RePower, Enron, DeWind, FRISIA, Pfleiderer, SEG, Weier, mTorres

DSP BASED CONTROL OF UNIVERSAL POWER QUALITY CONDITIONING SYSTEM

Dr. D. Graovac[1], Dr V. Katić[2], Dr A. Rufer[3], Mr J. Knežević[1]
[1]Baldor ASR GmbH, Dieselstraße 22a, Kirchheim-München, Deutschland, Dusan_Graovac@Baldor.com
[2] Faculty of Engineering, University of Novi Sad, Fruskogorska 11, Novi Sad, Yugoslavia
[3] EPFL-LEI, Laboratoire d'électronique industrielle, Ecole Polytechnique Fédérale, Lausanne, Suisse

Abstract: *The aim of this paper is to present an easy-to-implement real time digital control system for complex power electronics converter, such as universal power quality conditioning system (UPQS). Converter regulators are implemented on a modern digital signal processor (DSP). Experimental results have shown satisfying performance.*

Key words: ***Active Filtering, Control, Power Quality***

1. INTRODUCTION

In order to keep power quality under limits proposed by standards, it is necessary to include compensation. Modern solutions for active power factor correction can be found [1] in forms of active rectification or active filtering. Control demands for such individual converters are very strict [2], i.e. they ought to have fast reaction time as well as the accurate steady state operation. Usually, controlled variables are three-phase currents or voltages injected by the converter, together with the converters DC bus voltage. Performance is even more demanding when several converters have to work synchronously. Extreme example of such system is UPQS, whose main purpose is to compensate for supply voltage and load current imperfections, such as: sags, swells, imbalance, flicker, harmonics, and reactive currents. The aim of this paper is to present a simple and reliable DSP based control method for UPQS.

2. UPQS TOPOLOGY

UPQS [8] (fig. 1) consists of: Active Rectifier (AR) for real power transfer to/from common DC bus and DC bus voltage control; Series Filter (SF) that suppresses supply voltage harmonics, flicker, voltage sags/swells and unbalance; Parallel filter (PF) that eliminates load current harmonics and compensates load power factor.

Based on consideration presented in [3], reference converter signals can be calculated as:

$$\vec{U}_{sf} = K \cdot \vec{I}_{Sh} + \vec{U}_{comp} \tag{1}$$

$$\vec{I}_{pf} = \vec{I}_{lh} + \vec{I}_{lr} \tag{2}$$

where: Usf is the series filter voltage vector, Ish is the harmonic supply current vector and Ucomp is the voltage compensation vector. Also, Ipf is the parallel filter current vector, Ilh is the load harmonic current and Ilr is the load reactive current.

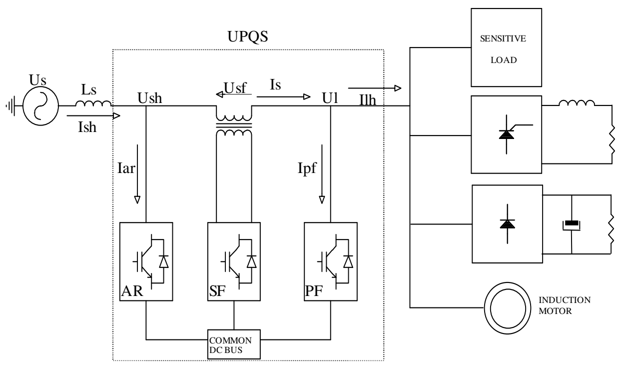

Fig. 1. *Topology of universal power quality conditioning system (UPQS)*

3. DERIVATION OF REFERENCE SIGNALS

Control schemes for both parallel and series active filtering usually use the instantaneous reactive power theory (pq theory) [7] for reference signals determination. Although this theory presents a very powerful tool, its implementation is quite involving, since it requires a large number of analog multipliers, dividers, filters etc. Development in DSP technology, its mathematical speed together with fast A/D conversion and different dedicated hardware (space vector modulators, fast digital PWM signal generators) enables the minimization of control hardware and thus the use of the synchronously rotating frame (dq) control. dq domain quantities of any voltage and current shown in fig. 1 are given by following equations:

$$\begin{bmatrix} \boldsymbol{i}_0 \\ \boldsymbol{i}_d \\ \boldsymbol{i}_q \end{bmatrix} = \sqrt{\frac{2}{3}}\boldsymbol{T} \cdot \begin{bmatrix} \boldsymbol{i}_a \\ \boldsymbol{i}_b \\ \boldsymbol{i}_c \end{bmatrix} \quad \text{and} \quad \begin{bmatrix} \boldsymbol{u}_0 \\ \boldsymbol{u}_d \\ \boldsymbol{u}_q \end{bmatrix} = \sqrt{\frac{2}{3}}\boldsymbol{T} \cdot \begin{bmatrix} \boldsymbol{u}_a \\ \boldsymbol{u}_b \\ \boldsymbol{u}_c \end{bmatrix} \tag{3}$$

$$T = \begin{bmatrix} 1/\sqrt{2} & 1/\sqrt{2} & 1/\sqrt{2} \\ \cos\vartheta & \cos\left(\vartheta - 2\pi/3\right) & \cos\left(\vartheta - 4\pi/3\right) \\ -\sin\vartheta & -\sin\left(\vartheta - 2\pi/3\right) & -\sin\left(\vartheta - 4\pi/3\right) \end{bmatrix} = T^{-1\,transp.}$$

$$\text{and} \quad \vartheta = \vartheta_0 + \int_0^t \omega dt \tag{4}$$

where θ is the instantaneous supply voltage angle, derived from the synchronization circuitry. Currents in rotating frame (either I_{lh}, I_{sh} etc.) can be decomposed in DC (50Hz) and AC (harmonic, subharmonic or interharmonic) component:

$$\boldsymbol{i}_d = \bar{\boldsymbol{i}}_d + \tilde{\boldsymbol{i}}_d \quad \text{and} \quad \boldsymbol{i}_q = \bar{\boldsymbol{i}}_q + \tilde{\boldsymbol{i}}_q \tag{5}$$

Where i_d corresponds to the reactive and i_q to the active power component. AC and DC components can be extracted by the means of filtering:

$$\tilde{i}_d(z) = HPF(z) i_d(z) \quad \text{and}$$

$$\tilde{\boldsymbol{i}}_q(z) = \boldsymbol{HPF}(z) \boldsymbol{i}_q(z) \tag{6}$$

$$\bar{i}_d(z) = i_d(z) - \tilde{i}_d(z) \text{ and}$$
$$\bar{i}_q(z) = i_q(z) - \tilde{i}_q(z) \qquad (7)$$

Advantage of a dq domain control lie in easy filtration, since the 50Hz components are transferred into DC quantities and all harmonic components are AC quantities and therefore no band pass filtering is necessary. So, HPF(z) is a high-pass digital filter transfer function which can be obtained by the digitalization of its well known first-order analog counterpart HPF(s):

$$HPF(z) = HPF(s)\Big|_{s=\frac{2}{T}\frac{1-z^{-1}}{1+z^{-1}}} = \frac{s}{s+\omega_c}\Bigg|_{s=\frac{2}{T}\frac{1-z^{-1}}{1+z^{-1}}}$$
$$= \frac{2\left(1-z^{-1}\right)}{(2+\omega_c T)-(2-\omega_c T)z^{-1}} \qquad (8)$$

T is the sampling period that for proper filtering has to be at least $T<T_h/4$, where T_h is the period of the highest harmonic component to be eliminated ($T_h=1/f_h$). For instance if a highest harmonic is 21. then T should approximately be 1ms. Based on these consideration, reference currents for parallel filter can be calculated as in left part of (9) if only harmonics are to be eliminated, or as in right part of (9) if power factor has to be corrected together with the harmonic elimination:

$$\begin{bmatrix} i^*_{pfa} \\ i^*_{pfb} \\ i^*_{pfc} \end{bmatrix} = \sqrt{\frac{2}{3}} \begin{bmatrix} \cos\vartheta & -\sin\vartheta \\ \cos\left(\vartheta - 2\pi/3\right) & -\sin\left(\vartheta - 2\pi/3\right) \\ \cos\left(\vartheta - 4\pi/3\right) & -\sin\left(\vartheta - 4\pi/3\right) \end{bmatrix} \cdot \begin{bmatrix} \tilde{i}_{lhd} \\ \tilde{i}_{lhq} \end{bmatrix}$$

$$\begin{bmatrix} i^*_{pfa} \\ i^*_{pfb} \\ i^*_{pfc} \end{bmatrix} = \sqrt{\frac{2}{3}} \begin{bmatrix} \cos\vartheta & -\sin\vartheta \\ \cos\left(\vartheta - 2\pi/3\right) & -\sin\left(\vartheta - 2\pi/3\right) \\ \cos\left(\vartheta - 4\pi/3\right) & -\sin\left(\vartheta - 4\pi/3\right) \end{bmatrix} \cdot \begin{bmatrix} \bar{i}_{lhd} + \tilde{i}_{lhd} \\ \tilde{i}_{lhq} \end{bmatrix} \qquad (9)$$

Reference voltages for the series active filter can be determined based on same procedure, starting from:

$$\vec{U}_{sf} = K \cdot G \cdot \vec{I}_{Sh} + \vec{U}_{comp} \qquad (10)$$

where Usf is the series filter voltage vector, Ish are harmonic supply currents vector and Ucomp is compensation voltage vector needed to remove supply voltage imperfections. Again, if only harmonic compensation is required, reference voltages are as in left part of (11), but if the voltage compensation is required, then reference voltages are as in right part of (11):

$$\begin{bmatrix} u^*_{sfa} \\ u^*_{sfb} \\ u^*_{sfc} \end{bmatrix} = K\sqrt{\frac{2}{3}} T^{-1} \cdot \begin{bmatrix} \tilde{i}_{shd} \\ \tilde{i}_{shq} \\ i_0 \end{bmatrix}$$

$$\begin{bmatrix} u^*_{sfa} \\ u^*_{sfb} \\ u^*_{sfc} \end{bmatrix} = K\sqrt{\frac{2}{3}} T^{-1} \cdot \begin{bmatrix} \tilde{i}_{shd} \\ \tilde{i}_{shq} \\ i_0 \end{bmatrix} + \begin{bmatrix} u_{compa} \\ u_{compb} \\ u_{compc} \end{bmatrix} \qquad (11)$$

where voltage compensation factor is presented in (12):

$$\begin{bmatrix} u_{compa} \\ u_{compb} \\ u_{compc} \end{bmatrix} = \sqrt{\frac{2}{3}} T^{-1} \cdot \begin{bmatrix} u_{compd} \\ u_{compq} \\ u_{comp0} \end{bmatrix}$$

$$\begin{bmatrix} u_{compd}(s) \\ u_{compq}(s) \\ u_{comp0}(s) \end{bmatrix} = \begin{bmatrix} \left(u_{dnom}(s) - u_d(s)\right) \\ \left(u_{qnom}(s) - u_q(s)\right) \\ \left(u_{0nom}(s) - u_0(s)\right) \end{bmatrix} \qquad (12)$$

where the nominal d, q, and zero voltage are precalculated from the ideal voltage supply waveform and are equal to: $U_{dnom}=0$, $U_{0nom}=0$ and $U_{qnom}=380$.

4. CONTROL OF CONVERTER

Constant DC bus voltage is essential for proper operation of both parallel and series filter. Also, DC bus voltage provided using the AR eliminates the need for DC voltage control loop in parallel/series filter control system. Therefore, it is necessary to have precise and fast control of an AR inside UPQS. Transfer function connecting reference current and dc bus voltage in synchronously rotating frame (dq) domain equals:

$$\frac{\tilde{u}_{dc}(s)}{\tilde{i}_{arqref}(s)} = K\frac{1 - s/\omega_0}{(1+s/\omega_{p1})(1+s/\omega_{p2})} \qquad (13)$$

and the parameters are:

$$K = \frac{3}{2}\frac{\sqrt{3}\sqrt{2}U - 2I_{ref}R}{U_{dc}\dfrac{2-U_L/U_{dc}}{R_L}},\ \omega_0 = \frac{\sqrt{3}\sqrt{2} - 2I_{ref}R}{LI_{ref}}$$

$$\omega_{p1} = \frac{2-U_L/U_{dc}}{R_L C},\ \omega_{p2} = \frac{1}{T_s} \qquad (14)$$

where i_{arqref} is the reference q-component current and $i_{ardref}=0$. U_L is the equivalent load voltage and R_L is the equivalent load resistance. In order to provide a faster response a feed-forward component that minimizes the influence of the boost converter positive zero is added. Feed-forward parameters are:

$$K_{ff} = (0.1 \div 0.2)\frac{U_{dcnom}}{I_{dcnom}},\ T_{ff} = (0.1 \div 0.15)T_s \qquad (15)$$

Now, the voltage control loop can be written as:

$$W(s) = \left(K_p + \frac{1}{sT_i} + sT_d\right)\frac{1}{g(s)}\frac{K}{s^2 + 2\zeta'\omega_n' s + \omega_n'^2} \qquad (16)$$

where Kp, Ti and Td are PID regulator parameters, g(s) is additional compensation function, intended to increase system robustness level, and the last factor is rewritten from (13), without a positive zero. If an internal model control procedure is implemented than the regulator parameters are:

$$T_d = \frac{1}{K},\ T_i = \frac{1}{T_d\omega_n'^2},\ K_p = 2\zeta'\omega_n' T_d T_i,$$
$$g(s) = s + 2\omega_n\zeta \qquad (17)$$

In order to provide fast current control, a hysteresis current controllers are used. Value of hysteresis band (H) should be chosen in order not to exceed allowed instantaneous and average (19) switching frequency for the chosen components.

$$f_{sw\max} = \frac{U_d}{4HL},\ f_{swav} = \frac{U_d}{4HL}\left(1 - \frac{m_{\max}^2}{2}\right) \qquad (18)$$

where m_{max} is the maximum modulation index presenting the ratio between highest actual and the rated phase current of the converter and L is overall inductance seen by the converter.

Control of PF currents is provided using the dq PI linear control, and then the modulating signals are later compared with the triangle carrier. PI regulator parameters are (empirically):

$$K_p = \frac{L\omega_s}{2U_d},\ K_i = \omega_s K_p \qquad (19)$$

where ωs is the switching angular frequency.

Control of SF voltages was implemented using PD regulators. It is not a good practice to include an integral part into the controller, since series active filter has a LC switching ripple filter at its output, having an oscillatory open loop characteristic:

$$\frac{U_{sf}(s)}{m(s)} = G(s) = \frac{K_{pwm}}{s^2 LC + 1} \tag{20}$$

where K_{pwm} is the gain of PWM technique and m is the modulating index. If a PD regulator is used, then overall closed loop transfer function of the system is:

$$\frac{U_{sf}(s)}{U^*_{sf}(s)} = \frac{\frac{K_{pwm}}{LC}(K_p + sK_d)}{s^2 + \frac{K_{pwm}K_d}{LC}s + \frac{K_{pwm}K_p + 1}{LC}} \tag{21}$$

From this equation it is obvious that Kp should be chosen according to the desired speed of response (i.e. according to desired undamped frequency ω_n) and Kp according to desired stability (i.e. according to desired damping factor ζ):

$$K_p = \frac{\omega_n^2 LC - 1}{K_{pwm}}, \quad K_d = \frac{2\zeta\omega_n LC}{K_{pwm}} \tag{22}$$

5. EXPERIMENTAL RESULTS

Complete system was extensively tested on single phase prototype. UPQS converter consists of three single phase half bridge converters. Control system is implemented on ADMC 401 DSP. Nominal rms supply voltage and load current are Unrms=60V, Inrms=1.5A. Fig. 2. (variables are presented per unit) shows behavior of the UPQS in the case of compound load consisting of linear RL load (R=330Ω, L=500mH). Therefore, UPQS has to work static VAr compensator. Fig. 3. (variables are presented per unit) shows behavior of the UPQS in the case of compound load consisting of parallel connection of inductively loaded diode bridge AC/DC converter (Rdc=250Ω, Ldc=750mH) and linear RL load (R=330Ω, L=500mH). Therefore, UPQS has to work both as a static VAr compensator and active filter. Supply voltage and current are displayed, together with currents drawn by the load and parallel filter. Resulting supply current has sinusoidal wave shape and is in phase with supply voltage. Corresponding spectrums are displayed in fig. 4 and 5. Total current harmonic distortion was reduced from THDIL=30.1% to THDIS=7.2%. Fig. 6. shows UPQS performance in the case of 30% under voltage. It can be seen load voltage retains sinusoidal shape, with rms value never drops below 93.5% of nominal voltage, which is quite acceptable for all loads. Finally, figures 7 and 8 show transient voltage regulation response.

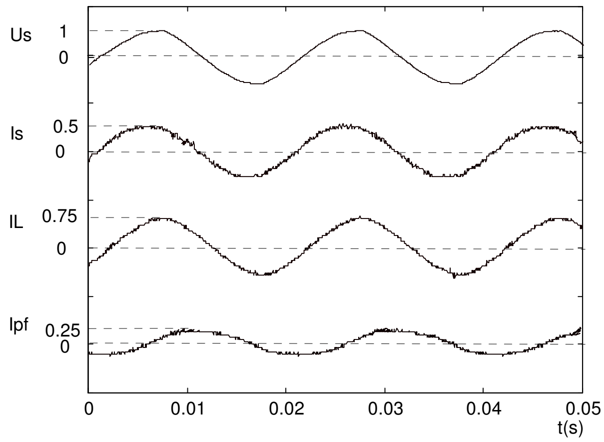

Fig. 2. *Typical voltage and current waveforms in the case of RL load*

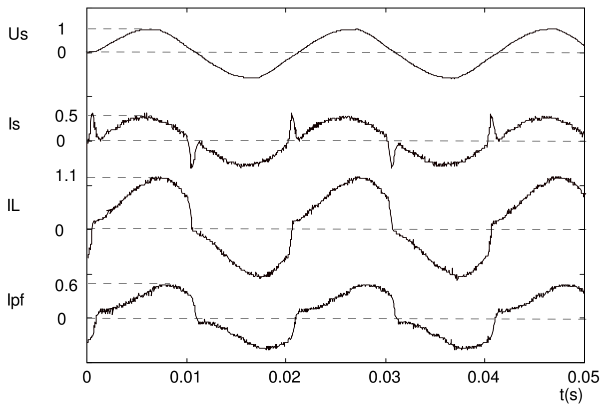

Fig. 3. *Typical voltage and current waveforms in the case of compound load*

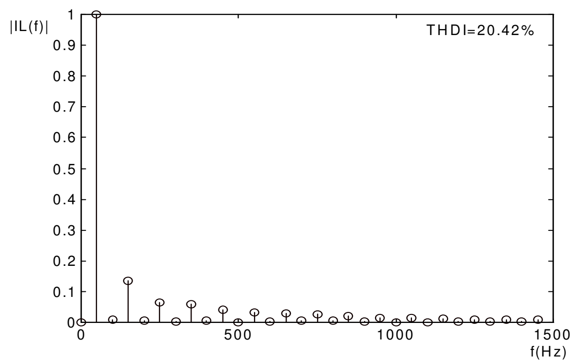

Fig. 4. *Load current spectrum*

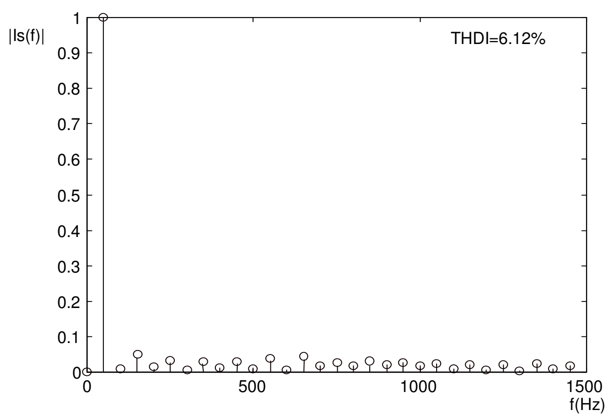

Fig. 5. *Supply current spectrum*

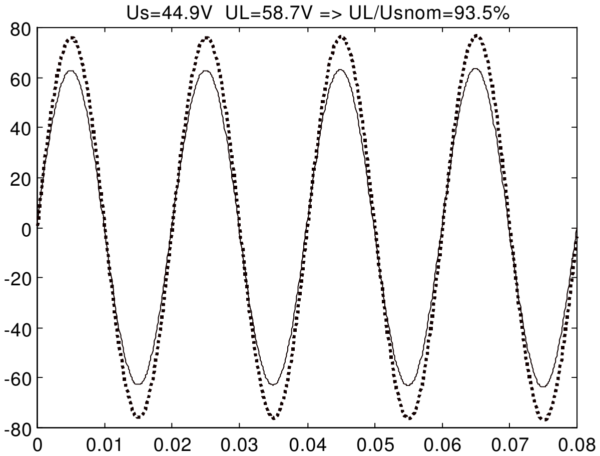

Fig. 6. Supply and load voltage in the case of 30% voltage sag

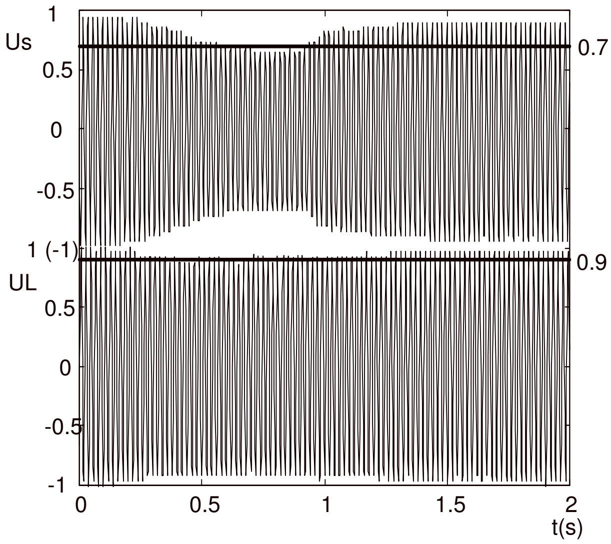

Fig. 7. *Supply and load voltage in the case of 30% voltage sag transient*

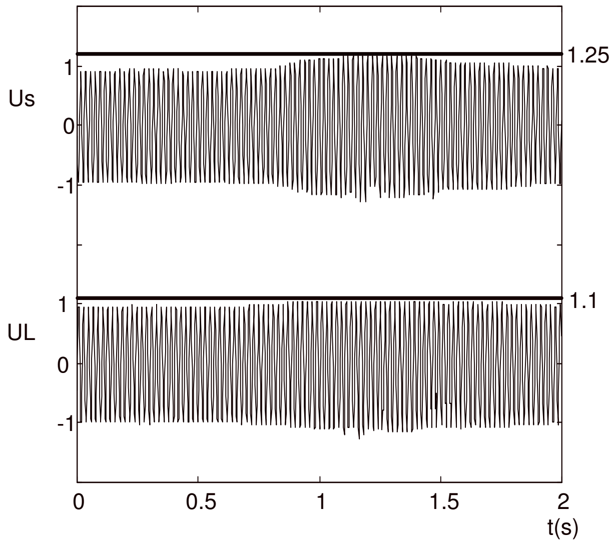

Fig. 8. *Supply and load voltage in the case of 25% voltage swell transient*

6. CONCLUSION

This paper presented a universal power quality conditioning system which is a combination of UPQC and shunt active filter at the load side. It can compensate sags, swells, interruptions, unbalance, flicker, harmonics, reactive currents and current unbalance. Active rectifier control system keeps constant DC bus voltage necessary for proper operation of the filters. Series filter provides sinusoidal load voltages and parallel filter compensates power factor of non-linear loads. Converter power level and price is somewhat higher than in conventional systems, but the compensation characteristics is superior. Both power level and price can be diminished if the reactive power compensation or voltage regulation is not desired. Control system for the UPQS have been developed using dq domain, thus enabling the easy filtering and flexible control implementation. Proposed regulators have shown satisfying performance when implemented on a complex power electronics converter, such as UPQS. They are easy to implement on different DSP families and have good dynamic and steady state characteristics.

7. REFERENCES

[1] D.Sabin, A.Sundaram, *"Quality Enhances Reliability"*, IEEE Spectrum, vol.33, no.2, Feb.1996, pp.34-41.

[2] M.Rastogi, R.Naik, N.Mohan, *"A Comparative Evaluation of Harmonic Reduction Techniques in Three Phase Utility Interface of Power Electronic Loads"*, IEEE - IAS Annual Meeting, Toronto (Canada), Oct.1993, pp.971-978.

[3] H.Akagi, *"New Trends in Active Filters for Power Conditioning"*, IEEE Trans. on Industry Applications, vol.32, no.6, Nov./Dec.1996, pp.1312-1322

[4] F.Z.Peng, *"Application Issues of Active Power Filters"*, IEEE Industry Applications Magazine, Sept./Oct. 1998, pp. 21-30

[5] H.Fujita, H.Akagi, *"Unified Power Quality Conditioner: The Integration of Series and Shunt Active Filter"*, IEEE Trans. on Power Electronics, vol.13, no.2, March 1998, pp.315-322

[6] J.W.Dixon, G.Venegas, L.A.Moran, *"A Series Active Filter Based on a Sinusoidal Current-Controlled Voltage-Source Inverter"*, IEEE Trans. on Industrial Electronics, vol.44, no.5, October 1998, pp.612-620

[7] H.Akagi, Y.Kanazawa, A.Nabae, *"Instantaneous Reactive Power Compensators Comprising Switching Devices without Energy Storage Components"*, IEEE Trans. on Industry Applications, vol.IA-20, no.3, May/June 1984, pp.625-630

[8] D.Graovac, V.Katić, A.Rufer, *"Solving Supply And Load Imperfections Using Universal Power Quality Conditioning System"*, PCIM-PQ'2000 Conference, Nuremberg, Germany, June 2000.

THE ANALYSIS OF DIODE VOLTAGE AND CURRENT RECTIFIER DUALITY

Radišić Vladimir, Vladimir Katić
Panonska Banka AD, Novi Sad; Faculty of Technical Sciences, Novi Sad

Abstract: *In the paper a theoretical approach with illustrative examples of possibilities of duality characteristics and relations application are given. They enable unification in electrical system applications. As example a voltage rectifier is transferred into current one using duality relations.*

Key Words*: duality, voltage rectifier, current rectifier, space phasors*

INTRODUCTION

In electrical engineering, application of knowledge obtained for a certain system, for solving problems in another system, can be of great importance. Such procedures enable savings in research time and efforts for development that second system, as well as other advantages due to unification.

Duality relations are the ones that enable expending and unification of certain theory, in that way that it is possible to make transfer of mathematical relations developed for one system to another, dual system.

One example of dual electrical circuits is three-phase converter, which can be dual in two directions:
1. duality of voltage and current converters and
2. duality of converter rectification and inverter mode

In the paper duality of three-phase rectifier with constant output DC voltage (in further text voltage rectifier) to three-phase rectifier with constant output DC current (in further text current rectifier) will be presented.

Using relation, who describes the rectifier, a mathematical model will be set. The model will be applied on the simplest rectifier type – the diode rectifier, using SIMULINK software.

CHARACTERISTICS OF DUALITY RELATIONS [1]

The pre-condition for existence of dual graph is two-dimension feature of initial graph (representation of the graph in plain without crossing). This condition is necessary and sufficient only if the initial graph does not comprise one of the graphs from Fig.1. These graphs are called *Kuratowsky-graphs.*

If the graph should represent an electrical circuit, a quantitive features (current and voltage) should be added to its theoretical structure (branches and nodes).

To find out a dual to a graph (i.e. electrical circuit), fulfilling two-dimension feature of initial graph, it is necessary to follow following rules:

1. Every area of initial graph, which is encircled by the legs, is copied into the node of dual circuit. It means that every loop is copied into node, to parallel connection is dual serial connection, and connection triangle is converted into star. The opposite is also good.

2. One more node is added to dual circuit, which corresponds to environment of initial circuit.

3. Nodes of dual networks are connected in such manner that every branch of initial circuit crosses only one branch of dual circuit.

4. Directivity, which exists in initial branch (for example: direction of current) is transferred to dual branch in such manner that initial branch is rotated in given positive direction until it coincide with the branch in dual circuit.

5. Every component in a branch of dual circuit is dual to corresponding component in initial circuit. Reciprocally are dual voltage and current source, capacitance and inductance, resistance and conductance.

6. Dual physical parameters are: voltage and current, magnetic flux and charge.

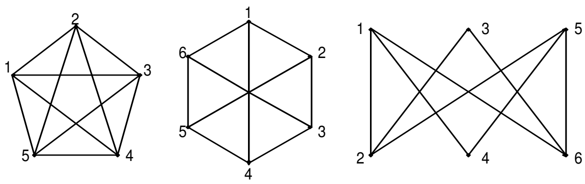

Fig.1. *Kuratowsky-graphs.*

DUALITY OF VOLTAGE AND CURRENT RECTIFIERS

Voltage and current rectifiers convert three phase AC current and voltages into DC, where electrical energy flow is from AC to DC (rectifier mode) or from DC to AC (inverter mode).

Converting is done by control of converter bridge switching components (S11...S23 on Figs. 2 and 3). The switching components is controlled by switching function, which can have two values: 1 – closed switch and 0 – open switch. In theory, for 6 switches there are 2^6 = 32 different converter bridge states. However, in real operation number of states is lower, due to existence of certain restrictions.

Voltage rectifier (Fig.2) consists of input CL filter (in further text input circuit), switching part (switching bridge with three legs – for every phase one leg with two switches), output capacitor and load (parallel connection of resistance and current source). The term output circuit will be used for the load and output capacitor. Tree-phase source has its inductance and resistance Lg and Rg.

The states of a converter bridge, in case of voltage rectifier, are defined by following equations

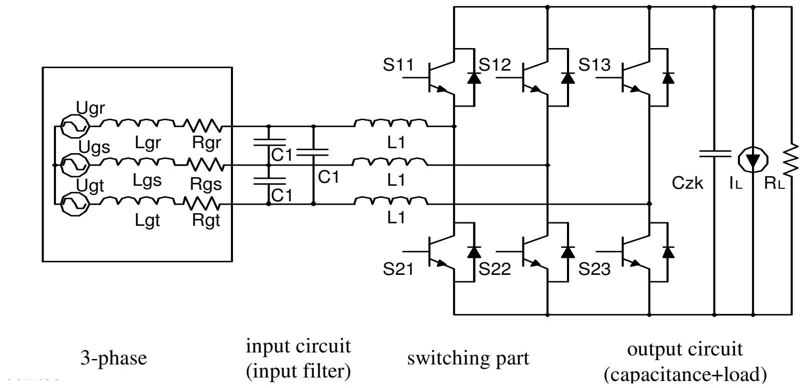

Fig.2. *Voltage rectifier*

$$
\begin{aligned}
S11 + S21 &= 1 \\
S12 + S22 &= 1 \\
S13 + S23 &= 1
\end{aligned}
\quad (1)
$$

Equation (1) means that in every leg of the bridge at the same time only 1 switch can be open. This enable constant flow of current in all phases, as there exists closed circuit for every phase. There are 8 different states.

Current rectifier (Fig. 3) consists of input LC filter, (in further text input circuit), switching part (switching bridge with three legs – for every phase one leg with two switches), output inductance and load (serial connection of resistance and voltage source). The term output circuit will be used for load and the output inductance. Three-phase source has Lg and Rg, as well as three-phase source of voltage rectifier

.

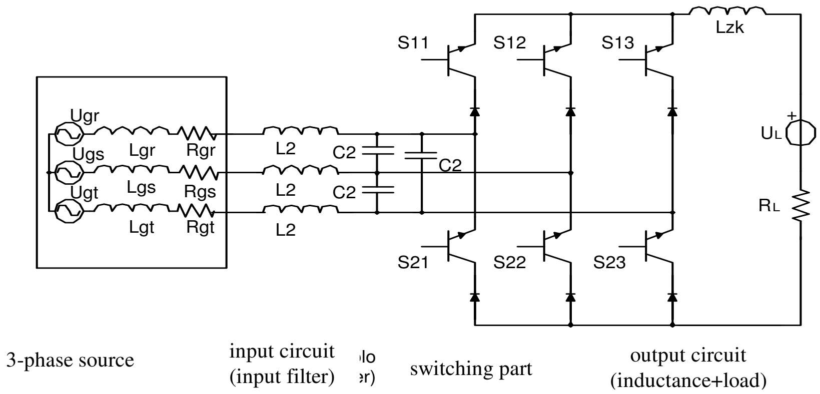

Fig.3. Current rectifier

The states of a converter bridge, in case of current rectifier, are defined by following equations:

$$
\begin{aligned}
S11 + S12 + S13 &= 1 \\
S21 + S22 + S23 &= 1
\end{aligned}
\quad (2)
$$

Equations (2) significance that only one switch in upper and lower part of the bridge can be open simultaneously. This enables existence of line voltage at bridge output. In this case there are 9 allowed states in total.

Fig. 4a shows simplified scheme of voltage rectifier, while fig. 4b transformed scheme after taking into account restrictions from (1).

Allowed switching states of voltage rectifier can be represented as states of individual legs using regular triplets. For example, according to fig.4b, if switch is Sx1=1, it means that it is in upper position.

Fig. 5 shows electrical circuit dual to the one from fig. 4. It is not easy to notice the duality due to existence of Kuratowsky sub-graph in circuit from fig.4. Therefore the duality is sought for every of 8 allowed states. The circuit from fig.5 is obtained by combining such partial dual systems. The switching part of the circuit from fig.5 fulfills the conditions (2), which means that this electrical circuit represents simplified current rectifier from fig.3.

Allowed switching states of current rectifier are described by two regular triplets (the first represents the state of the switch in upper part of the bridge from fig.5, while the second the state in lower part). For example, statement S1x=100 and S2x=001 means that upper switch from fig.5 is in further left position, while the lower in further right position.

Table 1 shows all allowed states of current and voltage rectifiers represented on figs.4b and 5, as well as corresponding output values of current and voltage arising as consequence of such states of the switching bridge.

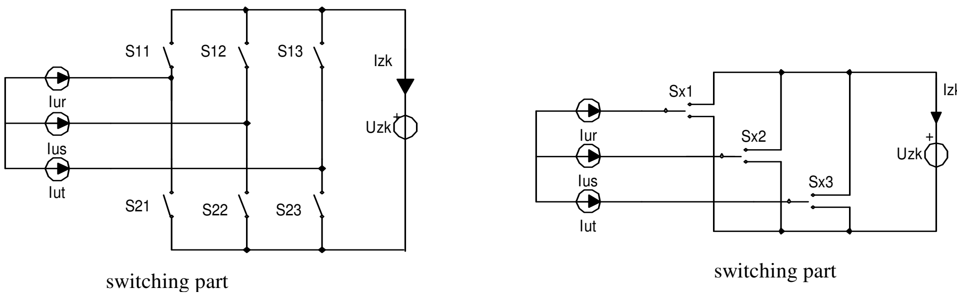

a) b)

Fig.4. *Simplified scheme of voltage rectifier: a) circuit formed on fig.2 basis, b) circuit deduced from fig.4a taking into account constraints from (1)*

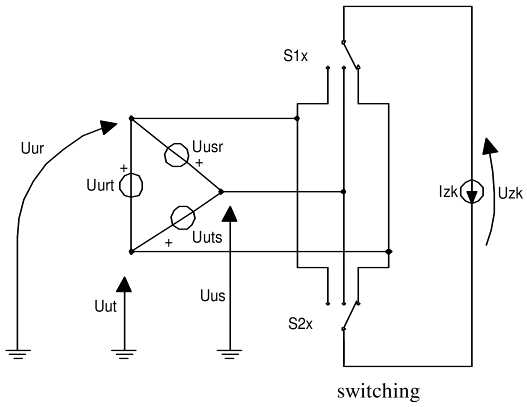

Fig.5. *Electrical circuit dual to circuit from fig.4 (simplified current rectifier)*

Table 1. *Allowed states of dual rectifiers (figs. 4b &5)*

	Voltage rectifier			Current rectifier		
	(Sx1 Sx2 Sx3)	Izk	k	(S1x),(S2x)	Uzk	k
1	000	0		(100), (100)	0	
2	001	Iut	4	(010), (010)	0	
3	010	Ius	2	(001), (001)	0	
4	011	-Iur	3	(001), (010)	Uut – Uus	4
5	100	Iur	6	(010), (100)	Uus – Uur	2
6	101	-Ius	5	(001), (100)	Uut – Uur	3
7	110	-Iut	1	(100), (001)	Uur – Uut	6
8	111	0		(100), (010)	Uur – Uus	5
9	-	-		(010), (001)	Uus – Uut	1

DEFINITION OF SPACE PHASOR [2]

The switching bridge and control method determine conversion between AC and DC side of the rectifier. There are several mathematical models for the switching bridge. In the paper, a complex model represented by state phasor, controlled by switching space phasor is used.

In three-phase system analysis, three sinusoidal phase lagging wave shapes can be represented in complex plane as three phasors that are 120° out of phase. Another mode is representing by space phasor, defined with:

$$\underline{X}(t) = \frac{2}{3}\left(Xr(t) + Xs(t)e^{j\rho} + Xt(t)e^{-j\rho} \right) \quad (3)$$

where X(t) is time-dependent space phasor, Xr(t), Xs(t), Xt(t) time-dependent variable functions of balanced three-phase system and $\rho = 2\pi/3$ angle.

If sum of functions *Xr(t), Xs(t), Xt(t)* is zero (balanced three-phase system), then there are inverse transformation, which enables reconstruction of the functions *Xr*(t), *Xs(t), Xt(t)* from theirs representatives using space phasor *X(t).* This can be seen on fig. 6a.

From r-s-t coordinate system, the space phasor can be represented in two dimensional α-β coordinate system also, by making projections of space phasor components onto α and β axis (fig. 6b).

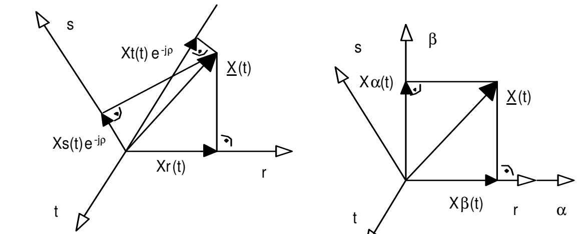

a) b)

Fig.6. *Space vector: a) in r-s-t coordinate system in two dimensional plane, b) in α-β coordinate system in two dimensional plane*

Switching space phasor *S(t)* defines a configuration of three-phase switching bridge, which means that it determines the momentarily state of every switch in switching bridge. By changing *S*, the state in switching bridge is also changed.

Positive aspect of using switching space phasor is ability to control whole switching bridge with only one function - *S.*

MATEMATICAL MODEL OF VOLTAGE AND CURRENT RECTIFIER

Figs. 7 and 8 show models of voltage and current rectifiers, developed using circuits from figs. 2 and 3, with labeled voltages and currents at the most important points. Three phase sources are simplified and presented with current or voltage sources. It is done in this way to make duality easier to be observed and make later simulation more efficient.

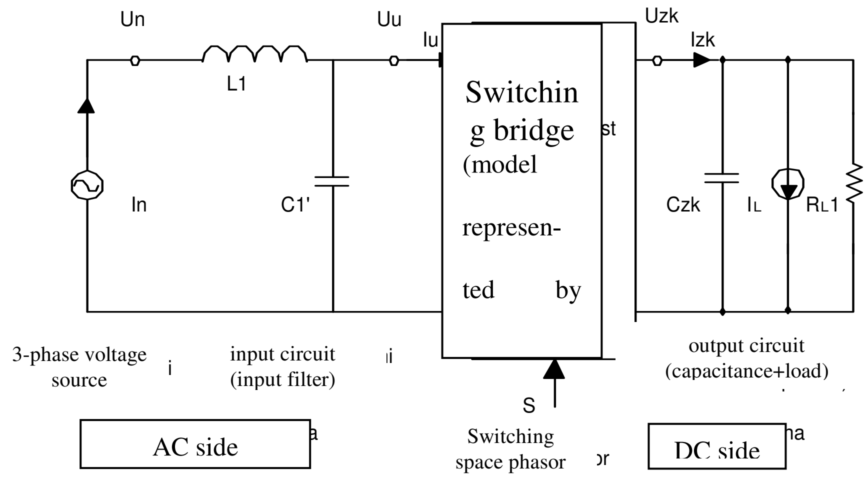

Fig.7. Model of voltage rectifier used in simulations.

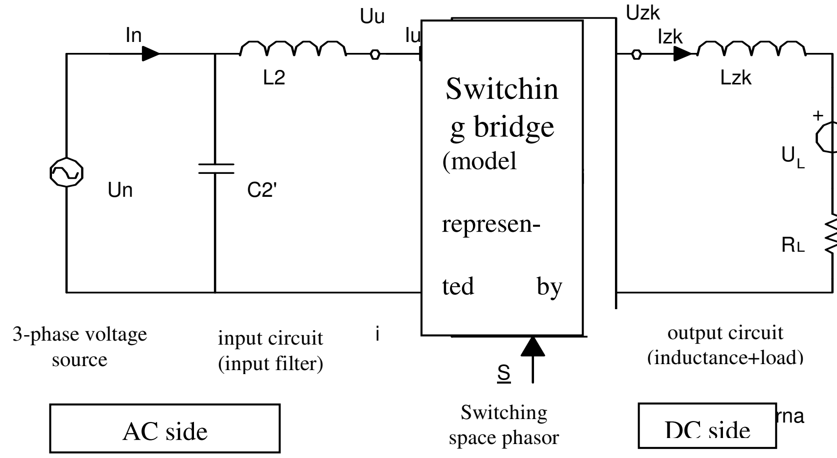

Fig.8. Model of current rectifier used in simulations.

Using duality feature, a current rectifier circuit can be obtained from voltage one in following manner:

1. Three-phase current source of amplitude Ig in connection Y (star) is transformed into three-phase voltage source of amplitude Ug connected in Δ (triangle). Further transformation of the three-phase source into connection Y (used in simulations) decrease of source amplitude for √3 and phase displacement of source for π/6 is consecution.
2. In input circuit capacitors C1 are transferred into inductances L2, and inductances L1 into capacitors C2.
3. In output circuit parallel connection of capacitors, current source and the load resistance is transferred into serial connection of inductance, voltage source and conductance, i.e. load resistance (Czk→Lzk, $I_L \to U_L$, $R_L \to 1 / R_L$)
4. Voltages in dual circuit become currents and reciprocal.
5. Switching bridge of voltage rectifier is transferred into switching bridge of current rectifier (figs. 4b and 5).

At AC side of figs. 7 and 8 all connections are three-phase, and all voltages and currents are three-phase vectors. Capacitors and inductances C1', C2', L1, L2 are diagonal matrices 3x3, where values are C1'=3·C1 and C2'=3·C2 due to transformation of connection Δ into Y.

Mathematical models of rectifiers are given in [1, 2]. Voltage rectifier is described by two sets of equations:

1. Equations that origin on basis of Kirchof's lows, applied on fig.7:

$$In - Iu = C1' \frac{dUn}{dt} \tag{4}$$

$$Un - Uu = L1 \frac{dIu}{dt} \tag{5}$$

$$Czk \frac{dUzk}{dt} = Izk - I_L - \frac{Uzk}{R_L} \tag{6}$$

2. Equations that models switching bridge:

$$\underline{U}u = \underline{S} \cdot Uzk \tag{7}$$

$$Izk = \frac{3}{2} \mathrm{Re}\left\{ \underline{S}^* \cdot \underline{Iu} \right\} \tag{8}$$

$$\underline{\mathrm{Iu}} = \frac{2}{3}\left(Iur(t) + Ius(t) e^{j\rho} + Iut(t) e^{-j\rho} \right) \tag{9}$$

$$\rho = 2\pi / 3$$

$$\underline{S} = \begin{cases} 0 \\ \frac{2}{3} e^{jk\frac{\pi}{3}} \qquad k = 1,2,\ldots,6 \end{cases} \tag{10}$$

Equations (7) and (8) connect AC and DC sides of switching bridge by switching space phasor *S,* defined with (10). S can have only six non-zero values shown on fig.9. The corresponding values of phasors and switching states are shown in Table 1, where values of parameter k from (10) are given.

Current rectifier is described by two sets of equations:

1. Equations that origin on basis of Kirchof's lows, applied on fig.8:

$$In - Iu = C2' \frac{dUu}{dt} \tag{11}$$

$$Un - Uu = L1 \frac{dIn}{dt} \tag{12}$$

$$Lzk \frac{dIzk}{dt} = Uzk - U_L - Izk \cdot R_L \tag{13}$$

2. Equations that models switching bridge:

$$\underline{Iu} = \underline{S} \cdot Izk \tag{14}$$

$$Uzk = \frac{3}{2} \mathrm{Re}\left\{ \underline{S}^* \cdot \underline{U}\, u \right\} \tag{15}$$

$$\underline{U}u = \frac{2}{3}\left(Uur(t) + Uus(t) e^{j\rho} + Uut(t) e^{-j\rho} \right) \tag{16}$$

$$\rho = 2\pi / 3$$

$$\underline{S} = \begin{cases} 0 \\ \frac{2}{\sqrt{3}} e^{j(\frac{\pi}{6} + k\frac{\pi}{3})} & k = 1,2,\ldots,6 \end{cases} \tag{17}$$

Equations (14) and (15) connect AC and DC side of switching bridge using switching space phasor S defined with (17). S differs from (10) for displacement angle $\pi/6$. Switching space phasor has only six non-zero values, which are shown on fig.10. Values of parameter k from (17), for corresponding state of the switch, are given in Table 1.

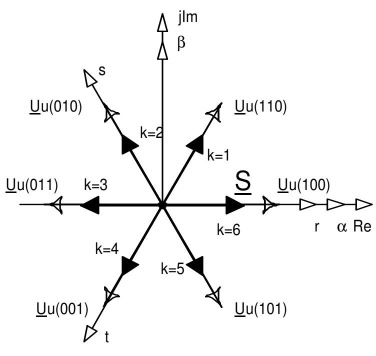

Fig.9. Possible values of switching phasor S of voltage rectifier in complex plane.

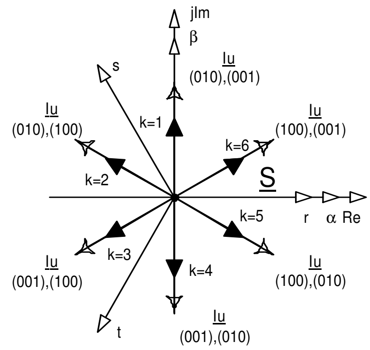

Fig.10. Possible values of switching phasor S of current rectifier in complex plane.

CONTROL SIGNALS

Control of the switching bridge, modeled in such a manner is obtained by a function, which takes values from an assembly 0, 1, 2, 3, 4, 5 and 6.

Simulations in this paper are limited to diode rectifier, so switching control should correspond to a switching of diode bridge. Such a control will be addressed in further text as diode control. There are two modes for achieving such control.

The first mode is using sequence generator, which repeats the row 5, 6, 1, 2, 3, 4, with the period of 20 ms. This method is simple and has good description of the converter, but only for a case when there is no input filter (L and C are 0)

The second mode of diode control for voltage rectifier is based on single direction of current flow, so detection of polarity of input current Iu is performed (i.e. their components Iur, Ius and Iut). On this basis, it is determined which of the 6 diodes conduct. Verification of such approach is generating of the row 5, 6, 1, 2, 3, and 4 with the period of 20ms, for the case when there is no input filter, which corresponds to the first mode. The second mode of diode control for current rectifier is based on determination of momentarily the biggest and the smallest input signals (Uur, Uus or Uut). On this basis the two direct polarized diodes are determined. As in previous case, the verification of the method is generating the row 5, 6, 1, 2, 3, 4 with period of 20ms, for the case without input filter.

RESULTS OF SIMULATION

As it was expected, the results of simulation with the models of voltage and current rectifiers, in case of diode bridge, gives similar wave shapes and values of signals of corresponding dual parameters. Simulations shown on Figs. 11-14 are performed for two cases:

1. without input circuit (Figs. 11 and 12)
2. with input circuit (Figs. 13 and 14)

CONCLUSION

In the paper a theoretical presentation and an illustration of application of duality characteristics and relations are given, which enable unification of converter models in electrical systems. As an example of dual circuits a voltage rectifier is transformed into current one using duality relations.

For analysis purposes, these two circuits are modeled and simulated using MATLAB – SIMULINK software. The most important part in this analysis is switching bridge. The complex model of switching bridge in representation with space phasor is used, which can be controlled by switching space phasor *S*. The advantage of such model is in its simplicity, as control is done by only one function.

As a consequence to duality characteristic, the voltage rectifier and his dual current rectifier can be controlled with identical function S. As for the voltage rectifier there are numerous developed control techniques, they can be easily applied on current rectifier as well using duality principle

Simulations in SIMULINK, which has been shown in part 7, are made only for uncontrolled (diode) voltage and current rectifier. Results of simulations verify duality of these two circuits.

REFERENCES

[1] J.W. Kolar, H.Ertl, F.C.Zach *"Analysis of the duality of three phase PWM converters with DC voltage link and DC current link"*, IEEE Trans. on Industry Applications, pp.724-737, 1989.

[2] P.Bauer *"Mathematical model of a three phase converter"*, ED & PE '94, High Tatras, Slovakia, pp.147-153, 1994.

[3] V.Katić, D.Graovac *"A method of real analysis of AC/DC converter line side harmonics"*, Facta Universitas (YU), Series: Electronics and Energetics, Vol. 10, No.1, pp.107-123, 1997.

[4] J.Žaček, J.Lettl *"PWM voltage stiff rectifiers"*, ED & PE '94, High Tatras, Slovakia, pp.219-224, 1994.

APPENDIX

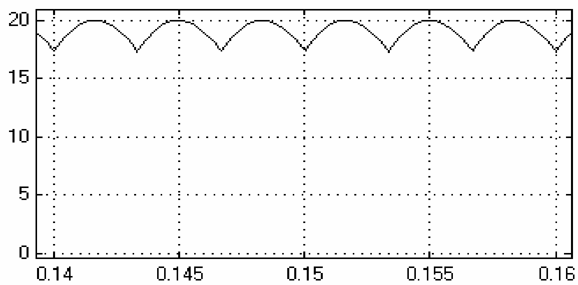

Fig.11. *Current (Izk) at the output of voltage rectifier from fig.7 and identical dual voltage (Uzk) at the output of current rectifier from fig.8, without input filter.*

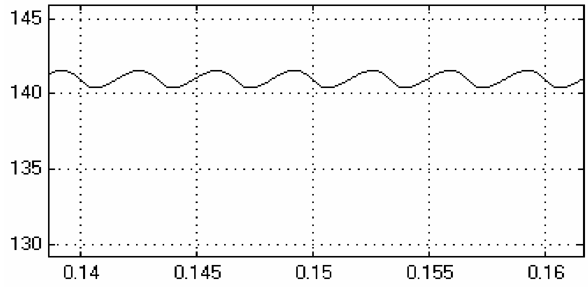

Fig.12. *Voltage (Uzk) at the output of voltage rectifier from fig.7 and identical dual current (Izk) at the output of current rectifier from fig.8, without input filter.*

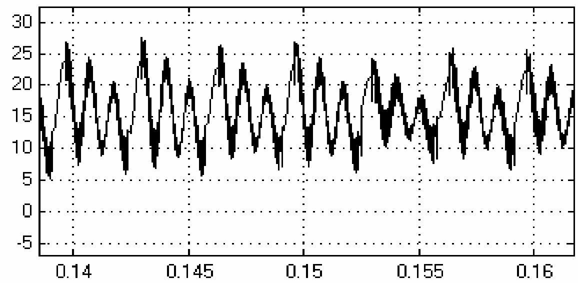

Fig.13. *Current (Izk) at the output of voltage rectifier from fig.7 and identical dual voltage (Uzk) at the output of current rectifier from fig.8, with input filter different from zero.*

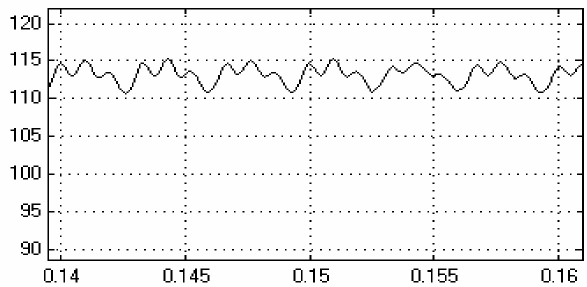

Fig.14. *Voltage (Uzk) at the output of voltage rectifier from fig.7 and identical dual current (Izk) at output of current rectifier from fig.8, with input filter different from zero.*

NONLINEAR DYNAMICS IN CURRENT CONTROL CONVERTERS

Zoltán Sütő1, István Nagy1,2
1Department of Automation and Applied Informatics, Budapest University of Technology and Economics, Budapest, Hungary, H-1111, Budafoki út 8., phone: (36-1) 463-1165, fax: (36-1) 463-3163, e-mail: {suto, nagy}@elektro.get.bme.hu
2Computer and Automation Institute, Hungarian Academy of Science, Budapest, Hungary

Abstract: *The paper reports periodic, quasi-periodic and chaotic operations of three-phase Voltage Source Inverter (VSI) equipped with an internal current feedback loop comprising three independent hysteresis current comparators on the AC lines. This Current Controlled Pulse Width Modulated (CC-PWM) converter system has been studied in two configurations with two and four independent energy storage filters on the AC side, respectively. The complex nature of the systems is shown by computer simulations. Frequently, coexisting system states develop, that is, system trajectories settle down in different steady-states at the same parameter setting depending only on the initial conditions.*

Key Words: ***Chaos, Nonlinear Dynamics, DC/AC Converters, Current Control***

INTRODUCTION

Nowadays, chaotic behaviors of various power electronic systems have been reported in large number of papers. Most efforts are made on exploring nonlinear phenomena in different types of DC/DC converters [1, 2, 3], and only a few publications have been dealt with non-linearity issues of three-phase converter systems and some electromechanical systems [4, 5]. The flavor of power electronic systems resides in their variable structure piecewise linear nature. System equations are represented by linear differential equations but at the change of the switching state of the converter, the state equations governing the evolution of the state variables are suddenly modified resulting in non-smooth system trajectories. As the timing of switching actions depends on state variables due to closed feedback loops, the power electronic system becomes strongly nonlinear and exhibits a wide spectrum of nonlinear phenomena.

This paper is concerned with the periodic, subharmonic, quasi-periodic and chaotic operations of three-phase Voltage Source Inverter (VSI) configurations with two and four independent energy storage AC side filters, respectively. The VSI is equipped with independent hysteresis current comparators, also called as free-running Hysteresis Current Controller (HCC), on the three AC lines. Pulse Width Modulated (PWM) three-phase VSIs providing nearly sinusoidal AC line currents eliminate stator current dynamics in high performance AC drives such as machine tools, robots, aerial servo systems, etc., and so offer substantial advantages. They are increasingly popular in AC/DC converters for suppressing network pollution. The closed loop CC-PWM method has inherent advantages. Applying in AC drives the nearly sinusoidal currents improve the system dynamics in wide frequency range, reduce the winding losses and torque pulsation. Applying in AC/DC converters the network pollution on the line side is suppressed. Furthermore, the instantaneous peak current is limited and the current overload problem is solved [6].

Some previous works have been concerned with the nonlinear behaviors of a VSI supplying power to an induction machine, where the HCC was operated with a quite sophisticated space-vector based switching algorithm with two concentric tolerance band circle [7, 8, 9 ,10]. Periodic, subharmonic and chaotic operations was explored. Various nonlinear phenomena, period doubling route to chaos, intermittency and a special period adding bifurcation route generated by a piece-wise linear discontinuous return map was studied. In [11], quasi-periodicity, period doubling, chaos and various crises was reported in a one-phase system controlled by hysteresis PWM technique and studied in the context of power electronics.

SYSTEM CONFIGURATIONS

The VSI is a simple three-phase bridge connection of six controlled bidirectional electronic switches (Fig. 1). It can be modeled by a 3×2 size switching matrix $\mathbf{S}=[s_n^m]$ (m=1,2,3; n=1,2) with boolean variables s_n^m in the matrix elements, where m is the row index and n is the column index. In each switching state of the VSI, three switches are on and the other three ones are off (in one phase one of the switches is always on the other one is off, or in other words, the rows of $\mathbf{S}$ are identity vectors).

Ideal voltage source v_1 is assumed in the DC side, while symmetrical three-phase circuit is built up in the AC side. Two configurations are studied. In Fig. 1(a) resonant L–C filters are applied in each phase, and symmetrical sinusoidal current sources $\mathbf{i}$ are considered

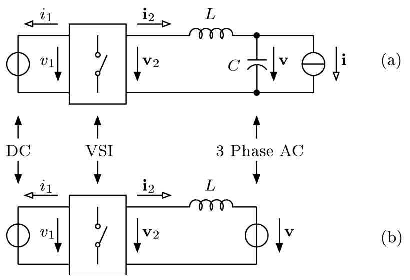

Fig. 1. *VSI configurations with different AC side filters.*

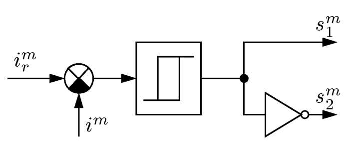

Fig. 2. *Hysteresis control of all three AC line currents (m = 1, 2, 3).*

as load. In the second case in Fig. 1(b), the capacitor C was left out, only the inductor L remained as AC side filter with ideal sinusoidal voltage sources $\mathbf{v}$ as load. AC side variables $\mathbf{v}_2, \mathbf{i}_2, \mathbf{v}$ and $\mathbf{i}$ used in the calculations are all column vectors. Variables expressed in both α–β stationary and d–q rotating reference frame are used in the simulations. The system equations written in α–β stationary reference frame for configuration in Fig. 1(a) is

$$\frac{d}{dt}\begin{bmatrix}\mathbf{i}_2\\ \mathbf{v}\end{bmatrix}=\begin{bmatrix}\mathbf{0} & -\frac{1}{L}\mathbf{I}_2\\ \frac{1}{C}\mathbf{I}_2 & \mathbf{0}\end{bmatrix}\begin{bmatrix}\mathbf{i}_2\\ \mathbf{v}\end{bmatrix}+\begin{bmatrix}\frac{1}{L}\mathbf{I}_2 & \mathbf{0}\\ \mathbf{0} & -\frac{1}{C}\mathbf{I}_2\end{bmatrix}\begin{bmatrix}\mathbf{v}_2\\ \mathbf{i}\end{bmatrix} \tag{1}$$

and for configuration in Fig. 1(b)

$$\frac{d\mathbf{i}_2}{dt}=\frac{1}{L}(\mathbf{v}_2-\mathbf{v}) \tag{2}$$

where $\mathbf{I}_2$ is a 2×2 identity matrix and $\mathbf{0}$ is null matrix. The output voltage vector $\mathbf{v}_2$, which acts as input for the state space models in (1) and (2), can be expressed algebraically from the DC side voltage v_1 by means of the switching matrix:

$$\mathbf{v}_2=\frac{2}{3}\begin{bmatrix}1 & -1/2 & -1/2\\ 0 & \sqrt{3}/2 & -\sqrt{3}/2\end{bmatrix}\mathbf{S}\begin{bmatrix}1\\ 0\end{bmatrix}v_1 \tag{3}$$

Hysteresis Control

The task of the HCC algorithm is to select an appropriate switching state $\mathbf{S}$ to track the reference current $\mathbf{i}_r$. Suffix r denotes reference signal. When the error current reaches the periphery of the tolerance band, the algorithm forces to switch into a new converter state. The paper evaluates the behavior of converter systems with the simplest hysteresis controller using three independent hysteresis comparators in the three AC lines of the VSI (Fig. 2). The AC line currents are obtained from the state variable $\mathbf{i}_2$ of system (1) or (2) as

$$\begin{bmatrix}i^1\\ i^2\\ i^3\end{bmatrix}=\begin{bmatrix}1 & 0\\ -1/2 & \sqrt{3}/2\\ -1/2 & -\sqrt{3}/2\end{bmatrix}\mathbf{i}_2 \tag{4}$$

In the evaluation of the simulation results error signals $\boldsymbol{\varepsilon}$ relative to the corresponding reference values are defined as

$$\boldsymbol{\varepsilon}=(\mathbf{x}_r-\mathbf{x})/\|\mathbf{x}_r\| \tag{5}$$

in both α–β and d–q reference frames for all state variables, inductor currents and capacitor voltages, respectively. Accordingly, $[\varepsilon_d^i\ \varepsilon_q^i]$ and $[\varepsilon_\alpha^i\ \varepsilon_\beta^i]$ are used for the inductor error currents, while $[\varepsilon_d^v\ \varepsilon_q^v]$ and $[\varepsilon_\alpha^v\ \varepsilon_\beta^v]$ are used for the capacitor error voltages. In the calculations reference voltage $\mathbf{v}_r$ was predefined as three-phase symmetrical sinusoidal voltage for the output voltage $\mathbf{v}$ of VSI in Fig. 1(a), all other reference values for currents and voltages were calculated from circuit parameters L and C and from the sinusoidal load current $\mathbf{i}$, respectively. All corresponding reference values were maintained in the other system configuration in Fig. 1(b).

NONLINEAR PHENOMENA

The main objective of the following study is the calculation of the error signals in steady-state in order to discover the various possible states of the converter systems shown in Fig. 1. The analysis was performed by simulation in Matlab enviroment. Matlab programs with Simulink models were developed for the calculation of state variables and error signals, respectively. In these simulations, only one system parameter, referred to as μ, has been changed. μ is defined as the ratio of the DC voltage v_1 over the magnitude of the reference voltage calculated for the output voltage $\mathbf{v}_2$ of the VSI. μ has been changed in the range $\left[2/\sqrt{3};\sqrt{2}\right]$.

Attractors

The behavior of nonlinear dynamical systems can exhibit three classical types: equilibrium, periodic including subharmonic and quasi-periodic states. Their trajectories are called *regular attractors*. However, an additional bounded solution, termed chaos can develop as well. Trajectory of this system state is frequently called as *strange attractor*. The tools useful to explore the complex and frequently chaotic behavior of nonlinear dynamical systems are essentially different from the ones applied in linear cases. Using conventional methods, looking at time histories or frequency spectra, the chaotic motion usually cannot be distinguished from stochastic noise, although there are profound difference between them. The response of our systems can be either periodic (subharmonic), quasi-periodic or chaotic. In general, varying a parameter the steady state is obtained after an initial transient process, where the lengths of transients could be very different even if the change of parameter was tiny. Sometimes, it is quite difficult to decide algorithmically, whether the system state observed is chaotic or chaotic transient. In the latter one, the simulation time should be increased to reach the real final state.

Periodic and subharmonic operation

Fig. 3 presents state-space trajectories at two periodic operations. The operation states are periodic as the curves are closed, but periodic and subharmonic orbits can not be distinguished by looking only at the trajectories.

Systems with either periodic or chaotic steady states are analyzed by a special discrete modeling technique, the so called *Poincaré map*. The Poincaré map is obtained by sampling the trajectory of the continuous system at time as it intersects a suitable chosen hyperplane in the state-space. For systems with periodic forcing, as in our case, the Poincaré map does not differ from the sampling of the system trajectory with a properly chosen sampling period T_s. With this sampling, a sequence of points are obtained $\{\mathbf{x}_0, \mathbf{x}_1, \mathbf{x}_2 \ldots\}$ in the state space. Periodic steady-state with period T_s is represented by a single *fixed point* $\mathbf{x}^*$ in the Poincaré map, that is, in the sequence of Poincaré

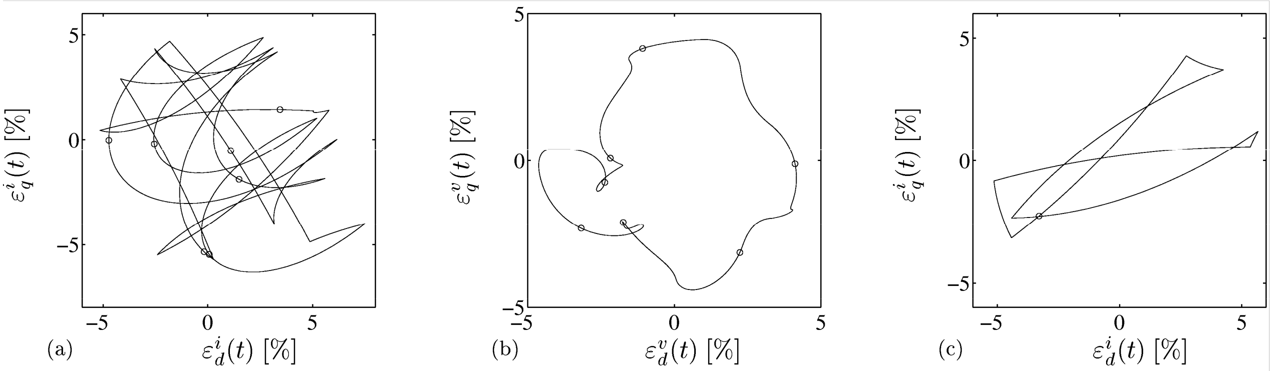

Fig. 3. *(a–b) 7th-order subharmonic trajectories for system in Fig. 1(a) (μ = 1.187). (c) Periodic trajectory for system in Fig. 1(b) (μ = 1.407).*

samples $\mathbf{x}_k = \mathbf{x}_{k+1} = \mathbf{x}^*$ for all $k > K_{tr}$. To get rid of the transient phase the first several points from $k = 1$ to $k = K_{tr}$ should be dropped. K_{tr} is the estimated number of sampling points taken in transient state. Kth-order subharmonic solutions with period KT_s correspond to fixed points $\{\mathbf{x}_1^*, \mathbf{x}_2^*, \ldots, \mathbf{x}_K^*\}$. These fixed points are repeated in the sequence of Poincaré samples, that is, $\mathbf{x}_k = \mathbf{x}_{k+K}$. In our case, Poincaré map is calculated by sampling the error signals ε. Sampling period T_s is selected to be $T_p/6$, that is, the sixth of the period T_p of the reference current signals $[i_r^1\ i_r^2\ i_r^3]$ [7]. Looking at these sample points now the difference between periodic and subharmonic states can easily be made and the order of subharmonic states can be counted in Fig. 3.

Coexisting Attractors

The coexisting system states belonging to the same parameter setting can complicate further the investigation of the system. In Fig. 4 the initial conditions influence the final state of the system. Three attractors exist at this parameter value μ=1.32, two different quasi-periodic states and a chaotic one, the system trajectories can approach any of them. Although, three attractors have been found, there is no proof that additional ones do not exist. Only scanning the full state-space would give answer, but it requires an extremely large amount of calculations.

Quasi-periodic operation

A quasi-periodic solution may be expressed as a countable sum of sinusoidal signals with incommensurate frequencies and its trajectories winds around a torus in state space. Because the ratio of frequency components is irrational, the trajectory never closes on itself and the torus becomes more densely filled in. In practice however, the torus cannot be identified so simple. Quasi-periodic solutions appear much the same as chaotic solutions. Frequently it is difficult to separate them only on the basis of trajectories (see Fig. 4(a), 4(b) and 4(c)). Quasi-periodicity is more readily identified by means of Poincaré map. The Poincaré map of a quasi-periodic trajectory is a set of separate points along one or more closed curves so densely populated that it looks like a curve (Fig. 4(d) and 4(e)). A quasi-periodic state however could be more complex. In case of more than two incommensurate frequencies, e.g. three frequencies the simple so called first order Poincaré map in general does not generate an image of closed curve as a result of plotting the two state variables sampled by one of the frequencies. In order to produce closed curve the samples of the first order Poincaré map have to be sampled once more by one of the other two incommensurate frequencies different from the one used for the first order Poincaré map. This, of course, requires a much longer running time [12]. Quasi-periodic state is discovered in the topology with the higher-order AC side filter in Fig. 1(a). Its state-space trajectories and a Poincaré map are drawn in Fig. 5. Two tori can be discovered in the Poincaré map. The sample points seem to be on their surfaces, on two closed curves. They must be closed curves otherwise the surfaces of the two tori would be completely blacked out. It implies that the quasi-periodic solution has no more than two incommensurate fundamental frequency components, but some of them has some higher order harmonic component.

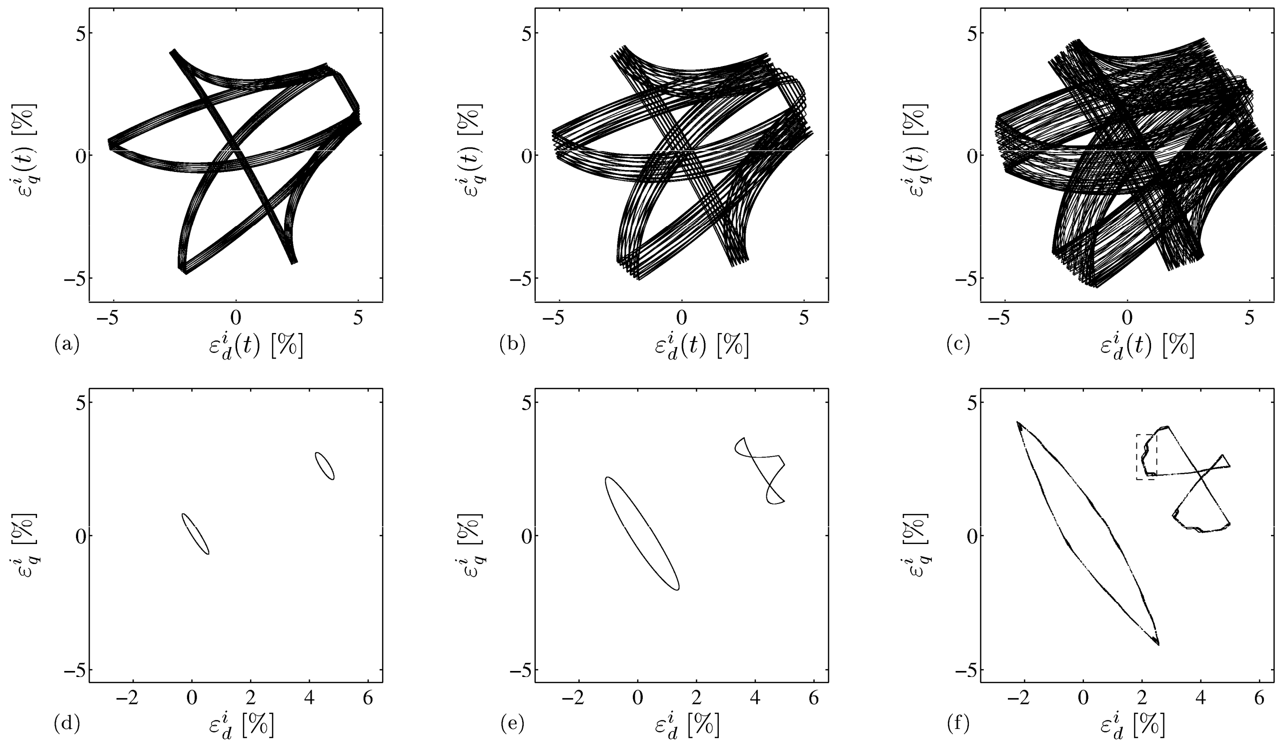

Fig. 4. *Coexisting quasi-periodic and chaotic states at the same parameter settings for system in Fig. 1(b) (μ = 1.32). (a–b) Two quasi-periodic error current trajectories. (c) Chaotic error current trajectory. (d–e) Poincaré maps belonging to subfigure (a) and (b), respectively. (f) Poincaré map of the chaotic state.*

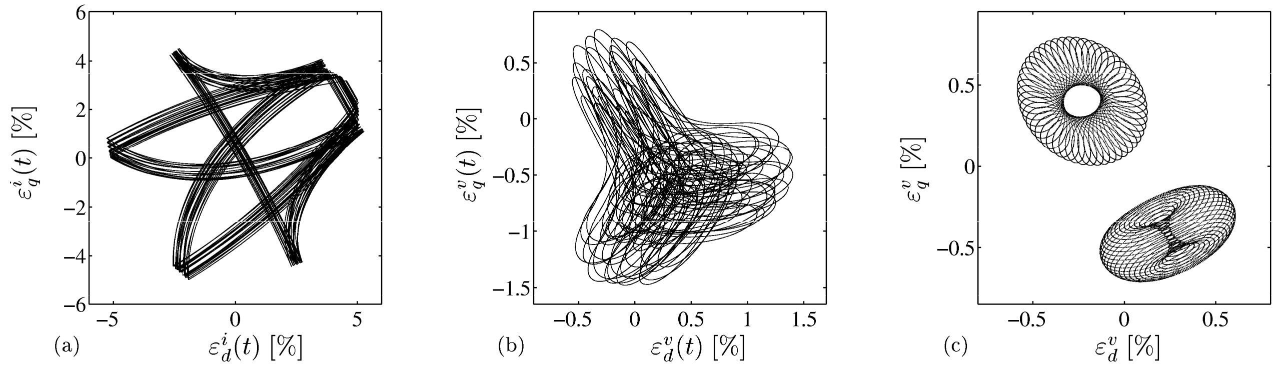

Fig. 5. *Quasi-periodic state for system in Fig. 1(a) (μ = 1.3). (a) Error current trajectory (b) Error voltage trajectory. (c) Poincaré map for the error voltage.*

Chaotic operation

Usually error current trajectories in our systems seem similar to the trajectory in Fig. 6(a) after a few periods of run. At first glance, the trajectory wanders in an apparently random way in the tolerance band. Integrating further the system equations, the tolerance band is filled out totally. This kind of trajectory could be a transient, or either a chaotic state. Sometimes, if the initial conditions are set unfortunately, the system runs into a extremely long transient process. Only a few periods are plotted in Fig. 6(a), but here 20000 periods of run are needed to reach the steady-state surely. After such a long run if any regular attractor is not reached, chaotic state is assumed. Chaotic states can be analysed more efficiently by plotting the Poincaré map samples (Fig. 6(b)). Usually a set of organized points are obtained in these diagrams reflecting a complex multilayered structure and order in the chaotic attractor. It is a direct consequence of the deterministic nature of the system. In our systems, basically two different chaotic states could be distinguished. In case of the first one, trajectories, as in Fig. 6(a), can reach points in the whole tolerance band. In the other case, as it was shown in Fig. 4(c), trajectories remain in narrower bounded areas. In the latter one the switching states follow each other periodically, and we can speak about a somehow "lower order" of chaos. For this case, viewing and comparing to the previous one, the Poincaré map exhibits a much understandable structure in Fig. 4(f) resembling to the Poincaré map of the quasi-periodic state (Fig. 4(e)). At first glance, the diagram shows a closed curve, which would imply a quasi-periodic solution, and the similarity in their trajectories would also support this idea.

However, zooming the small area marked by dashed-line box, a very interesting structure stands out with a self-similarity property in Fig. 6(c) revealing a chaotic state.

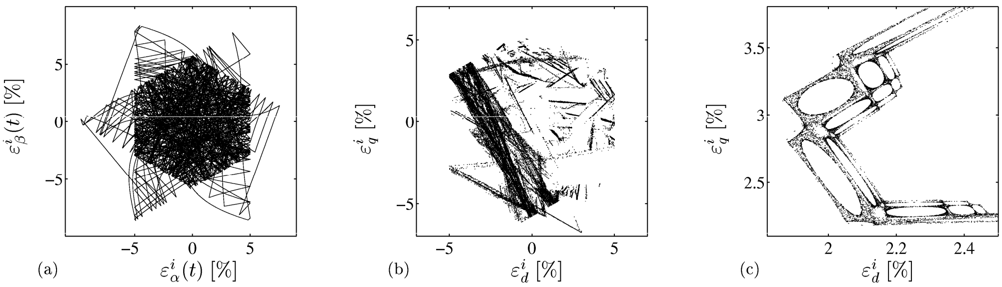

Fig. 6. *(a) Chaotic trajectory in α–β coordinates for system in Fig. 1(b) (μ = 1.3). (b) Poincaré map in d–q coordinates belonging to subfigure (a). (c) Poincaré map zoomed from Fig. 4(f).*

CONCLUSIONS

Astonishing nonlinear phenomena occurring in voltage source inverter furnished with hysteresis current controller has been studied with two and four independent energy storage filters on the AC side. The analysis was carried out by simulation in Matlab environment. These systems can exhibit periodic, subharmonic, quasi-periodic and chaotic responses. To make the picture more colourful here even coexisting system states can develop at the same parameter settings. The system trajectories have been attracted to different quasi-periodic and chaotic states depending on the initial conditions.

REFERENCES

[1] Hamill, D. C., Deane, J. H. B. and Jefferies, D. J. *“Modeling of chaotic DC-DC converters by iterated nonlinear mappings,”* IEEE Transactions on Power Electronics, vol. 7, pp. 25–36, Jan. 1992

[2] Chakrabarty, K., Poddar, G. and Banerjee, S. *“Bifurcation behavior of the buck converter,”* IEEE Transactions on Power Electronics, vol. 11, pp. 439–447, May 1996.

[3] Banerjee, S. and Chakrabarty, K. *“Nonlinear modeling and bifurcations in the boost converter”,* IEEE Transactions on Power Electronics, vol. 13, pp. 252–260, Mar. 1998.

[4] Kuroe, Y. and Hayashi, S. *“Analysis of bifurcation in power electronic induction motor drive systems,”* in Proceedings of the IEEE Power Electronics Specialists Conference (PESC'89), pp. 923–930, June 1989.

[5] Robert, B., Marion-Pera, M. and Goeldel, C. *“Dynamic behavior of a step motor analysed by chaos theory,*|” in Proceedings of the 6th International Conference ELECTRIMACS'99, vol. I, (Lisboa, Portugal), pp. 115–120, Sept. 14–16, 1999.

[6] Nagy, I. *“Novel adaptive tolerance band based PWM for field-oriented control of induction machines,” IEEE Transactions on Industrial Electronics, vol. IE-41*, pp. 406–417, 1994.

[7] Sütő, Z., Nagy, I., Backhausz, L. and Zabán, K. *“Controlling chaos in current forced induction motor,”* in Proceedings of the 7th International Power Electronics and Motion Control Conference (PEMC'96), vol. 3, (Budapest, Hungary), pp. 282–286, Sept. 2–4, 1996.

[8] Tsuboi, H. and Vajda, I. eds., *Applied Electromagnetics and Computational Technology II*, vol. 16 of *Studies of Applied Electromagnetics and Mechanics*, ch. Sütő, Z. and Nagy, I.: Study of Chaotic and Periodic Behaviours of a Hysteresis Current Controlled Induction Motor Drive, pp. 233–244. Amsterdam, The Netherlands: IOS Press, 2000.

[9] Sütő, Z. and Nagy, I. *“Bifurcation due to discontinuity of return map in hysteresis current control of induction motor,”* in Proceedings of the 6th International Conference ELECTRIMACS'99, vol. III, (Lisboa, Portugal), pp. 275–280, Sept. 14–16, 1999.

[10] Banerjee, S. and Verghese, G. C. eds., “*Nonlinear Phenomena in Power Electronics: Bifurcations”,* Chaos, Control and Applications, ch. Nagy, I. and Sütő, Z.: Nonlinear Phenomena in the Current Control of Induction Motors, pp. 328–338. IEEE Press, 2001.

[11] Magauer, A. and Banerjee, S. *“Bifurcations and chaos in the tolerance band PWM technique,”* IEEE Transactions on Circuits and Systems-I., vol. 47, pp. 254–259, Feb. 2000.

[12] Parker, T. S. and Chua, L. O. “*Practical Numerical Algorithms for Chaotic Systems*.” New York, USA: Springer-Verlag, 1989.

[13] Carton, D., Robert, B. and Goeldel, C. *“Self-similarity and chaos in a current mode PWM bridge,”* in Proceedings of the 6th International Conference ELECTRIMACS'99, vol. I, (Lisboa, Portugal), pp. 109–114, Sept. 14–16, 1999.

[14] Woywode, O. and Güldner, H. *“Application of statistical analysis to DC-DC converters,”* in Proceedings of the International Power Electronic Conference IPEC2000, (Tokyo, Japan), pp. 90–94, 2000.

[15] Chen, J.H., Chau, K.T. and Chan, C.C., *“Analysis of Chaos in Current-Mode-Controlled DC Drive Systems”,* IEEE Trans. Industrial Electronics, Vol.47, No.1, 2000, pp. 67-76.

[16] Vajk, I., Hetthéssy, J. and Charaf, H. *“Neural Network Approximators in Modelling Dynamic Nonlinear Systems”,* Electrotechnik und Informationstechnik, Springer, 2000, pp. 43-48.

[17] El Aroudi, A., Benadero, L., Toribio, E. and Machiche, S. *“Quasiperiodicity and Chaos in the DC-DC Buck-Boost Converter”,* International Journal of Bifurcation and Chaos, Vol.10, No.2, 2000, pp. 359-371.

[18] Iu, H.H.C. and Tse, C.K. *"Bifurcation Behaviour of Parallel-Connected Buck Converters"*, IEEE Transactions on Circuits and Systems I, Accepted

ACKNOWLEDGEMENTS

The authors wish to thank the Hungarian Research Fund (OTKA T029026) and the Control Research Group of the Hungarian Academy of Science for their financial support.

CLASS E INVERTER WITH MATCHING CIRCUIT FOR HF INDUCTION HEATING

Jacek Junak, Bogusław Grzesik
Silesian University of Technology, Institute of Theoretical and Industrial Electrotechnics, Gliwice, Poland, junak@polsl.gliwice.pl, grzesik@polsl.gliwice.pl

Abstract: *The paper deals with a Class E inverter including the LC matching circuit operates at constant frequency. The inverter is designed for high frequency induction heating. The matching circuit is used to match load to inverter (therefore the hf matching transformer is not needed) and also to reduce influence of the load parameters variation on the output power of the inverter and its characteristics. The presented matching circuit is of "T" type. The analysis of the inverter with matching circuit leads to extended topologies of Class E inverter such as Class E inverter with series choke.*

Key Words: ***resonant inverters, induction heating, class E inverter, matching circuit, high frequency***

INTRODUCTION

The paper concerns a Class E inverter (Fig.1) with *LC* matching circuit (Fig. 7,8,9). The inverter operates at constant frequency (1MHz) and it is designed for high frequency induction heating.

The main advantage of the resonant Class E inverter is significant reduction in switching loss due to soft commutation. Therefore the high frequency together with high efficiency could be achieved [1].

The significant problems arise when one applies the resonant inverter to high frequency induction heating. It results from character of the load (excitation coil with sample). Such load is of low impedance and its parameters changes due to the temperature of the sample and its position inside coil. Therefore in order to achieve the assumed output power the matching the load to the inverter is required and also reduction of the load parameter changes.

Because of significant advantages of the Class E inverter, this inverter is taken into account also as a supplying source for high frequency induction heating. Due to character of load it is impossible to apply basic topology of Class E inverter (Fig.1). It is so because of two problems that are needed to be solved: matching the load to the inverter and reduction of variation of equivalent parameters of the load. Matching could be done by means of high frequency matching transformer. Reduction of load parameters variation could be done using frequency control [2] or switched reactive components [3].

There is the inverter with *LC* matching circuit presented in the paper. This additional circuit ensures matching the load to inverter and reduction of load parameter variation without transformer at constant frequency.

CLASS E INVERTER – BASIC TOPOLOGY

The basic topology of the Class E inverter is shown in Fig.1. The inverter is supplied form DC voltage source E through DC choke L_{DC}. The DC choke reduces the ripple in supplying current. The inverter embraces also one transistor, two capacitors C_1 and C_2 and load *RL*.

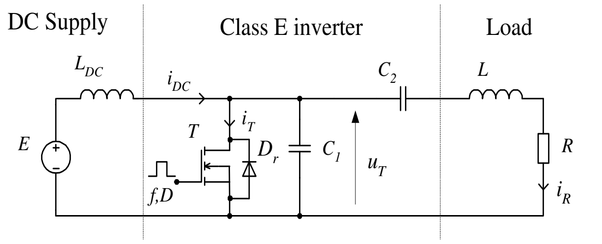

Fig.1. *Class E inverter (basic topology)*

For given parameters of load and control (*f,D*) it is possible to select value of C_1 and C_2 to achieve waveforms of the transistor as it is presented in Fig.2. It is the optimum mode of inverter operation [1].

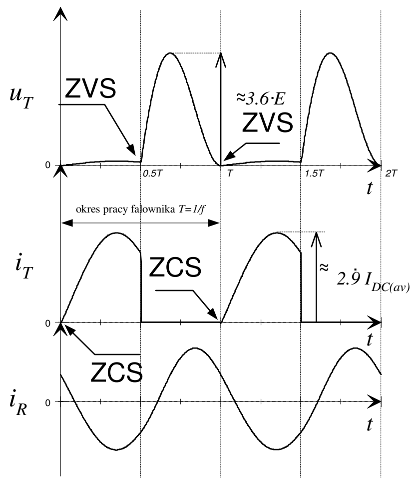

Fig.2. *Optimum mode (point) of inverter operation*

When parameters of load changes its values the suboptimum or no optimum mode of operation can be achieved – Fig.3. In suboptimum mode, a switch of the inverter turns on and off at ZVS (Fig.3.a). Due to ZVS of the switch this mode of operation is acceptable. The third mode of operation, shown in Fig.3b, this is nonoptimum mode of operation. Due to NZCS of the switch this mode often is not acceptable.

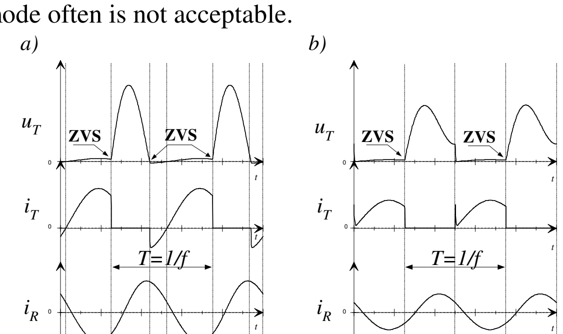

Fig.3. *Suboptimum (a) and nonoptimum (b) mode of operation*

Range of the load parameters for which ZVS switching is achieved is shown on the surface of load parameters *RL* in Fig.4. In this figure there the border curve of suboptimum mode is depicted. Parameters R_o and L_o refer to optimum mode of operation.

Inside this curve there are load parameters for which ZVS holds [4]. ZVS of the transistor leads to reduction of switching loss and high efficiency at high operation frequency.

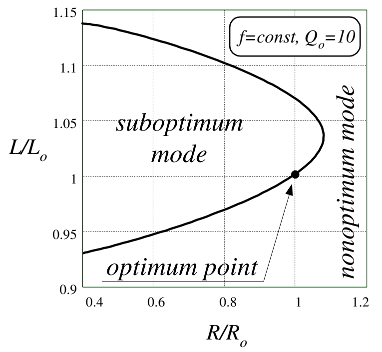

Fig.4. *Border curve of the suboptimum mode*

EQUVALENT PARAMERES OF THE LOAD

The excitation coil with sample is the load for AC supply (the Class E inverter in this case) . Dimensions of the assumed coil and sample is shown in Fig.5.a. Inside of copper coil cooled with water is crucible with solid nonmagnetic (Cu, Al) solid sample. View of the coil with sample is shown in Fig.5.b.

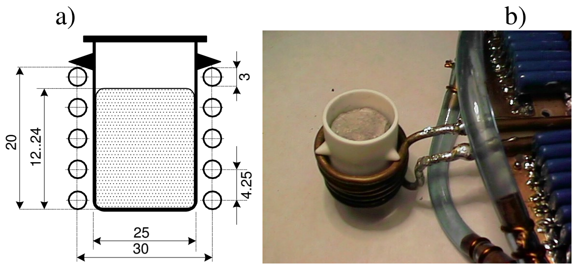

Fig.5. *Dimensions (a) and view (b) of the excitation coil and crucible with sample*

Equivalent parameters of coil with sample (at frequency 1MHz) are illustrated in Fig.6. Changes in parameters result from changes of temperature of sample θ_{ws}. In case of no load condition (coil without sample) the inductance increases significantly up to L=600uH.

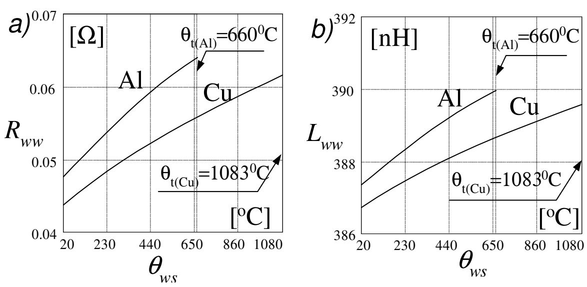

Fig.6. *Equivalent parameters of the coil with sample as a function of the temperature of the sample* θ_{ws}

1. CLASS E INVERTER WITH MATCHING CIRCUIT

The matching circuit is inserted between inverter and load as it is presented in Fig.7.a [7]. Assuming that output current is almost sinusoidal the *LC* matching circuit with load can be replaced by equivalent circuit R_ZX_Z (seen from *ca* port)- Fig.7.b.

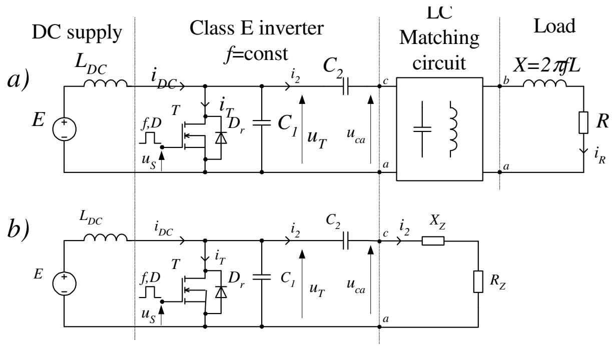

Fig.7. *Class E inverter with matching circuit (a) and with equivalent circuit of the load (b)*

The assumed matching circuit is of *T* type – Fig.8. Matching is mainly realized due to value of C_r capacitor. At the same time proper selection of C_s ensures that matching circuit act as impedance inverter [5]. Load parameters variation can be reduced during heating and also under no load condition (coil without sample).

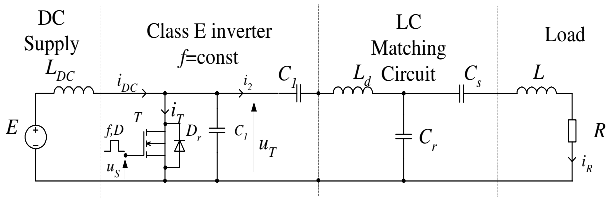

Fig.8. *Class E inverter with LC matching circuit of T type*

In the Class E inverter with matching circuit of "T" type the capacitor C_2 can be removed, and the inverter with series choke is achieved. This inverter is shown in Fig.9. In this case capacitors C_r and C_s are selected due to parameters of the matching circuit and C_1 and L_2 in order to achieve optimum point of operation.

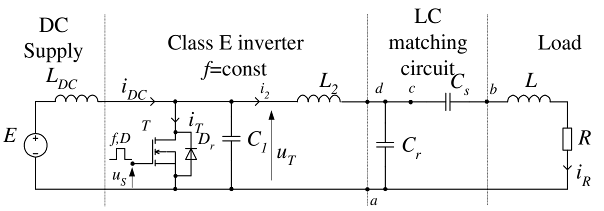

Fig.9. *Class E inverter with series choke*

The matching circuit is used to match load to inverter (due to low impedance of the load) and also to reduce load parameters variation and its influence on inverter output power. The parameters of the matching circuit were selected in order to reduce changes in equivalent resistance R_Z. Changes in load parameters as a function of temperature of the sample as shown in Fig.10.

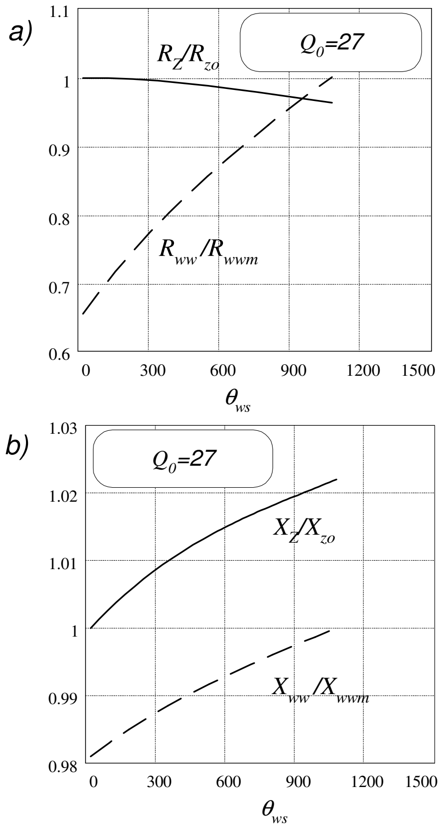

Fig.10. *Parameters of matching circuit with load – R_ZX_Z and parameters of the load $R_{ww}X_{ww}$ (Cu) as a function of temperature of the sample: resistance (a) and reactance (b); R_{Zo}, X_{Zo} – parameters of equivalent circuit at optimum mode of operation; R_{wwm}, X_{wwm} – maximum values of load parameters at temperature ($\theta_{ws}=1083^0C$)*

Load parameters variation can be also shown on the R_ZX_Z surface – Fig.11. On this surface is also presented border curve of suboptimum mode of inverter. This curve is valid for q-factor Q=27. Such q-factor results from parameters of the load.

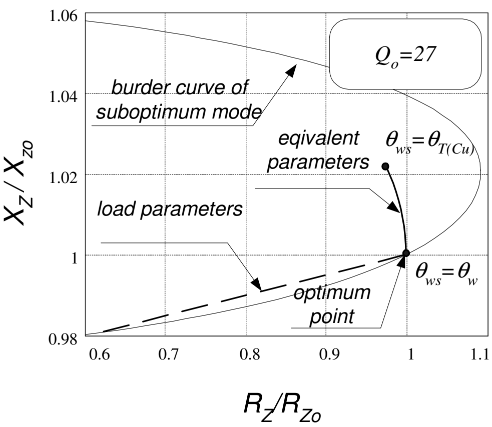

Fig.11. *Parameters of matching circuit with load – R_ZX_Z and parameters of the load (dotted line) on surface RX;*

As a result of stabilization of equivalent resistance R_Z the higher output power could be achieved during heating of the sample. This output power of inverter with and without matching circuit as a function of the temperature of the sample is shown in Fig.12.

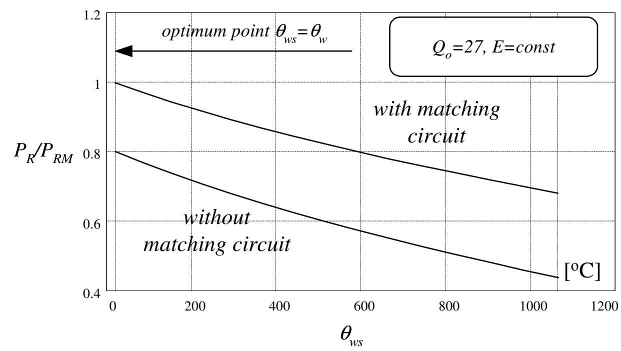

Fig.12. *Output power of the inverter P_R with and without matching circuit as a function of the temperature of the sample; P_{RM} –maximum output power which could be achieved for given transistor*

EXPERIMENTAL RESULTS

The Class E inverter with series choke was built and tested at frequency of 1MHz. Schematic diagram of the laboratory version is shown in Fig.13. Laboratory measurement were done at output power of 0.5kW-1kW. Transistor MOSFET IRFP350 was used. Example parameters of the circuit: $C_s=2\cdot C_{s1}$=104nF, C_r=192nF, $L_2=2\cdot L_{21}$=1.05uH, C_1=5.2nF. The equivalent parameters of the load are shown in Fig.6.

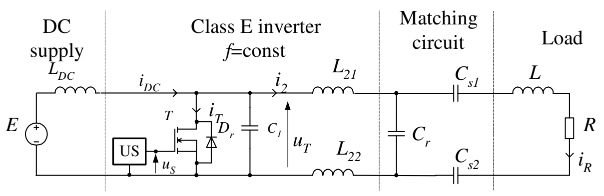

Fig.13. *Class E inverter with series choke for high frequency induction heating*

There are voltage/current waveforms of transistor under load condition for cold copper sample ($\theta_{ws}=20^0C$) and melted ($\theta_{ws}=1083^0C$) are presented in Fig.14.a and Fig.14.b respectively. According to reduction of parameters variation of equivalent circuit, inverter in wide range of load parameters variation operates with ZVS (suboptimum mode) near optimum mode.

a)

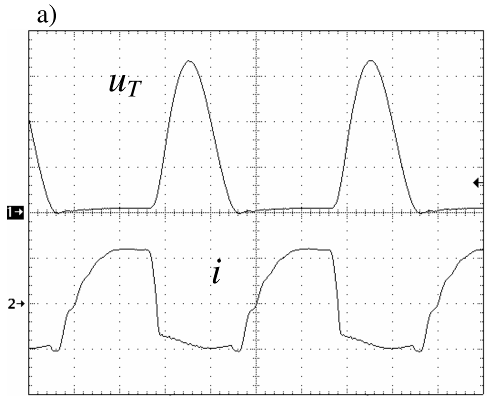

b)

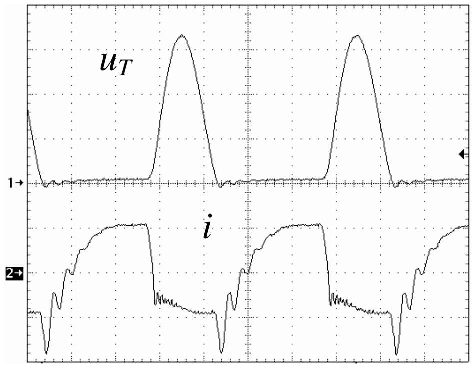

Fig.14. *Experimental results: waveforms of switch voltage u_T – 100V/div and switch current i_T – 20A/div in optimum point (θ_{ws}=20^{0}C) and sub-optimum mode of operation (θ_{ws}=1083^{0}C) (time 250 ns/div) (E=95V)*

Also in case of no load condition (coil without sample) inverter operates in suboptimum mode –Fig.15.

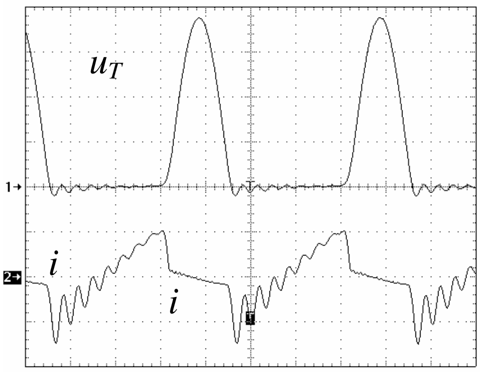

Fig.15. *Experimental results: waveforms of switch voltage u_T – 100V/div and switch current i_T – 20A/div under no load condition (time 250 ns/div) (E=95V)*

CONCLUSIONS

The Class E inverter with matching circuit operating at constant freqency is presented in the paper. The inverter is designed for high frequency induction heating. The example inverter was examined at frequency of 1MHz.

Applying the *LC* matching circuit allows inverter to operate in wide range of load parameters in suboptimum mode (ZVS). It leads to reduction of output power variation of inverter and allows inverter to operate under no load condition at constant supplying voltage *E*=const.

The presented matching circuit is of “T” type. The analysis of the inverter with matching circuit leads to extended topologies of Class E inverter - Class E inverter with series choke.

The additional advantage is that the auxiliary *LC* matching circuit do not change the installed power of the inverter.

REFERENCES

[1] Kazimerczuk M.K., Czarkowski D.: *“Resonant Power Converters”,* John Wiley & Sons Inc., 1995.

[2] Grzesik B, Kaczmarczyk Z, Kasprzak M.: *“Control of class E inverter with variable parameters of the load”*, PCIM'99 Europe, ZM Commun. GMBH. 1999, Nurnberg, Germany, pp.193-8.

[3] Hinchliffe S., Hobson L., Collins D.: *“Optimized Class-E amplifier with load variation”,* Electronics Letters, vol.23, no. 18, August 1987, pp. 973-974

[4] Grzesik B., Junak J. Kaczmarczyk Z.: *“Characteristics of Class E inverter with variable load in sub-optimum mode”,* XV Symposium EPNC’98, Liege (Belgium), September 1998.

[5] Kazimierczuk M.K, Bui X.T.: *“Class E amplifier with capacitive impedance inverter”,* IEEE Transactions on Industrial Electronics, Vol. 36, No.3., August 1989, pp.425-433.

[6] Grzesik B., Junak J.: *“LC matching circuits for Class E inverter with non-stationary load”,* European Conference on Circuit Theory and Design ECCTD’99, Stresa (Italy), 29.08-02.09.1999r., vol. I, pp. 575-578

[7] Junak J.: *“Application of Class E inverter for high frequency induction heating”* Ph.D. thesis (in Polish), Silesian University of Technology, Institute of Theoretical and Industrial Electrotechnics, Gliwice, 2001

MULTISTEP INDUCTORLESS DC-DC TRANSFORMER WITH HIGH VOLTAGE RATIO

Josif Ḱosev, Goce L. Arsov
University of Skopje, Faculty of Electrical Engineering, Skopje, Macedonia
j.kosev@ieee.org

Abstract: *A four-stage (five-step) high-voltage-ratio inductorless DC-to-DC converter is analyzed. Geometric progression for capacitance distribution among stages is proposed. Significant improvement of the output resistance is obtained. A prototype is constructed with capacitance geometric ratio of two and output power of approximately 300W. The characteristics are examined by PSPICE simulations and laboratory measurements.*
Key Words: ***Power Converter, Inductorless***

2. INTRODUCTION

Inductorless power converters are subjects of intensive research activities recently. They are mainly low-power high-frequency converters (several watts to several tens of watts) intended for hybridization.

The earliest known inductorless converter is the Cockcroft-Walton voltage multiplier [1]. This simple circuit provides low-power high voltage but at an expense of high number of capacitors for the voltage ratio (double than the classical converter). Classical converters have output-to-input voltage ratios equal to the number of capacitors [2] or voltage ratios that grow by the Fibonacci series [3] with the number of capacitors. All previous converters operate in two steps i.e. have two functional states in which charge is transferred.

A special type of DC-DC transformers (DC-DC converters without regulation) are the high-voltage-ratio transformers [4] that operate in more than two steps. Their voltage ratio grows at a geometric progression with the number of capacitors. They have been well investigated in the case of ideal components (capacitors and switches), but with all the capacitors equal. While equal capacitors seams reasonable for the classical converters, since their capacitors have equal voltages, a geometric-ratio capacitances in the high-voltage-ratio ones may result with better performances. This article proves the previous assumption by analytical means, simulations and prototype measurements on a four stage converter from 42V (emerging car-battery voltage) to 620V (needed for PWM generation of AC-line voltage) at 0.5A .

3. PRINCIPLE OF OPERATION

The circuit is shown in Fig. 1 and the timing diagrams of the switches are shown in Fig. 2. There are four steps (one more than the number of capacitors) in one cycle. This is illustrated in Fig. 3. It also shows the voltages of the capacitors at no load. Each of the capacitors is charged during one of the steps consecutively, and discharged during the following steps. The ideal voltage ratio is 2^n where n is the number of stages (switched capacitors). The last capacitor is actually the filter capacitor that supplies the load during the first n (four) steps and charges during the last (n+1)-th (fifth) step.

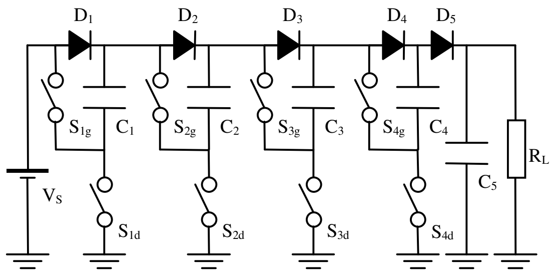

Fig. 1. *Circuit diagram*

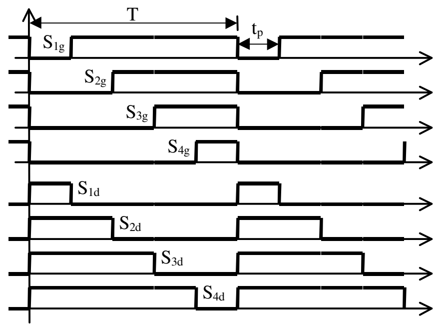

Fig. 2. *Timing diagrams*

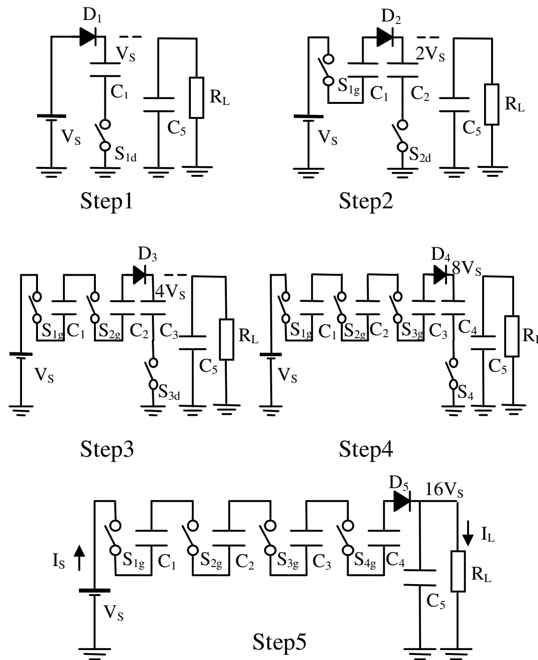

Fig. 3. *Circuit operation steps*

4. THE CONVERTER ANALYSIS

It has been shown in [4] that in the case of ideal components the output-to-input average-current ratio is independent on capacitor values and depends only on circuit configuration:

$$\bar{I}_L = \frac{\bar{I}_S}{2^n}, \tag{1}$$

where $\bar{I}_L$ is the average load current and $\bar{I}_S$ is the average current through the source V_S. For the four-stage converter we obtain $\bar{I}_L = \bar{I}_S / 2^4$.

For derivation of the output voltage expression the capacitances of the capacitors are needed. The assumption for geometric distribution of the capacitances among converter stages can be expressed with the following relationships:

$$C_5 = C; C_4 = kC; C_3 = k^2C; C_2 = k^3C; C_1 = k^4C. \tag{2}$$

The output voltage (as shown in the Appendix) can be expressed with the following equation:

$$\bar{V}_L \approx V_{Lm} - \bar{I}_L \cdot R_O, \tag{3}$$

where V_{Lm} is the no-load output voltage

$$V_{Lm} = 2^4 \cdot V_S, \tag{4}$$

and R_O is the so-called switched-capacitor resistance:

$$R_O = \frac{1}{fC}\frac{43 + 11k + 3k^2 + k^3}{k^4}. \tag{5}$$

Here $f = 1/T$ is the switching frequency and $R_0 = 1/fC$ is the "basic" switched-capacitor resistance.

The DC-output efficiency expression follows directly from the previous equations:

$$\eta = \frac{\bar{V}_L \bar{I}_L}{V_S \bar{I}_S} = \frac{\bar{V}_L}{2^4 V_S} = 1 - \frac{\bar{I}_L R_O}{2^4 V_S}. \tag{6}$$

It is obvious that lowering the output resistance R_O can increase the efficiency of the converter. This imposes the dependence of the efficiency on parameter *k*. There are two cases in practice: discrete component converter and on-chip converter.

With discrete component converter a general rule is applicable: higher value capacitors are available at lower voltage ratings. This is in perfect agreement with the reverse voltage-rating dependence of the capacitors in this converter compared with the capacitance dependence. The normalized output resistance dependence on the parameter *k* (i.e. compared with the resistance at *k*=1) is shown in Fig. 4.

A steep reduction of the output resistance can be noticed up to values of 1.5 to 2 for the parameter *k*, after which the curve becomes nearly flat.

For on-chip converters the most important is the total area that is occupied by the converter which actually means the total capacitance:

$$C_{tot} = C_1 + C_2 + C_3 + C_4 + C_5. \tag{7}$$

In this case the output resistance expression becomes:

$$R_O = \frac{1}{fC_{tot}}\frac{(43 + 11k + 3k^2 + k^3)(k^4 + k^3 + k^2 + k + 1)}{k^4}. \tag{8}$$

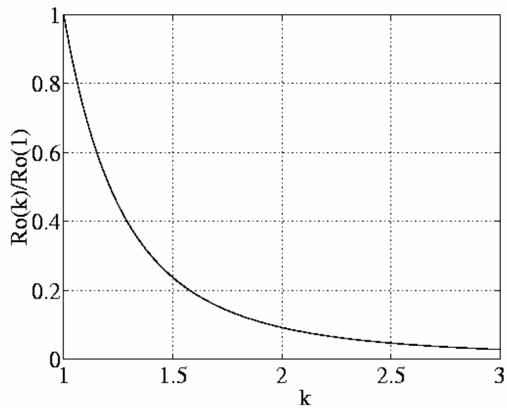

Fig. 4. *Normalized output resistance for discrete component converter*

The graphical representation of the normalized resistance dependence on the parameter *k* is presented in Fig. 5.

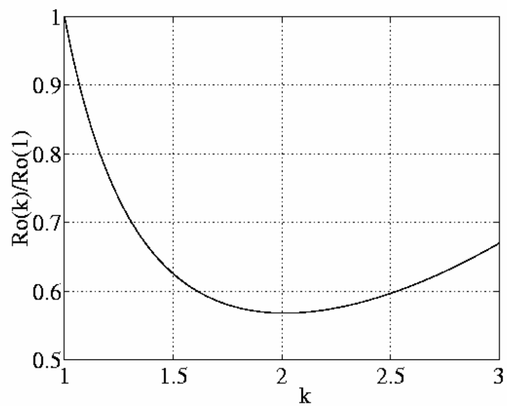

Fig. 4. *Normalized output resistance for the on-chip converter*

A minimum at *k*=2 can be noticed where the output resistance reduction is nearly 45% with the same total chip-area occupied.

Another important issue is the output voltage ripple. A conservative result is obtained by assuming that C_5 is supplying the load alone during all of the cycle:

$$V_{Lr} \approx \frac{I_L T}{C_5} = \frac{I_L}{fC}. \tag{9}$$

5. EXPERIMENTAL RESULTS

A prototype has been constructed with discrete components (Table 1).

Table 1. *Prototype components*

Stage:	1	2	3	4	5
Capacitance μF	2200	800	440	220	110
Voltage V	63	400	250	400	800
Measured ESR mΩ	40	120	70	120	240
Switch	IRFZ 44	IRF 540	IRF 640	IRF 840	
RDSon mΩ	22	52	180	850	
Photocouplers	Sharp PC 847 (⇔ 4x4N36)				

The idea is to obtain a voltage of about 600V from the 42V (emerging) car-battery voltage at power level (approx. 300W i.e. I_L≈0.5A) that is an order of magnitude higher than the usual for discrete inductorless converters. At this power level, limitations appear for the RMS current through the capacitors (especially C_1). The absolute average value of it's current is 8A and the form-factor (see Appendix) is al least 1.3 which means RMS current of 10.4A. If highest quality electrolytic capacitors are used than their capacitance (at 50–63V voltage rating) should be at least 5600µF [5]. At capacitance ratio of k=2, the output capacitance should be C_5=350µF with voltage rating higher than 700V and, consequently, the frequency for 1% output voltage ripple would be

$$f \approx \frac{I_L}{V_{Lr}C} = \frac{0.5}{6 \cdot 0.35 \cdot 10^{-3}} = 240Hz\,. \qquad (10)$$

Since electrolytic capacitors have best performances at frequencies of 1-5kHz, as a compromise a frequency of 2kHz has been chosen with the values of the components from Table 1 and intermittent operation of the converter. This allows the use of ordinary photocouplers for the driving circuitry.

The dependence of the characteristics on various parameters of the converter has been investigated by PSpice simulation and is presented in Fig. 5 through Fig 7. The measured characteristics of the prototype are shown in Fig. 8.

It is interesting to note that all of the simulation diagrams show extremely high overlapping of the efficiency and normalized output voltage curves. This means that the equation (6), derived for the idealized converter, is also valid for the non-idealized converter. The main difference that appears in the measured characteristics is because of the power for the switch-driving circuitry that was taken from the input voltage source.

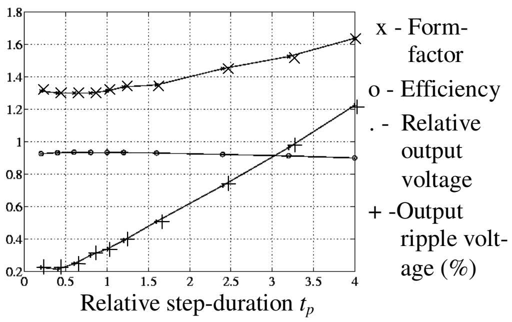

Fig. 5. *Simulated* c*onverter characteristics dependence on step duration*

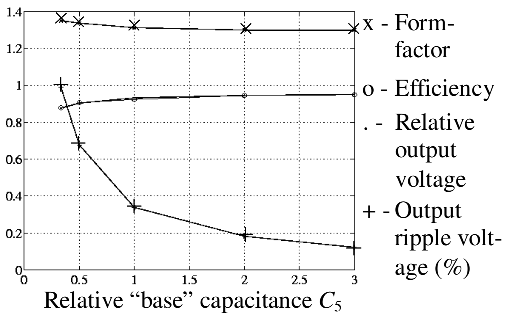

Fig. 6. *Simulated* c*onverter characteristics dependence on »base« capacitance C*

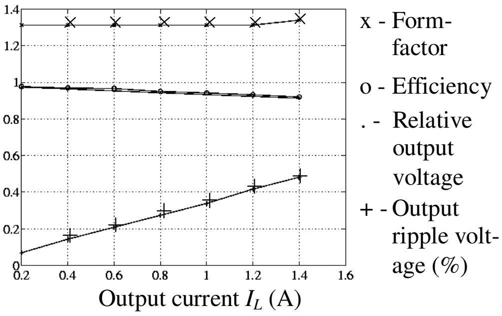

Fig. 7. *Simulated* c*onverter characteristics dependence on output current I_L*

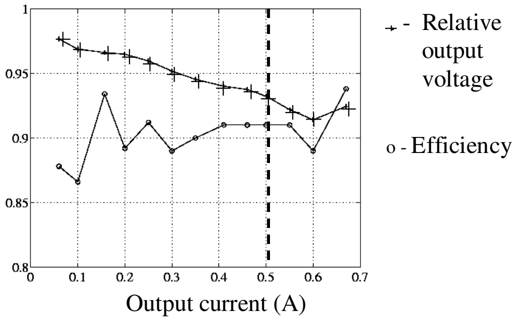

Fig. 8. *Measured* c*onverter characteristics*

6. CONCLUSIONS

The non-uniform distribution of the capacitance, in a form of geometric series, in the multistep inductorless DC-DC transformer with high voltage ratio, results in significant improvements of the converter characteristics. This is derived analytically for the idealized converter and shown by simulation for the real converter.

Measurements of the prototype characteristics show high stability of the output voltage within wide load variations and more than 90% efficiency.

7. REFERENCES

[1] J. D. Cockcroft, E. T. S. Walton, "Further developments on the method of obtaining high-velocity positive ions", in Proc. Roy. Soc., London, U.K., 1932, p. 131, p. 619

[2] F. Ueno, T. Inoue and T. Umeno: Analysis and Application of Switched-Capacitor Transformers by Formulation, Electronics and Communications in Japan, Vol.73, No.9, Sept. 1990

[3] M. S. Makowski and D. Maksimovic: Performance limitis of switched-capacitor DC-DC converters, IEEE PESC'95, pp. 1215-1221

[4] I. Oota, F. Ueno and T. Inoue: Analysis of a Switched-Capacitor Transformer with a Large Voltage-Transformer-Ratio and Its Applications, Electronics and Communications in Japan, Part 2, Vol. 73, No. 1, 1990

[5] Cornell-Dubilier: Aluminum Electrolytic Capacitors; www.cornell-dubilier.com

8. APPENDIX

Following the methodology in [4] we can write: Let $\Delta Q_{Ci}^{(j)}$ denote the charge transferred into capacitor C_i during the step j. The charge into the load during one cycle is:

$$\Delta Q_L = \bar{I}_L \cdot T \ . \qquad \text{(A1)}$$

In steady state total charge transfer into each capacitor is zero and each capacitor is charged only once – at the beginning of the corresponding step. The charge transferred through the switched-capacitors (1 through 4) during the fifth step is the total charge delivered to the load. From this follow the equations:

$$\Delta Q_{C1}^{(5)} = \Delta Q_{C2}^{(5)} = \Delta Q_{C3}^{(5)} = \Delta Q_{C4}^{(5)} = -\Delta Q_L \qquad \text{(A2)}$$

$$\Delta Q_{C4}^{(4)} = -\Delta Q_{C4}^{(5)} = \Delta Q_L \qquad \text{(A3)}$$

$$\Delta Q_{C1}^{(4)} = \Delta Q_{C2}^{(4)} = \Delta Q_{C3}^{(4)} = -\Delta Q_{C4}^{(4)} = -\Delta Q_L \qquad \text{(A4)}$$

$$\Delta Q_{C3}^{(3)} = -\Delta Q_{C3}^{(4)} - \Delta Q_{C3}^{(5)} = 2\Delta Q_L \qquad \text{(A5)}$$

$$\Delta Q_{C1}^{(3)} = \Delta Q_{C2}^{(3)} = -\Delta Q_{C3}^{(3)} = -2\Delta Q_L \qquad \text{(A6)}$$

$$\Delta Q_{C2}^{(2)} = -\Delta Q_{C2}^{(3)} - \Delta Q_{C2}^{(4)} - \Delta Q_{C2}^{(5)} = 4\Delta Q_L \qquad \text{(A7)}$$

$$\Delta Q_{C1}^{(2)} = -\Delta Q_{C2}^{(2)} = -4\Delta Q_L \qquad \text{(A8)}$$

$$\Delta Q_{C1}^{(1)} = -\Delta Q_{C1}^{(2)} - \Delta Q_{C1}^{(3)} - \Delta Q_{C1}^{(4)} - \Delta Q_{C1}^{(5)} = 8\Delta Q_L \qquad \text{(A9)}$$

The total charge from the source is:

$$\Delta Q_S = \Delta Q_{C1}^{(1)} - \Delta Q_{C1}^{(2)} - \Delta Q_{C1}^{(3)} - \Delta Q_{C1}^{(4)} - \Delta Q_{C1}^{(5)} = 16\Delta Q_L \qquad \text{(A10)}$$

From (A1) and (A10) we obtain:

$$\bar{I}_S = \frac{\Delta Q_s}{T} = 2^4 \bar{I}_L \quad . \qquad \text{(A11)}$$

The output voltage expression can be derived by following the voltages of the capacitors at the end of each step $V_{Ci}^{(j)}$:

$$V_{C1}^{(1)} = V_S \qquad \text{(A12)}$$

$$V_{C1}^{(2)} = V_S - \frac{\Delta Q_{C1}^{(2)}}{C_1} = V_S - \frac{4\Delta Q_L}{k^4 C} \qquad \text{(A13)}$$

$$V_{C1}^{(3)} = V_{C1}^{(2)} - \frac{\Delta Q_{C1}^{(3)}}{C_1} = V_S - \frac{6\Delta Q_L}{k^4 C} \qquad \text{(A14)}$$

$$V_{C1}^{(4)} = V_{C1}^{(3)} - \frac{\Delta Q_{C1}^{(4)}}{C_1} = V_S - \frac{7\Delta Q_L}{k^4 C} \qquad \text{(A15)}$$

$$V_{C1}^{(5)} = V_{C1}^{(4)} - \frac{\Delta Q_{C1}^{(5)}}{C_1} = V_S - \frac{8\Delta Q_L}{k^4 C} \qquad \text{(A16)}$$

$$V_{C2}^{(2)} = V_S + V_{C1}^{(2)} = 2V_S - \frac{4\Delta Q_L}{k^4 C} \qquad \text{(A17)}$$

$$V_{C2}^{(3)} = V_{C2}^{(2)} - \frac{\Delta Q_{C2}^{(3)}}{C_2} = 2V_S - \frac{\Delta Q_L}{k^4 C}(4+2k) \qquad \text{(A18)}$$

$$V_{C2}^{(4)} = V_{C2}^{(3)} - \frac{\Delta Q_{C2}^{(4)}}{C_2} = 2V_S - \frac{\Delta Q_L}{k^4 C}(4+3k) \qquad \text{(A19)}$$

$$V_{C2}^{(5)} = V_{C2}^{(4)} - \frac{\Delta Q_{C2}^{(5)}}{C_2} = 2V_S - \frac{\Delta Q_L}{k^4 C}(4+4k) \qquad \text{(A20)}$$

$$V_{C3}^{(3)} = V_S + V_{C1}^{(3)} + V_{C2}^{(3)} = 4V_S - \frac{\Delta Q_L}{k^4 C}(10+2k) \qquad \text{(A21)}$$

$$V_{C3}^{(4)} = V_{C3}^{(3)} - \frac{\Delta Q_{C3}^{(4)}}{C_3} = 4V_S - \frac{\Delta Q_L}{k^4 C}\left(10+2k+k^2\right) \qquad \text{(A22)}$$

$$V_{C3}^{(5)} = V_{C3}^{(4)} - \frac{\Delta Q_{C3}^{(5)}}{C_3} = 4V_S - \frac{\Delta Q_L}{k^4 C}\left(10+2k+2k^2\right) \qquad \text{(A23)}$$

$$V_{C4}^{(4)} = V_S + V_{C1}^{(4)} + V_{C2}^{(4)} + V_{C3}^{(4)} = 8V_S - \frac{\Delta Q_L}{k^4 C}\left(21+5k+k^2\right) \qquad \text{(A24)}$$

$$V_{C4}^{(5)} = V_{C4}^{(4)} - \frac{\Delta Q_{C4}^{(5)}}{C_4} = 8V_S - \frac{\Delta Q_L}{k^4 C}\left(21+5k+k^2+k^3\right) \qquad \text{(A25)}$$

$$V_L \approx V_{C5}^{(5)} = V_S + V_{C1}^{(5)} + V_{C2}^{(5)} + V_{C3}^{(5)} + V_{C4}^{(5)} = 16V_S - \frac{\Delta Q_L}{k^4 C}\left(43+11k+3k^2+k^3\right) \qquad \text{(A26)}$$

The form factor (FF) of the current through C_1 can be obtained from Fig. A1:

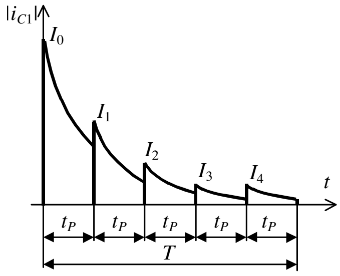

Fig. A1. *Absolute current through C_1*

The average and RMS values of the waveform are:

$$I_{AVG} = \frac{1}{T}\sum_i \int_0^{t_P} I_i e^{-\frac{t}{\tau}} dt = \frac{\tau}{T}\left(1 - e^{-\frac{t_P}{\tau}}\right)\sum_i I_i \qquad \text{(A27)}$$

$$I_{RMS}^2 = \frac{1}{T}\sum_i \int_0^{t_P} I_i^2 e^{-\frac{2t}{\tau}} dt = \frac{\tau}{2T}\left(1 - e^{-\frac{2t_P}{\tau}}\right)\sum_i I_i^2 \qquad \text{(A28)}$$

where $I_1 = I_0 / 2$, $I_2 = I_0/4$ and $I_3 = I_4 = I_0/8$.

The two limiting cases are:

a) $t_P << \tau$ (nearly "flat" current pulses; partial charge transfer) $\Rightarrow$

$$I_{AVG} \approx \frac{t_P}{T}\sum_i I_i \ \text{ and } \ I_{RMS} \approx \sqrt{\frac{t_P}{T}}\sqrt{\sum_i I_i^2} \qquad \text{(A29)}$$

Knowing t_P=T/5 and current relations given above, we obtain:

$$FF_a = \frac{I_{RMS}}{I_{AVG}} \approx 1.296 \, . \qquad \text{(A30)}$$

b) $t_P >> \tau$ (Down to "zero" current pulses; complete charge transfer) $\Rightarrow$

$$I_{AVG} \approx \frac{\tau}{T}\sum_i I_i \ \text{ and } \ I_{RMS} \approx \sqrt{\frac{\tau}{2T}}\sqrt{\sum_i I_i^2} \qquad \text{(A31)}$$

In this case:

$$FF_b = \frac{I_{RMS}}{I_{AVG}} \approx 0.916\sqrt{\frac{t_P}{\tau}} \, . \qquad \text{(A32)}$$

The boundary of complete charge transfer is $t_P \approx 3\tau$, which gives $FF \approx 1.587$

INDUCTION MOTOR WITH VECTOR CONTROL FOR THE DRIVE OF POSITION AXIS ON CNC MACHINE

Radiša Jevremović, Milan Živić*
University of Novi Sad, Faculty of Engineering, Novi Sad, Yugoslavia, jevrem@uns.ns.ac.yu
**Livnica Kikinda AD, Kikinda, Yugoslavia,* numerika@eunet.yu

Abstract: *Consideration of different issues and problems with CNC machine. In brief, grinding technology was discussed including requirements it imposes. Description of an existing design of CNC grinder in "Livnica Kikinda" AD. Suggestion of a new design of mechanical axis drive with induction motor and vector control. Implementation of the existing CNC controller MPK-90, manufactured in Yugoslavia Design and manufacture of developing model with vector control for induction motor, using DSP TMS320F240. Afterwards, regulator is connected to the CNC machine's MPK-90 controller. Incremental encoder is used for speed and position measuring. All desired motions are realized through controller's control board or preprogrammed. In such a manner,very precise positioning of grinder's mechanical axis is being implemented.*

Key words: *CNC machine, CNC grinder, induction motor, MPK-90 controller, DSP TMS320F240, PLC LM628,*

1. INTRODUCTION

CNC machines are tool machines with CNC (Computer Numeric Control) control. Application of modern controllers significantly enhances and increases: productivity, accuracy, quality of treated surfaces and safety during work.

Throughout years "Livnica Kikinda" AD company manufactures CNC machines. So far, for the drive of mechanical axis, only servomotors were used (DC motors, SMPM and step motors).

Top world manufacturers of CNC machines use induction motors to drive mechanical axis, because of multiple advantages. Hardware development enabled application of vector control and accurate positioning with induction motor. Because of market competition, further tasks are obtained for a design of solution implementing induction motor on CNC machine. Condition is not to decrease speed of dynamic response, and maximal allowed deviation can be up to 1µm. Requirements also imply the application of existing MPK-90 controller, which was earlier designed and implemented with CNC machines. It is decided fo the new regulator to have analog speed reference. With analog speed reference, regulator can be connected to every controller, which supports positioning card based on square signals of incremental encoder. Goal is to design, manufacture, test regulator and examine reliability and drive's dynamics.

2 EXISITNG SOLUTION OF CNC MACHINE

Following, only CNC grinders are taken in consideration. Grinding technologicaly requires high accuracy, for the piece to be treated correctly. Therefore, it is requered for the electric motor drive to satisfy very strict demands related to positioning accuracy. Designing grinder drive, we may say that the same will fullfill drive requirements that belong to other types of tool machines.

Fig.1. *CNC grinders UB300 with SIEMENS controller SINUMERIK 840D*

Fig. 2. *SINUMERIK 840D controller*

2.1. CNC Grinder

Fig. 1. shows a very accurate CNC grinder with SIEMENS made controller, while Fig. 2. only shows SINUMERIK 840D controller. Moreover are presented servomotors with regulators.

Fig. 3 shows a very accurate plain grinder PRB 500/1000. It is intended for plain (skin deep) grinding of pieces in large series . Maximal grinding width is 500mm, while operating length is 1000mm. With this machine it is possible to realize plain grinding by grazing method during continual regulation of:

- movement speed of side table (hydraulics),
- transversal movement of pillar with a spindle of a grinding board (electromotor drive), and
- vertical movement of grinding board spindle (electromotor drive).

Likewise, it is possible to grind deep profiles, with a single trace. It is a so-called cutting method.

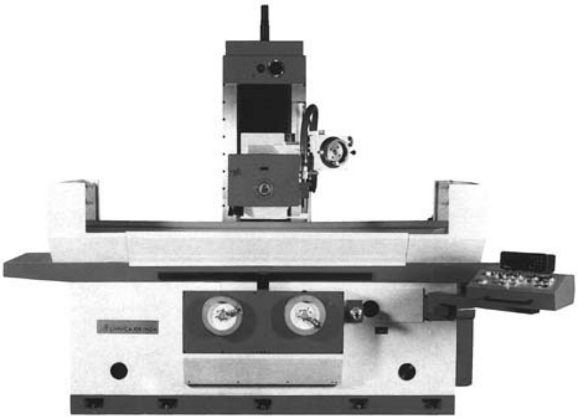

Fig. 3. *PRB 500/1000 Grinder*

Piece that is supposed to be grinded is being fixed with a magnetic board at a side table. Grinding board spindle is moved, either manually or automatically (programmed movements) along two axis (transversal and vertical). Piece (operating part) is fixed here, and grinding is realized with synchronous movements of the table and pillar with stone spindle (Fig. 4.). Table is moved by hydraulics, while movements for a pillar are realized by electric motor. It implies the existance of two regulators, two positioning cards and controller.

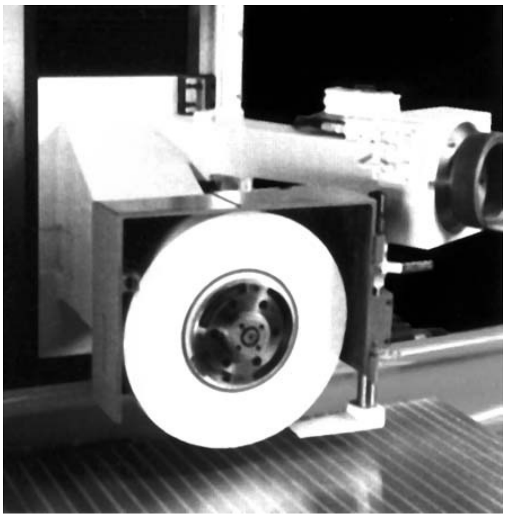

Fig. 4. *Grinding board (stone) spindle*

2.2. CNC Grinder Controller

MPK-90 controller is used for the grinder control, which is developed and manufactured in Livnica Kikinda, that so far proved to be very reliable. Controller is predicted to be without restrictions when electric motor drive selection is concerned. It is possible to choose from a wide collection of regulators and corresponding motors. Regardless of its obsolence, MPK-90 is still applied with CNC machines, while with PRB grinder its use is a must.

Fig. 5. shows an external view of MPK-90 controller, whose implementation will be explained in this paper. It is a programmable controller with modular composition. Primarily, it is intended for the control of numerical tool machines, and may also be successfully used as universal PLC.

Fig. 6. shows block scheme of entire MPK-90 configuration, that consists of:

- *CPU card* with Intel 8085 A2 microprocessor, with a operating frequency clock 5 MHz and instruction clock 0.8 μs,
- *memory card* with possibility of installing 4x8 kB EPROM and 16 kB RAM,
- *control board*, provides communication between operator and controller,
- *input and output card* with 24 input/outputs (extendable up to 336 I/O ports),
- *DC motor controller card*, which is used for the control of DC motor regulator or synchronous motor (PMSM); MPK software supports existance of two mechanical axis, each having its own motor, regulator and controller card,
- *additional keyboard module* which should be supported with an input and an output card, for the purpose of scaling keyboard matrix and display refreshment,
- *logic of an electronic wheel*, that serves to recieve impulses and determine rotation of manual impulse generator,

Fig. 5. *MPK-90 controller*

- *logic for the control of step motor*, used to generate signals for step motor regulator, or SMD (Step Motor Drive); MPK supports up to two step motors, which excludes the possibility of installing DC controller cards,
- *LED indication module*, which may be installed for each input card, and
- *module for output amplifiers*, that enables plugin and plugout of more powerful load,

Controller task is to provide:

- definition of movement parameters for mechanical axis,
- position PID regulator parameter definition
- generation of reference rotation speed (set) for regulators of used motors, and
- desired input/output logic, namely programmable logic control (PLC),

Moreover, simple data input through the keyboard of controller command table is required.

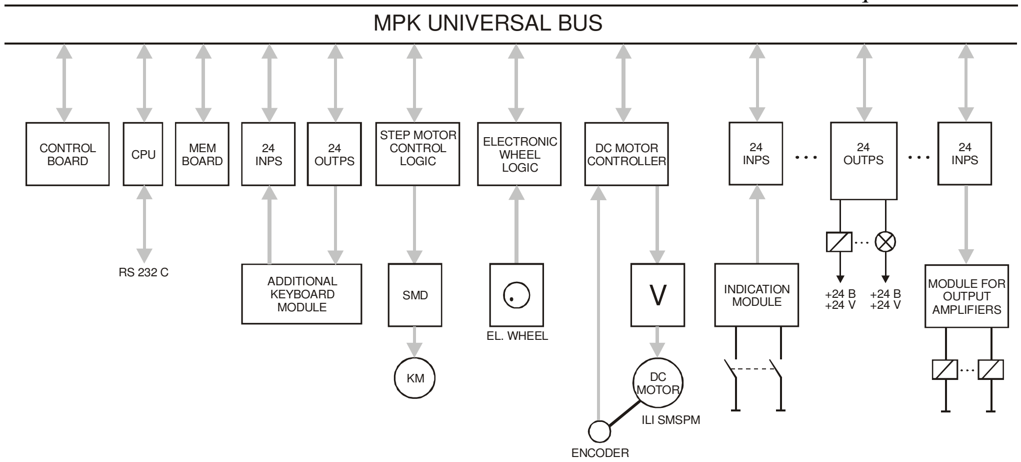

Fig. 6. *Complete MPK-90 configuration*

2.3. Existing grinder motor drive

In PRB grinders by default there are two independent electric motor drives with Siemens motors of 1FT5 and/or 1FT6 series (Fig. 7.). Motor power is in range 0.54kW-2.5kW. Motors are connected with regulators Simodrive 611A, with common feeder module. Control of speed regulators is implemented through cards(card of a DC motor controller). DC motor controller card is most substantial for accurate functioning of regulation system. It is based on a particular processor LM628, which is intended for the control of position and speed servomechanisms with square incremental reversal signals. Thanks to this, complex computational problems are solved in real-time and qualitative digital control is accomplished.

Main processor (8085) communicates to LM628 through control/data port, which enables programming of trapezoidal speed response, as well as parameters of PID.

Output (8-bit or 12-bit) is taken to external DAC, which generates analog signal for the motor regulator control. Feedback loop is closed with digital encoder. Generator of trapezoid speed profile computates required path for speed or position operating mode. While moving LM628 subtracts actual position (reverse connection) from the one required (trajectory generator) and passes the result of position error through digital PID propelling motor to the demanding position.

Generator of speed trapezoidal trajectory finds the required motor position in time domain. In position operating mode, main processor (8085) defines acceleration, maximum speed and final position. LM628 uses this information to move the motor with specified operating conditions. Slopes of start and deceleration are equal. In any moment during rotation, maximal speed and final position may be altered

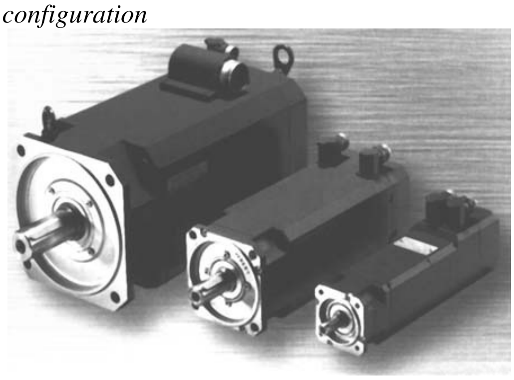

Fig. 7. *1FT5 servomotors*

Recent solutions satisfy all technological requirements concerning operating accuracy and desired drive dynamics, but is relatively expensive due to high costs of servomotors. Besides, maintanance of applied electric motors also appears to be expensive. These disadvantages initiated new solution for motor drive. Nowadays, well-known as induction motor.

3. NEW SOLUTION OF ELECTROMOTOR DRIVE

Development of fast electronic components and appearance of digital signal processors (DSP) enables execution of very complex algorithms in real-time. Due to this fact, it is possible to provide a high-quality vector control of induction motor. This way, performance of servomotor and electromotor drive are the same.

Clear demands related to the grinding technology, that motor drive with regulator must fullfill are:

- accuracy of holding a given position with ±1μm resolution, where load is less than nominal (in steady state),

- ❑ taking desired position with trapezoidal start and breaking, with an overthrow less than 1µm,
- ❑ movement without concussions and vibrations,
- ❑ continual movement with a speed of 30000µm/s,
- ❑ incremental movement with speed up to 1000µm/s,
- ❑ acceleration up to 100 mm/s^2.

All conditions are related to linear movement of mechanical axis. Specialized DSP TMS320F240 made by Texas Instruments is chosen for the realization of speed vector regulator of induction motor. Additional condition for the design of regulator is for the controler input/output logic to remain same.

Fig. 8 is a simple scheme for the manipulation of regulator by controller (PLC-Programmable Logic Controller).

PLC task is to provide controlled

turn on/off of switch C2, regulator start and to supervise current state of a *ready* signal.

Software implementation of the PLC logic is the following Fig. 9. :

1. output Q0.3 unconditionally turns on/off C2 switch (regulator supply),
2. after the turn on of a switch, program waits 300 ms, and after that time interval examines status of I2.6 input, which is connected to *ready* contact of regulator's relay:
   - ❑ *If I2.6=0 (disconnected contacts X4/1 and X4/2, or 203 and 200) ⇒ outputs Q0.3 and Q0.4 are disconnected, while display outputs text ″REGULATOR NOT READY″,*
   - ❑ *If I2.6=1 (interconnected contacts X4/1 and X4/2) ⇒ outputs neither change nor an error is given to output,*
3. output Q0.4 cannot be turned on, if Q0.3 is not previously turned on; when, anyway, it is attempted, Q0.4 is automatically turned off and the output message is ″SWITCH″, which informs that prior to enabling regulator, switch to three-phase supply should be activated ,

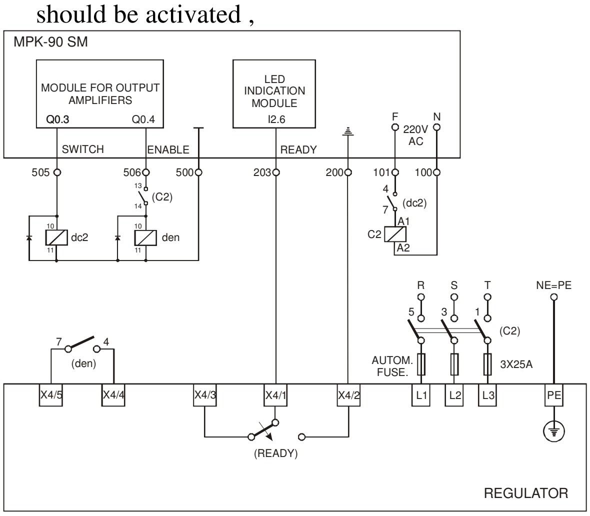

Fig. 8 PLC for vector control of induction motor

4. in the case that during its operation *ready* regulator relay disconnects its operating contact, input will be nullified (I2.6=0) what causes *enable* signal turnoff (Q0.4) and the turn off of the supply (Q0.3); this is necessary for the purpose of protecting regulator.

Described PLC configuration enables safe vector control of induction motor.

Fig. 9 pictures block scheme of position servomechanism with induction motor for the motion control of one mechanical axis of a CNC machine. Positioner card with LM628 has a role as position PID and generator of motion path. Speed regulator is implemented using DSP.

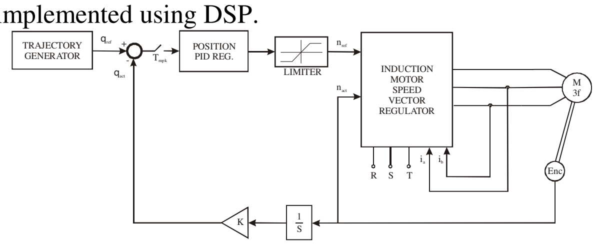

Fig. 9 *Position regulation system configuration*

3.1. Electromotor drive configuration

Fig. 10 shows simplified block scheme of entire system hardware. System consists of following parts:

- ❑ *controller*, that controls the operation of entire machine (MPK),
- ❑ *DSP Starter Kit* (*DSK*), with an embedded processor which is intended for control of induction motor,
- ❑ *measuring board*, having a central role in proceeding, processing of measuring and control signals,
- ❑ *regulator*, that incorporates power electronics elements, apropos three-phase transistor inverter with supply and protection,
- ❑ *LEM board*, through which phase currents of a motor are measured and,

three-phase induction motor with encoder, representing controlled object.

MPK-90 *controller* is based on Intel processor 8085. Using controler control table can obtain parameters of movement trajectory of the dynamics (connected to motor shaft) and parameters of PID regulator. To generate path and control position special LM628 controller is applied. Controler closes position feedback of the encoder. Communication to DSP is realized through measuring board. Control signals which refer to the regulator are derived from the direct loop (*enable*, *ready* signal)

DSP Starter Kit (*DSK*) card contains, for this project most substantial, TMS320F240 processor, which loads program for vector control. Connection to PC is over serial port (RS232). Exists special software for *debugging* and manipulation with DSP.Communication between the DSP and surrounding is over measuring board.

Regulator only includes power electronics and presents an executive module of a system. During examination of a model, structure of the Fig. 10 showed to be more feasable System design is alleviated, but many unwanted lines appeared. In a final design of the device, these shortages are surpassed, while all hardware blocks, apart from controller, will be placed in a common housing.

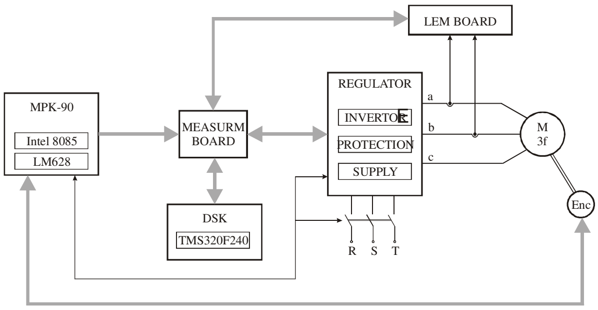

Fig. 10 *Simplified hardware system*

For high-quality control of induction motor it is necessary to provide accurate measurment of the following analog parameters:

- rotation speed n_{act},
- motor shaft position ϑ_{act},
- motor phase currents i_a and i_b,
- DC intercircuit voltage U_m, as well as
- speed reference n_{ref}.

All above mentioned parameters are converted into electric signals, and afterwards processed (scaled) and sampled using A/D converter.

Fig. 11 pictures simplified control block scheme of the entire system, which is very crucial for the explanation of electric motor drive operation [3]. Broken lines mark hardware entities, while measuring board is purposely omitted in order to have better picture.

Noticing the existance of four closed loops: two of the current, one for speed and another for position. It refers to digital control system, and imposes a question related to choosing corresponding selection periods: T_{mpk}, T_{speed}, i T [4]. T_{mpk} is beforehand fixed and equals *341.33* μs. It cannot be altered by software, beacuse it was initially defined using controller hardware.

Current selection period T simultaneously determines operating frequency of three-phase PWM inverter, and therefore must satisfy following conditions:,

- T period length must be large enough to execute all algorithmic instructions for vector control, in order to operate in real-time,
- T period length must be large enough to execute all algorithmic instructions for vector control, in order to operate in real-time,
- simultaneously length of T period should be sufficiently small, so that carrier frequency of inverter may be increased (recommended value ≈ 10 kHz),
- T certainly must be less than both the smallest time constant of the controled object (motor) and transportation delay,
- requirement for the identical measuring resolution of actual and reference rotation speed also affects selection of period T. Selected value is $T=102,4$ μs, that satisfies all requirements and defines inverter frequency *9765 Hz.*

Speed selection period T_{speed} should fulfill following conditions:

- should be at least twice smaller than mechanical time constant, so that sampling theorem may be applied (we consider that motor current time constant is compensated with current regulators),
- for high-quality of system dynamic behaviour in closed feedback, it does not make practical sense to decrease T_{speed} below $t_{usp}/10$, where t_{usp} is restore time for speed step-response of a system compensated with closed feedback,
- should be large enough so that during that time interval steady values for currents are established (twenty times period T is enough),
- should enable, along with encoder resolution of *5000 imp/obr* and $T=102,4$ μs, measuring equal resolutions of actual and reference speed.

Compromise value is $T_{speed}=20T=2,048$ *ms* , which fullfills all previously mentioned requirements.

Electric motor drive showed at Fig 13. may work in position and speed mode of operation:

- in *position* mode path generator acomplishes desired position ϑ_{ref} with defined maximal speed V_{lim} and acceleration a (trapezoidal speed profile),
- in *speed* mode desired speed is obtained with constant increment of reference speed with an increase(slope) corresponding the required speed.

Position PID regulator, according to position error signal (ϑ_{ref} - ϑ_{act}), provides control variable representing reference speed n_{ref} for speed regulator.

Speed PI regulator has a task to generate reference of conversion torque, that will enable good supervision of given rotation speed. Speed error (n_{ref} -n_{act}) is sampled by period T_{speed}, so that speed regulator control variable changes after every T_{speed} period. Following are two current PI regulators for control of direct i_d and transversal i_q current components in transformed dq domain. Using synchronous reference speed ($w_{o}=w_s$) during transformation, poli-phasor of rotor flux in every moment coincides with rotating d axis. Angle ϑ_s , used as transition from phase into dq domain and vice verse, can be estimated according to measuring of phase currents of motor and actual rotation speed. That angle also represents position of rotor flux. Both current regulators work with selection period T, while current q regulator is nothing else, but torque regulator, and current d regulator presents flux regulator (excitation). Their use provides independent torque and excitation control of induction machine. Current PI regulators have on disposal 20 PWM T periods to

obtain proper reference values. Actual current values i_{sd} and i_{sq} are obtained by Park transformation, according to measured motor phase currents and estimated position of rotor flux

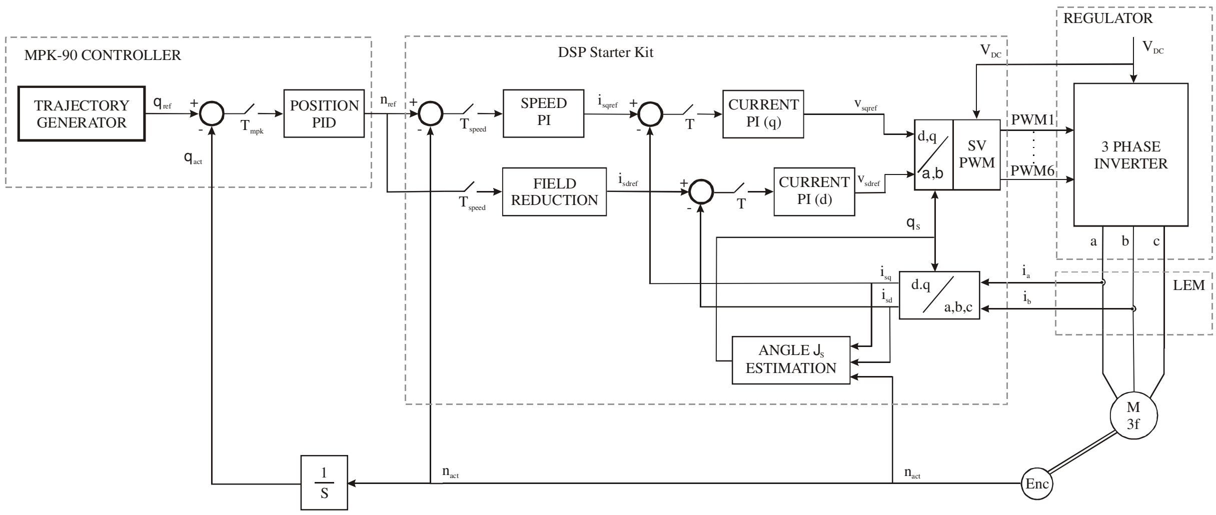

Fig. 11 *Simplified regulation of electromotor drive*

.Current regulators are intended, in predicted time interval (V_{sqref} , V_{sdref}), to acomplish control that will provide best accordance between given and actual current components. Current *q* regulator picks its reference from the output of speed PI regulator, while current reference i_{sdref} is found using n_{ref} after each T_{speed} period.

Block field reduction has role to enable rotation speed bigger than nominal, what is accomplished only by the reduction of excitation flux, respectively decreasing i_{sdref}. Every motor has its own function $i_{sdref}=f(n_{ref})$. That function is being ″scanned″ and approximated with mathematcial function, and afterwards implemented in the form of field reduction model. In this project, induction motor still operates in the area of constant torque($|n| < n_{nom}$), and flux reference is constant and set to optimal value, according to design motor parameters.

Stator control voltages, which are transfered from *dq* into $\alpha\beta$ domain using inverse Park transformation, are acquired from the outputs of current regulators. Afterwards, based on voltage vector in $\alpha\beta$ domain, PWM (block SVPWM) signals are generated, which will (with three-phase inverter) produce necessary phase voltages, motor stator currents respectively. This way is finally obtained conversion torque, necessary to achieve desired rotation speed and overcome external mechanical load torque.

From the previously described control it may be concluded that this is indirect vector control of induction motor, because rotor flux is determined measuring rotor position and calculating slip effect. Main disadvantage in this control is direct dependence of motor parameters. From that aspect, particulary critical is rotor time constant T_r, with a value highly temperature). For this reason, induction motor needs additional cooling.

4. SOFWARE IMPLEMENTATION

In total, two interrupts are used:

- hardware RESET interrupt, which is active immediately after establishement of voltage source and T1UNDERFLOW interrupt, which appears periodically, every *T=102,4 μs.*

After reset, controler starts program execution from the address 0000h in program memory. That address contains jump instruction indicating c_int0 procedure, which performs harware and variable initialization.

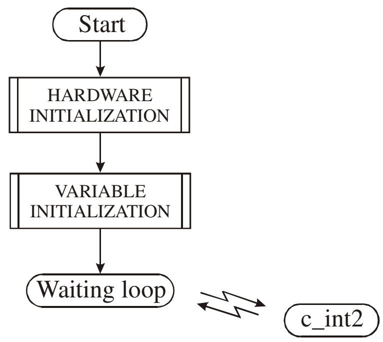

Fig. 12 Main program algorithm

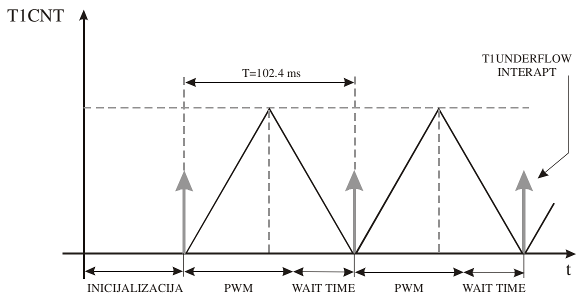

Fig. 13 Program execution time diagram

After execution of c_int0 subroutine, program waits for interrupt on the INT2. It is so-called NOP loop or Waiting loop. It presents the main program.

Timer GP1 counts from 0000h to T1PR=PWMPRD=1024dec=0400h, and afterwards counts down 0000h and after finishing, sends interrupt on INT2 (T1UNDERFLOW). Because of CPUCLK=*50ns*, it is clear that this interrupt appears every

$T=2*1024*50ns=102,4\ \mu s$ and generates carrier PWM inverter freqency $f=1/T=9.765kHz$.

After reception and recognition of T1UNDERFLOW interrupt, controler starts the execution of c_int2 subroutine which presents PWM routine.

Fig. 12 gives main program algorithm, while Fig. 13 illustrates processor time share over the state of counter GP1 [5].

Now it only remains to analyze c_int2 subroutine. Its algorithm is showed on Fig. 14

Saving contents of accumulators and status registers is necessary when main program is not a NOP loop, but performs some other task (serial communication, for example). In continue, follows examination of conditions for motor start:

- PC keyboard,
- *start* is hardware entry (pin IOPB3), used by *run* is software condition, it is enabled through controller (MPK) to give permission to DSP to start operating, and
- *not ready* hardware entry (pin IOPB4), through which regulator informs DSP of its ability to start operating.

In the case that any of these previously mentioned values is zero, motor will not start. Output pin EN.DSP (pin IOPB5) is set to zero and regulator does not have *enable*. Simultaneously registers $V_{S\alpha ref}$ and $V_{S\beta ref}$ are nullified.

When all operating conditions are fullfilled (*run=start=not ready*=1), output EN.DSP is set to one and regulator acquires *enable*. Registers $V_{S\alpha ref}$ and $V_{S\beta ref}$ do not equal zero any more, but equal result of procedure consisting of multiple subroutines.

First comes measuring of rotor phase currents, followed by transition into $\alpha\beta$ domain (Clark transformation). Continued a decision block whether to proceed with or without precise speed measuring. It is important to stress that there are two methods of measuring speed, where precise (n_p) is used for small, while nonprecise (n_m) for large velocities. Precise measuring is conducted every $T=102,4\ \mu s$, but only if $|n_m|<23.4375rpm$ *(32dec).* Imprecise meeasuring is always active, because it is used for decision. Therefore follows an obligatory reading of encoder impulses.

Therein is being set decision block for speed loop. It appears after every 20 PWM periods, namely $T_{speed}=20T=2,048\ ms$.

During this loop rotation speed is calculated (imprecise measuring), measured DC voltage of the međukola and reference speed value, calculated parameters of speed regulator and is realized digital PI speed regulator.

Continuing are subroutines for: computation of sinuses and cosinuses of angle ϑ_S , for transition in *dq* domain (Park transformation) and estimation of angle ϑ_S.

At the output of speed PI regulator we obtain reference current i_q, while reference current i_d depends on desired rotation speed (Field reduction).

Following are current PI regulators (d i q) which accomplish independent torque control (q component of the current) and excitation control (d component of the current) of induction machine. This type of control is possible only in transformed *dq* domain [1].

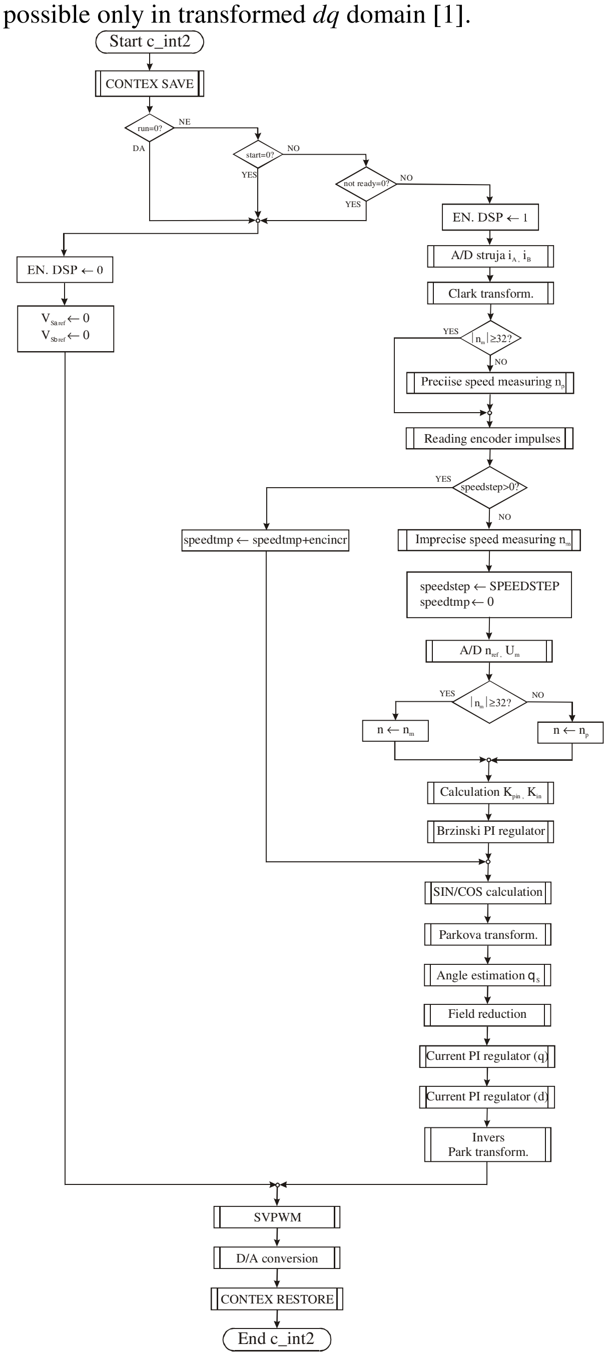

Fig.14. *Algorithm of the c_int2 subroutine*

At the output of current regulators we obtain stator control voltages, which should be mapped in dq and αβ domain. Thus we obtained necessary values in registers $V_{S\alpha ref}$ and $V_{S\beta ref}$ for the accomplishment of desired rotation speed n_{ref}, together with existing external load torque m_m.

It now remains to generate PWM signal according to previous values, which will produce necessary phase stator voltages on the inverter bridge. Space Vector PWM subroutine does that.

Before terminating c_int2 routine one more D/A conversion is performed, respectively on the external data bus is being sent optional (specified) variable, in order to be monitored at the oscilloscope. After resumption of saved contents , again we are in main program (Waiting loop), which continues its execution from the point where T1UNDERFLOW interrupt stoped it

5. REGULATOR IMPLEMENTATION

Standardized structure of three-phase PWM inverter with associated surrounding is implemented drivers, three-phase converters, DC intercircuit, chopper resistance, protection, etc.

Fig. 15. shows the block scheme of regulator itself. Power components and blocks are interconnected with thick lines, to indicate the presence of high currents.

SEMIKRON's IGBT modules SKM50GB100D are used, as well as three-phase diode bridge SKD50/12A3. Controled is SEVER's induction motor ZK80A2, of power equaling to 0.75kw. Predimensioning of regulator hardware is obvious. Authours would mentioned that while selecting electronic components they were restricted from material aspect and mainly oriented to existing resource.

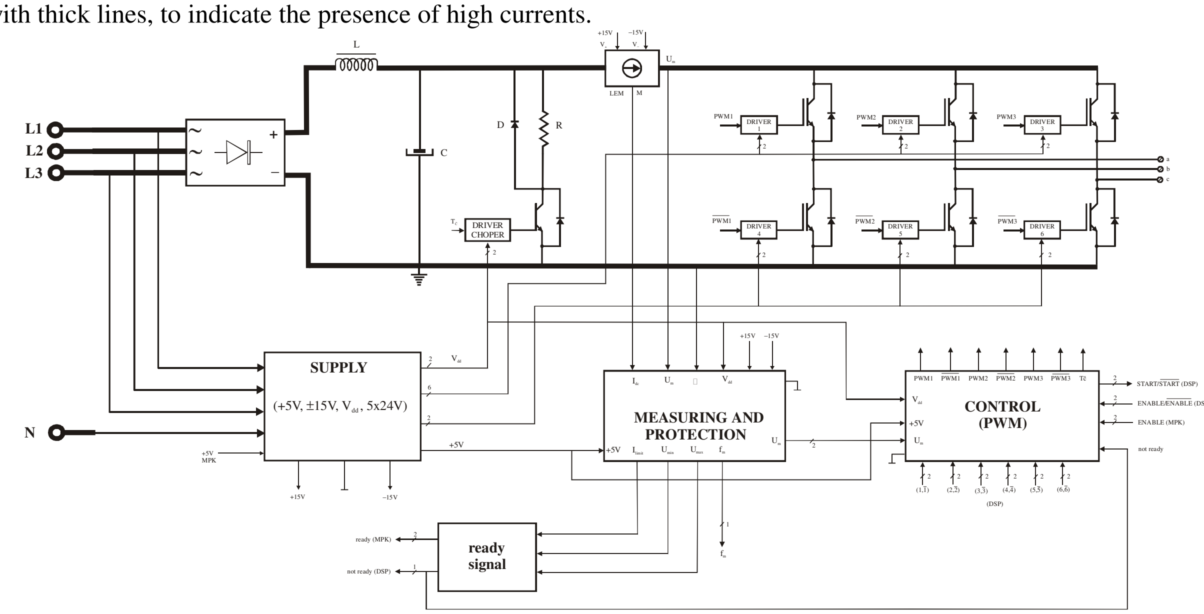

Fig. 15. Induction motor hardware regulation block scheme

6. CONCLUSION

For economic reasons complete control over CNC machine is not implemented. MPK-90 controler which is kept, though outdated, has high operative reliability. It was decided to improve electromotor drive using induction motor and vector regulator. That significantly reduces the price of machine, and deos not allow bad dynamics. Described is model design for a drive of single mechanical axis with induction motor for CNC grinder. Due to space limits it was not possible to present results of simulations and parctical measurings. Selection procedure of optimal regulation parameters is also omitted.

It should be stressed that regulator has embedded net filter, otherwise controller would crash down because of ″dirty″ supply. During its operation regulator is very silent. Motor also works silently and holds its position well. Forced motor cooling is provided with a particular cooler

Based on experiences with servomotors and recently announced tests, very good results during grinding are expected

7. REFERENCES

[1] V. Vučković, *″Opšta teorija električnih mašina″*, Nauka, Beograd, 1997.

[2] *Dokumentacija i katalozi proizvođača*, Livnica Kikinda AD, Kikinda, 2000.

[3] V. Vučković, *″Električni pogoni″*, ETF Univerziteta u Beogradu, Beograd, 1997.

[4] M. Stojić, *″Digitalni sistemi upravljanja″*, Nauka, Beograd, 1997.

[5] TI Documentation, *″TMS320C240/'F240 DSP Controllers Data Sheet″*, May 1998.

[6] TI Documentation, *″Implementation of a Speed Field Orientated Control of 3-phase AC induction Motor using TMS320F240 DSP″*, March 1998.

[7] TI Documentation, *″TMS320C2XX Assembly Language Tool″*, March 1998

.

STATE OF TECHNOLOGY OF POWER SOURCES FOR AUTONOMOUS ELECTRIC SYSTEMS

Miloš Živanov, Ljiljana Živanov
Faculty of Engineering, Novi Sad, Yugoslavia

Abstract: *Electrical power sources are the main problem of electrical vehicles (EVs), portable autonomous electrical systems. Here we review the state of technology of power sources for these systems. The main power sources for these systems are chargeable batteries. The batteries can be separated to two groups: rechargeable, and recycling/refueling batteries. First, we analyzed performance of nickel metal hydride and lithium batteries. Also, we analyzed fuel cells, for its functionality and applications. The newest state of metal oxide batteries is discussed. Some other sources, as flywheels, are mentioned as possible solution in some application.*

Key Words: ***batteries, fuel cells, specific energy, energy density, power density***

INTRODUCTION

Simple calculations are showing that 1 kg gasoline has 44 MJ or if calculate in conventional way that means 12 kWh/kg. Common lead-acid batteries have 30 Wh/kg or 400 times less than gasoline. Taking into account low efficiency of internal combustion engines (ICE) this is still huge disparity. As result, energy density of power sources for long period of time is main problem.

Many other types of batteries have higher energy density than lead-acid. However, many of them have greater level of unsafety or important influence on living environment. That means that investigation of ideal battery for EV is going on optimization: seeking which technology of batteries gives the best combination of energy characteristics, time of using and price, with satisfying safety and influence on living environment.

Three main characteristics: energy characteristics, power and life (actual time and charge-discharge cycles): increase one than one or both of others must decrease. For example, increase the size of current collector in the battery to boost power, there will be less room for active electrode materials, which will decrease energy density.

Characteristics of batteries also are connected with market demands. These demands can't be simple measure and main characteristics are connected. For example, usually way for improving the power of batteries is lowering the thickness of electrode, but that usually lowering the density of energy and living time.

To improve characteristics of batteries important for applying in EV is necessary to maximize specific energy, specific power and living cycles and minimize cost. Probably the key of EV batteries is theirs specific energy, than specific power and expenses connected with lifetime of batteries. The important characteristic is necessary time for charging batteries. In Table 1 are shown typical demands for batteries for EVs and hybrid electrical vehicles (HEV). These demands are set in beginning of 90s [2].

Table 1*: Typical demands for batteries for EVs and HEVs.*

Parameter	**Batteries for EVs**	**Batteries for HEVs**	**Typical lead-acid battery**
Specific energy, Wh/kg	80-200	8-80	25-35
Power density, W/dm^3	135-300	9-100	≈70
Specific power, W/kg	75-200	625-1600	80-100
Expected life, cycles, (years)	600-1000 (5-10)	103-105 (5-10)	200-400 (2-5)
Price, US $/kWh	100-150	170-1000	≈100

For every electrode system can be calculated the maximum theoretical value of specific energy. However, practical calculation for really batteries is something different. Some factors influenced to maintain specific energy below theoretical maximum. Every practical battery needs constructive materials, which rise its mass, and don't produce electrical energy. These materials build current collectors, separators, connectors, terminals and box of battery. All together these materials limited specific energy, for example, for lead-acid batteries on about 35 Wh/kg; even theoretical limit is 171 Wh/kg.

Question is – how many times battery may have charging cycles? Ideally will be that battery has life long as vehicle. This intent is very difficult to achieve because is expected that EV will last very long. It is reasonable that one EV will drive 250,000 km. If we take that 250 km is reasonable range for EV with battery on one charge, batteries have to be able for 1000 "charge-discharge" cycles. Really battery is rarely deep discharged between two charging. We can ask – is battery is good for 1000 complete cycles if can maintain 2000 cycles for 50 % discharging? Answers to these type questions depend of battery technology. On some types the flow of energy is constant as in zinc/nickel-oxide. Other, as lead-acid, partly cycles will help and they will last longer. Other types are prior described calendar life rather than number of cycles.

Expenses, of course, are also important. To that is especially important in case when batteries must be replaced once or more times during exploitation of vehicle. It is clear that we must avoid using expense materials. About using batteries based on silver and mercury we discuss very rarely. Nickel with price 7 US$/kg is between most expensive materials, sulphur has cost less than 0.10 US$/kg. But cost of materials is not main expensive factor in producing batteries. Even when cost of materials is multiplicated as in case of ferro/nickel batteries, can't make decisive impact to price.

That is not all. EV batteries must be also: more safe in driving than reservoir of fuel, tolerant in abuse (electrical or mechanical), safe for environment and produced of nonstrategy materials. Batteries must be with minimum maintaining. Also, must have high great energy efficiency in “charge-discharge” processes, closely to 100 % of energy.

In this article we will not discuss lead acid batteries, because this technology is mute, and practically proved that they can’t achieve requirements for EVs. They can be used only in stationary systems and some industrial applications.

NICKEL-METAL HYDRIDE BATTERIES

At this moment many manufactures of EVs intend to replace lead-acid batteries with batteries with higher specific energy batteries as nickel-metal hydride (NiMH). Also, NiMH batteries probably very convenient for Hybrid EV (HEV), for they have good power properties, because they can accept and give high powers in small time interval. NiMH batteries are incorporated in Toyota HEV Prius, which is mass manufactured and sale in Japan [1,2].

Advantage of NiMH batteries in comparing to other batteries as Ni-Cd, is specific alloy in which is possible, to deposit huge quantities of hydrogen, with high volumetric density, comparative to liquid hydrogen, giving high energy density. In NiMH cells, nickel hydroxide positive electrode is coupled with metal hydride negative electrode. During charge, hydrogen is generated by reaction with electrode and stored in metal alloy (M) in the negative electrode. At the positive electrode, a hydrogen ion is ejected while the nickel is oxidized to a higher valence within the brucide structure of nickel hydroxide (Fig. 1). Reaction of discharge is fully opposite.

This reactions charge and discharge makes NiMH unit with simple hydrogen-transfer batteries, in which hydrogen is transferred back and forth between nickel hydroxide and metal hydride without soluble intermediates or complex phase changes. For this reason, the NiMH batteries are known “rocking chair” or “swing” battery.

Soluble chemicals between electrodes in conventional batteries, as lead acid, and nickel cadmium have irreversible reactions whose kinetics can influenced to power and cycle life. The simplicity of the NiMH batteries makes theirs good energy properties and long life.

Another value of NiMH batteries is their tolerance on electrical abuse. If conventional batteries are not charged in full cycle irreversible reactions can damaged battery or influenced on safe operation. In NiMH battery overcharging generates oxygen at positive electrode, which can easily recombined at the negative electrode, for that, oxygen can’t be to high generate. In conventional batteries similar process makes nonreversible changing. In to deep discharge the hydrogen is generated on positive electrode, which can be easily recombined on negative electrode. In this process is provided that generated gas does nod exceeding recombined gas. As result of this reaction there is not chemical reactions in overcharge and discharge.

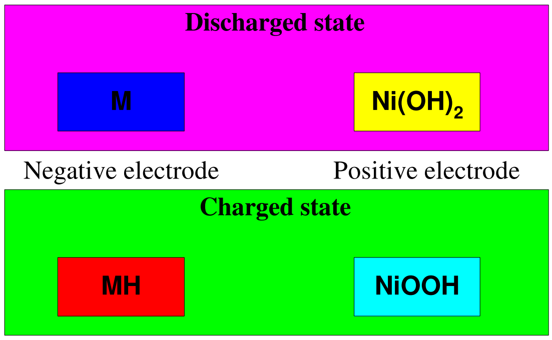

Fig. 1: *Operation of NiMH batteries.*

Because of these oxygen and hydrogen cycle recombination reactions small overcharge and small over-discharge are tolerated without damage to electrodes and safety concern. This tolerance for electrical abuse is important for high voltage systems, where we have many cells connected in series. In such system we may expect that some cells over-charged or over-discharged. Recombination reactions in NiMH do not need expensive systems for monitoring and controlling processes in individual cells.

In contrast to simplicity of its operation NiMH the battery construction of it is complex. The electrodes for storage hydrogen are made of disordered multi component alloys. For example, the negative electrodes in batteries produced in company Ovonic Battery Co. made by complex alloy of vanadium, titanium, zirconium and nickel. It is expected that materials under development will double energy capacity. Materials in nickel hydroxide positive electrode also based on disorder materials concepts.

Prices of batteries will drop, as production will rise. For example, it’s expected that in case that production is batteries for 100,000 vehicles that price for one battery system will decrease. However, price for NiMH batteries for consumer electronics are around 4000$/kWh, what is 10 times greater than acceptable price for EVs. Last reports show that prices for NiMH batteries for EVs are drooped near to level of prices of lead-acid batteries.

LITHIUM BATTERIES

The associations of EVs and HEVs are agree that batteries based on lithium will give the best long-term hope for commercially practical vehicles. This view was long in development because of risk involved in using lithium in large batteries. The hope for this batteries are amplified after big success in theirs developing at last years, especially in power capabilities for HEV applications.

But only one leading automaker is testing EV with lithium batteries in the U.S.A. (Nissan Altra, which uses Sony lithium-ion batteries). Still there is no application in HEVs. Lithium chargeable batteries are usually used in consumer products as computers, cellular application etc.

EV designs have been reported specific energies over 100 Wh/kg and peak powers more than 1000 W/kg.

Lithium-polymer batteries, using metallic lithium in their negative electrode along with solid polymer electrolyte have yet to find their way into consumer applications. They have even higher specific energies - up to 200 Wh/kg and to cost less to manufacture than other types of lithium batteries because of their solid-state design. Their biggest disadvantages are that they must warmed to around 70 ^{o}C for adequate performance, and metallic lithium electrodes are short-lived in recharge application because dentric growth of the metal conduces to internal self-shorting.

All the lithium battery design requires precise control because of their low tolerance to overcharging. This difficulty is acceptable for its higher energy efficiency than lead- and nickel-based batteries.

Table 2: *Important characteristics of batteries.*

Batteries	**Manufacture and type**	**kg**	**Ah**	**Wh/kg**	**Wh/dm^3**	**W/kg ^{b}**	**$\eta_{Ah}{}^a$ %**	**$\eta_{Wh}{}^a$ %**	**cycles^d**
Sodium/sulphur	Asea-Brown Boveri, B-11	25.3	238	81	83	152	100	91	592
	Silent Power Ltd. Rawcorn, UK PB-MK3	29.2	292	79	123	90	100	88	795
Lithium/monosulphid	SAFT of America INC.Cockkeysville, Md.Prismatic	2.94	203	66	133	64	95	81	163^d
Zinc/chrome	SEA, Austria ZBB-5/48	81.0	126	79	56	40	93	75	334
Nickel/zinc	Electro-chemical, Mountain View, Calif. R&D cell	1.89	69	67	142	105	91	77	114^d
Sodium/Nickel Chloride	Beta R&D, Ltd. UK Zebra Z5-278-ML-64	195	64	91.2	200	164	100	98	>1000
Nickel/metal-hybrid	Ovonic Battery Co. C-cells Ext.C-cells. H-cells 13-EV-90	 0.081 0.093 0.628 18	 3.6 4.5 428 90	 54 57 55 70	 186 209 152 170	 158 105 175 200	 92 90 90 90	 80 74 80 80	 333 108 380d 600
Ferro/nickel	Eagle-Picher Ind. Mo NIF200	25.0	203	51	118	99	74	58	918d

a- for 3 hours discharge with constant current
b- for charging deep to 80 %
c- for charging deep to 100 % (if not differently given)
d- for charging deep to 80 %

OTHER BATTERIES FOR EVS

Up to now many electrochemical sources are searched for applying in EVs. All factors of impotence for manufacturing and exploitation batteries are search. In the world different kinds of batteries have been developed. For example, Mercedes-Benz AG (Studgart, Germany) investigated application of high temperature sodium/nickel-chloride battery (Table 2).

Sodium/Nickel Chloride (Zebra) batteries are developed in Beta R&D Ltd, UK, showed very good characteristics. They using molten sodium chloroaluminate as a secondary electrolyte a series of solid translation metal chlorides can be used as positive electrodes and beta alumina as the solid electrolyte [11]. Nickel chloride was chosen because of simple cell chemistry and it has the advantage of high open cell voltage is 2.58 V. They have specific energy around 100 kW/kg and specific power > 150 W/kg for complete pack . They are colombically 100 % efficient (Ah). There no self discharge, the cell is fully sealed and maintenance free. Zebra cells fail to a low resistance so they are convenient for series assemblies for high voltages. The life cycle is around 1000 fully charge/discharge cycles. The average range per one cycle in EVs is around 200 km.

The temperature of operation is around 300 ^{o}C. The cells are in insulated box that has very high temperature resistance. So they are convenient to operate at wide temperature range –40 ^{o}C to +70 ^{o}C. The disadvantage of this batteries is that they need starting heating (usually by grid electricity) and theirs specific power is low for application in hybrid vehicles. Theirs prices is still higher than expected listed in Table 1.

This batteries also suitable for load leveling, peak storing and power conditioning applications in the range 100 kWh to 10 MWh.

Silient Power GmbH (Essen, Germany) made big steps in technology of sodium/sulphur batteries. Investigation shows that they have very high energy density of 150 Wh/kg. In practice energy density is 80-95 Wh/kg, with power peak around 100 W/kg. Company Asea Brown Bowery improved cells with liquid cooling instead air-cooling and energy density was 104 Wh/kg. These batteries were for long period the lowest weighted battery. They have 100 % charge efficiently, no self-charging. In cars they have good results from 160 to 240 km range and maximum speed about 120 km/h. The working temperature is high (400 ^{o}C) and sulphire is very reactive, for this batteries must be designed with high degree of safe. Beside high price, this are most limited factors for spreading these batteries in EVs.

Some companies are trying to develop zinc/brom batteries. Energy density is 72 Wh/kg is good motive for develop this batteries. However, the power density is 53 W/kg what is lower than in other concurrent batteries. This battery has some constructive advantages. The battery may be set between wheels of car. Reservoir may be design as part of vehicle. Also, reservoir and electrodes can be put in different part of car. The investment is small. It was tested in Panda and Electtrica vehicles, but haven't spread much.

Ferro/nickel have long life period. The battery produced by Eagle-Picher, NIF 200 had 918 full charging cycles. Energy density is 50 Wh/kg, peak of power density is 100 W/kg, and system needs maintaining. Energy efficiency is very low, and system needs to overcharge 50 %. Some batteries have energy density 54 Wh/kg, power peak 174 W/kg and relatively long lifetime. They are safe for environment.

The most prospecting nickel/cadmium batteries approach energy density of 55 Wh/kg obliged to sealing and ventilation systems, better nickel-hydroxide electrode and rising the efficiency of cadmium. Power peak is more than 190 W/kg. These batteries are not safe for environment because cadmium is toxic. Also this batteries are heavy. In Table 2 there are comparative data for some batteries according data from 1992 and 2000 years.

Fuel cells

Recently fuel cells have very fast development. Although principles of working fuel cells were discovered in the 1839 by Sir William Grove in London, before 1990 they have very rarely applications. They were used in space programs in NASA [1] and Soviet Union [9], for some military applications and for making electricity for public use. All this solutions were technically complex and expensive. In the beginning of the 90ns professor Billard bought license from NASA for fuel cells. After that company Billard Power Systems Inc. Burnaby, British Columbia, make high efforts for developing fuel cells for application in EVs.

The operation of fuel cells based on electrochemical conversion of chemical energy via thermal and kinetic energy into electric energy. In all fuel cells hydrogen (H_2) and in high temperature fuel cells carbon monoxide (CO) as well, is oxidized cattalyticaly in a process also referred to as cold combustion. The principle of operation of fuel cells is illustrated in Fig.2.

Fuel cells may be categorized by their operating temperature and type of electrolyte they use. Not every fuel cell is suitable for application to EVs. Most kinds operate in unacceptable for EVs high temperatures, between 300 ^{o}C and 1200 ^{o}C, and use electrolytes, such phosphoric acid and molten salt. For use in EVs are interesting proton exchange membrane (PEM), which operate at 80 ^{o}C. Other fuel cells systems are used for stationary electrical plants. They are interesting for power supply of military bases, ships, oil platforms, etc.

A fuel cell on the PEM type consists of two porous electrodes separated by polymer membrane. The membrane allows hydrogen ions (H+) to flow and blocks to flow both electrons and gasses. Fuel (hydrogen) flows along the surface of one electrode, the anode, while oxygen or air flows along the surface of the cathode. The catalyst (usually platinum) aids to break of hydrogen atoms into proton and electrons. The anode reaction can be described as a hydrogen molecule being disassociated into two hydrogen ions and two electrons ($H_2 \rightarrow 2H^+ + 2e^-$) Protons go throw polymer membrane. Electrons throw external circuit go from anode to cathode and make electrical work in external devices. Protons, electrons and oxide in porous cathode make water, which is product of reaction ($1/2O_2 + 2H^+ + 2e^- \rightarrow H_2O$). In process heat is realized which in this case dissipated.

A single cell produces an open circuit potential of approximately 1V. On load voltage dropped to approximately 0.7 V. Cells can be joined together in series arrangement to form a cell stack that provides higher voltage. The current rating is a function of the size of cells active area or current–producing surface. Present practical designs yield current densities of around 10 kA/m^2 with power density excess 1 kW/liter of stack volume. To suit particular application, the voltage and current characteristics of a fuel cell can be varied by altering the number of cells in stack and the size of the active area. Separate fuel cell stacks can also be arranged in series or parallel to provide the required power characteristics. With these characteristic fuel cells are better in many characteristics than any battery system. They have low emissions and fast start up and fast response to transients. From all this fuel cells have very high chances to replace ICE in vehicles.

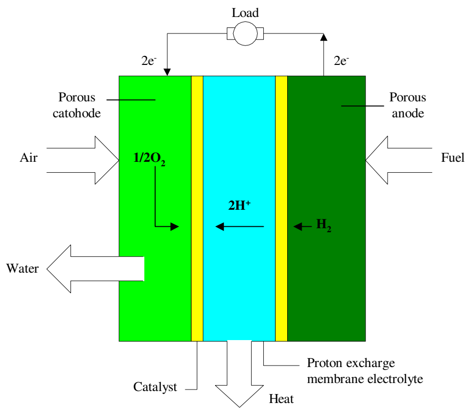

Fig. 2: *Principles of operation of PEM fuel cells.*

Fuel cells must integrate several subsystems in order to function. That is similar as in ICE vehicle. Subsystems are required to store and control fuel, compress and control oxidant air and provide thermal management, control and power conditioning. Some system includes reformer: a small chemical reactor to extract hydrogen-rich gas from readily available fuels such as natural gas, methanol and gasoline.

The fueling can be with pure hydrogen when the subsystem is primarily consists with pressure-regulated and flow control devices. Complexity grows into fuel subsystems if an on-board reformer is used to generate the hydrogen from some other fuel. A reformatory system carries a hydrogen carbonate fuel on board, using reformer to extract hydrogen for use in the fuel cells. Methanol-reforming technology is the most advanced, although there is an increasing emphasis on gasoline reforming methods to take advantage of the world's existing infrastructure.

Every day we may read in different articles about new application of fuel cells in electrical vehicles. Well known is demonstration the buses in Chicago as result of activities the Chicago Transit Authority, British Columbia Transit and Dbb Fuel Cell Engines. The 200 kW engines are fueled by hydrogen stored in cylinders in the buses' oversized roof spaces. The fuel cell engine occupies about as much room as conventional diesel engine would. The buses have a range of about 400 km.

Daimler-Benz AG, in Stuttgard, Germany, unveiled NECar 3 at the Frankfut Auto Show in 1997. This car based on Mercedes-Benz A-class automobile, the vehicle is the world's first fuel cell passenger car to use methanol as its stored fuel. The liquid fuel makes for quick and easy refueling with minimal emissions and excellent range. The NECar's fuel tank holds 40 liters of methanol, which gives it a range of 400 km. This is fourth demonstration vehicle wheeled out by Daimler-Benz (DB has also produced a fuel cell bus and two other NECars).

Even fuel cells are fully electrical system it must be accompanied with chargeable batteries. That is necessary for lighting on parking and some auxiliary use of electricity. Also, for peak powers is good to have hybrid systems. In this case, the installed power can be smaller. Also, in breaking the regenerate energy may be charge batteries and later returned energy to system. For example, Chrysler Corp. (now Daimler Chrysler) proposed vehicle, which has hybrid system with 25 kW fuel cells and gasoline reformer with batteries to supply peak power. Many other automakers, and association currently working on vehicles based on fuel cells [1], what shows that this is very promising source for EVs. (For limited space we will omit detailed data.)

Recently, new approaches of fuel cells are described in [9]. Company Medis Technologies, Inc, developed fuel cells, which instead polymer electrolyte uses liquid electrolyte mixed with methanol, plus propriety catalyst. At this moment this full cells will be use for powering portable electronics. However, this approach may be used for EVs. (Interesting for those fuel cells that they were investigated for use in Soviet space programs.)

METAL OXIDE BATTERIES

Hydrogen is very efficient fuel; each kilogram of it packs 42 kWh of energy - tree times as the some weight as gasoline and a thousand times as mach as a lead acid battery of the some weight. In practical situation one liter of fuel contens of hydrogen at pressure of 35 MPa (over 350 atmospheres) weights only 31 g and contains 1.3 kWh of energy. In the same time containment vessel weighs more than the gas.

A liter of solid aluminum, in contrast, weighs 2.7 kg and can theoretically yield over 10 times as much energy. Zinc has lower specific energy than aluminum, but because it is denser it winds up packing almost as much as energy as lighter metal in the same amount of space.

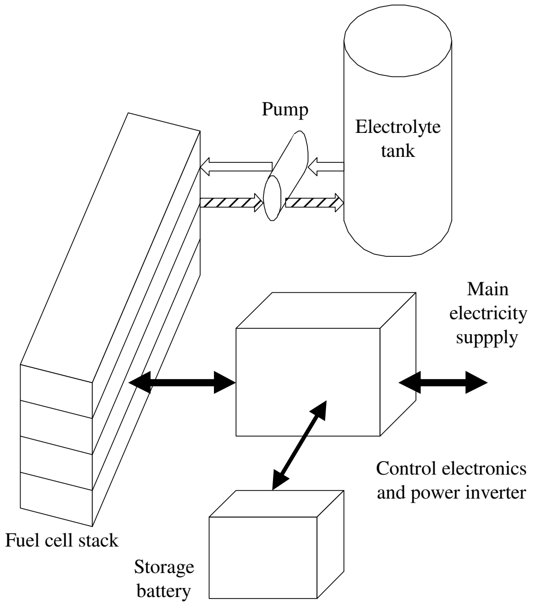

Fig.3: *Principles of operations of aluminum-air system.*

The problem with hydrogen is that, to be a practical fuel, it be must stored and transported under pressure. For safety, it needs government's regulation to store and transport it. Building a refueling or recharging infrastructure is a major - perhaps the major – difficulty to overcome. Hydrogen were not already established as irreplaceable part of modern life, it would probably newer be approved as a fuel in today's regulatory environment. Because hydrogen light element it is difficult to keep it in bottles. When hydrogen leaks, the gas tends to rise and dissipate and it is very flammable.

Aluminum and zinc, in contrast are benign materials that are also perceived to be benign. They can be transported without restriction and stored just about anywhere. True fuel cells based on these metals do produce wasters that cannot simply be dispersed into atmosphere. The waste products - aluminum and zinc oxide - are widely recognized as nonflammable, nontoxic materials that present no shipping or storage problems. And they can easily recycled.

Still, aluminum is not without problems of its own. A big one is parasitic corrosion. Leave plates the electrolytes used in fuel cells, and they will rapidly disappear, losing a few present of their mass per hour. One solution of this problem is to separate the plates from the potassium hydroxide electrolyte. Backup fuel cell systems keep the caustic alkaline solution in a separate tank and pump it into the stack only when it's time to deliver power.

The system has five main components: the fuel cell stack, the electrolyte tank, a pump, a storage battery and control electronics (Fig. 3). In case of a power failure, the battery provides instantaneous backup and also powers the pump, which transforms the electrolyte from its storage tank into stack. Once that transfer is made, the stack immediately begins generate electricity, providing backup power and recharging the battery. When the emergency is over, pump removes the electrolyte from the stack, shutting down fuel cell and prevents parasitic corrosion. When aluminum plates in the stack are depleted, the cell is refueled by simply replacing them.

Although theoretically able to store only quarter as much energy per unit mass as aluminum (around 4 kW/kg) zinc (around 1 kW/kg) can be used to make quite comparative fuel cells. Practical zinc air-fuel cells can be made to achieve ratings of about 350-500 Wh/kg compared with perhaps 800 Wh/kg for aluminum.

Unlike aluminum, zinc will corrode only slowly when immersed in its alkaline electrolyte, which is also potassium hydroxide. To keep a zinc-air fuel cell from losing capacity while in standby mode, it is only necessary to shut off its air supply. That obviously, is easier to do than to separate from the electrolyte.

There are systems, which includes refueling system. The "spent" fuel (zinc oxide), along with some of the liquid electrolyte solution, is pumped from fuel cell into vending-machine-sized refueling unit. At the same time, zinc pallets, about a millimeter across, pumped into the fuel along with replacement liquid electrolyte from the same refueled. Using electricity from grid, the unit converts the zinc oxide back into metallic zinc and released oxygen into atmosphere. During operation the zinc oxide is continuously washed by a recirculating flow of electrolyte.

This system is accompanied with small battery, which is necessary for powering pumps for air and electrolyte. In EVs that battery may be proper sized to have hybrid system. That may overcome problems of low specific powers of metal-air fuel cells

SOME OTHER ELECTRICAL SOURCES

The electromechanical flywheels have specific power ratings that are greater than electrochemical batteries and even the most efficient ICEs. For two reasons they are not spread: the specific energy and safety, because rotor can disintegrated or break free of its bearings. Trinity Flywheel Power Inc., San Francisco produces such electromechanical battery.

The module, which sinks or sources power to dc bus on demand, stores energy on two composite flywheel rotors that spin in opposite directions to negate the gyroscopic effect torque. During charging, an on board generator transfers electricity to the module, accelerating the rotors to as much as 48800 rpm. At discharge the unit acts as a variable voltage, variable frequency ac generator who's output converted to dc for driving the bus's electric traction motors. The 227-kg unit has a voltage range of 550-800 V, can assist the engine during acceleration or hill climbing by delivering a 750 kW burst for 3 seconds or 200 kW for as much as 15 seconds (specific power is 3300 W/kg).

For safety, Trinity believed it has the problem licked. They believed that their static gravitational force approaches 100 000 g_n – too high to be effected by shocks encountered during driving.

For example, company Magnet Motor GMH, Germany, recently showed the application of flywheel in track 8x8, 25 t [12]. The system has power500 kW and stored energy 6 kWh. This system doubled installed power from 20 kW/t to 40 kW/t for intermittent operation.

CONCLUSIONS

In recently years developing of energy sources for EVs and other applications with autonomous power supplies are accelerated. We analyzed different kinds of chargeable batteries. First, we analyzed NiMH batteries, which meet requirements for EVs and lowered its manufacturing prices close to the level of price for lead-acid batteries. Very rarely in experimental proceedings are lithium batteries, because of risk involved in using lithium in large batteries. Some bateries as sodium/nickel chloride showed also very good characteristics.

Fuel cells are very promising for EVs and autonomous power systems. They have high power efficiency and can use many kinds of hydrocarbons as fuel, and pure hydrogen. They can operate in all kind of environment conditions.

The newest developing of metal oxide batteries probably will solve a problem of economical, safe and simple powering EVs and autonomous power systems. These batteries are between classical chargeable batteries and fuel cells. They are recycling batteries. For extremely high powers in extremely short time flywheel systems are very convenient.

Finally, we may notice, that nowadays trends of developing of power sources will for sure spread applications of EVs and autonomous power systems in many living fields.

LITERATURE

[1] J. Riezenman, "Engineering the EV future", *IEEE Spectrum,* no.11, 1998, pp.19 -52

[2] J. Riezenman, "Electric Vehicles", p.18 and "The great battery barrier", *IEEE Spectrum,* no.11, 1992, p.97

[3] C.C. Chan, "An overview of electric vehicle technology", *Proc. of the IEEE*, Vol.1, No.9, 1993, pp.1203-1213

[4] Lj. @ivanov, D. Te{anovi}, V. Teodorovi}, M. @ivanov, “Analyzes of properties of batteries for application in light electrical vehicles", *Journal of Sources of Electrical Energy*, Belgrade, 2, 1994, p.15

[5] M.B. @ivanov, Lj.D. @ivanov, “Review modern technologies for application in electrical vehicles”, *Monographia “Electrodigger”,* Agriculture Faculty, Novi Sad, in press, 31 pages

[6] Willie D. Jones, “Batteries no match for its fuel cell, clams Israeli start up”, "*IEEE Spectrum,* no.11, 2001, p.25

[7] J. Riezenman, "Flywheels spin again", *IEEE Spectrum,* no.6, 2000, p.25

[8] M.B. @ivanov, Lj.D. @ivanov, “Analysis of power sources for automotive electric vehicles”, *Proc. of the Conf. ACEV’01*, paper no.41,. Den Hag, January, 2002. 10 pages

[9] J. Riezenman, "Metal fuel cells", *IEEE Spectrum,* no.6, 2001, p.54

[10] R.N.Bull, A.R.Tilley, “Development of new types of Zebra batteries for various vehicle applications’, ”, *Proc. of the Conf. EVS’18*, Berlin, 2001

[11] A.R.Tilley, R.N.Bull, “The Zebra Electric vehicle batteries - recent advances”, *Conf. Autoch’97*, Birminhghm, UK, 10 pages, 1997

[12] G.Reiner, P.Ehrhart, “MDS flywhell storage system in a 25 t, 8x8 wheel electric vehicle”, *Proc. of the Conf. ACEV’01*, paper no.62,. Den Hag, January, 2002. 8 pages

DIRECT PARAMETER ESTIMATION OF INDUCTION MOTOR BASED ON CONTINUOUS TIME MODEL

Teoharie Ganciu, Vasile Horga, Iulian Graur**
Technical University "Gh.Asachi", Faculty of Automatic Control and Computer Engineering
**Technical University "Gh.Asachi", Faculty of Electrical Engineering*
Iaşi, Romania

Abstract: *This paper presents a method of estimating the parameters of squirrel cage induction motor. Using a continuous parametric model, estimated off-line by a technique based on Poisson moment functional theory, the connection between its parameters and those of equivalent phase circuit is obtained.*

Keywords: *Modeling, Identification, Estimation, Vector-Controlled Induction Motor Drives*

INTRODUCTION

It is known that the estimating techniques based on nonparametric models are less precise than the models based on parametric models [1]. Although they imply more complex experimental conditions, the latter avoid the possible errors of conversion that may appear in a nonparametric - parametric change of representation. In digital control of processes, where the zero-order hold is used, a discrete parametric model is generally preferred. Implicitly, the methods of parameter estimation use the discrete models of the investigated processes, ensuring thus a series of facilities [2]:

- both data measuring and processing are of discrete nature;
- discrete models are more flexible than the continuous ones, and it is simpler to use them for simulation, control and prediction.

However the obtained coefficients have a synthetic character and their physical interpretation is difficult for models of order greater than two.

On the contrary, identification methods based on continuous model of the process offer the following advantages [3]:

- the possibility of physical interpretation and evaluation of process parameters (time constants, eigenfrequencies, damping coefficients);
- embedding of a priori knowledge about partially known processes in terms of poles, zeroes or physical quantities like mass, stiffness, resistance or capacities:
- easier evaluation of the model at the supervision level of the adaptive systems;
- sampling frequency of control system may be different from one used in identification algorithm.

It is well known that in designing of controllers, estimators and observers for high performance drive systems the continuous model parameters are used and not the discrete ones. Thus, an increasing in the precision of these parameters can be achieved if a direct technique for their estimation is used, avoiding conversion errors that can appear due to the discrete-continuous change of representation.

THE INPUT-OUTPUT MODEL OF SQUIRREL CAGE INDUCTION MOTOR

In order to estimate the electrical and/or mechanical parameters of the induction motor it is useful to highlight a linear form in the parameters by using only measurable quantities:

$$y(t) = \varphi^T(t)\theta \qquad (1)$$

The complex space-vector model of induction motor in a stator reference frame is considered:

$$\begin{cases} \underline{u}_s = R_s \underline{i}_s + \dfrac{d\underline{\psi}_s}{dt} \\ 0 = R_r \underline{i}_r + \dfrac{d\underline{\psi}_r}{dt} - j\omega_r \underline{\psi}_r \\ L_s \underline{i}_s + L_m \underline{i}_r = \underline{\psi}_s \\ L_m \underline{i}_s + L_r \underline{i}_r = \underline{\psi}_r \end{cases} \qquad (2)$$

Using Laplace integral transform, system (2) becomes

$$\begin{cases} \underline{u}_s = R_s \underline{i}_s + s\underline{\psi}_s \\ 0 = R_r \underline{i}_r + (s - j\omega_r)\underline{\psi}_r \\ L_s \underline{i}_s + L_m \underline{i}_r = \underline{\psi}_s \\ L_m \underline{i}_s + L_r \underline{i}_r = \underline{\psi}_r \end{cases} \qquad (3)$$

and the operational inductance is obtained:

$$l(s) = \frac{\underline{\psi}_s}{\underline{i}_s} = L_s \frac{\sigma T_r (s - j\omega_r) + 1}{T_r (s - j\omega_r) + 1} \qquad (4)$$

Stator circuit admittance will be:

$$\frac{\underline{i}_s}{\underline{u}_s} = \frac{\underline{b}_1 s + \underline{b}_0}{s^2 + \underline{a}_1 s + \underline{a}_0} \qquad (5)$$

The coefficients of the continuous linear model have the following physical significance:

$$\begin{cases} \underline{b}_1 = \dfrac{1}{\sigma L_s}; \\ \underline{b}_0 = \dfrac{1}{\sigma L_s T_r} - j\dfrac{\omega_r}{\sigma L_s}; \end{cases}$$

$$\begin{cases} \underline{a}_1 = \dfrac{1}{\sigma}\left(\dfrac{1}{T_r} + \dfrac{1}{T_s}\right) - j\omega_r \\ \underline{a}_0 = \dfrac{1}{\sigma T_s T_r} - j\dfrac{\omega_r}{\sigma T_s} \end{cases} \qquad (6)$$

where:

$$T_r = \frac{L_r}{R_r},\ T_s = \frac{L_s}{R_s},\ \sigma = 1 - \frac{L_m^2}{L_s L_r} \qquad (7)$$

In time domain the operational model (5) becomes:

$$\frac{d^2 \underline{i}_s}{dt^2} + \underline{a}_1 \frac{d\underline{i}_s}{dt} + \underline{a}_0 \underline{i}_s = \underline{b}_1 \frac{d\underline{u}_s}{dt} + \underline{b}_0 \underline{u}_s \qquad (8)$$

or

$$\underline{i}_s = \left[-\frac{\mathrm{d}\underline{i}_s}{\mathrm{d}t} \quad -\frac{\mathrm{d}^2\underline{i}_s}{\mathrm{d}t^2} \quad \underline{u}_s \quad \frac{\mathrm{d}\underline{u}_s}{\mathrm{d}t} \right] \left[\frac{\underline{a}_1}{\underline{a}_0} \quad \frac{1}{\underline{a}_0} \quad \frac{\underline{b}_0}{\underline{a}_0} \quad \frac{\underline{b}_1}{\underline{a}_0} \right]^T \quad (9)$$

ESTIMATING PRINCIPLE OF CONTINUOUS MODEL PARAMETERS OF THE PROCESS

Let's take a dynamic linear system described by:

$$\sum_{i=0}^{n} a_i \frac{d^i}{dt^i} y(t) = \sum_{j=0}^{m} b_j \frac{d^j}{dt^j} u(t) \qquad (10)$$

or:

$$\sum_{i=0}^{n} a_i y^{(i)}(t) = \sum_{j=0}^{m} b_j u^{(j)}(t) \qquad (11)$$

where a_i, b_j are constant or slow varying coefficients, $a_0=1$.

As the model is linear in parameters, in principle, all estimation methods for discrete models may be used. But, in contrast to the ARMA models used in the discrete domain, model (11) is not only a linear combination of input u(t) and output y(t) samples; it also contains pure time derivatives of these signals. In practice time derivatives of process signals are difficult to obtain. To overcome this difficulty the usual solution is to perform some suitable Linear Dynamical Operation (LDO) on both sides of eqn. (11) changing thus initial model into an *estimation model* which verify a differential equation similarly to the original one but in which the pure derivative of the input-output signals are not present any longer. In this way using a suitable linear dynamic operation we can obtain equivalent signals that help us to determine the continuous model parameters [4,5].

The Poisson Moment Functional (PMF) method can be interpreted as a technical application of the modulating function. Considering a chain of k continuous identical filters, each of the form:

$$G(s) = \frac{1}{s+\lambda} \qquad (12)$$

the equivalent transfer function is:

$$G_k(s) = \frac{1}{(s+\lambda)^k} \qquad (13)$$

which has the weighting function:

$$g_k(t) = L^{-1}\{G_k(s)\} = \frac{t^{k-1}}{(k-1)!} e^{-\lambda t} \qquad (14)$$

On the basis of convolution theorem one can define as LDO of k degree, the processing realized by the chain of k+1 continuous filters over the "∘" signal applied at the input (PMF of k degree):

$$M_k\{\circ\} \overset{def}{=} \int_0^{t_0} \frac{(t_0 - t)^k}{k!} e^{-\lambda(t_0 - t)} \circ \, dt \qquad (15)$$

Based on (15) a signal, y(t), filtered by a single filter can be expressed as:

$$y_0^0(t) = M_0\{y(t)\} = \int_0^{t_0} e^{-\lambda(t_0 - t)} y(t) dt \quad (16)$$

By generalizing we can say that if at the input of (k+1) filters chain is applied a signal signifying the n-order derivative of y(t) it results

$$y_k^n(t) = M_k\left\{\frac{d^n y(t)}{dt^n}\right\} = \int_0^{t_0} \frac{(t_0 - t)^k}{k!} e^{-\lambda(t_0 - t)} \frac{d^n y(t)}{dt^n} dt \quad (17)$$

The equivalent transformed model can be obtained by applying the k-order PMF, proper chosen in concordance with system's order. On obtains:

$$\sum_{i=0}^{n} a_i M_k\{y^{(i)}(t)\} = \sum_{j=0}^{m} b_j M_k\{u^{(j)}(t)\} \quad (18)$$

or:

$$\sum_{i=0}^{n} a_i y_k^i(t) = \sum_{j=0}^{m} b_j u_k^j(t) \qquad (19)$$

In vector form, (19) will be:

$$y_k^0(t) = \varphi^{*T}(t)\theta \qquad (20)$$

where:

$$\varphi^{*T}(t) = \left[-y_k^1(t) \ -y_k^2(t) \ \ldots - y_k^n(t) \ u_k^0(t) \ u_k^1(t) \ \ldots \ u_k^m(t) \right]$$

$$\theta^T = \left[a_1 \ a_2 \ \ldots . \ a_n \ b_0 \ b_1 \ \ b_m \right]$$

As in discrete model parameter estimation, if at any moment the vector $\varphi^{*T}(t)$ can be built, then the vector of parameters, θ, can be obtained trough standard procedure.

At this moment the problem is to obtain the vector $\varphi^{*T}(t)$ in terms of available signals through recurrence, that is:

$$\begin{cases} y_k^p = f\left(y_0^0(t), \ y_1^0(t), \ \ldots . . y_{k-1}^0(t), y_k^0(t)\right) \\ u_k^p = f\left(u_0^0(t), \ u_1^0(t), \ \ldots . . u_{k-1}^0(t), u_k^0(t)\right) \end{cases} \qquad (21)$$

Integrating by parts in (17), for n=1 on obtains:

$$y_k^1(t) = M_k\left\{\frac{dy(t)}{dt}\right\} = \int_0^{t_0} \frac{(t_0 - t)^{k-1}}{(k-1)!} e^{-\lambda(t_0 - t)} y(t) dt -$$

$$- \lambda \int_0^{t_0} \frac{(t_0 - t)^k}{k!} e^{-\lambda(t_0 - t)} y(t) dt - \frac{t_0^k}{k!} e^{-\lambda t_0} y(0) \qquad (22)$$

or

$$y_k^1(t) = y_{k-1}^0(t) - \lambda y_k^0(t) - g_{k+1}(t_0) y(0) \quad (23)$$

Similarly, for n=2, on obtains:

$$y_k^2(t) = M_k\left\{\frac{d^2 y(t)}{dt^2}\right\} = \int_0^{t_0} \frac{(t_0 - t)^{k-2}}{(k-2)!} e^{-\lambda(t_0 - t)} y(t) dt -$$

$$2\lambda \int_0^{t_0} \frac{(t_0 - t)^{k-1}}{(k-1)!} e^{-\lambda(t_0 - t)} y(t) dt + \lambda^2 \int_0^{t_0} \frac{(t_0 - t)^k}{k!} e^{-\lambda(t_0 - t)} y(t) dt$$

$$-\left(\frac{t_0^{k-1}}{(k-1)!} e^{-\lambda t_0} - \lambda \frac{t_0^k}{k!} e^{-\lambda t_0} \right) y(0) - \frac{t_0^k}{k!} e^{-\lambda t_0} \frac{dy(0)}{dt}$$

(24)

or in a condensed form:

$$y_k^2(t) = y_{k-2}^0(t) - 2\lambda y_{k-1}^0(t) + \lambda^2 y_k^0(t) -$$

$$- \left(g_k(t_0) - \lambda g_{k+1}(t_0) \right) y(0) - g_{k+1}(t_0) \frac{dy(0)}{dt} \quad (25)$$

Since the filters are stable and causal the last terms in (22) and (24) -which take into account the combined effects of initial conditions-will be ignored.

In matrix form, for k=1... n on obtains:

$$\begin{bmatrix} y_n^0(t) \\ y_n^1(t) \\ y_n^2(t) \\ .. \\ y_n^n(t) \end{bmatrix} = \begin{bmatrix} 0 & 0 & .. & 0 & 1 \\ 0 & 0 & .. & 1 & * \\ 0 & 0 & .. & * & * \\ .. & .. & .. & .. & .. \\ 1 & * & .. & * & * \end{bmatrix} \begin{bmatrix} y_0^0(t) \\ y_1^0(t) \\ y_2^0(t) \\ ... \\ y_n^0(t) \end{bmatrix}$$
(26)

where term $*_{ij}$ is expressed as:

$$*_{ij} = (-1)^{n+j-i} C_{i-1}^{(i+j-n-2)} \lambda^{(i+j-n-2)} \quad (27)$$

Based on (20), if an off-line Least Square (LS) method is used, the θ parameter's vector will be:

$$\hat{\theta} = \left[\sum_{t=1}^{N} \varphi^*(t) \varphi^{*T}(t) \right]^{-1} \left[\sum_{t=1}^{N} \varphi^*(t) y_n^0(t) \right] \quad (28)$$

EXPERIMENTAL RESULTS

In order to estimate the parameters of model (2), the squirrel cage induction motor, presented in appendix, is connected as shown in fig. 1.

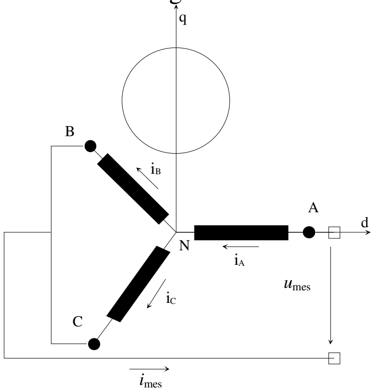

Fig.1. *Connection diagram for experiments*

This configuration is characterized by the following relations between phase values (voltages, currents) and measured values:

$$\begin{cases} i_B = i_C = -\dfrac{i_A}{2} = -\dfrac{i_{mes}}{2}; \\ u_A = \dfrac{2}{3} u_{mes}; u_B = u_C = -\dfrac{1}{3} u_{mes} \end{cases} \quad (29)$$

By using space vectors power invariant definition the d-q axis components have the following values:

$$i_{sd} = \sqrt{\frac{3}{2}} i_{mes}; i_{sq} = 0; u_{sd} = \sqrt{\frac{2}{3}} u_{mes}; u_{sq} = 0 \quad (30)$$

Obviously, in such a configuration, the motor doesn't develop significant electromagnetic torque, i.e.

$$m_e = pL_m (i_{sq} i_{rd} - i_{sd} i_{rq}) = 0 \quad (31)$$

and so rotor speed (ω_r) is zero.

Now eqn. (8) will be:

$$\frac{d^2 i_{sd}}{dt^2} + a_1 \frac{di_{sd}}{dt} + a_0 i_{sd} = b_1 \frac{du_{sd}}{dt} + b_0 u_{sd} \quad (32)$$

where the coefficients of the new model are:

$$a_1 = \frac{1}{\sigma}\left(\frac{1}{T_r} + \frac{1}{T_s} \right); a_0 = \frac{1}{\sigma T_s T_r}; b_1 = \frac{1}{\sigma L_s}; b_0 = \frac{1}{\sigma L_s T_r} \quad (33)$$

From (33) the following motor parameters can be obtained:

$$T_r = \frac{b_1}{b_0}; R_s = \frac{a_0}{b_0}; T_s = \frac{a_1}{a_0} - \frac{b_1}{b_0}; \quad (34)$$

$$L_s = \frac{a_0}{b_0}\left(\frac{a_1}{a_0} - \frac{b_1}{b_0} \right); \sigma = \frac{1}{a_0 T_s T_r} \quad (35)$$

If the stator leakage inductance is known (estimated by another experiment)

$$L_{\sigma s} = L_s - L_m \quad (36)$$

then the remainder parameters can be obtained from:

$$L_m = L_s - L_{\sigma s};\ L_r = \frac{L_m^2}{(1-\sigma)L_s};\ R_r = \frac{L_r}{T_r} \quad (37)$$

Since a LS estimator is used a persistent input signal is required. Strictly speaking this implies that all the natural modes of the system have to be excited during the experiment. In practice this rich frequency signal is obtained by using a Pseudo Random Binary Sequence (PRBS) signal. Experiments were performed by the means of o multifunction test bench described in [6]. Fig.2. presents a sequence of the required signals recorded with a 1 kHz sampling frequency.

In this case the induction motor model (9) become:

$$i_{sd}(t) = \left[-\frac{di_{sd}}{dt} \quad -\frac{d^2 i_{sd}}{dt^2} \quad u_{sd} \quad \frac{du_{sd}}{dt} \right] \left[\frac{a_1}{a_0} \quad \frac{1}{a_0} \quad \frac{b_0}{a_0} \quad \frac{b_1}{a_0} \right]^T \quad (38)$$

The signals required in (20) can be obtained by digital filtering using two chains with three stages and processing intermediate values in accordance with (26).

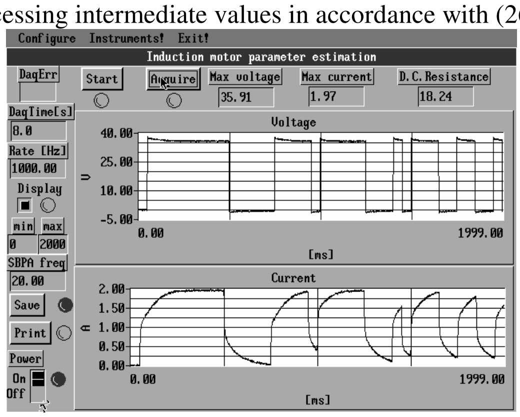

Fig. 2. *Front panel with acquired values of input/output signals*

In order to normalize the dc gain each filter element has a transfer function of the form:

$$G(s) = \frac{\lambda}{s + \lambda} \quad (39)$$

In this case (26)-(27) become:

$$\begin{bmatrix} y_n^0(t) \\ y_n^1(t) \\ y_n^2(t) \\ .. \\ y_n^n(t) \end{bmatrix} = \begin{bmatrix} 0 & 0 & .. & 0 & * \\ 0 & 0 & .. & * & * \\ 0 & 0 & .. & * & * \\ .. & .. & .. & .. & .. \\ * & * & .. & * & * \end{bmatrix} \begin{bmatrix} y_0^0(t) \\ y_1^0(t) \\ y_2^0(t) \\ ... \\ y_n^0(t) \end{bmatrix} \quad (40)$$

$$*_{ij} = (-1)^{n+j-i} C_{i-1}^{(i+j-n-2)} \lambda^{(i-1)} \quad (41)$$

Now using eqns. (40) and (41) we can write:

$$\begin{bmatrix} i_{sd2}^{0}(t) \\ i_{sd2}^{1}(t) \\ i_{sd2}^{2}(t) \end{bmatrix} = \begin{bmatrix} 0 & 0 & 1 \\ 0 & \lambda & -\lambda \\ \lambda^2 & -2\lambda^2 & \lambda^2 \end{bmatrix} \begin{bmatrix} i_{sd0}^{0}(t) \\ i_{sd1}^{0}(t) \\ i_{sd2}^{0}(t) \end{bmatrix} \quad (42)$$

$$\begin{bmatrix} u_{sd2}^{0}(t) \\ u_{sd2}^{1}(t) \\ \# \end{bmatrix} = \begin{bmatrix} 0 & 0 & 1 \\ 0 & \lambda & -\lambda \\ \# & \# & \# \end{bmatrix} \begin{bmatrix} u_{sd0}^{0}(t) \\ u_{sd1}^{0}(t) \\ u_{sd2}^{0}(t) \end{bmatrix} \quad (43)$$

The state equations of the filtering chains have the expressions:

$$\begin{bmatrix} \frac{dy_0^0(t)}{dt} \\ \frac{dy_1^0(t)}{dt} \\ \frac{dy_2^0(t)}{dt} \end{bmatrix} = \lambda \begin{bmatrix} -1 & 0 & 0 \\ 1 & -1 & 0 \\ 0 & 1 & -1 \end{bmatrix} \begin{bmatrix} y_0^0(t) \\ y_1^0(t) \\ y_2^0(t) \end{bmatrix} + \lambda \begin{bmatrix} 1 \\ 0 \\ 0 \end{bmatrix} y(t) \quad (44)$$

Finally based on eqns. (42)-(43) an equivalent vector form of eqn (38) can be obtained:

$$i_{sd2}^{0}(t) = \left[-i_{sd2}^{1}(t) \quad -i_{sd2}^{2}(t) \quad u_{sd2}^{0} \quad u_{sd2}^{1}\right] \left[\frac{a_1}{a_0} \quad \frac{1}{a_0} \quad \frac{b_0}{a_0} \quad \frac{b_1}{a_0}\right]^T \quad (45)$$

In this way the matrix equation of LS estimator (28) can be used and then on the basis of eqns. (34)-(37), the physical parameters of the induction motor can be obtained.

The λ parameter must be chosen as a compromise value in such a way that one hand to eliminate the initial condition effects (increasing values) and on the another hand to remove the noise effects (decreasing values). In this order stator resistance was used as reference value, the later being obtained in steady state installed during the interval 0.4-0.5s. The λ parameter was adjusted until the estimated value matched the measured one. By this adjusting procedure value λ=100 rad/s has been obtained

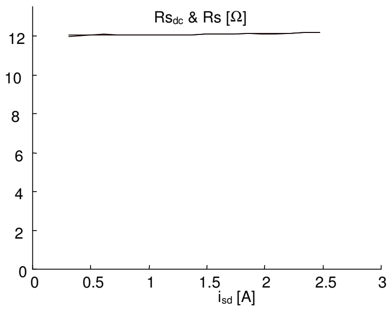

Fig. 3. DC measured and estimated stator resistance

By performing trials at different magnitudes of PRBS signals and data processing we obtained the parameters whose saturation dependency is shown in Fig. 3 - Fig. 10 ($L_{\sigma s}$=0.0348H).

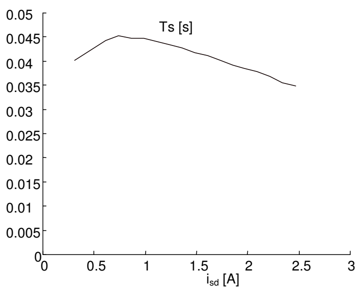

Fig.4. *Stator time constant*

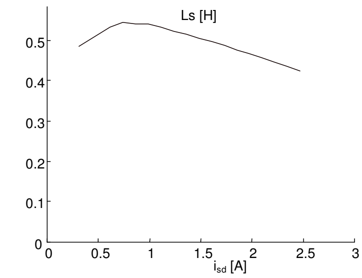

Fig.5. *Stator inductance*

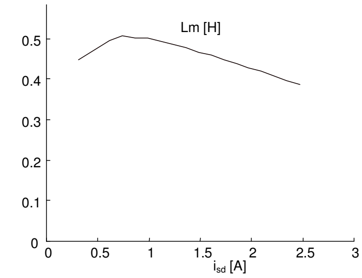

Fig.6. *Mutual inductance*

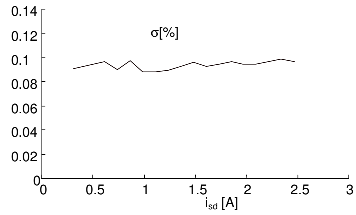

Fig. 7. *Global leakage factor*

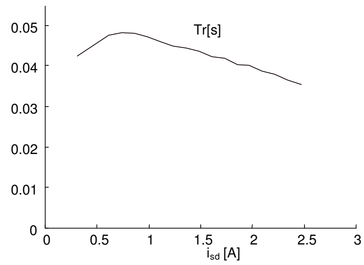

Fig.8. *Rotor time constant*

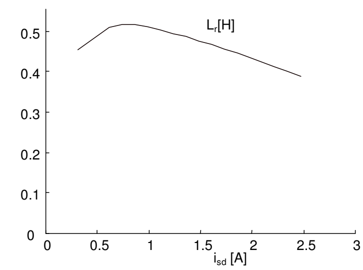

Fig.9. *Rotor inductance*

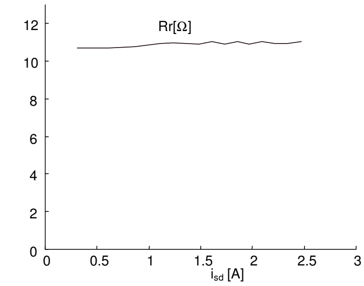

Fig.10. *Rotor resistance*

METHOD VALIDATION

In order to validate the proposed method a standstill current decay test [8] was performed for the same motor. The mutual inductance obtained from the both methods is presented in Fig. 11. Notice that saturation dependence of inductance estimated by the proposed method is smother due to noise filtering and his trace in terms of i_{sd} is more realistic.

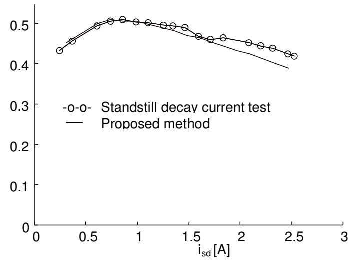

Fig.11. *Comparative results for L_m*

CONCLUSIONS

This paper presents a direct off-line parameter estimating method of squirrel cage induction motor continuous model based on Poisson moment functional theory. The method has a synthetic character; it take into account the combined effect of the parameters dependency in terms of saturation degree of magnetic circuits, the spectrum of used signal, core loses etc.

For a priori specified operating conditions of drive system, the estimating method may be automated and included in a self-commissioning procedure of control system. The configuration presented in fig.1 (or an equivalent one) is obtained through an adequate command of the inverter legs.

Appendix

Main parameters of the induction machine

Δ/Y	220/380V	3.05/1.76A
P=0.55 kW		cosφ=0.687
n_n=930 rev/min	f_n=50 Hz	

REFERENCES

[1] T. Soderstrom, P. Stoica, "*System identification*", Prentice Hall, 1989.

[2] M. Tertişco, P. Stoica, Th. Popescu, "*Computer-aided identification of systems*", Ed.Tehnică, Bucureşti, 1987 (in romanian).

[3] R. Isermann *et al*, "*Adaptive Control Systems*", New York, Prentice Hall, 1992.

[4] H.Umbehauen, G. Prasada Rao, "*Identification of Continuous Systems*", Amsterdam, North Holland, 1987.

[5] A.Patra, G.Prasada Rao, "Parameter Estimation in a Converter Driven DC Motor System via General Hybrid Orthogonal Functions", IEEE Trans. on Ind. Electr., Vol.38, No.5, 1991.

[6] V.Horga, M.Răţoi, I.Graur, "Multifunction Testbench for Electric Drives Study", *The Second International Conference on Electromechanical Systems*, Chisinau 8-9 October 1999, Vol.1, pp.201-206.

[7] D.E. Borgard *et al*, "Accuracy Issues for Parameter Estimation of Field Oriented Induction Machine Drives", IEEE Trans. on Ind. Applic., Vol.31, No.4, 1995.

[8] I.Boldea, "*Electrical Machines Parameters. Identification, estimation, validation*", EAR, Bucureşti, 1991 (in romanian).

LABVIEW VIRTUAL INSTRUMENTATION FOR A SWITCHED RELUCTANCE MOTOR

V. Trifa, A.Graur**, O. Rabulea**
**Dept. of Electric Drives, Technical University of Cluj-Napoca*
15 C. Daicoviciu St., RO-3400 Cluj-Napoca, Romania
***Dept. of Electrical Engineering, "Stefan cel Mare" University of Suceava,*
1 Universitatii St., RO-5800 Suceava, Romania
adriang@eed.usv.ro

Abstract: *This paper presents the switched reluctance motor investigation using LabVIEW virtual instrumentation. The system provides an easy and user friendly investigation of electro-magnetical and - mechanical characteristics of the SRM. An 8/6 4-phase SRM has been tested using this equipment. A large palette of experimental results is presented.*

Key Words: ***Switched reluctance motor, Virtual instrumentation***

INTRODUCTION

The Switched Reluctance Motor (SRM) has imposed itself in latest years, especially in variable speed applications. Some of its advantages are the simplicity of rotor construction, the possibility to overload without supplementary ventilation, a relatively constant torque on a large range of speed. The main disadvantages of SRM are high torque ripples and the need of a position transducer [1].

The knowledge of dynamical behaviour of the SRM is very important for control strategies and performance evaluation.

SRM taken into consideration has the following features: 8 stator poles, 6 rotor poles, 4 phases, stroke angle = 15 degrees, I_N = 8A, R = 1.2Ω, L_{min} = 1.1mH, L_{max} = 18 mH, where I_N is rated current, R is the phase resistance, L_{min} is the phase inductance in unaligned position and L_{max} is the phase inductance in aligned position.

A 4-quadrant operation of SRM is possible by choosing a multi-sensor position transducer [2]. In the particular case of 4-phase 8/6 SRM there are used 4 opto-electronic sensors. The transducer consists of a 6-slot disk placed on the rotor axis and 4 opto-electronic sensors A-B-C-D, whose axes are shifted with 15 degrees. The 4-sensor system is shifted with 3.75 degrees from phase 1 axis. Principled configuration of motor-transducer system is given in figure 1.

SRM phases are supplied from a dual-voltage inverter. A principled scheme of the dual voltage inverter for one phase is given in figure 2. The motor phase is supplied with the high voltage V1 until the phase current reaches the nominal value I_N. At this time Q1 is turned off and the motor phase is supplied from low voltage V2. This low voltage maintains the current at I_N value. Usually the ratio V1/V2 is 10. The scheme uses active suppression by D1 – D2 diodes.

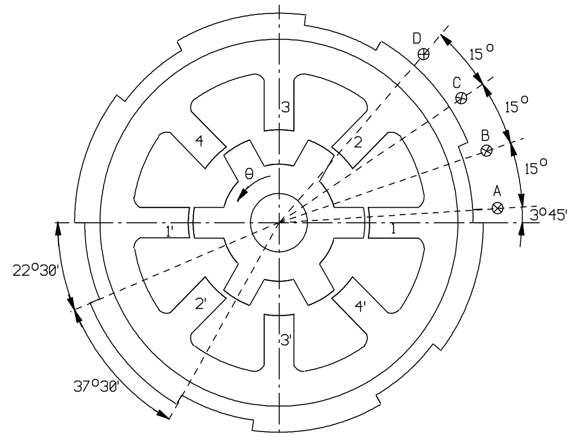

Fig. 1. *8/6 SRM and angular transducer*

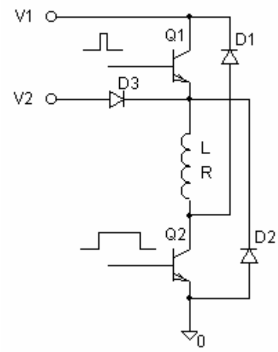

Fig. 2. *Principled scheme of dual-voltage inverter*

LABVIEW IMPLEMENTATION

The LabVIEW virtual instrument is built with National Instruments I/O card Lab PC 1200, which is programmed by G graphical programming language [3]. The main tasks of the virtual instrument are:

- configures the card ports in order to use them for data acquisition from the transducer
- filters the acquired signals
- compensates the phase resistance value due to the thermal effect of the current
- computes the flux-linkage, phase inductivity and electromagnetic torque involved in the SRM
- presents the data in a user-friendly mode
- save the data acquired and processed.

The controller acquires the phase currents and voltages, which are then post-processed. The post-processing of analog data is preferred for an optimal use of system resources in real time.

EXPERIMENTAL RESULTS

Experimental tests have been made using a set-up arrangement consisting in SRM with angular transducer and electro-magnetical brake, dual-voltage inverter, a PC including Lab PC 1200 card and LabVIEW environment, LEM voltage and current transducers and various measurement devices.

Figure 3 shows the phase voltage and current. The high voltage V1 (50V) forces the current to the nominal value, after that a low voltage V2 (5V) maintains the current at this value. Better results can be obtained if it is used a higher V1 voltage (e.g. 200V). Both waveforms are registered in an acquisition buffer and then are displayed and saved as TXT files by LabVIEW during the operation process.

The rest of the waveforms are registered on-line and displayed off-line. To eliminate the influence of electromagnetic noise and of sampling frequency a special filter has been used before calculating and displaying the curves of flux, inductivity and torque, as seen below.

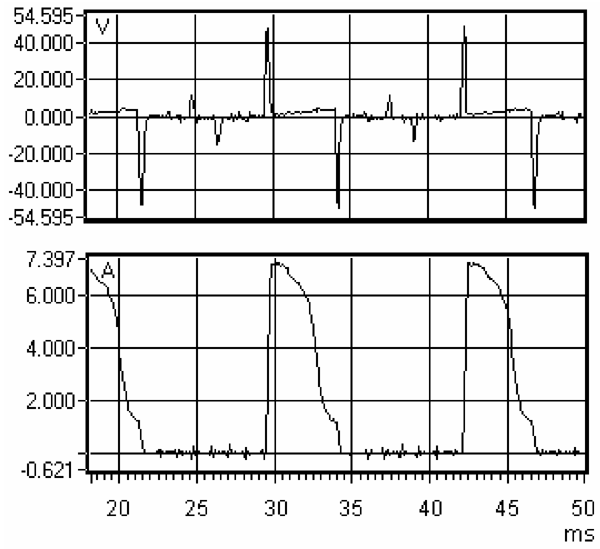

Fig. 3. *Phase voltage and current*

Figure 4 presents the flux-linkage in the four SRM phases at 150 rpm speed. The flux-linkage has been obtained using the on-line values of phase currents and voltages, by a digital integration of the classical voltage equation:

$$V = R \cdot i + \frac{d\psi}{dt} \qquad (1)$$

As observed, the magnitude of flux presents a not high rise at switch-on time of the phase, due to the low inductivity corresponding to unaligned rotor position, in spite of high rise of phase current. But, as the rotor moves from unaligned position, the magnitude of flux increases significantly due to the rise of phase inductivity with position.

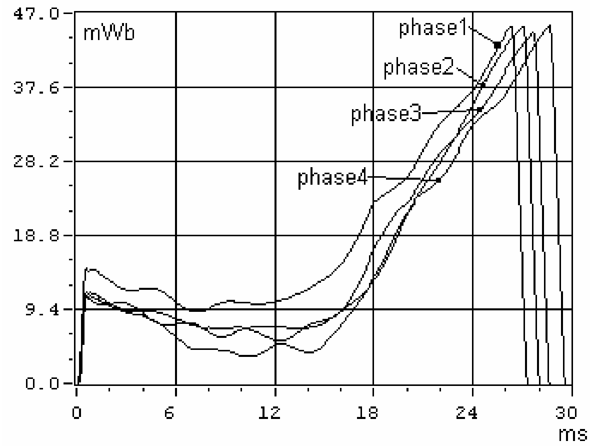

Fig. 4. *Flux-linkage in SRM phases at 150 rpm*

Figures 5 and 6 present the flux-linkage in one of SRM phase for speeds in the range of 100 rpm – 3400 rpm. One can observe the influence of the motor speed to the flux peak-value. The explanation of this phenomenon consists in the decrease of turn-on time per phase with the speed increasing. This is a normal process in synchronous machines supplied from a constant voltage source, known as "flux weakening". This fact leads to the idea of V/f=const. control of the SRM.

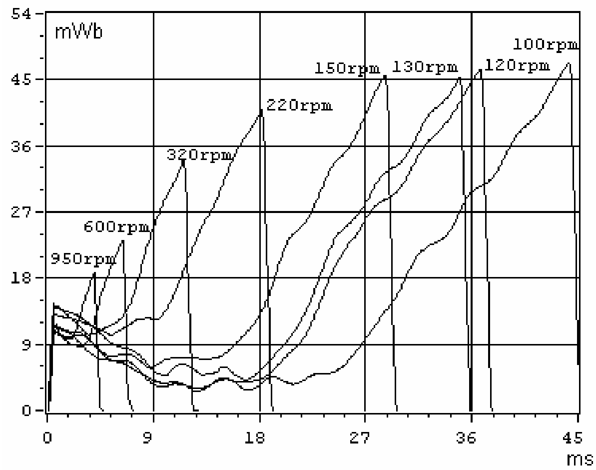

Fig. 5. *Flux linkage in phase A at low speed*

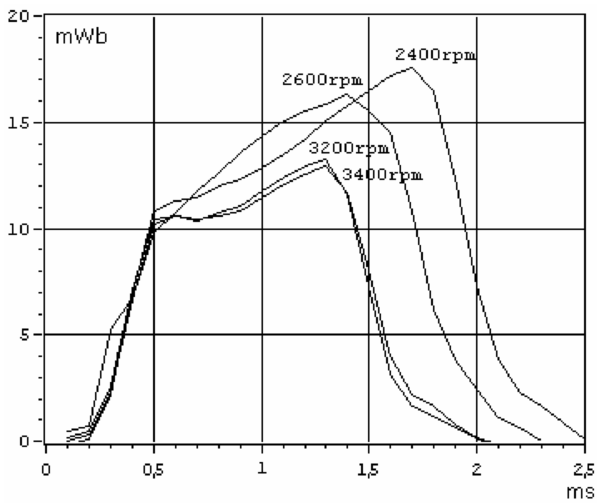

Fig. 6. *Flux-linkage for high speed*

Figure 7 depicts the variation of the phase inductivity in the four phases of the SRM during the turn-on time of the phase. Its magnitude has been obtained from the recorded values of currents and from calculated values of flux linkages, using the simple expression:

$$\psi = L \cdot i \qquad (2)$$

where Ψ is flux-linkage, L is phase inductivity and i is phase current.

These variations are time dependent, but they can be converted in inductivity-position curves using the time variation of rotor angle. These curves could be very useful in sensorless control of the SRM [4,5].

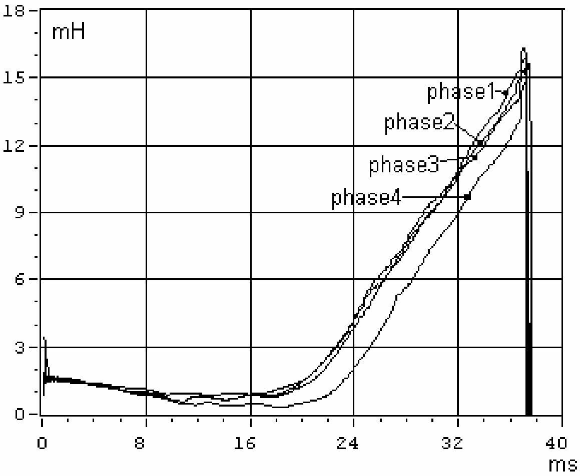

Fig.7. *Phase-inductance at 120 rpm*

Figure 8 presents the total electromagnetic torque variation. This waveform has been also obtained indirectly using the expression:

$$M = \left.\frac{dW}{d\theta}\right|_{i=const} = \frac{1}{\omega}\cdot\left.\frac{d(\psi \cdot i)}{dt}\right|_{i=const} \qquad (3)$$

where M is total electromagnetic torque, W is magnetic co-energy, ψ and i are phase flux-linkage, respectively phase current, θ is rotor angle and ω is angular speed.

As expected, important torque ripples occur due to the rapid switching of phase currents. Additional techniques for reducing torque ripples are recommended in some applications [6].

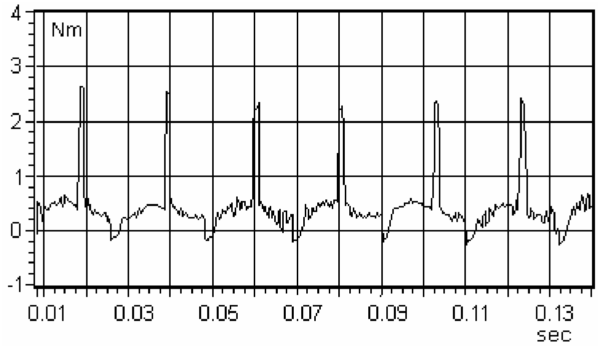

Fig. 8. *Electromagnetic torque*

CONCLUSIONS

As main conclusion one can say that a LabVIEW implementation is the cheapest solution to investigate a new SRM drive system, as it offers a rapid and flexible tool both for hardware and software approach. This LabVIEW instrument is useful for a professional investigation of SRM and is recommended at the beginning of the research. The dual voltage inverter is useful especialy for high-speed drives, where a PWM current control is not possible, the motor being fed with current pulses.

REFERRENCES

[1] T.J.E. Miller, "Switched Reluctance Motors and their Control". Magna Physics and Clarendon Press, Oxford, 1993.

[2] V. Trifa, Ramona Galatus, A. Szekely, Cs. Szasz, "Aspects Concerning the Commutation of Switched Reluctance Motors". Proceedings of 3rd International Conference Electromotion'99, Patras, Greece, 1999, pp. 125-130.

[3] LabVIEW package: DAQ Lab-PC-1200 User Manual, G Programming Reference Manual, Function and VI Reference Manual, LabVIEW Data Acquisition Basics Manual

[4] Ehsani, M., Ramani, K.R., - "Direct control strategies based on sensing inductance in switched reluctance motors". IEEE Transactions on Industry Applications, No. 1/1996, pp.74-82

[5] Fahimi, B., Suresh, G., Ehsani, M. – "Review of sensorless control methods in SRM Drives". IEEE Transactions on Industry Applications, No. 5/2000, pp.1850-1857

[6] Diril, O., Tuncay, R.N. – "The torque ripple minimisation of switched reluctance motors by torque waveform control". Proceedings of International Conference of Electrical Machines, ICEM'2000, Espoo, Finland, 2000, pp. 1070-1074

.

VOLTAGE DIP IMMUNITY TEST SET-UP FOR INDUCTION MOTOR DRIVES

Kurt Stockman, Frederik D'hulster, Kevin Verhaege, Jan Desmet, Ronnie Belmans***
** Hogeschool West-Vlaanderen, dept. P.I.H., Graaf Karel de Goedelaan 5, B-8500 Kortrijk, Belgium*
*** K.U.Leuven, dept. ESAT/ELEN, Kasteelpark Arenberg 10, B-3001 Leuven, Belgium*

Abstract: *A growing number of industrial facilities is using adjustable speed induction motor drives in order to increase the quality of their products and the flexibility in the production process. The reliability of the production plant decreases with the number of installed drives due to their sensitivity towards voltage dips. This paper presents a test set-up to determine the immunity of standard induction motor drives against supply voltage dips under various load conditions. Furthermore, the measurements are compared to simulation results.*

Key Words: ***Adjustable speed drives, voltage dips, dip immunity, ride through***

INTRODUCTION

A voltage dip is a momentary reduction of the rms voltage at a customer position. Bollen [1] characterises a voltage dip by a magnitude and a duration (0.5 – 30 cycles). The voltage dips are caused by faults in the utility distribution system and transported to all facilities on the same distribution network.

Voltage dips are widely recognised as the main cause of disturbances in production plants, equipped with adjustable speed drives (ASD). McGranaghan et al. [2] show that the economic impact of the possible loss of production due to voltage dips can be very high. In order to prevent tripping of an ASD during a dip, the immunity of drives should be taken into account during the design stage of production plants. This paper gives the design engineers a helpful insight in the possible ride-through ability of standard drives for induction machines under typical load conditions.

ENERGY CONSIDERATIONS

Fig. 1 shows the topology of an AC adjustable speed drive. It consists of three major parts: a diode rectifier, a DC buffer link and a controlled inverter.

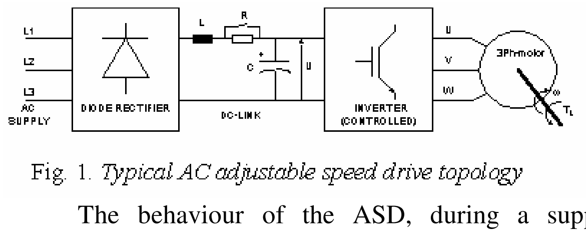

Fig. 1. *Typical AC adjustable speed drive topology*

The behaviour of the ASD, during a supply voltage dip, can be represented by an energy balance .

$$E_C + E_{kin} = E_L \tag{1a}$$

$$\frac{C}{2}\left(U_C^2(t_2) - U_C^2(t_1)\right) + \frac{J_L}{2}\left(\omega^2(t_2) - \omega^2(t_1)\right) = \int_{t_1}^{t_2} T_L.\omega.dt \tag{1b}$$

Note that, if the symmetrical voltage dip is below the DC-link voltage U_C, no energy is fed from the AC-supply into the DC-link because of the reverse biased diodes in the rectifier.

When analysing the energy balance, we can determine three main parameters influencing the behaviour of an ASD during a supply voltage dip of duration $(t_2 - t_1)$:

- The DC-link capacitor C: determines the electric energy E_C stored in the DC-link;
- The load inertia J_L: determines the mechanical energy E_{kin} stored in the rotating parts;
- The motor load profile $T_L(\omega)$: the energy consumer.

In low-inertia systems, the discharge-rate of the capacitor determines the survival-duration of the loaded drive. Typical values for the DC-link capacitor are between 75 and 360 µF/kW [1]. Fig.2 shows the decay of the DC-link voltage with such capacitor size under constant power demand P as expressed in

$$U(t) = \sqrt{U_0^2 - \frac{2P}{C}.t} \tag{2}$$

The energy-amount in a loaded capacitor is not enough to drive the load longer than 1.5 periods, with a DC-link undervoltage protection of 65% U_0 (= $U_{DC\ nom}$). If the DC-link voltage drops below the minimum voltage protection level $U_{DC\ min}$, the inverter is inhibited and the charging resistor R (Fig. 1) is activated, limiting the charging current at return of the supply voltage. If the voltage is restored, before reaching the DC-link undervoltage protection, the transient behaviour is mainly determined by the R-L-C combination in the supply and DC-link. Poor damping of this electrical second order system results in a DC-overvoltage and a peak supply current, at the re-entry of the supply voltage after a dip. This peak current can cause severe stress on the drive rectifier unit.

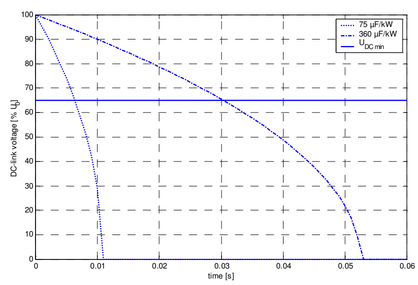

Fig. 2. *Influence of capacitor size on DC-link voltag*

SIMULATION MODEL

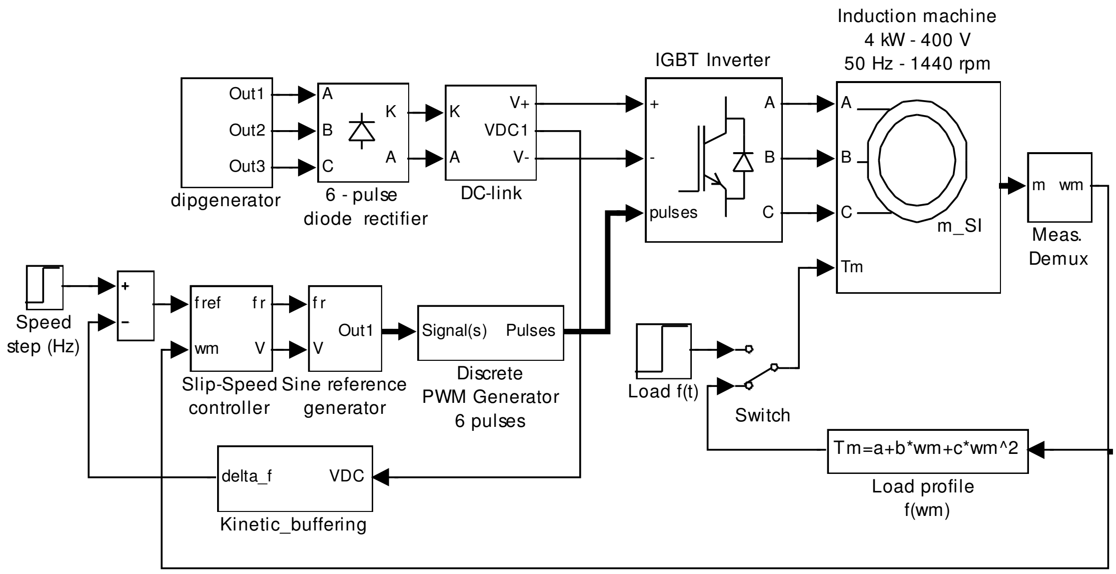

Fig.3. *Simulation model of an ASD with PWM-pulse control*

Fig.3 represents a Matlab® / Simulink® discrete model of an ASD with PWM-pulse control. The dipgenerator feeds the rectifier with a three-phase controllable power source. A PWM-pulse generator controls the switching pattern of the IGBT's in the inverter.

The slip-speed controller generates the required frequency and amplitude for the sine reference generator The U/f-ratio is kept constant over the overal speed range. In order to simulate the behaviour of standard induction motor drives under various load conditions, one can select whether the load is function of time or speed. Different voltage dip ride-through techniques, e.g. kinetic buffering can be implemented in the model. Fig. 4 shows the RMS supply line voltage, the DC-link voltage, the rotor speed, the load torque, the motor current and the electromechanical power delivered by the motor. This model is used to analyse the behaviour of a standard induction motor drive under different voltage dips and load conditions.

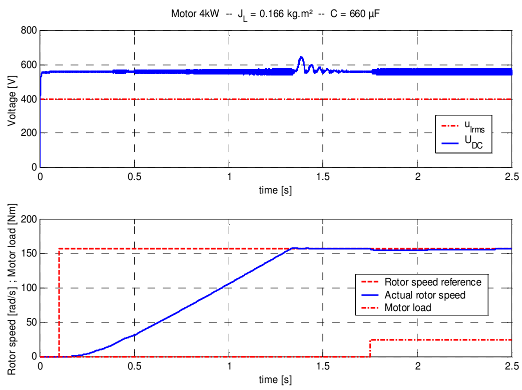

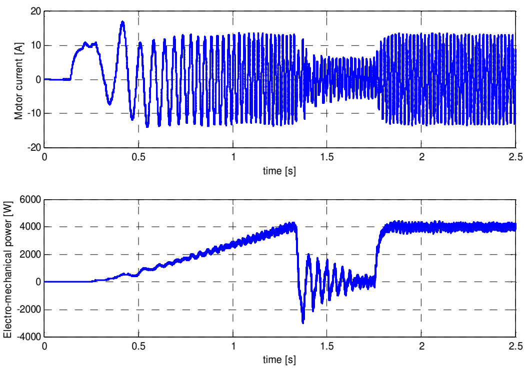

Fig. 4. *Simulation results of the behaviour of a PWM-pulse controlled 4kW induction motor*

TEST SET-UP

An experimental test set-up is build to measure the immunity of variable speed drives towards voltage dips under different load profiles. Fig. 5 shows the experimental set-up. It consists of four major parts: a programmable power source, the adjustable speed drive, the load machine and the load controller. A programmable power source (3x5kVA) is used to generate both balanced and unbalanced voltage dips according to the IEC 61000-4-11 standard [3]. The EUT, consisting of an adjustable speed drive with induction motor (up to 11kW) is loaded by a torque controlled DC-machine. Using a dSpace® DS1103 PPC controller-board, a Matlab® / Simulink® program is run to control the test set-up in real-time. Speed and load torque are measured to generate the necessary corrections, according to the selected loading profile. With the real-time user-interface ControlDesk®, different load profiles can be programmed in the controller. All signals are isolated in order to protect the controller-card against EMC, ground loops and overvoltages.

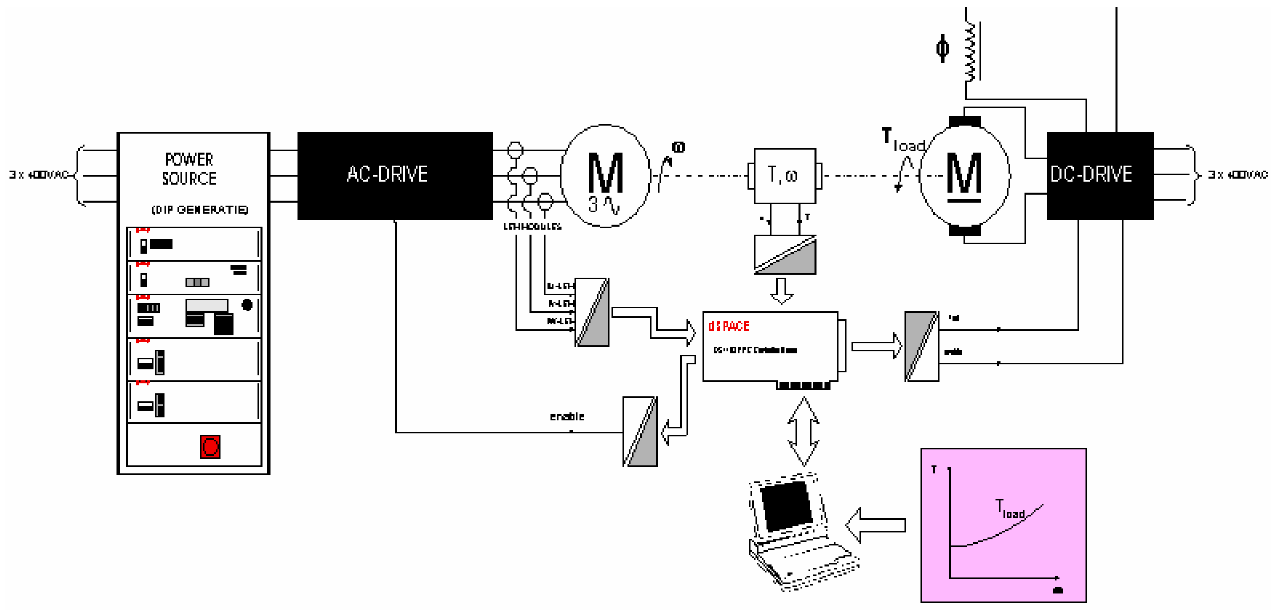

Fig. 5. *Experimental set-up*

MEASUREMENT RESULTS

Several standard induction motor drives have been subjected to balanced and unbalanced voltage dips. The measurement results are compared to the simulation results in order to prove the validity of the model. Fig. 6 shows a voltage dip measurement of the transient behaviour of a 4kW ASD under full load condition.

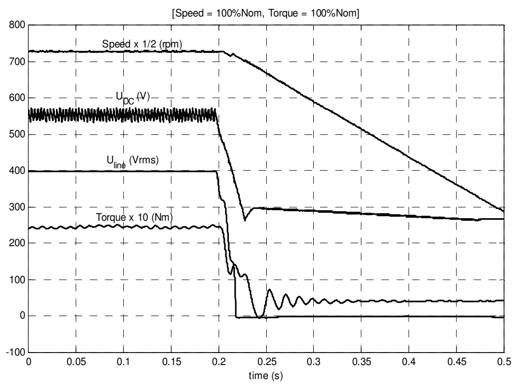

Fig. 6. *Voltage tolerance measurement (4kW ;T_{rated} ; n_{rated})*

The transition in slew rate of the DC-link voltage marks the drive tripping point.

To represent the behaviour of drives under dip conditions, voltage tolerance curves are used. A voltage tolerance curve divides the dip magnitude - duration plane in a ride-through (pass) and a trip (fail) area. The only standard that currently describes how to measure the voltage tolerance of three-phase equipment is IEC 61000-4-11. However, this standard does not mention anything about voltage tolerance curves. Only some discrete dips (depth and duration) should be measured to define the voltage tolerance. Using these predefined measurements, the voltage tolerance curve cannot be constructed as not all measurements are pass-fail transition points. On the test set-up, the depth and duration of voltage dips were continuously changed in order to define the limits of ride-through (voltage tolerance).

Fig. 7 compares the simulated and measured voltage tolerance curve for a 4kW ASD at full load (T = 25Nm). If the remaining voltage during the dip is below the undervoltage limit of the ASD, the drive will always trip. The rectifier stops conducting and all energy has to be taken from the capacitors. As seen from Fig. 7, the drive trips after 17 ms.

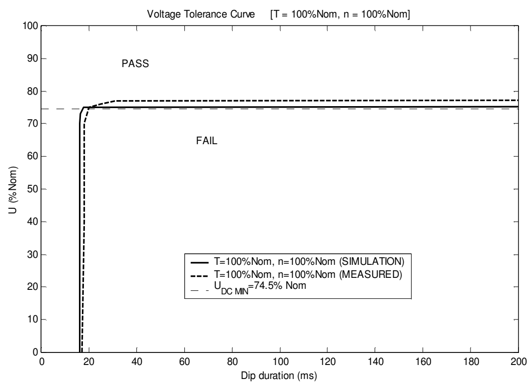

Fig. 7. *Voltage tolerance curve (4kW ;T_{rated} ; n_{rated})*

By reducing the depth of the dip, one can find a supply line voltage for which the drive does no longer trip. Depending on the torque and speed conditions of the machine, this value differs from the undervoltage treshold level due to the ripple on the DC-bus voltage. Fig. 8 represents the influence of the motor load on the voltage tolerance curve.

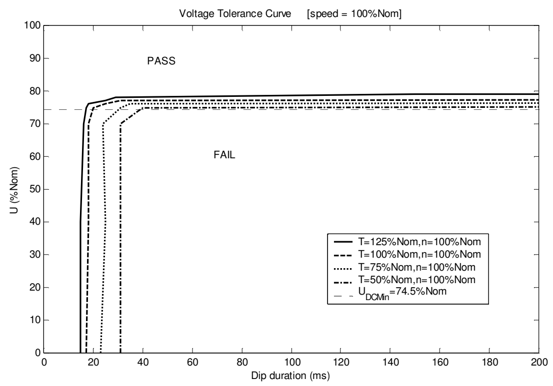

Fig. 8. *Influence of motor load on voltage tolerance curve (measurement)*

Considering a constant torque and reducing the speed of the machine results in a decreasing power demand. The ripple on the DC-bus voltage thus becomes smaller. Fig. 9 shows that the operation at reduced speed improves the immunity against voltage dips.

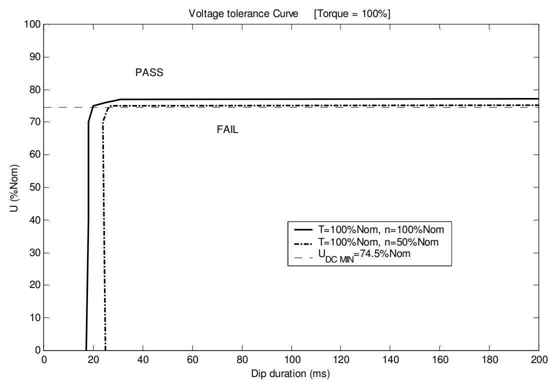

Fig. 9. *Influence of motor speed on voltage tolerance curve (measurement)*

The point on wave at which the voltage dip occurs, also has an influence on the possible ride-through time. Fig. 10 shows the influence of the dip start-time for a three-phase balanced dip. For the same dip-duration, the dash-dotted voltage curve trips and the solid curve survives, due to a higher energy level in the DC-link at dip-initiation.

Up to now, only balanced dips have been discussed. In practice, however, unbalanced dips occur more frequently. Single-phase-to-ground (SPTG) faults do not strongly affect the behaviour of an ASD (Fig. 11). The three-phase rectifier acts as a single-phase rectifier. In this case the DC-link can recharge every 10 ms from the two remaining supply lines. Fig. 5 shows a simulation of the DC-link with a SLTG fault (40ms) in the power supply. At full motor load (4 kW), the DC-link voltage never reaches the undervoltage protection level (U_{DCmin}=74.5%). For a two-phase-to-ground (TPTG) fault, the remaining line voltage at the rectifier equals the system phase voltage. The maximum available DC-link voltage is:

$$U = \frac{U_0}{\sqrt{3}} \tag{3}$$

If the undervoltage limit cannot be reduced under this voltage level, the behaviour can be compared to a balanced voltage dip. Fig. 11 shows a simulation of a SPTG fault versus a TPTG fault.

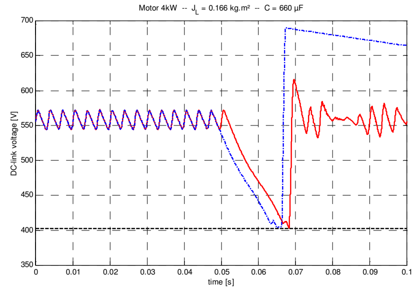

Fig. 10. *Influence of the voltage dip-initiation time (simulation)*

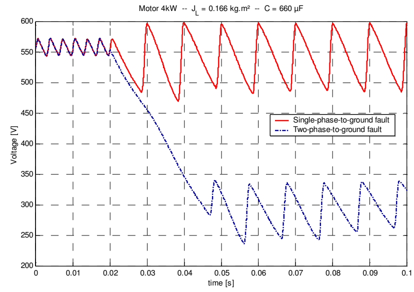

Fig. 11. *SPTG versus TPTG fault (full load) (simulation)*

CONCLUSIONS

This paper introduces a test setup to obtain voltage tolerance curves for ASD under different load conditions. Furthermore, the measurement results are verified with the simulation model. Standard ASD are very sensitive to voltage dips. The main restriction is the DC-link undervoltage protection level, defined by the manufacturer. It can be seen from Fig. 2 that increasing the capacitor value is not a very effective way to improve the ride-through time.

Further research and measurements will concentrate on the improvement of the immunity of the ASD. New tolerance curves for ASD with kinetic buffering, boost modules and other ride-through equipment will help the design engineer to choose the correct mitigation equipment to reach the desired level of ride-through.

ACKNOWLEDGEMENT

The authors wish to thank the Flemish Government for granting the project 'Invloed van spanningsdips bij snelheidsgeregelde aandrijvingen' (IWT-HOBU).

REFERENCES

[1] Math H.J. Bollen, *"Understanding Power Quality Problems, Voltage Sags and Interruptions"*, IEEE Press Series on Power Engineering, 2000.

[2] M.F. McGranaghan, D.R. Mueller, M.J. Samotuj, *"Voltage Sags in Industrial Systems"*, IEEE Transactions on Industry Applications, Vol 29, No.2, March/April 1993, pp. 397-403.

[3] “Voltage dips, short interruptions and voltage variations immunity tests”, IEC Std. 61000-4-11.

A NEW DISTRIBUTED CONTROL ARCHITECTURE FOR FUTURE POWER ELECTRONICS SYSTEMS

Ivan Celanovic[1], Nikola Celanovic[2] and Dushan Boroyevich[3]
[1]Laboratory for Electronic and Electromagnetic Systems, The Massachusetts Institute of Technology 77 Massachusetts Avenue, Cambridge, MA 02139, ivanc@mit.edu
[2]Power Electronics Systems, ABB Corporate Research Ltd, CH-5405 Baden-Dattwil, Switzerland
[3]Center for Power Electronics Systems, Virginia Polytechnic Institute and State University, Blacksburg, VA 24061-0111, USA

Abstract: *This paper proposes a novel open-architecture approach to the design of digital controller hardware for power electronics systems. The paper discusses the benefits of such an approach and compares it to the more conventional centralized controller approach. Prototypes of the three key open-architecture functional blocks: high-speed serial communication link, hardware manager and application manager were built in order to test their performance on a representative three-phase 100 kVA converter. Experimental results verify the feasibility of the proposed approach.*
Key Words: ***Power electronics building blocks Distributed controller, Fiber optic network, Three-phase voltage source inverter***

1. INTRODUCTION

Control of today's medium and high-power converters is, in most cases, based on a centralized digital controller, as explained in [1]. This approach has several drawbacks with perhaps the biggest one being the large number of point-to-point signal links that connect power stage and sensors on one side with the centralized controller on the other. Furthermore, the signals in typical power electronics systems come in variety of different formats and are transmitted through a variety of physical media. This makes the standardization and modularization of power electronics systems and subsystems very difficult, if not impossible.

In this paper we approach the issue of standardization in power electronics by standardizing the signal distribution network, which allows for open architecture distributed controller approach. The standardization of communication interface allows partitioning of power electronics system into flexible, easy-to-use, multifunctional modules or building blocks, which should significantly ease the task of system integration [2-4], [6-8].

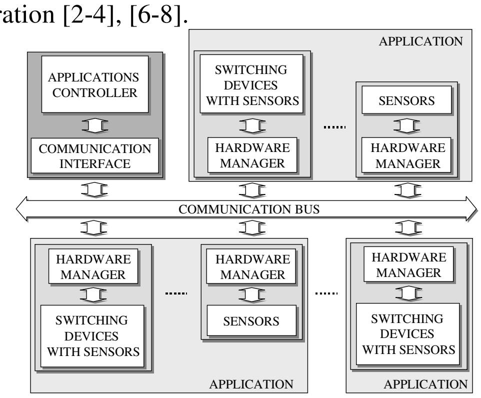

Fig. 1. *Partitioning of power electronics system based on open-architecture distributed control approach.*

Fig. 1 shows the functional diagram of an open architecture distributed controller approach suitable for application in power electronics systems.

The concept of a distributed controller is widely accepted in motion control and factory automation systems [9]. More along the lines of distributed control at the converter level was reported by Malapelle et al. [7] who proposed a distributed digital controller for high-power drives. They partitioned the system controller into a regulator and a bridge controller, which were connected via a relatively slow parallel bus. Toit et al. [6] have proposed a control structure where phase-leg controllers are connected to a higher-level controller through a (2.5 Mbits/sec) daisy-chained fiber optic link. In their structure the current control is implemented locally in a phase-leg controller, while the voltage control is implemented in a higher-level controller.

This paper proposes a real-time, digital control network suitable for medium- and high-power converters where the network communication protocol is designed to support modular and open-system design approach in power electronics.

Decentralizing and distributing the controller requires new building blocks. Therefore we have proposed the new architectural blocks named applications manager and hardware manager.

The application manager is higher level controller liberated from any hardware-oriented tasks. It is universal and totally converter independent architectural block that can be configured to control any type of power electronics hardware. At the same time, hardware manager is designed as an integral part of either switching or sensing hardware and it handles all the hardware specific tasks. Hardware manager makes power stage transparent for the application controller and masks all the hardware peculiarities (such as soft-switching, dead time etc.)

This concept of distributed "intelligence" allows for plug and play design of power electronics modules. Indeed the partition of power electronics into proposed architectural blocks, will allow the development of a layered control software structure, with the hardware device drivers, libraries of standard control functions, and eventually with compilers from higher-level control design and simulation tools.

2. COMMUNICATION PROTOCOL

Each power electronics system is an inherent noise generator, and distributed controller must be able to work in such a harsh and noisy environment. Considering these requirements, and in order to eliminate the large number of point to point links between the controller and the power stage; the serial fiber optic ring network, like the one shown in Fig. 2 is chosen. The bit rate that this network needs to have can be found as a multiple of hardware managers in the network, number of bits per communicated word (including the control overhead bits) and converter switching frequency. Therefore, for a system with four nodes in the network, with ten twelve bit long words that need to be exchanged in every switching cycle and a fifty kilohertz switching frequency a channel capacity of about 36 Mbit/s is required. Furthermore, as shown in [5] the synchronization error between nodes should not exceed 0.1-0.2% of the switching frequency in order to eliminate low-frequency harmonics due to the synchronization jitter.

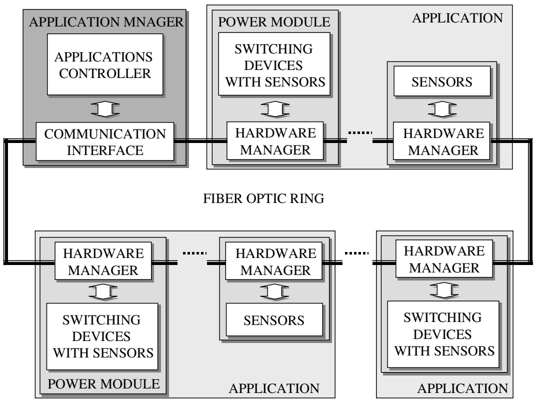

Fig. 2. *Daisy-chained fiber optic control network for distributed control of power converters.*

The communication network in this paper is designed as a master-slave ring network that runs over plastic 125 Mbit/s optic fiber. In this type of network topology, application manager is a master node controlling the communications where all the hardware managers are operating in the slave mode.

2.1. Communication Protocol Functional Description

Master-slave protocol that is implemented insures deterministic response of the network. If the error occurs during transmission, corrupt data is not used. Instead the new data simply overwrites the previous data. This way the data flow is kept strictly predetermined.

Shown in Fig. 3 are two basic types of information communicated through the control network: time-critical data (exchanged in every switching cycle) and time non-critical data transmitted only after all the critical time variables have been passed to all nodes. Time-critical information include

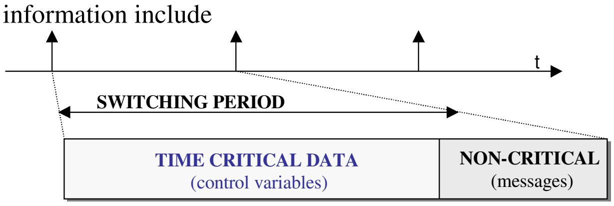

Fig. 3. *Time allocation on the communications bus.*

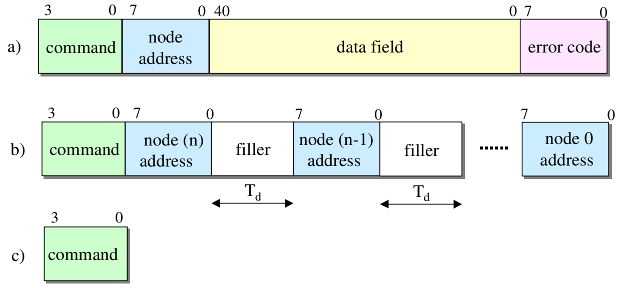

Fig. 4. *Data formats in distributed controller network data frame b) synchronization frame c) command frame*

all the control variables such as: switching frequency information, duty cycle information and all the sensor information. Provision for non-critical data transfer is designed to support tasks such as initialization and software reconfiguration of the hardware managers. Non-critical data transfer is allowed only after all the time critical data is exchanged. Fig. 4 shows three types of time critical data frames: control data frame, synchronization frame and command frame.

The data frame consists of command indicating the beginning of the data packet, address of the node, data field and error check. The way data field is configured depends on the particular application and type of the hardware manager.

In a ring type of network, each node introduces a delay in data propagation path. Meaning that if we send synchronization command through the network, each node is going to receive the command with as many time delay T_d, as there are nodes between that node and the master node. The time delay, T_d, in the hardware test-bed implemented is typically around 460 ns. This means that the error in synchronization will generate time shifted PWM signals at the outputs, causing low frequency harmonics. This problem is solved with the synchronization sequence.

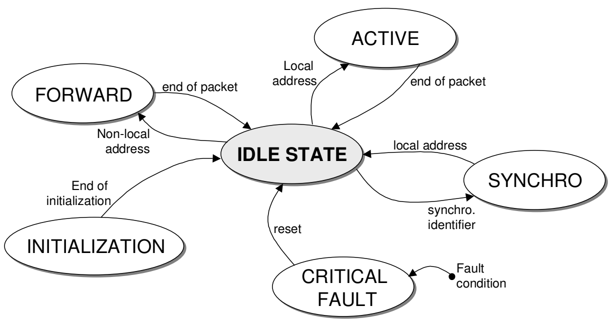

Fig. 6. *State transition diagram for communication controller.*

Format of the synchronization frame is shown in Fig. 4(b). The Frame starts with Synchronization command, and is followed by 8 bit long data blocks containing addresses of slave nodes and 'filler' fields, which are T_d long and are used for propagation delay compensation. The first address to be transmitted is of the slave node that is last to receive the frame. The number of address data blocks sent equals the number of slave nodes on the ring, which we want to synchronize. The first field is a synchronization command that alerts the nodes to wait for their time to synchronize. Next are the address fields of the nodes being synchronized. After the synchronization command is passed, the node awaits its address field. When the address is received, the node generates the synchronization signal. Because all the addresses are in reverse order and time delayed for the node propagation delay all the addresses will arrive at the destination nodes at almost the same time. Using this type of synchronization scheme in proposed 125 Mb/s fiber optical link synchronization error is reduced bellow 80 ns.

3. HARDWARE MANAGER DESIGN

Hardware manager in power electronics distributed network is designed to provide control and communication functions for the module it is associated with. It is designed to support all module specific control tasks thus making the module specific functions, such as for example soft switching, invisible to the applications manager. In the following sections two types of hardware managers will be discussed: a hardware manager for the power switching device, and a hardware manager for the current or voltage sensor.

3.1. Hardware Manager for Soft-Switched-Phase-Leg

The hardware manager shown in Fig. 5 is designed to control soft-switched phase leg. The following are the functions of this type of hardware manager:

- PWM generation for main and auxiliary switches;
- isolated gate drive for both main and auxiliary switches;
- over-current protection and indication;
- current, voltage and temperature sensing with A/D conversion; and
- communication of PWM, status and measurement information.

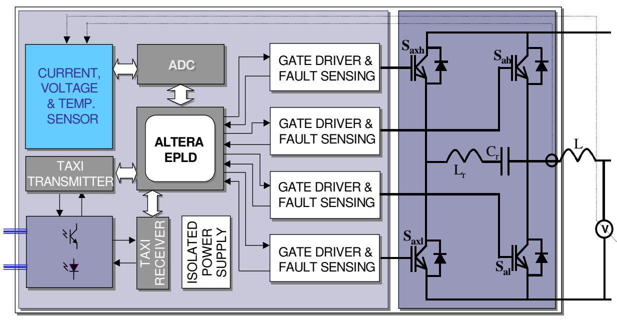

Fig. 5. *Block diagram of designed hardware manager controlling soft-switched phase leg.*

The only information the hardware manager communicates is a standardized serial data packet. All the necessary data for proper module operation are encoded in the data field of control data packet that was previously explained.

The hardware manager, shown in Fig. 5, consists of gate drives, a high speed ALTERA 10K PLD, two A/D converters, a high-speed ECL logic data transmitter and receiver, and a 125 Mbits/sec optical transceiver.

The communication interface within the hardware manager is built in three layers (according to ISO/OSI reduced reference model) defined as: physical layer, data link layer and application layer.

Physical layer is provided by means of an inexpensive plastic optic fiber, while interface between data link layer and physical layer is achieved using Hewlett Packard optical transceiver.

Data link layer is provided by TAXIchip™, (transmitter and receiver) [10]. An incoming optical signal is fed to the transceiver and then to the TAXIchip™ [10] receiver. The receiver converts the serial stream into parallel, which is then loaded into the PLD for final data processing. Similarly, outgoing data from the PLD (in parallel form) are converted by the TAXIchip™ transmitter into a serial stream, amplified by the optical transceiver [11] and transmitted through the optical fiber.

The communication and control block, which is implemented in hardware (PLD), handles all application layer functions. The communication and control subsystem can be viewed as a state machine, shown in Fig. 6, receiving commands through the network and changing states and outputs accordingly. Its basic states are described as:

- idle mode (waiting for the data packet to arrive),
- forward mode (passing the information to the subsequent node),
- active mode (incoming data packet has the address of the node): when the data is being first verified by CRC checker and then stored in corresponding buffers and the packet is then forwarded with the results of current/voltage/temperature measurements and local status information,
- synchronization mode (after receiving SYNC command from application manager): which reloads the double buffers, initiates A/D conversion and resets PWM generator and
- initialization mode: which initializes the whole system and dynamically assigns the node address.

PWM generator and local fault protection are also realized in the PLD. Three main parameters necessary for proper operation of PWM generator are: duty cycle, switching period and the synchronization command. The duty cycle data, when received and validated for proper transmission, are stored in the input buffer. The duty cycle becomes active only after it receives synchronization command from the application manager, which moves the duty cycle information to executable buffer used for PWM generation. Period information (which controls switching frequency of the leg) is also double-buffered for the sake of proper synchronization.

A digital comparator compares the content of the counter with duty cycle creating a control pulse for the switch. The dead time generator and fault protection are the final stages in PWM generation, providing shoot-through and over current/voltage/temperature protection.

Fig. 7. *Prototype of phase leg module integrated with hardware manager.*

Most of today's control systems in power electronics are based on full-state feedback, which requires per-switching cycle current and voltage measurement. Therefore, the designed hardware manager consists of current, voltage and temperature sensors. Measurement of module voltage and current is performed simultaneously per switching cycle using two 12-bits AD converters, while temperature measurement is performed with 10 times slower rate. Proper timing is achieved also through synchronization command received from application manager. Measurement results are stored in the output buffer, ready to be packed into a corresponding data packet and sent to applications manager.

3.2. Hardware Manger for Distributed Sensor

Although the hardware manager has built-in current, voltage and temperature sensors for some applications, additional system sensors such as position, velocity etc. are needed to provide feedback to the application controller. To overcome this limitation a new architectural block smart sensor is introduced. It is designed to follow the same communication protocol, has a built in A/D converter and sensor and same communication interface as smart module. Fig. 8 shows the functional diagram and the hardware prototype of the smart sensor. The instants of A/D conversion are synchronized with the rest of the network using the already explained synchronization frame.

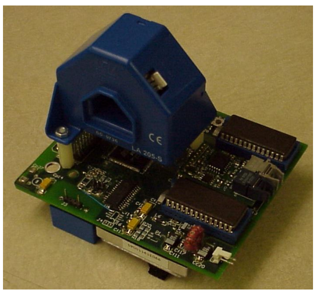

Fig. 8. *Prototype of the distributed current sensor.*

4. APPLICATIONS MANAGER

The application manager, is a high-level controller liberated from low-level hardware oriented tasks. It is designed to provide the system with flexibility and software reconfigurability.

The prototype application manager (Fig. 9) is built around Analog Devices 21062 SHARC floating point DSP processor, with an onboard ALTERA 10K PLD and fiber-optic communication interface that provides open control architecture capable of controlling multiple independent modules. This allows the applications manager hardware architecture to be independent of the converter topology, number of switches, sensors, etc. and allows system reconfiguration through software only.

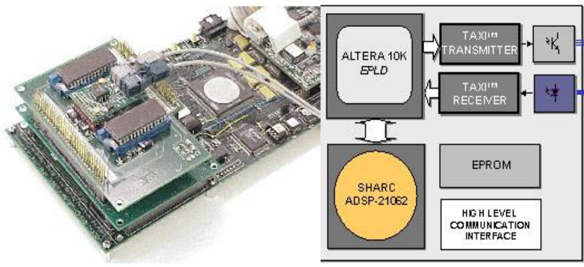

Fig. 9. *Block diagram and application manager prototype.*

5. EXPERIMENTAL RESULTS

To verify the idea of a distributed controller, a three-phase voltage source inverter (VSI) driving a simple R-L load was designed as shown in Fig. 10. Prototype of the converter consists of three smart hardware managers controlling soft-switched phase leg modules, connected via fiber optic communication link, while the application manager performs control tasks related to controlling the output currents of the inverter in closed-loop manner.

Each phase leg is designed using 1200 V, 300 A IGBT phase-leg modules as main switches. Fig 12 shows output current waveforms of the three-phase VSI with the closed current loops in DQ reference frame.

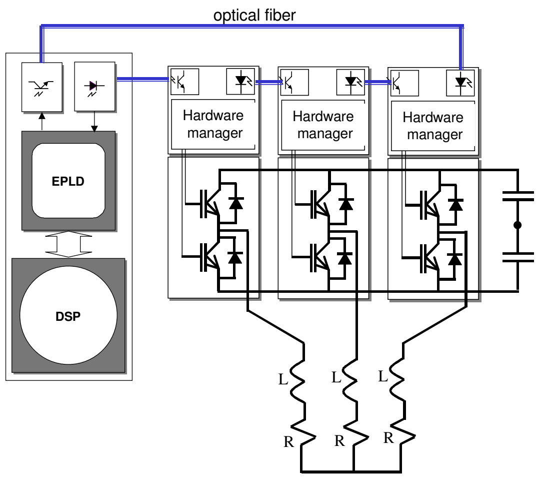

Fig. 10. *Block diagram of three-phase VSI built using distributed control approach.*

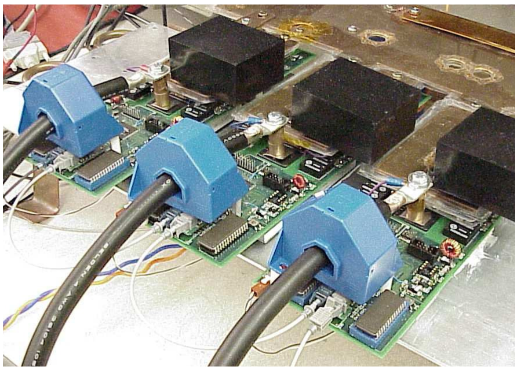

Fig.11. *Prototype three-phase VSI built using smart modules and distributed controller approach.*

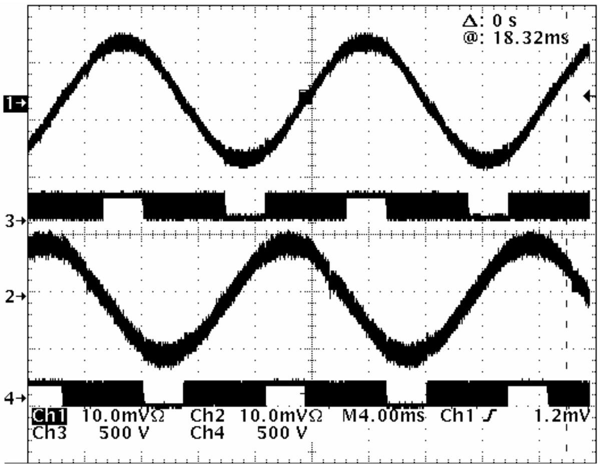

Fig. 12. *Output phase currents (50 A/div) and output phase voltages (500 V/div) PWM waveforms.*

5. CONCLUSION

This paper presented a novel approach to power electronics system design based on the open architecture distributed digital controller and modular power electronics building blocks. The most important features of the new concept are:

- Open and flexible communication protocol for distributed control of power electronics systems;
- Flexible, and easy to use power converter modules;
- Hardware independent, applications manager capable of controlling several different types of converters in parallel, and
- Simple system integration and re-configuration.

We believe that distributed digital controller environment together with open-system communication protocol provides solid ground for object oriented software design in power electronics. This will also enable easier integration of higher-level graphically oriented design and simulation tools with power electronics hardware.

Finally, we anticipate that both hardware and software standardization and modularization will lead to user friendly, plug and play, system oriented design in power electronics as opposed to today's predominantly circuit oriented, custom design practice.

6. REFERENCES

[1] V. Vlatkovic, and D. Borojevic, *"Digital-Signal-Processor-Based Control of Three-Phase Space Vector Modulated Converters,"* IEEE Transactions on Industrial Electronics, June 1994, Vol. 41, No. 3, pp. 326-332.

[2] T. Ericsen, A. Tucker, *"Power Electronics Building Blocks and Potential Power Modulator Applications,"* IEEE Conference Record of the Twenty-Third International Power Modulator Symposium, New York, NY, 1998, pp. 12-15.

[3] Van Wyk, F.C. Lee, *"Power Electronics Technology at the Dawn the New Millennium-Status and Future",* IEEE PESC Conference Proceedings, 1999.

[4] I. Celanovic, I. Milosavljevic, D. Boroyevich, G. Jinhong, R. Cooley, *"A New Distributed Controller for the Next Generation Power Electronics Building Blocks,"* 15th Annual IEEE Applied Power Electronics Conference Proceedings, February 2000, pp. 889-894.

[5] I. Milosavljevic, Z. Ye, D. Borojevic, C. Holton, *"Analysis of Converter Operation with a Phase-Leg in Daisy–Chained or Ring Type Structure",* IEEE PESC Conference Proceedings, June 1999.

[6] J.A. Du Toit, A.D. Le Roux, J.H.R. Enslin, *"An Integrated Controller Module for Distributed Control of Power Electronics,"* IEEE APEC'98 Proceedings, February 1998, pp. 874-880.

[7] P.L.G. Malapelle, G. Torri, R. Moruzzi, A. Oliva, *"A New, Modular, Programmable, High Speed Digital Control for Large Drives",* IEEE IECON 20th International Conference on Industrial Electronics, Control and Instrumentation, 1994; vol.1, pp. p.210-14.

[8] I. Milosavljevic, D., Borojevic., I. Celanovic, *"Modularized Communication and Control Structure for Power Converters",* 8th European Conference on Power Electronics and Applications, EPE, September 1999.

[9] E. Bassi, F. Benzi, L. Lusetti, G.S. Buja, *"Communication Protocols for Electrical Drives",* IEEE IECON Proceedings, 1995, Vol. 2, pp.706-711.

[10] *"TAXIchip™ Integrated Circuits"*, Data Sheet and Technical Manual, Publication#07370, AMD, April 1994.

[11] "Plastic Optical Fiber and HCS® Fiber Cable and Connectors for Versatile Link", Technical Data 5963-3711E, Hewlett Packard, November 1994.

OPTIMUM CONTROL OF CLASS E INVERTER WITH VARIABLE LOAD

Zbigniew Kaczmarczyk, Boguslaw Grzesik*
Silesian University of Technology, Faculty of Electrical Engineering, Gliwice, Poland,
kaczm@polsl.gliwice.pl, *grzesik@polsl.gliwice.pl

Abstract: *An idea of construction and basic features of the optimal control of Class E inverter that has the load of variable parameters (R, L) have been described in the paper. Such a solution has not been reported in the literature of the subject until now. In spite of the variable parameters of the load the proposed solution guarantees maximum soft switching of the transistor (on: ZVS+ZCS and off: ZVS+NZCS). The solution is based on frequency and duty ratio control. The paper contains the results of simulation (SPICE) and experiment. They were carried out for the load of variable parameters (R and L) according to which switching frequency and duty ratio were adjusted to ensure maximum soft switching. The measurements confirmed theoretical predictions.*

Key Words: ***Class E inverter, Soft switching, High frequency, MOSFET***

INTRODUCTION

The advantages of Class E inverter are commonly known - [1], [4]. The inverter is usually used in the case its load is not variable where maximum soft switching is ensured (on: ZVS+ZCS, off: ZVS+NZCS). The frequency in such typical circumstances is kept constant with duty ratio 0.5. The attempt of using this type of inverter, in the system where the load changes its parameters, shows some difficulties. It results in lower voltage/current capability of the transistor or even in its failure. To find the suitable solution using Class E inverter, which is the one not sensitive to the changes of the load parameters, was the challenge for the authors.

There are only a few articles in the literature concerning Class E inverters where the load has variable parameters. Three papers, [2], [3], [5], are representative. In the first one [1] the inverter with switched capacitors, switched inductors and frequency adjustment is presented. The main drawbacks of this solution are its high complexity and necessity of application of switches for changing the value of capacitances and inductance. The second work [3] reports on the inverter in which matching inductance is used. It ensures proper operation with variable load. In the paper [5] the control is based on *PLL* system, which changes switching frequency due to the variation of load parameters. In all these papers the inverters realise suboptimum mode of operation (parallel diode is conducting).

2. OPERATION MODES OF CLASS E INVERTER

The schematic diagram of Class E inverter is given in Fig. 5. The switch S in the inverter consists of transistor T and parallel diode D. It is possible to distinguish three operation modes of the inverter. They are: optimum mode - Fig. 6.a, suboptimum mode - Fig. 2.a and non-optimum mode - Fig. 2.b. The maximum soft switching takes place in optimum mode. The suboptimum mode is characterised by conduction of parallel diode that results in reduction of efficiency and occurrence of parasitic oscillations of higher frequency. Non-optimum mode means short-circuiting of charged capacitor connected in parallel with transistor.

In general, a given mode of operation is the result of chosen capacitances C_1, C_2, actual current parameters of the load R, L and control that is characterised by switching frequency f and duty ratio D.

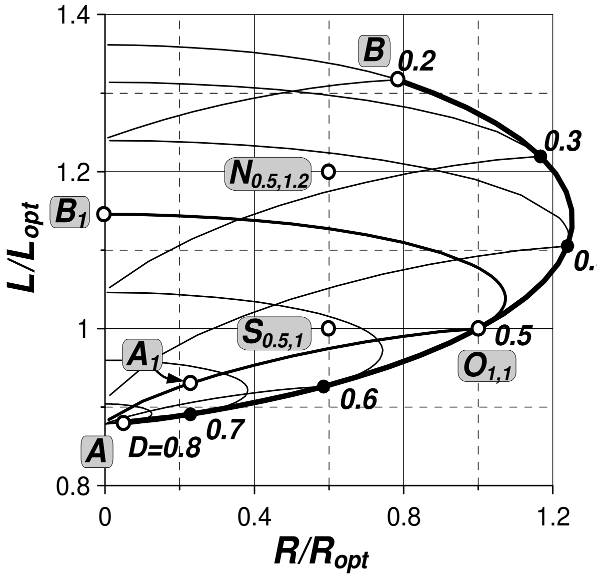

Fig. 1. *Operation modes of Class E inverter - geometrical interpretation on plane of load parameters (R/R_{opt}, L/L_{opt}) at $Q_{opt}=10$, $f/f_{opt}=1$, $D_{opt}=0.5$*

Assuming particular value of quality factor Q_{opt} ($Q_{opt}=(2\pi f_{opt}L_{opt}/R_{opt})$), e.g. $Q_{opt}=10$, and constant capacitances C_{1opt}, C_{2opt} such that for f_{opt}, $D_{opt}=0.5$, L_{opt}, R_{opt} the inverter operates in optimum mode, the different operation modes can be interpreted as a function of load parameters R, L using the plot in Fig. 1. For constant switching frequency $f/f_{opt}=1$ and duty ratio $D_{opt}=0.5$ (defined as turn-on time divided by one period of the switching cycle) the mode of operation is determined by the curve A_1-$O_{1,1}$-B_1. Point $O_{1,1}$ corresponds with optimum mode - Fig. 6.a. For parameters of the load (R/R_{opt}, L/L_{opt}) that lays outside the area bounded by curve A_1-$O_{1,1}$-B_1, e.g. $N_{0.5,1.2}$, the inverter operates in non-optimum mode, c.f. Fig. 2.b. For load parameters that are inside the area bounded by curve A_1-$O_{1,1}$-B_1, for example $S_{0.5,1}$, the inverter operates in suboptimum mode, compare Fig. 2.a.

Analysis of Fig. 1 results in observation that the mode of operation for the load parameters given by point $N_{0.5,1.2}$ can be non-optimum or suboptimum that for constant frequency depends on duty ratio D. For instance, for D=0.5 the inverter operates in non-optimum mode while for D=0.4 or 0.3 in suboptimum mode.

Taking any point of curve A-$O_{1,1}$-B one ensures optimum mode of operation for constant frequency f/f_{opt}=1 and constant capacitances C_1=C_{1opt}, C_2=C_{2opt} by choosing relevant duty ratio D from the range 0.2÷0.8.

The method of calculation of these characteristics is described in work [4] in details.

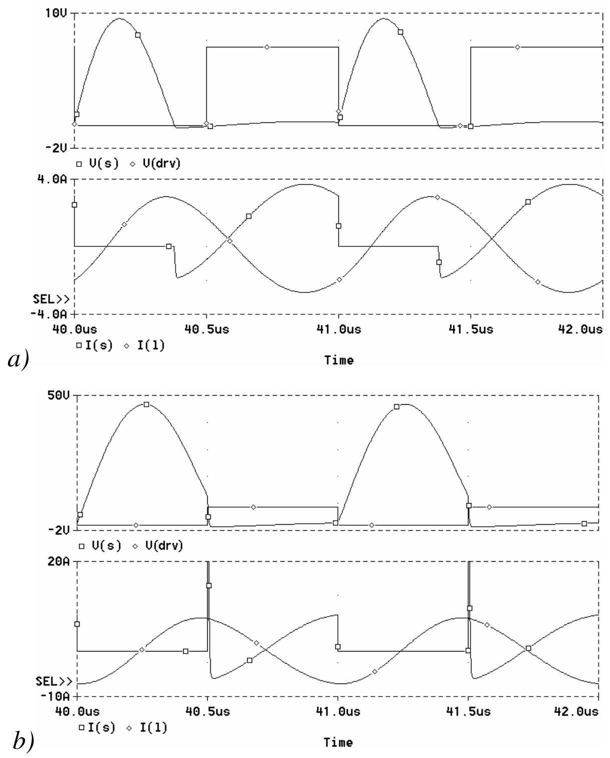

Fig. 2. *Simulation results (SPICE) for R/R_{opt}=0.5, L/L_{op}= =1 - $S_{0.5,1}$ (suboptimum mode) - a; simulation results for R/R_{opt}=1.2 - $N_{0.5,1.2}$ (non-optimum mode) - b*

3. OPTIMUM CONTROL

In order to design the Class E inverter that would operate in optimum mode when the load changes its parameters (R, L) the characterisations like that in Fig. 3 and 4 are needed. The global characterisation from Fig. 3 indicates optimum mode of operation in 3-dimensional space of (R/R_{opt}, L/L_{opt}, f/f_{opt}). The optimum mode takes place when parameters are given by this surface. The surface in this figure is calculated for the following parameters: optimum Q-factor Q_{opt}=10 and optimum capacitances of C_{1opt}, C_{2opt}. Values of C_{1opt}, C_{2opt} can be calculated from R_{opt}, L_{opt}, f_{opt} and D_{opt}=0.5. The value of duty ratio D relates to control of the transistor and results from the demand of maximum soft switching (optimum mode) for given R/R_{opt}, L/L_{opt}, f/f_{opt}.

The Fig. 4 presents cross-sections (solid curves) of surface from Fig. 3 for constant frequency f/f_{opt}=const. Curve A-$O_{1,1}$-B (it is also depicted in Fig. 1) is related to the frequency f/f_{opt}=1. The dot-and-dash lines are calculated for constant value of duty ratio D=0.4, 0.6.

Brief analysis of Fig. 3 and 4 reveals that having frequency f and duty ratio D as input control variables it is possible to ensure the optimum mode for certain region of parameter space, which describes permissible variation of parameters R, L. The dot-and-dash line for D=0.4 (Fig. 4) is the global limit of the region. It will be explained in the next section.

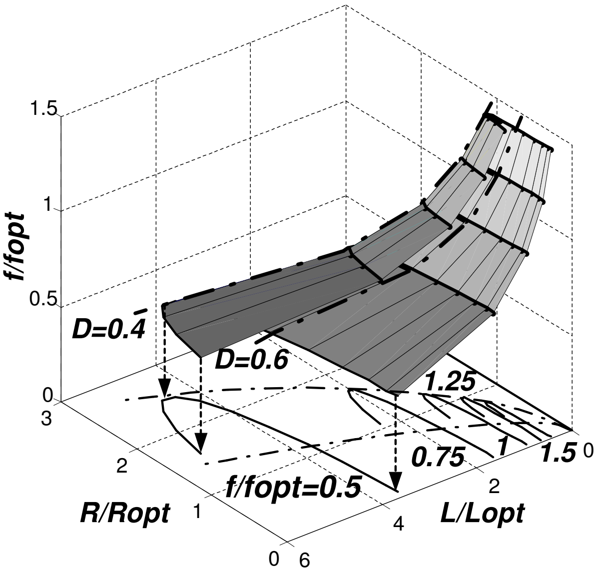

Fig. 3. *Surface of optimum mode in space of relative parameters (R/R_{opt}, L/L_{opt}, f/f_{opt}) of Class E inverter*

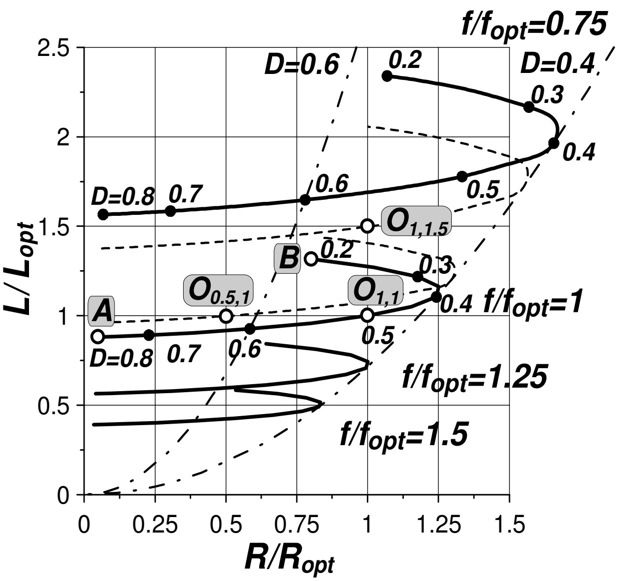

Fig. 4. *Curves of parameters (cross-sections of Fig. 3) ensuring optimum mode of operation for given f and D*

4. REALISATION OF OPTIMUM CONTROL

The idea of optimum control of the Class E inverter in case the load parameters change its values consists in proper variation of frequency f and duty ratio D to ensure optimum mode of operation.

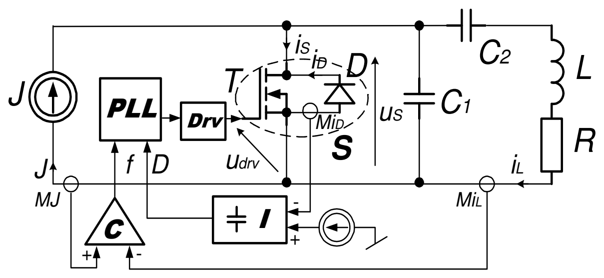

Fig. 5. *Schematic diagram of Class E inverter with indicated control system*

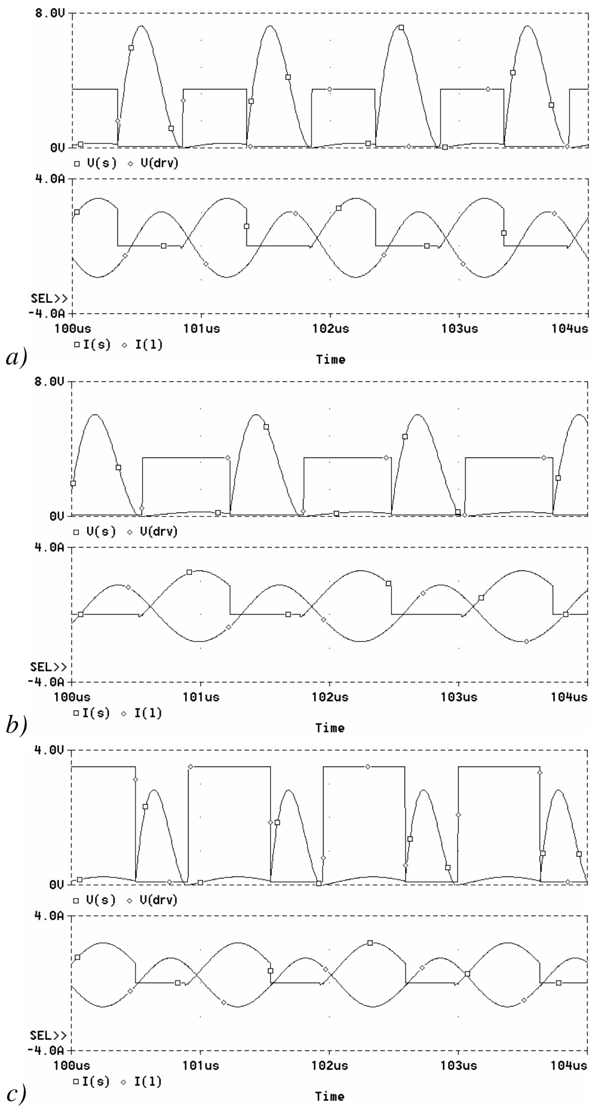

Fig. 6. *Simulation results (SPICE) for $R/R_{opt}=1$, $L/L_{opt}=1$, $f/f_{opt}=1$, $D_{opt}=0.5$ - $O_{1,1}$ - a; for $R/R_{opt}=1$, $L/L_{opt}=1.5$, $f/f_{opt}=0.8$, $D=0.54$ - $O_{1,1.5}$ (L changed) - b; for $R/R_{opt}=0.5$, $L/L_{opt}=1$, $f/f_{opt}=0.96$, $D=0.61$ - $O_{0.5,1}$ (R changed) - c*

This is realised by means of *PLL* control, schematic diagram of which is given in Fig. 5. The proposed optimum control is slightly similar to that which is used in series resonant inverters, and which results in ZCS. Apart from *AC* current i_L, supplying *DC* current J and diode current i_D are used for the control. It comprises seven parts: Mi_L - measurement of *AC* load current i_L, *MJ* - measurement of *DC* supplying current J, Mi_D - measurement of diode current i_D, C - comparator, I - integrator of diode current, *PLL* - phase locked loop and *Drv* - driver of the transistor T. The principle of operation of the control is as follows. The instant when currents J and i_L are equal is recognised as the time the transistor has to be turned-on. It results in ZCS. In order to have switching on at zero voltage (ZVS) the conduction of parallel diode should be eliminated. It is done by the integrating circuit I that forms duty ratio D, which determines the time instant the transistor has to be turned-off. It means, that when parameters R, L change, the control should adjust properly frequency f and duty ratio D. In order to obtain it one have to keep the point of the inverter's parameters on the surface of parameters given in Fig. 3. The movement of the point of parameters on the surface can be observed using its 2-dimensional projection in Fig. 4. The analysis of control starts from optimum mode of operation that corresponds to the point $O_{1,1}$ (R/R_{opt}=1, L/L_{opt}=1, f/f_{opt}=1 and D_{opt}=0.5). In case of constant resistance R/R_{opt}=1 and the change of the inductance to the value L/L_{opt}=1.5 the controls adjusts frequency to f/f_{opt}=0.8 and duty ratio to D=0.54 (dashed curve - point $O_{1,1.5}$). Changing for instance the resistance and keeping the inductance constant (R/R_{opt}=0.5, L/L_{opt}=1) the point of parameters moves to $O_{0.5,1}$, resulting in f/f_{opt}=0.96, D=0.61. The relevant waveforms (SPICE) illustrate the operation of the control strategy in Fig. 6. They were obtained for the following data: J=1A, C_{1opt}=29.8nF, C_{2opt}=18.3nF, L_{opt}=1.59µH, R_{opt}=1Ω (Q_{opt}==10), R_{ON}=0.1Ω, f_{opt}=1MHz, D_{opt}=0.5.

5. EXPERIMENTAL VERIFICATION

To have the theory confirmed not only by simulation the relevant verification of measurements has been carried out. The schematic diagram of the measured inverter is depicted in Fig. 5. The controls allows to set needed switching frequency f and duty ratio D. Two MOSFET transistors of IRF740 (400V, 10A) with its inherent diodes connected in parallel have been used as a switch S. The parameters of the inverter have been synthesised using the method described in [4]. Then the capacitances C_1 and C_2 of the inverter have been changed in order to obtain optimum mode of operation for the experimental inverter operating at frequency f=1MHz with duty ratio of D=0.5 - compare Fig. 7.a.

Table 1. *Parameters of the inverter*

	C_1[nF]	C_2[nF]	L[µH]	R[Ω]	Q	η[%]
measured	4.12	2.45	11.55	7.31	9.93	95.2
calculated	4.21	2.51	11.55	7.31	9.93	95.1

After that change, the capacitances C_1, C_2 and the efficiency η were measured and gathered in Table 1 (capacitance C_1 is the equivalent one that contains output capacitance of the transistors $2C_{OSS}$=0.66nF). Parameters C_1, C_2, L, R were measured using impedance measuring instrument HP4294A at 1MHz. The measured efficiency was 95.2% for supplying the inverter from voltage source of 40.4V with current of 2.42A (input power 97.8W). On-state resistance of the transistors was taken from oscillograms in Fig. 7.b and it is R_{ON}=0.3Ω. Then the design computation of parameters were repeated for resulting quality factor Q_{opt}=9.93, load resistance R_{opt}= 7.31Ω and f_{opt}=1MHz, D_{opt}=0.5, taking into consideration R_{ON} in this case. The results are placed in Table 1.

In order to check the possibility of realisation of proposed controls the following experiment was carried out. The parameters of the load were changed by additional *R, L* circuit that was connected to the optimum one in parallel. After that switching frequency *f* and duty ratio *D* were adjusted to have optimum mode of operation, resulting in *f*=1.18MHz and *D*=0.6. For this frequency the following values of load parameters were measured: *L*=8.05μH, *R*=4Ω. This means a relative change: L/L_{opt} = 8.05/11.55 ≈ 0.7, R/R_{opt} = 4/7.31 ≈ 0.55. Oscillograms for this case are given in Fig. 8 where supplying voltage and current were 25.9V and 4A respectively. That gives input power of 103.6W. The efficiency in this case was 87%. The reduction of the efficiency results from increased current of the transistors, which in turn increases conduction and turn-off losses - c.f. Fig. 7.b and 8.b.

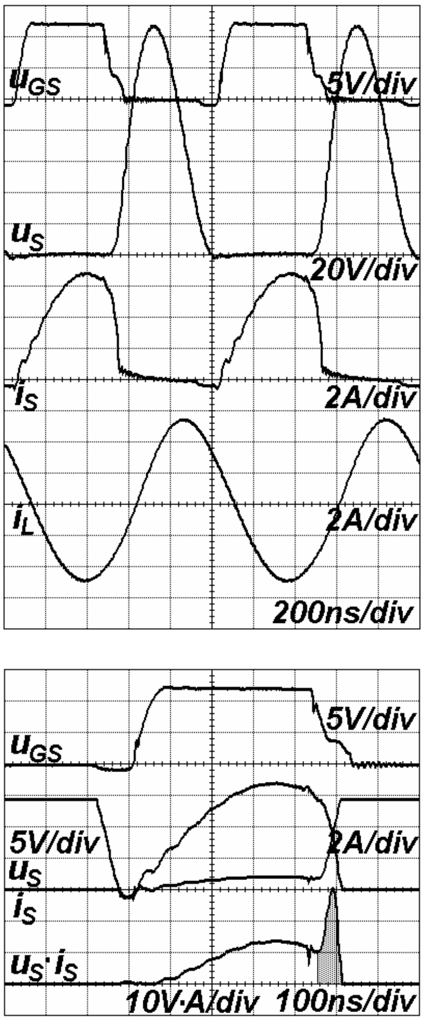

a)

b)

Fig. 7. *Voltage and current waveforms for optimum mode (R/R_{opt}=1, L/L_{opt}=1, f=f_{opt}=1MHz, D_{opt}=0.5) - a; instantaneous losses of power u_S·i_S -b; u_{GS} - gate voltage, u_S - voltage across the switch, i_S - current of the switch*

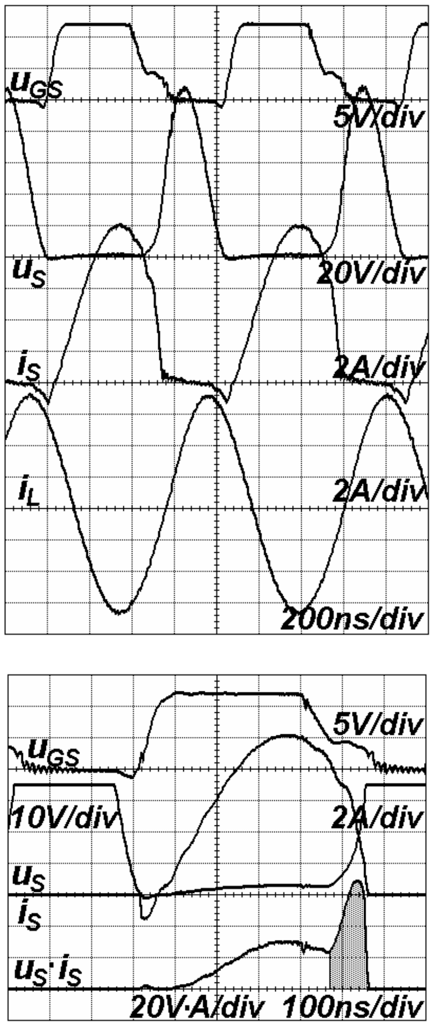

a)

b)

Fig. 8. *Voltage and current waveforms for optimum mode (R/R_{opt}=1, L/L_{opt}=1, f=1.18MHz, D=0.6) - a; instantaneous losses of power u_S·i_S - b*

It is necessary to stress that the results obtained from simulation and calculation are in good agreement with those measured for given change of parameters R/R_{opt}=0.55, L/L_{opt}=0.7. These taken from simulation and calculation are: *f*=1.17MHz, *D*=0.58, η=88%.

6. SELECTED FEATURES OF THE CONTROL

Optimum control of Class E inverter ensures maximum soft switching even if the load changes its parameters. Such switching eliminates turn-on losses and reduces turn-off ones. Additionally it also reduces parasitic oscillations that are caused by output capacitance of the transistor and connection inductances.

Analysis of optimum control with the help of Fig. 3 and 4 leads to the following. 1) The duty ratio *D* is the response mainly for change of load resistance R/R_{opt}. 2) As for the switching frequency *f*, it is essentially the function of load inductance L/L_{opt}. Approximate value of switching frequency can be calculated using formula $f/f_{opt}≈(L/L_{opt})^{-0.5}$.

The other features of Class E inverter operating in optimum mode characterised by its efficiency η and relative output power P/P_{opt} were calculated - Fig. 9, 10. They were obtained for the same parameters as parameters of the laboratory inverter - Table 1. The relative output power was calculated assuming that the inverter is supplied from voltage source of constant value of voltage. The power of P/P_{opt}=1 is obtained for the load parameters R/R_{opt}=1, L/L_{opt}=1 (f/f_{opt}=1, D_{opt}=0.5, C_1/C_{1opt}=const=1, C_2/C_{2opt}=const=1).

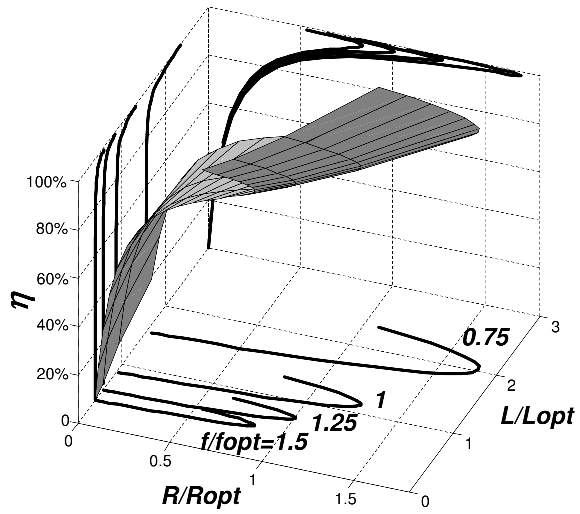

Fig. 9. *Efficiency η of the inverter as a function of parameters R/R_{opt}, L/L_{opt} for optimum control*

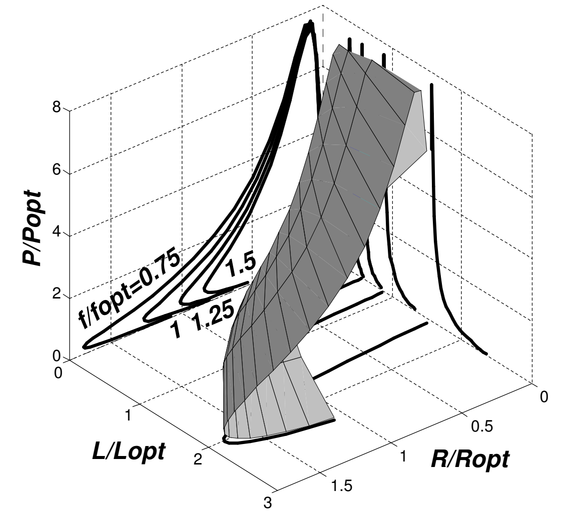

Fig. 10. *Relative output power P/P_{opt} of the inverter as a function of R/R_{opt}, L/L_{opt} for optimum control*

The efficiency of the inverter (Fig. 9) almost entirely depends on the load resistance. It is the result of an increase in transistor current. For R/R_{opt}>0.5 the efficiency of the inverter is approximately higher than 90%. The reduction of the load inductance increases slightly the efficiency.

For supplying the inverter from voltage source the output power is the function of load parameters - Fig. 10. The reduction of load resistance results in an increase of output power P/P_{opt}. This reduction in the range R/R_{opt}=1 to R/R_{opt}=0.5 increases output power approximately by 3. The output power is less dependent on load inductance and a decrease of L/L_{opt} results in a small increase of power P/P_{opt}.

7. CONCLUSIONS

Analysis of proposed control strategy results in the following conclusions:

1. It is possible to realise optimum control of Class E inverter in certain range of load parameters (*R*, *L*). It needs proper adjustment of switching frequency *f* and duty ratio *D*. Such a control strategy has not been reported in literature yet.
2. Laboratory tests confirmed correctness of the proposed control. Future work will be devoted to the construction of the controls of inverter and its laboratory verification.
3. Class E inverter shows particularly advantageous features for load parameters which are kept within the range $0.5 \le R/R_{opt} \le 1$ and $0.5 \le L/L_{opt} \le 1.5$. Wider variability of the parameters leads to a considerable reduction of the efficiency and higher variability of output power of the inverter.
4. Proposed control strategy can be enhanced by means of switched capacitances C_1, C_2 and/or application of passive matching circuits.
5. The same control strategy can be applied to Class E frequency multipliers and to Class DE inverters.

8. REFERENCES

[1] Sokal N. O., Sokal A. D., *"Class E - a new class of high-efficiency tuned single-ended switching power amplifiers"*, IEEE J. Solid-State Circuits, vol. SC-10, no. 3, June 1975, pp. 168-176.

[2] Hinchliffe S., Hobson L., Collins D., *"Optimised Class-E amplifier with load variation"*, Electronics Letters, vol. 23, no. 18, August 1987, pp. 973-974.

[3] Kazimierczuk M., Bui X. T., *"Class E amplifier with an inductive impedance inverter"*,IEEE Transactions on Industrial Electronics, vol. 37, no. 2, April 1990, pp. 160-166.

[4] Kaczmarczyk Z. *"An analysis high frequency power electronics Class E inverter"*, Ph.D. Thesis, Silesian Technical University, Gliwice 1996. (in Polish)

[5] Grzesik B., Kaczmarczyk Z., Kasprzak M., *"Control of Class E Inverter with Variable Parameters of the Load"*, 20th International Conference, Power Conversion Intelligent Motion, PCIM'99, Nuremberg (Germany) 22-24.06.1999, pp. 193-198.

DSP CONTROL OF SYNCHRONOUS MACHINE WITHOUT POSITION AND SPEED SENSORS

Radu Giuclea, Liviu Kreindler, Aurelian Sarca
Polytechnica University of Bucharest – Romania
Department of Electrical Engineering, 313 Spl. Independentei, Bucharest – Romania
Luciano Antognini, Virtual Research, Neuchatel – Switzerland

Abstract: *The paper presents and compares two methods for estimating speed and position in AC motors vector control applications illustrating them for the case of permanent magnet synchronous motors (PMSM).*
One method implies two observer blocks — one for the speed, and the other for the electrical position, using the voltage equations in the (d,q) reference frames. The other method estimates the same variables starting from the calculation of instantaneous reactive power. The tests have proved excellent behaviour in steady state (method 1) as well as in transient state (method 2). The implementation has been made on the 16 bits fixed-point DSP controller.

1. INTRODUCTION

AC motors vector control schemes require the knowledge of the rotor flux position at each sampling. Based on this position and on the torque demand, the control system can compute the required current distribution in the stator phases in order to obtain maximum efficiency from the motor.

Various sensorless solutions have been proposed as the number of applications requiring such approach constantly increases. In the followings, the authors present and compare two sensorless methods that were implemented for PMSM motors.

2. SPEED AND POSITION OBSERVED DIRECTLY FROM THE VOLTAGE EQUATIONS

This method is based on two observer blocks: one for the speed, and the other for the position of the rotor flux.

The principle used in both cases is that of a reference model applied to the voltage equations in the (d,q) reference frame (Equation 1).

$$\begin{aligned} v_q &= Ri_q + L\frac{di_q}{dt} + Li_d\omega + \varphi_0\omega \\ v_d &= Ri_d + L\frac{di_d}{dt} - \omega L i_q \end{aligned} \tag{1}$$

where R and L are equivalent-phase resistance and inductance; i_d and i_q are the motor currents in the (d,q) frame; ω is the motor speed; φ_0 is the flux of the permanent magnets; and v_q is the voltage on the q-axis.

2.1. The speed observer

The q-axis voltage equation is used as a reference model for the speed observer block. The ideal $\hat{v}_q$ voltage computed from the equation is compared to the applied voltage, v_q , calculated from the DC bus voltage and the inverter dead time values.

The estimated speed $\hat{\omega}$ is obtained by integrating the voltage error considering a speed estimation gain k_{spd}

$$\hat{\omega} = k_{spd}\int\left(v_q - Ri_q - L\frac{di_q}{dt} - \varphi_0\cdot\hat{\omega}\right)dt \tag{2}$$

which translated to the discrete domain with a sampling time Ts gives the equations (2) presented under the mode in which they were implemented on the DSP:

$$\begin{aligned} I_i &= I_{i-1} + k_{spd}\left(v_q - R\cdot i_q - \varphi_0\cdot\hat{\omega}\right)T_s \\ \hat{\omega} &= I_i - k_{spd}\cdot L\cdot i_q \end{aligned} \tag{3}$$

2.2. The position observer

The d-axis voltage equation is used to minimise the angle error between a hypothetical (δ,γ) reference frame and the actual (d,q) reference frame.

$$v_\delta = Ri_\delta + L\frac{di_\delta}{dt} - \hat{\omega}\cdot L\cdot i_\gamma \tag{4}$$

$$e_\delta \overset{\Delta}{=} v_d - v_\delta = \omega\cdot\varphi_0\cdot\sin\delta \tag{5}$$

Integrating the *d*-axis voltage difference minimises the error angle δ. With $J = \frac{1}{2}e_\delta^2$ as minimising criteria, k_{pos} the gain of the position observer and $\frac{d\delta}{dt} = -k_{pos}\cdot\frac{dJ}{d\delta}$, one obtains

$$\begin{aligned} \delta = -k_{pos}\int&\left(v_d - Ri_d - L\frac{di_d}{dt} + \hat{\omega}\cdot L\cdot i_q\right) \\ &\cdot\omega\cdot\varphi_0\cdot\cos\delta\cdot dt \end{aligned} \tag{6}$$

Considering small variations near the operation point, when $\delta\to 0$ one has $\cos\delta\approx 1$, $i_\delta\to i_d = 0$ and ω constant during a current sampling period. Then, the rotor flux position estimated angle can be computed as

$$\hat{\theta} = \int\hat{\omega}\cdot dt + \delta \tag{7}$$

Thus, the implementation on the DSP follows the equation (8):

$$\hat{\theta}_i = \hat{\theta}_{i-1} + \hat{\omega}\left[1 - k_{pos}\varphi_0\cdot\left(u_d + \hat{\omega}\cdot L\cdot i_q\right)\right]T_s \tag{8}$$

Finally, a correction is applied in steady state regime to compensate for the uncertainty and variation of the motor parameters. The error between the estimated position angle increment ($theta\_inc$) and a target value ($theta\_inc*$) computed from the speed reference is used to adjust the motor model parameters on-line and correct the speed estimation. The magnet flux coefficient (noted $k\varphi_0$) was chosen to be the on-line adjustable model parameter:

$$k\varphi_0 = k\varphi_0 + gain\_k\varphi_0(theta\_inc * - theta\_inc) \quad (9)$$

where $gain\_k\varphi_0$ represents the integrator gain that cancels the error between desired synchronous speed and estimated speed for constant reference.

Figure 1 presents the block diagram of the DSP sensorless control implementation scheme.

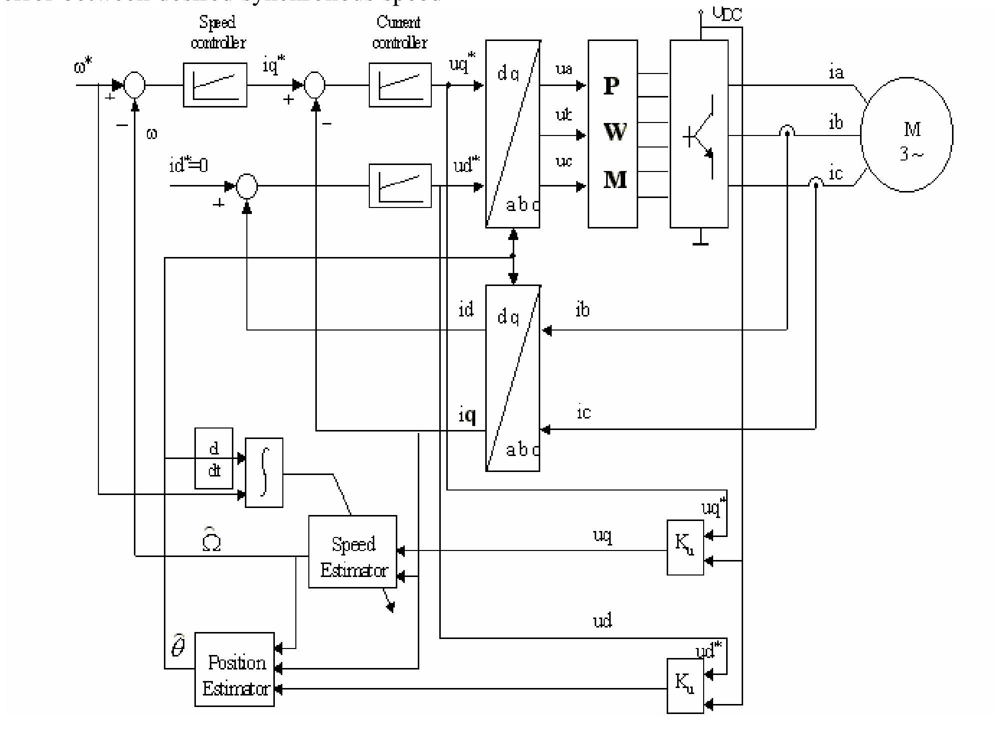

Figure 1. *Sensorless control implementation of method 1 – block diagram*

Tests of this method have been made on different types of permanent magnet brushless motors in different applications. Figure 2 presents the start-up ramp for a 60 W brushless motor. An incremental encoder was used to compare the estimated speed and position with the actual ones (*omg_ref* - speed reference *omg1* - actual speed, *omg* - estimated speed, *theta1* - actual electrical position, *theta* - estimated electrical position).

Figure 3 presents the statistical data gathered on a wide speed range for steady state application with a 1 kW motor.

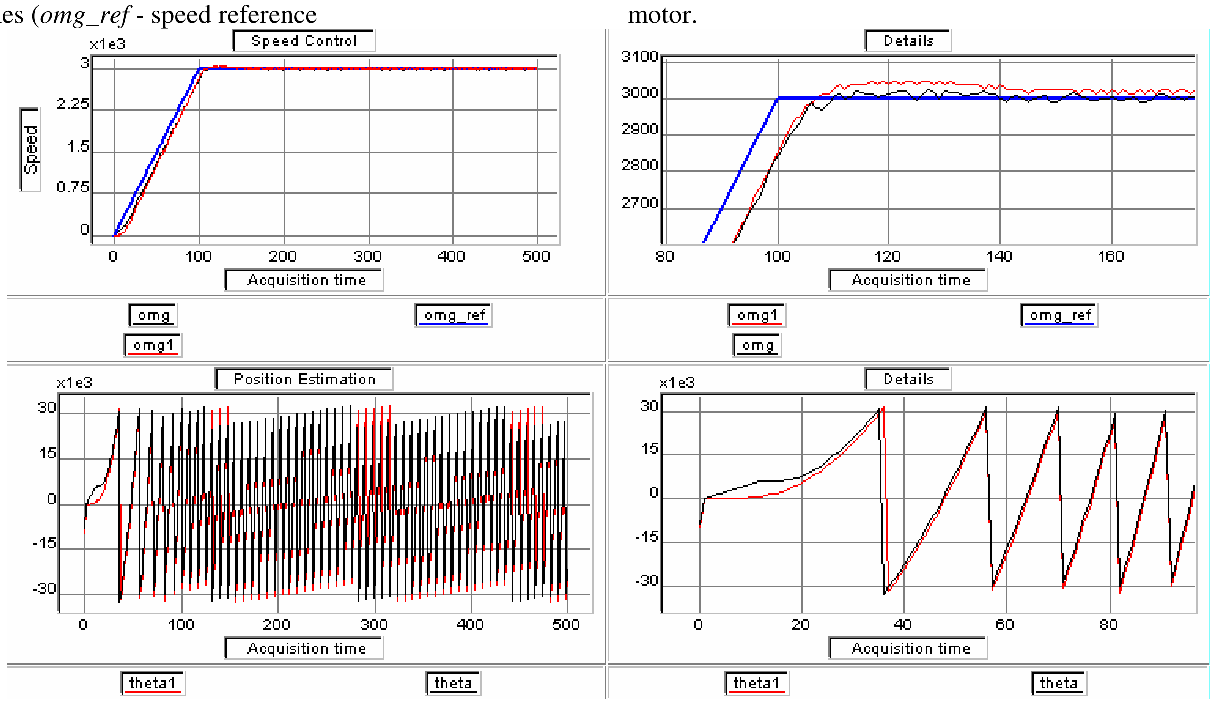

Figure 2. *Sensorless control of 60 W brushless motor - experimental results, method 1*

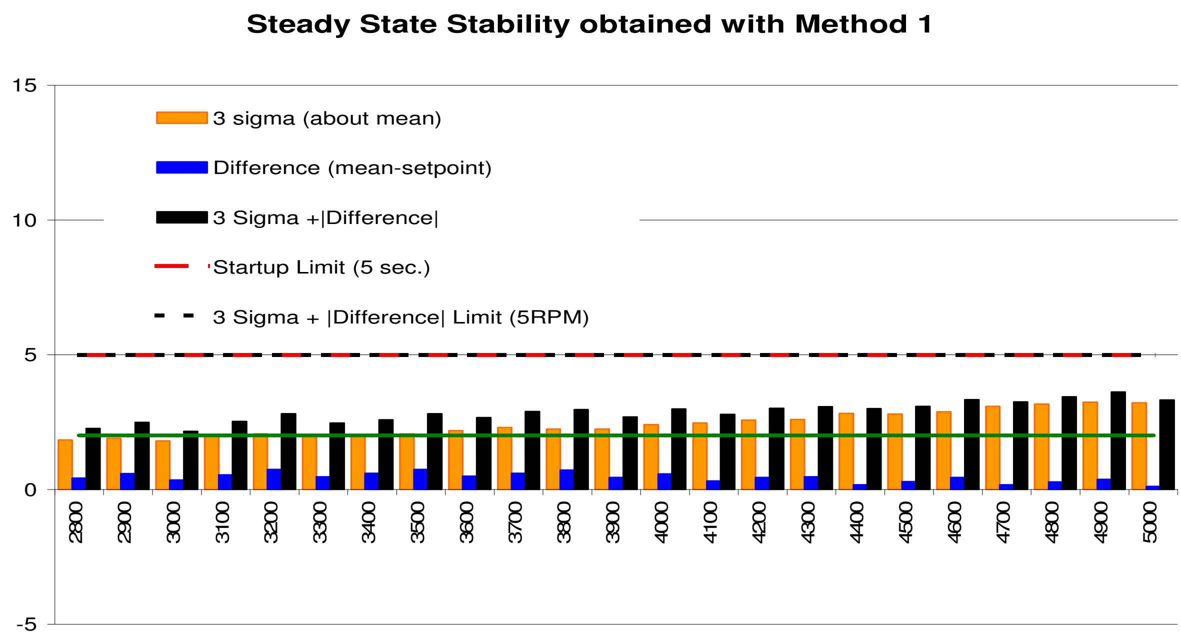

Figure 3. *Method 1 experimental results on 1 kW motor – excellent steady state stability in a wide speed range*

3. SPEED ESTIMATION FROM THE INSTANTANEOUS REACTIVE POWER

The principle used in this method is that of a reference model applied to the instantaneous reactive power computed from the voltage equation in the (d,q) reference frame (1).

The instantaneous reactive power, q, is by definition:

$$q = u_q i_d - u_d i_d \qquad (10)$$

and also, starting from (1), can be expressed as:

$$q = \omega L_d i_d^2 + \omega L_q i_q^2 + \omega\varphi i_d + L_q i_d \frac{di_q}{dt} - L_d i_q \frac{di_d}{dt} \qquad (11)$$

3.1. The reference model

Equation (10) is considered the reference model for the reactive power:

$$q_{ref} = u_q i_d - u_d i_d \qquad (12)$$

In order to eliminate the perturbations caused by the variations of the DC bus voltage level, a DC bus level compensation is included in q_{ref} computation.

3.2. The adaptive model

The adaptive model construction is based on the equation (11).

Assuming:

$$\frac{di_q}{dt} = 0 \,; \quad \frac{di_d}{dt} = 0$$

and $L_d = L_q = L_s$

equation (11) can be further written as:

$$q_{est} = \omega L_s \left(i_d^2 + i_q^2\right) \qquad (13)$$

The term $\omega\varphi i_d$ has been intentionally left out.

A proportional integral controller is used to adjust ω so that $q_{est} = q_{ref}$.

If $q_{est} = q_{ref}$ then $\omega\varphi i_d = 0 \Rightarrow i_d = 0$ so the d axis of the control is aligned with the d axis of the rotor flux. In order to enhance the functionality of the control in dynamic regimes such as the braking mode, a correction is added to the synchronous speed computed by the PI controller.

In order to enhance the functionality of the control in dynamic regimes such as the braking mode, a correction is added to the synchronous speed computed by the PI controller. The correction is based on the d axis voltage model.

Starting from the d axis voltage equation:

and assuming $i_d = 0$,

$$u_d = R i_d + L_s \frac{di_d}{dt} - \omega L_s i_q$$

$$\hat{u}_d = -\omega L_s i_q \qquad (14)$$

The ideal d axis voltage is compared to the actual applied voltage, computed from the d axis current controller output and the DC bus voltage. A second proportional controller minimizes the error between the two voltages (ideal and actual). The controller output is added as a correction to the estimated (electrical) speed.

In order to obtain the position of the rotor, the synchronous speed is properly scaled and integrated.

The block diagram of the DSP sensorless control implementation scheme is presented in Figure 4.

Sensorless control experimental results obtained with this method on a 200W brushless motor are presented in the last two figures. Figure 5 captured the start-up and steady state operation in case of constant torque reference. Figure 6 presents closed loop speed control performances. An incremental encoder was also used to present the accuracy of the speed estimation.

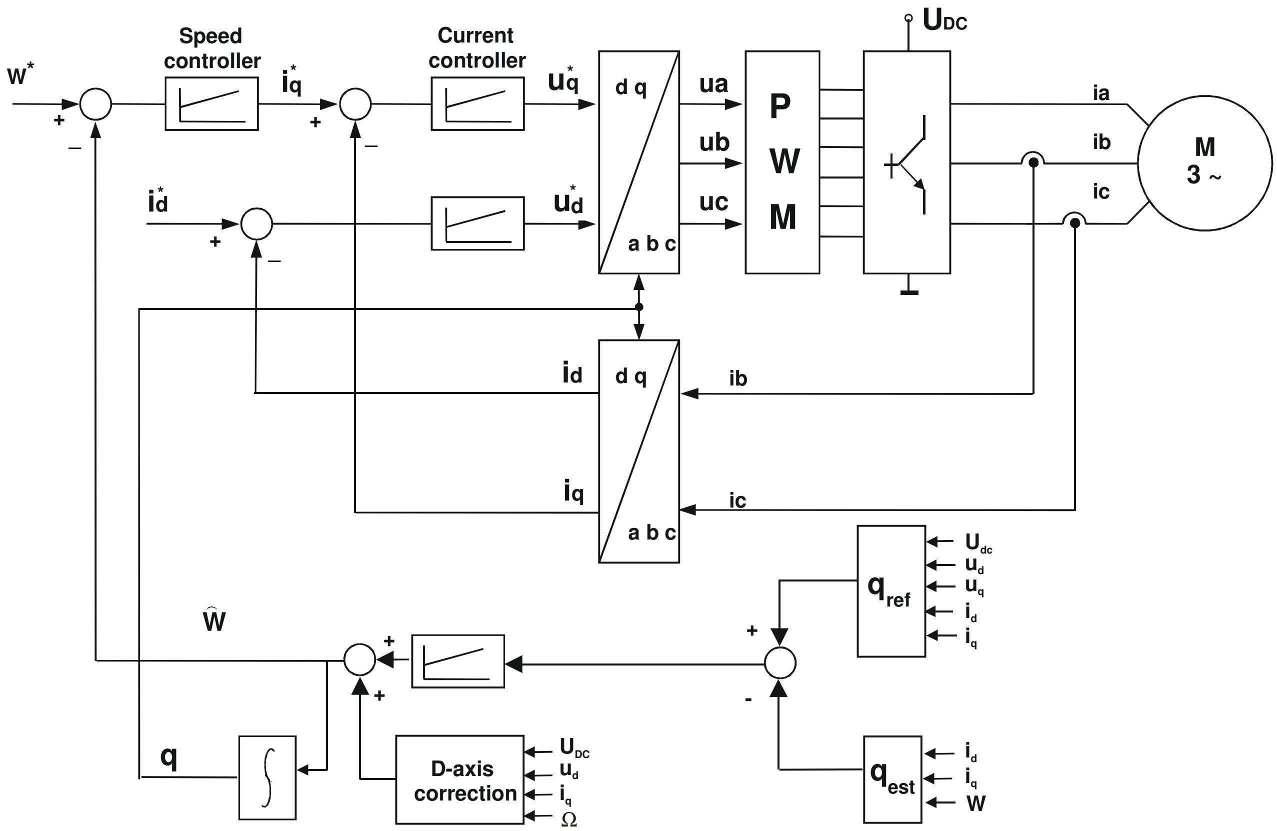

Figure 4. *Sensorless control implementation of method 2 – block diagram*

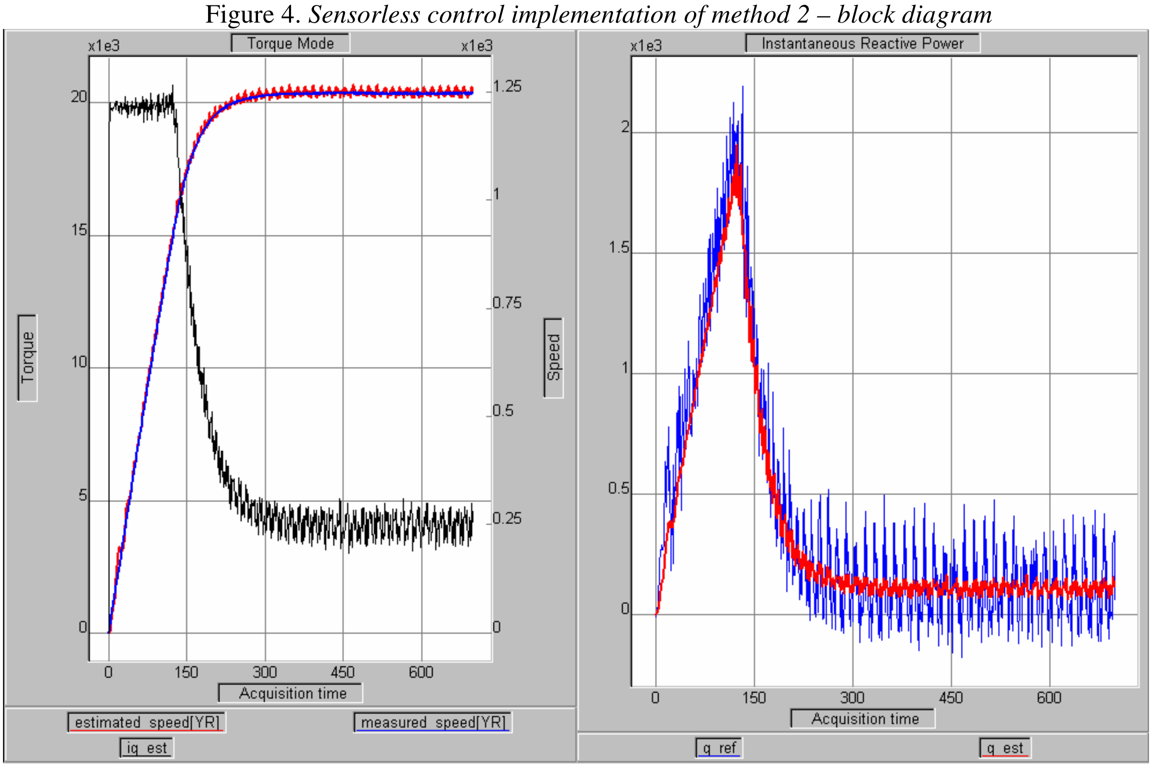

Figure 5. *Sensorless torque control of 200W brushless motor - experimental results, method 2*

4. CONCLUSIONS

Two sensorless methods for estimating speed and position in PMSM vector control applications have been presented and compared.

Method 1 estimates the speed and the electrical position directly from the voltage equations in the (d,q) reference frames. Method 2 estimates the same variables by applying a reference and adaptive model to the instantaneous reactive power. Extensive tests have been made with both methods validating them in industrial applications.

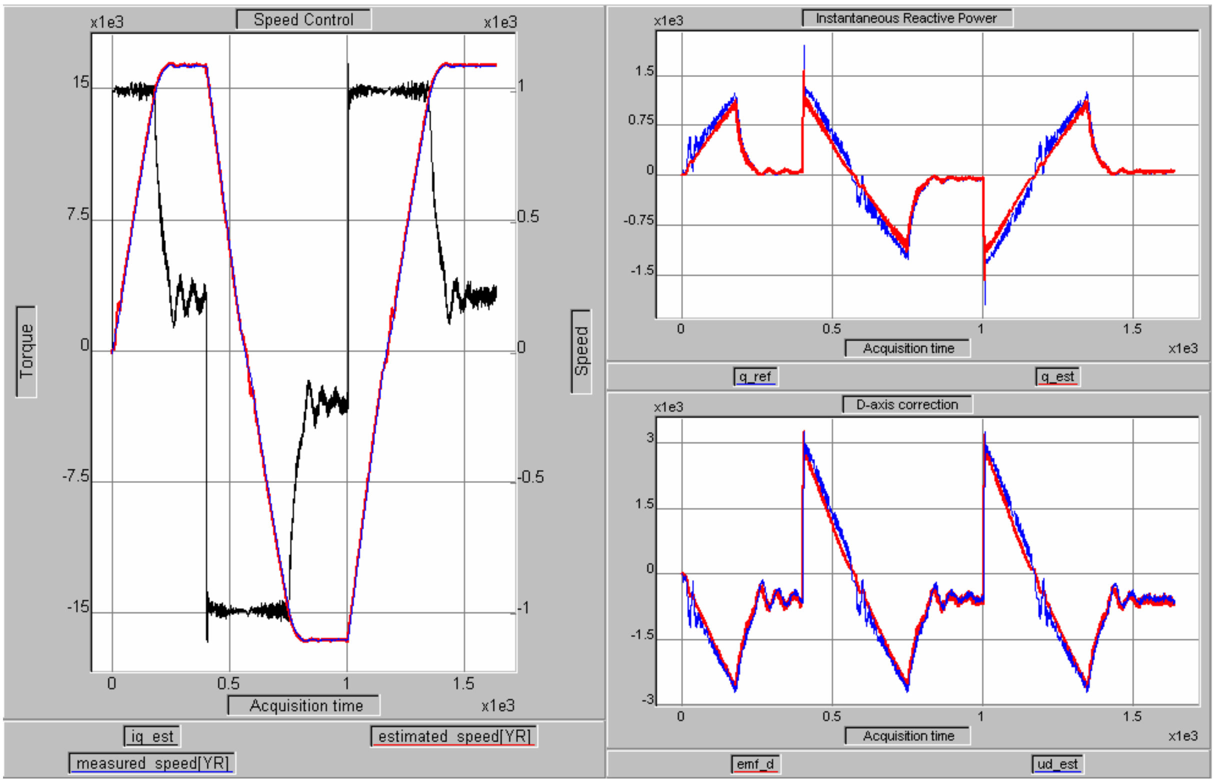

Figure 6. *Sensorless speed control of 200W brushless motor - experimental results, method 2*

Method 1 demands an exhausting tuning procedure due to the great number of parameters. Having fewer parameters, method 2 can be much easily adapted to a new motor.

The tests have proved excellent behaviour in steady state regime for the first method. When fine-tuning was accomplished, this method proved very good stability on a wide speed range. Even more, the speed control error was found less than 5 rpm in a whole range from 2800 to 5000 rpm that is remarkable for a sensorless solution (see Figure 3).

Tests recommend the second method for its robustness in dynamic regimes. Specific application requirements characterised by random power interruptions were satisfied by this implementation. Method 2 proved to have the possibility to gain control of a running motor without having to wait for a complete stop before restarting the motion.

A DSP solution was used for implementation - the 16 bit fixed-point DSP TMS320F240. A high bandwidth was attained with the H/W and S/W solution adopted: 1 ms speed loop, 100 microsec current loop, 20 kHz symmetric PWM modulation frequency.

5. REFERENCES

[1] H.Tajima, Y.Hori, *"Speed Sensorless Field-Orientation Control of the Induction Machine"*, IEEE Trans.Indus.Appli., vol.29, no.1,pp.175-180, January/February 1993.

[2] M.Tsuji, E.Yamada, *"Advanced Vector Control for Induction Motor Drives"*, Proc. of SPEEDAM 1998, pp.A1-1-A1-8, Sorento, Italy.

[3] R.Giuclea, V.Burtea, L.Kreindler, A.Dumitrescu, T. Jokinen, *"Sensorless Motion Control Of Permanent Magnet Synchronous Motor"*, Paper 238, ICEM 2000 Conference, Helsinki, Finland

STATOR CURRENT ERROR AS SOURCE OF INDUCTION MOTOR ROTOR SPEED ESTIMATION

Veran Vasić, *Faculty of Engineering, Novi Sad, Yugoslavia*
Slobodan Vukosavić, *Electrical Engineering Faculty, Belgrade, Yugoslavia*

Abstract: *The aim of this paper is to show some of possibilities for realization of drive without speed transducer on induction motor (IM) shaft. Absence of speed transducer on shaft is condition for use of suitable estimators and cognition of motor parameters. Detuning of IM parameters causes error in estimated speed, rotor flux space vector orientation and orientation of synchronously rotated reference frame. In this paper steady state mathematical model is represented. This model is used for investigation of parameter detuning on steady state.*

Keywords: *Speed transducer, induction motor parameters, steady state.*

1. INTRODUCTION

In actual industrial and technological processes with speed variable drives, DC motors are replaced by IM. The rotor speed or speed transducer are the necessary for realization of speed variable drives. Application of speed transducer [1-2] decreases robustness and reliability of IM drive. In drives with high rotor speed values, sometimes it is not possible to mount speed transducer [3-5]. In the literature there are several possibilities for realization of speed estimation. The most of drives with vector controlled IM are for general use [1-10], where satisfied drive performances can be achieved without speed transducer.

Actual magnitude value and position of rotor flux space vector are necessary for realization of simultaneous flux and torque control. The measurements of adequate quantities are used in estimation of flux space vector with competent IM mathematical models based on classical general theory of electrical machines.

2. SYNCHRONIZATION BY Q-COMPONENT CURRENT ERROR

Position of synchronously rotated reference frame is very significance for realization of vector control algorithm. There are more different methods for achievement of vector controlled sensorless IM drives. The number of methods for determination of reference frame position in sensorless drives is reasonably higher in comparison with the same for drives with speed transducer. In this article the position of synchronously rotated reference frame is determined on basis of difference between referent and actual q-component currents [9]. The position of reference frame is changed until convergation of these two values.

Fig. 1 represents one of possible equivalent IM circuits.

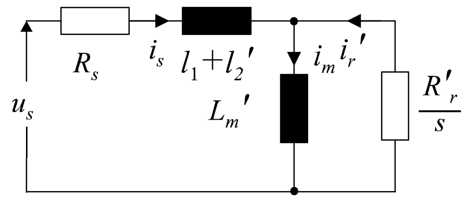

Fig. 1: *Equivalent IM circuit*

where:

$L'_m = L_m^2 / L_r$; $l'_2 = L_{\gamma r} L_m / L_r$; $R'_r = R_r (L_m / L_r)^2$;

$L_1 = l_1 + l'_2 + L'_m = \lambda + L'_m$;

$l_1 = L_{\gamma s}$, $L_{\gamma r}$ - leakage inductance.

PWM inverter voltage supplied IM has constant electromotive force E_q with neglecting of RI voltage. With these circumstances current i'_r and developed torque are proportional with slip s. IM vector diagram is shown on Fig. 2.

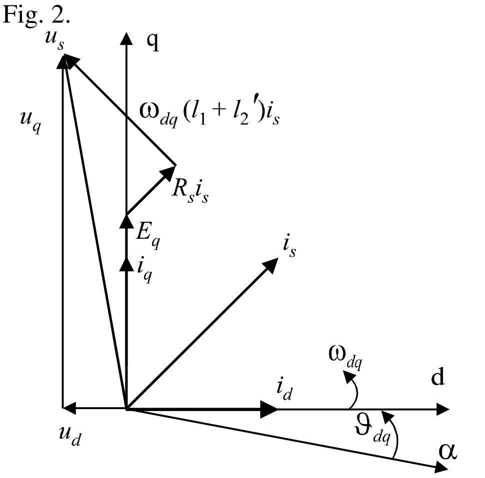

Fig. 2: *Vector diagram*

Synchronously rotated reference frame with speed W_{dq} is marked with d-q axis. Surmised that electromotive force E' is collinear with q-axis, stator voltage is composed with RI voltage and electromotive force E_q. PWM voltage inverter secure motor voltage which is identical with reference one. Voltage space vector $\underline{u}_s$ is controled by reference voltage u^*_d, u^*_q and ϑ_{dq}.

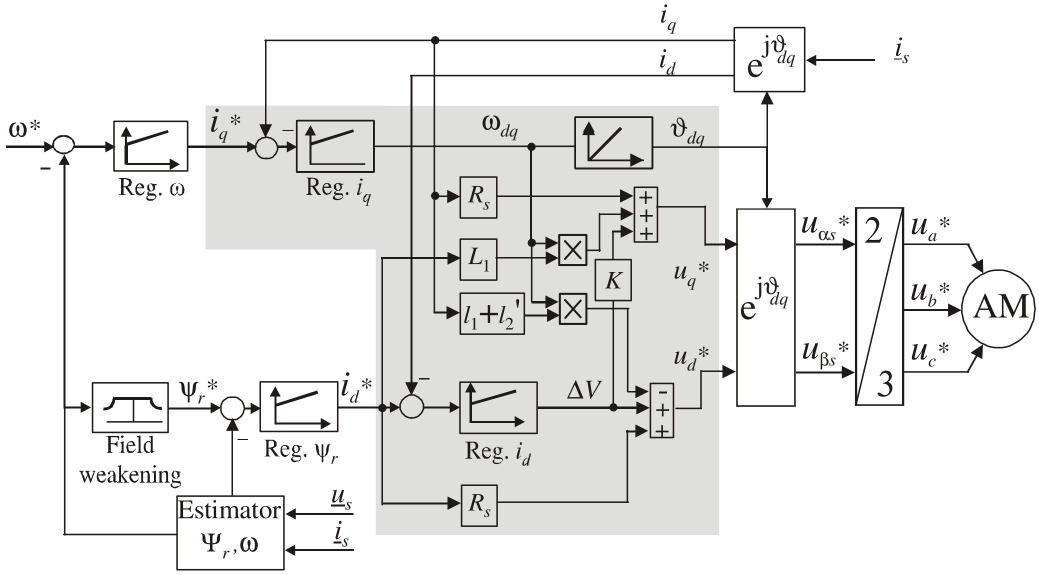

Fig. 3: *Synchronization by q-component current stator error*

On Fig. 3 is represented regulation structure of vector controlled IM drive. It is predicted the possibility of work in the area of field weakening. Speed and torque regulators reconstitute adequate current values by q- and d- axis, respectively. Stator current regulations are realized in synchronously rotated reference frame. Synchronization is realized on basis of error in stator q-component current. Output of current regulator, i_q, is reference value of synchronous speed W_{dq}. Position of synchronously rotated reference frame is obtained by W_{dq} integration. Reference value of voltage space vector $\underline{u}^*_s$ is determined with:

$$u_d = u_d^* = R_s i_d^* - \omega_{dq}(l_1 + l_2')i_q + \Delta V \quad (1)$$

$$u_q = u_q^* = R_s i_q + \omega_{dq} L_1 i_d^* + K\Delta V \quad (2)$$

Output of current regulator i_d is marked with ΔV. The voltage u_d is controlled according with equation (1). It enabled re-establishing of the i_d current which is identical with i^*_d. That is the way for conditioning of constant flux value operation in IM. Changes of ϑ_{dq} and u_q have the influence on i_d current in accordance with equation (2).

Determination of position of synchronously rotated reference frame is simultaneous with speed estimation:

$$\hat{\omega} = \omega_{dq} - \omega_{kl} \quad ; \quad \omega_{kl} = \frac{i_q}{T_r i_d} \quad (3)$$

3. STEADY STATE MATHEMATICAL MODEL

In this part is represented steady state mathematical model for sensorless drive where position of synchronously rotated reference frame and rotor speed are obtained from q-component current error. This solution for prescribing of position of flux space vector has parameter sensitivity. On Fig. 3 is shown regulation structure for realization of synchronization based on q-component current error in sensorless drive. Flux and speed feedbacks are closed with estimated ones. Flux space vector is estimated by voltage u_s-i_s estimator.

Steady state mathematical model of IM drive (Fig. 3) is described with equations (4)-(8):

$$u_d = R_{sm} i_d - \omega_{dq}\left(\left(L_{\gamma s} + M\right) i_q + M i_Q\right) \quad (4)$$

$$u_q = R_{sm} i_q + \omega_{dq}\left(\left(L_{\gamma s} + M\right) i_d + M i_D\right) \quad (5)$$

$$0 = R_{rm} i_D - \omega_{kl}\left(\left(L_{\gamma r} + M\right) i_Q + M i_q\right) \quad (6)$$

$$0 = R_{rm} i_Q + \omega_{kl}\left(\left(L_{\gamma r} + M\right) i_D + M i_d\right) \quad (7)$$

$$m_e = \frac{3}{2} pM\left(i_q i_D - i_d i_Q\right) \quad (8)$$

where, M is magnetizing inductance.

Unknown variables in these equations are: u_d, u_q, i_d, i_q, i_D, i_Q, W_{dq} and slip W_{sl}. There are eight unknown variables in five equations, supposing that load torque is known and it has the same value with IM load torque.

IM on Fig. 3 is voltage supplied and u_d, u_q are known quantities determined with (1) and (2). In steady state $i_q = i^*_q$. For every load torque value exist adequate m^*_e, i.e. i^*_q, so that i_q current can be observe like known one determined with:

$$i_q = \frac{2 m_e^* L_r}{3 p L_m \psi_r^*} \quad (9)$$

Synchronous speed is:

$$\omega_{dq} = W + \frac{i_q}{T_r i_d} \quad (10)$$

W is mark for steady state value of estimated speed that is equal with reference one, W^*.

Another more additional equation can be written for estimated flux. Rotor flux is:

$$\hat{\psi}_r^2 = \hat{\psi}_{\alpha r}^2 + \hat{\psi}_{\beta r}^2 = \psi_{DV0}^2 + \psi_{QV0}^2 = \psi_r^{*2} \quad (11)$$

where:

$$\psi_{DV0} = \frac{L_r}{\omega_{dq} L_m}\left[u_q - R_s i_q - \omega_{dq}\sigma L_s i_d\right]$$

$$\psi_{QV0} = \frac{L_r}{\omega_{dq} L_m}\left[-u_d + R_s i_d - \omega_{dq}\sigma L_s i_q\right] \quad (12ab)$$

When eqs. (1) and (2) are put in eq. (12ab), we have deficient equation:

$$\left(\frac{\psi_r^* L_m}{L_r}\right)^2 = \frac{1}{\omega_{dq}^2}\left[\Delta V^2 + \left(\omega_{dq} L'_m i_d + K\Delta V\right)^2\right] \qquad (13)$$

System equation which describes steady state (Fig. 3) is represented with (13)-(17), using (9) and (10):

$$0 = (R_{sm} - R_s) i_d - \omega_{dq}\left(\left((L_{\gamma s} + M) - l_1 - l'_2\right) i_q + M i_Q\right) - \Delta V \qquad (14)$$

$$0 = (R_{sm} - R_s) i_q - \omega_{dq}\left(\left((L_{\gamma s} + M) - L_1\right) i_d + M i_D\right) - K\Delta V \qquad (15)$$

$$0 = R_{rm} i_D - \omega_{kl}\left((L_{\gamma r} + M) i_Q + M i_q\right) \qquad (16)$$

$$0 = R_{rm} i_Q + \omega_{kl}\left((L_{\gamma r} + M) i_D + M i_d\right) \qquad (17)$$

Described system should solved by i_d, i_D, i_Q, W and ΔV. If magnetic circuit saturation is neglected than $M = L_m = L_{mn}$.

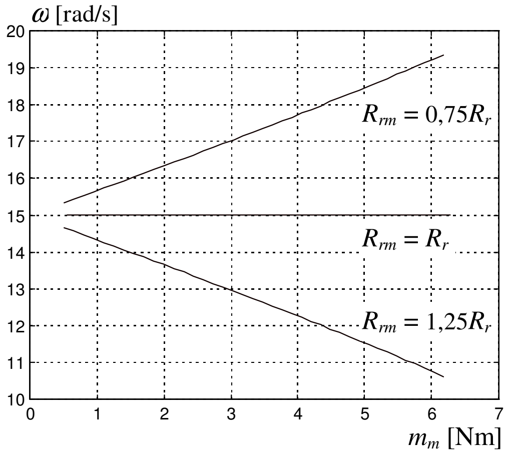

Fig. 4: *Drive speed vs. load torque*

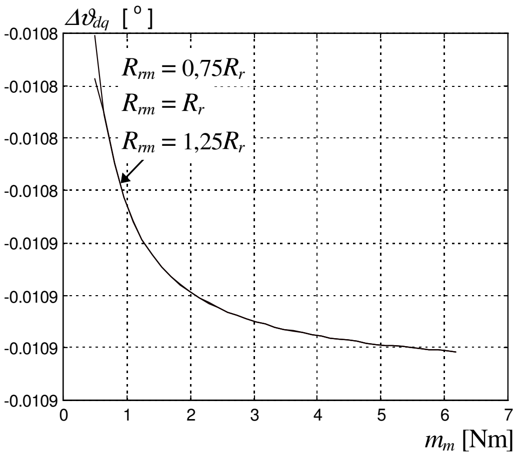

Fig. 5: *Error in position of rotor flux space vector in function with load torque*

On Figs. 4 and 5 are shown results obtained with steady state mathematical model when rotor resistance is detuned in eq. (3).

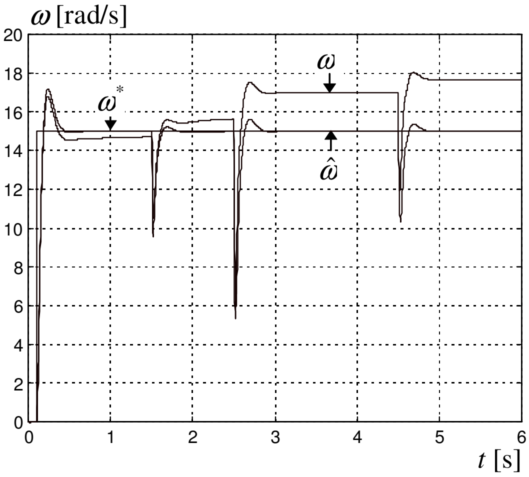

Fig. 6: *Drive speeds; $R_{rm} = 0.75R_r$*

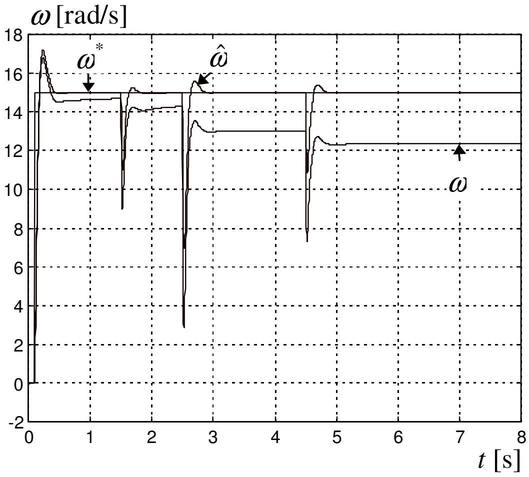

Fig. 7: *Drive speeds; $R_{rm}=1.25R_r$*

On Figs. 6 and 7 are represented simulation results of time response for IM drive (Fig. 3). The aim was verification of results obtained by steady state mathematical model. IM start is simulated with R_r detuned. Motor is unloaded until t = 1.5 s, then loaded in 1.5 s with 1 Nm, in 2.5 s with 3 Nm and in 4.5 s with 5 Nm. Rotor resistance detuning has influence just on estimated speed, when influence on space vector rotor flux orientation is neglected as shown on Fig. 5. Correlation of results on Figs. 4 and 5 with results of steady state mathematical model on Figs. 6 and 7 is excellent.

Influence of stator resistance variation on steady state is significantly higher than R_r detuning. It is shown on following figures.

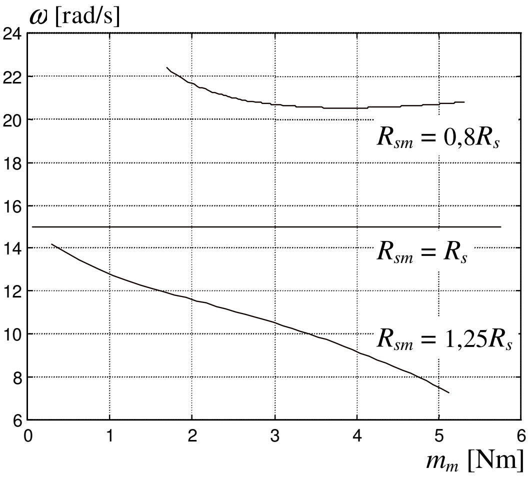

Fig. 8: *Drive speed vs. load torque*.

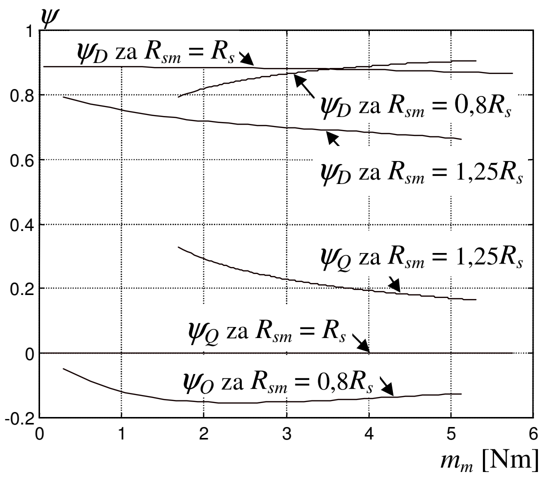

Fig. 9: *Error in rotor flux orientation vs. load torque*

On Figs. 12 - 15 are presented simulation results of time response of drive. The aim was verification of results obtained with steady state mathematical model. Reference speed is 15 rad/s. Motor is unloaded until t = 0.5 s, then loaded in 0.5 s with 1 Nm, in 2.5 s with 3 Nm and in 4.5 s with 4 Nm. There is absolute correlation of results obtained by steady state mathematical model (Figs. 8-11) with the same ones obtained by dynamic model (Figs. 12-15).

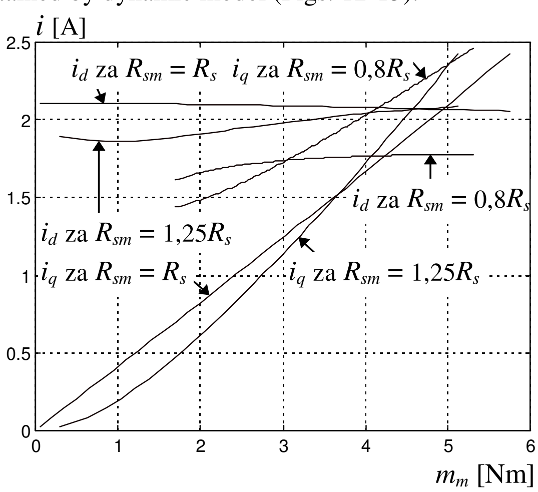

Fig. 10: *IM currents id and iq vs. load torque*

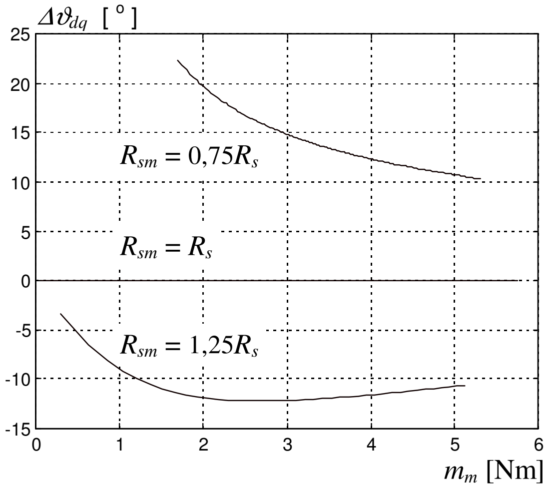

Fig. 11: *Error in rotor flux orientation vs. load torque*

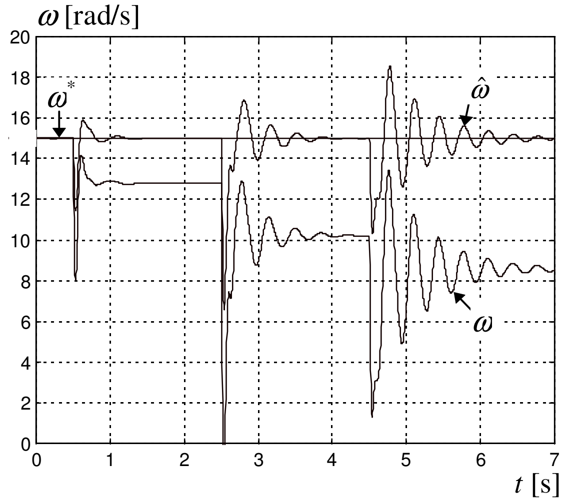

Fig. 12: *Drive speeds*

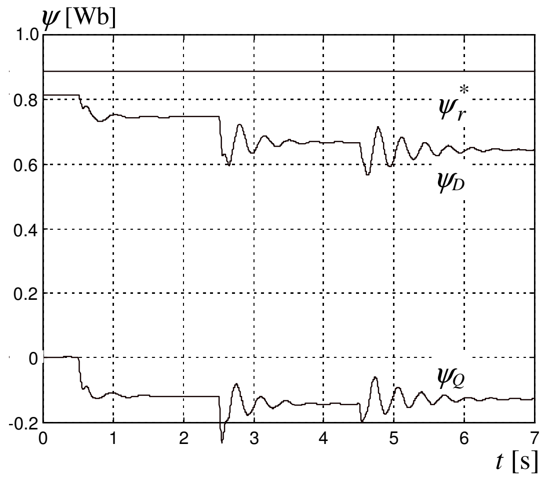

Fig. 13: *Motor fluxes*

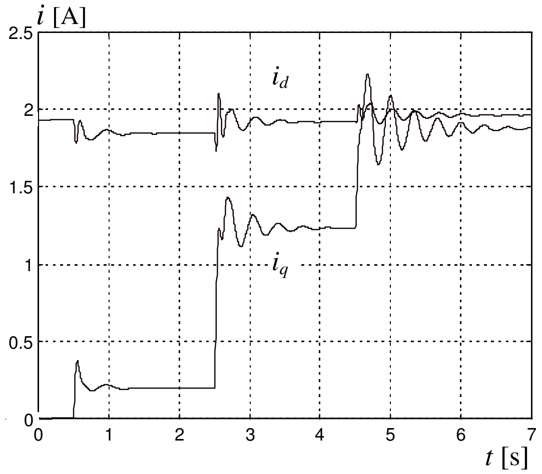

Fig. 14: *d- q- components of stator current*

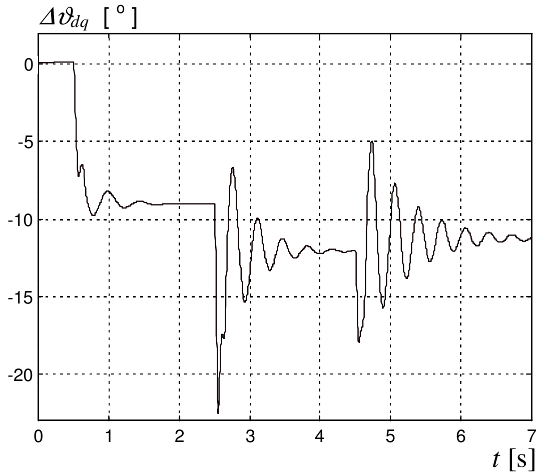

Fig. 15: *Error in rotor flux orientation*

4. CONCLUSION

In this paper is represented one manner for realization of sensorless drive. For that purposes it is used synchronization on basis of q-component current stator error. It is established steady state mathematical model for sensorless drive. Steady state mathematical model is effective tool for investigation of parameter detuning influence and adequate estimator parameters. It is observed R_s and R_r detuning influence in rotor flux estimator model in relation with values in IM. Intensive examinations showed that ignorance of exact R_s value is a reason for variation of real IM speed from reference one. Load torque has small influence on speed error.

5. REFERENCES

[1] C. Schauder, "Adaptive speed identification for vector control of induction motors without rotational transducers," in Conf. Rec. IEEE Ind. Appl. Soc. Ann. Meet., 1989, pp 493-499.

[2] G. Yang and T. H. Chin, "Adaptive speed identification scheme for a vector - controlled speed sensorless inverter - induction motor drive," IEEE Trans. Ind. Appl., vol. 29, no. 4, pp. 820-824, July/August, 1993.

[3] Tajima and Y. Hori, "Speed sensorless field - rientation control of the induction machine," IEEE Trans. Ind. Appl., vol 29, no. 1, pp. 175-180, January, 1993.

[4] F. Z. Peng and T. Fukao, "Robust speed identification for speed sensorless vector control of induction motors," IEEE Trans. Ind. Appl., vol 30, no. 5, pp. 1234-1240, September/October, 1994

[5] Y. Hori and T. Umeno, "Implementation of robust flux observer based field orientation (FOFO) controller for induction machines," in Conf. Rec. IEEE Ind. Appl. Soc. Ann. Meet., 1989, pp 523-528.

[6] H. Kubota, K. Matsuse and T. Nakano,"DSP - based speed adaptive flux observer of induction motor," in Conf. Rec. IEEE Ind. Appl. Soc. Ann. Meet., 1991, pp. 380-384.

[7] H. Kubota and K. Matsuse, "Speed sensorless field-oriented control of induction motor with rotor resistance adaption," IEEE Trans. Ind. Appl. vol 30, no. 5, pp. 1219-1224., September/October, 1994.

[8] R. Bowes and J. Li "New robust adaptive control algorithm for high performance AC drives," in Conf. Rec. IEEE Ind. Appl. Soc. Ann. Meet., 1997, pp. 1-7.

[9] T.Okuyama, N.Fujimoto, T.Matsui, Y.Kubota, "A High Performance Speed Control Scheme of Induction Motor Without Speed and Voltage Sensors," IEEE Ind. Appl. Soc. Ann. Meet.,1986, pp. 106-111.

[10] R. Jonsson, "Method and Apparatus for Controlling an AC Induction Motor by Indirect Measurement of the Air-gap Voltage", United States Patent, Patent Number: 5,294,876, Date of Patent 15, Mar. 1994.

ANALYSIS OF INDUCTANCE CHARACTERISTICS OF DISPLACEMENT SENSOR

Mirjana Damnjanović, Laslo Nađ, Ljiljana Živanov, Faculty of Engineering, Novi Sad, Yugoslavia

Abstract: *This paper analyzes the inductance characteristics of displacement inductive sensor in printed circuit board (PCB) technology. It also describes the design, realization and the input inductance measurement of planar inductive sensor. The displacement in two directions (less than 0.5 mm) can be detected by using two meander coils. One of the coils is short-circuited (so the sensor has one port, only). Three sets of inductive sensor are considered, having different width and thickness and composition of conductors. Using the concept of partial inductance, the self and mutual inductance of displacement sensor were calculated. Using the measured impedance of the sensor, the correction of the model was made. Disagreements present in earlier version of sensor were corrected. So, a good agreement between measured and modeled inductance was found. Difference was less than 6 %.*

Keywords: *Inductive sensor, modeling, displacement measurement.*

1. INTRODUCTION

Planar sensors are growing rapidly in importance because of their simplicity, robustness and low cost. The full potential of these sensors can be used in the area of the integrated system. Measurements of displacement, location or level are very important in the process industry and robotics. In order to measure one phenomenon it is often necessary to measure another. For motion measurement applications, the sensors might be involved in monitoring variables such as displacement, velocity, and acceleration.

Displacement sensors are varied, ranging from a potentiometer-type displacement sensor to the LVDT-type sensor (Linear Variable Differential Transformer). Some inductive sensors are based on the principle of variation of inductance by insertion of core material into an inductor. Others are based on the change of the coupling coefficient, due to mechanical deformation of the sensors' structure. The inductance variations serve as a measure of displacement.

For on-board modules for industrial application low profile of the module, often less than 0.5 inches, is one of the key design requirements. Inductive structures are usually bulky and do not lend themselves naturally to low profile. Thus, recently a different approach in the design of inductive components has emerged, called "flat structures". Flat structures are low-profile realized using printed circuit board [1], thick and thin film [2,3,4] and micromachining techniques [5].

Goal of this work is to realize sensor that can be used to detect small displacements in the plane, in direction of *x*- and *z*-axes in this case. For this purpose, we have chosen meander type inductors. The prototype was designed in printed circuit board technology (PCB). It can detect small displacements (less than 0.5 mm).

The applications of meander type inductive sensors are discussed in [2], [3] and [4]. Small displacement can be detected by using two meander coils [2]. The ECT (eddy-current testing) probe can detect the existence of a defect in material, and can extract detailed information regarding the nature of defect, such as position, shape, length, and direction [3]. Also, the ECT probe consisting of planar meander and mesh coils can be used for investigating trace defects on printed circuit boards [4].

In this paper, we describe as follows:

1. Design of the meander type inductive sensor.
2. Comparison of calculated and measured values (with and without correction of disagreement) of sensor's input inductance L_{IN} (that is, inductance between terminals *P* and *Q*, as it is shown in Fig. 1).
3. Construction of the displacement inductive sensor in the plane.

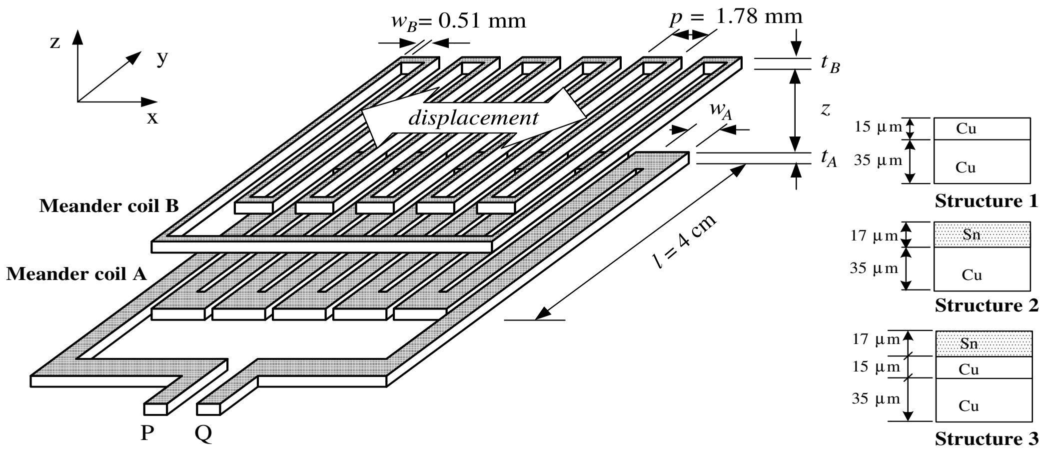

Fig. 1. *Inductive sensor for small displacements in two directions and three different conductor structures.*

2. DESIGN OF INDUCTIVE SENSOR

The construction of meander type inductive sensor is shown in Fig. 1. It consists of two meander coils, faced one another. One of the coils is fixed (meander coil *A*) and between its terminals *P* and *Q* the input inductance L_{IN} was measured. Other coil (meander coil *B*) is short-circuited, so the sensor has only one port. Coil *B* is moved above the coil *A*, in directions of *x*- and *z*-axes. (Sensor cannot be moved in direction of y-axis.)

Preliminary the characteristic's measurements of the inductive sensor have shown that resistance of coil *B* has significant influence on the input impedance between terminals *P* and *Q*. Therefore, we had to use thicker meander coil conductors to minimize that resistance. Three different sets of inductive sensor were considered:

- *Structure 1*, composed of basic 35 μm Cu layer and additional 15 μm Cu layer.
- *Structure 2*, composed of basic 35 μm Cu layer and additional 17 μm Sn layer.
- *Structure 3,* composed of basic 35 μm Cu layer and two additional layers: 15μm Cu and 17μm Sn.

Specifications of meander coils *A* and *B* are shown in Table 1.

Table 1. *Specification of meander coils*

	Number of turns	Width ***w***	Pitch ***p*** *	Thickness ***t***
Meander coil *A*	$N_A = 10$	0.51 mm, 1.27 mm, 1.52 mm	1.78 mm	**1.** Cu 50 μm, **2.** Cu 35μm + Sn 17 μm **3.** Cu 50 μm + Sn 17 μm
Meander coil *B*	$N_B = 10$	0.51 mm	1.78 mm	

* *p* - distance between axes of two neighbouring segments

3. INDUCTANCE CALCULATIONS

The distance between meander coils is small, so the computation of mutual inductance is very complex. The inductance of such complex structures can be calculated by means of conformal mapping or by splitting the conductors in a finite number of filaments [6]. Therefore, the segments of meander coil are divided into parallel filaments having small, rectangular cross sections. The self and mutual inductance were calculated using the concept of partial inductance [7, 8, 9], as it is shown in Fig. 2.

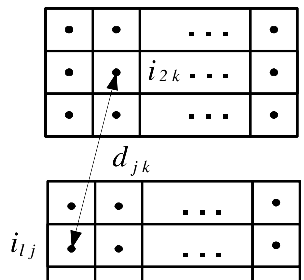

Fig. 2. *Partitioning of rectangular cross sections of meander coils A and B.*

The working frequency was relatively low (1 MHz), so the skin effect can be neglected. It means that the current of conductors is uniformly distributed over whole cross section.

For a straight conductor of rectangular cross section the self-inductance is

$$L_i = 2 \cdot l \cdot \left(\ln \frac{2l}{w+t} + 0.25049 + \frac{w+t}{3l} + \frac{\mu}{4} T \right) \text{[nH]}, \tag{1}$$

where L_i is the inductance in (nH), *l, w* and *t* are length, width and thickness of the conductor in (cm), respectively, μ is the conductors permeability, and *T* is a frequency-correction parameter [9].

The mutual inductance between two straight parallel conductors of rectangular cross section can be calculated as

$$L_{ij} = 2l \left(\ln \left(\frac{l}{GMD} + \sqrt{1 + \left(\frac{l}{GMD} \right)^2} \right) - \sqrt{1 + \left(\frac{GMD}{l} \right)^2} + \frac{GMD}{l} \right), \tag{2}$$

where *l* is the conductors' length, *GMD* is geometric mean distance between the conductors [10]

$$\ln GMD = \ln d - \left(\frac{1}{12} \left(\frac{d}{w} \right)^2 + \frac{1}{60} \left(\frac{d}{w} \right)^4 + \frac{1}{168} \left(\frac{d}{w} \right)^6 + \right. \\ \left. + \frac{1}{360} \left(\frac{d}{w} \right)^8 + \frac{1}{660} \left(\frac{d}{w} \right)^{10} + \ldots \right) . \tag{3}$$

Meander coil consists of straight segments parallel with *x*-axis and segments parallel with *y*-axis. Assume that every segment of meander coil is divided into elementary filaments with rectangular cross section. Then the total self-inductance of meander coil can be calculated as the sum of the partial self-inductances of all elementary filaments L_i and the sum of all mutual inductances between all elementary filaments L_{ij}

$$L = \sum_{i=1}^{n} L_i + \sum_{i=1}^{n} \sum_{j=1}^{n} L_{ij}, \quad \text{where } i \neq j. \tag{4}$$

Similarly, assume that meander coil *A* is divided into n_1 and meander coil *B* is divided into n_2 elementary filaments with rectangular cross sections. Then the total mutual inductance between these two coils can be calculated as the sum of the partial mutual inductances between all elementary filaments of meander coils *A* and *B*

$$M = \sum_{i=1}^{n_1} \sum_{j=1}^{n_2} L_{ij} . \tag{5}$$

4. EVALUATION OF THE INPUT INDUCTANCE

In order to analyze our inductive sensor and calculate self and mutual inductance of meander coils *A* and *B*, we have developed a program written in FORTRAN language. Using the equivalent circuit of meander type inductive sensor (Fig. 3), we were able to determine the sensor's input impedance as

$$Z_{IN} = R_1 + \frac{k^2 \omega^2 L_1 L_2 R_2}{R_2^2 + \omega^2 L_2^2} + j\omega L_1 \cdot \frac{R_2^2 + \omega^2 L_2^2 (1 - k^2)}{R_2^2 + \omega^2 L_2^2}, \tag{6}$$

where R_1 and L_1 are resistance and self-inductance of meander coil A, R_2 and L_2 are resistance and self-inductance of meander coil B, while k is coupling coefficient between coils

$$k = M / \sqrt{L_1 L_2} \; . \tag{7}$$

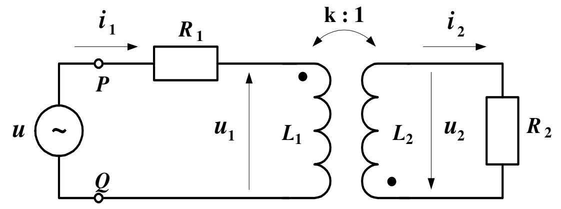

Fig. 3. *Equivalent circuit of inductive sensor.*

As it is shown in Fig. 1, meander coils consists of basic Cu and one (structure 1 and 2) or two additional layers (structure 3). Structure 1 consists of two layers with the similar specific resistivity. Due to the absence of the skin effect there is no need for vertical partitioning of this structure on more than one layer.

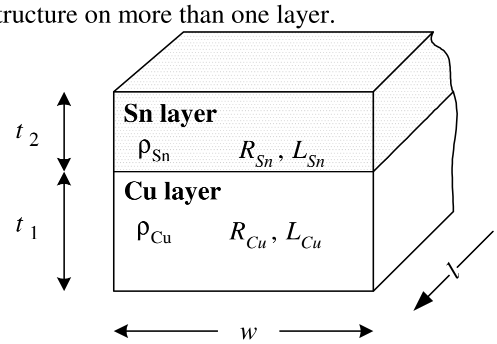

Fig. 4. *Structure 2 and 3 meander coils consist of two layers with different specific resistivity.*

For structures 2 and 3 the calculation of the coils' impedance is more complex (Fig. 4). Using the equivalent circuit of meander coil (Fig. 5), which consists of two layers with different specific resistivity, we were able to determine the coil's self-inductance as

$$L = \frac{R_{Cu}^2 L_{Sn} + R_{Sn}^2 L_{Cu} + 2R_{Cu}R_{Sn}k_1\sqrt{L_{Cu}L_{Sn}}}{(R_{Cu}+R_{Sn})^2 + \omega^2(L_{Cu}+L_{Sn}-2k_1\sqrt{L_{Cu}L_{Sn}})^2} + \\ + \omega^2 \cdot \frac{L_{Cu}L_{Sn}(1-k_1^2)\cdot(L_{Cu}+L_{Sn}-2k_1\sqrt{L_{Cu}L_{Sn}})}{(R_{Cu}+R_{Sn})^2+\omega^2(L_{Cu}+L_{Sn}-2k_1\sqrt{L_{Cu}L_{Sn}})^2}, \tag{8}$$

and resistance as

$$R = \frac{R_{Cu}R_{Sn}(R_{Cu}+R_{Sn})}{(R_{Cu}+R_{Sn})^2+\omega^2\cdot(L_{Cu}+L_{Sn}-2k_1\sqrt{L_{Cu}L_{Sn}})^2} + \\ +\omega^2 \cdot \frac{R_{Cu}\cdot(k_1\sqrt{L_{Cu}L_{Sn}}+L_{Sn})^2 + R_{Sn}\cdot(k_1\sqrt{L_{Cu}L_{Sn}}+L_{Cu})^2}{(R_{Cu}+R_{Sn})^2+\omega^2\cdot(L_{Cu}+L_{Sn}-2k_1\sqrt{L_{Cu}L_{Sn}})^2}, \tag{9}$$

where R_{Cu} and L_{Cu} are resistance and self-inductance of Cu layer of meander coil, R_{Sn} and L_{Sn} are resistance and self-inductance of Sn layer of meander coil. k_1 is coupling coefficient between two layers of meander coils.

$$k_1 = M_{SnCu} / \sqrt{L_{Cu}L_{Sn}} \; . \tag{10}$$

When meander coil A is moved above the meander coil B, mutual inductance fluctuates according to the displacement, and the input impedance Z_{IN} is changed. In this paper will be only considered the variation of the input inductance, L_{IN}.

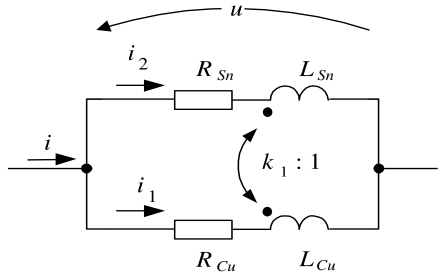

Fig. 5. *Equivalent circuit of the meander coil that consists of two layers with different specific resistance (structure 2 and structure 3).*

4. COMPARISON OF MEASURED AND CALCULA-TED VALUES OF INPUT INDUCTANCE

Results of comparison of measurement and simulation with correction of disagreement for structure 1 of meander coil, where w_A=w_B= 0.51 mm, are shown in Fig. 6. Three different gaps between meander coils has been observed: z = 0.1 mm, z = 0.2 mm and z = 0.3 mm.

All sensors were electrically tested using a Hewlett Packard Impedance Analyzer HP4277A, at the frequency of 1 MHz. Measured values of the inductance L_{IN} are presented with dot line. On the base of measured values of input inductance L_{IN}, program for calculation of input inductance has been corrected. Results of simulation with correction are presented with solid line in Fig. 6.

As it can be seen in Fig. 7, the same form of the inductance-displacement characteristic for measured (dot line) and calculated inductances (solid lines) were found. Difference between measured and calculated value of inductance without correction was less than 8 %. To achieve even better accuracy, the correction of program for calculation was made. That upgraded program includes:

- The measured value of self-inductance of meander coil A, L_1 (which is, in fact, maximal value of input inductance L_{IN}),
- The measured value of resistance of meander coil A R_1 (minimal value of input resistance R_{IN}),
- The estimated value of self-inductance of meander coil B, L_2, determined on the base of measured value of self-inductance of meander coil A, L_1, for corresponding (identical) conductor structure

$$L_2 = \frac{L_{2C}}{L_{1C}} \cdot L_1 , \tag{11}$$

where L_{1C} and L_{2C} are calculated values of self-inductance of meander coils A and B, respectively,
- The estimated value of resistance of meander coil B, determined on the base of measured value of resistance of meander coil A, R_1, for corresponding (identical) conductor structure

$$R_2 = \frac{R_{2C}}{R_{1C}} \cdot R_1 , \tag{12}$$

where R_{1C} and R_{2C} are calculated values of resistance of meander coils *A* and *B*, respectively.

After correction of program was made, the difference between measured and calculated values of input inductance was less than 6 %. Note that the same form of inductance-displacement characteristic for measured and calculated inductances with correction of program were found (Fig. 7).

Table 2 shows measured values of inductance L_{IN} for three different structures and two different combinations of conductor widths w_A. It contains minimal L_{INmin} and maximal L_{INmax} value of inductance, absolute inductance variation

$$\Delta L_{IN} = L_{IN\,max} - L_{IN\,min} \tag{13}$$

and relative inductance variation, determined as

$$\delta = \frac{L_{IN\,max} - L_{IN\,min}}{L_{IN\,max}} . \tag{14}$$

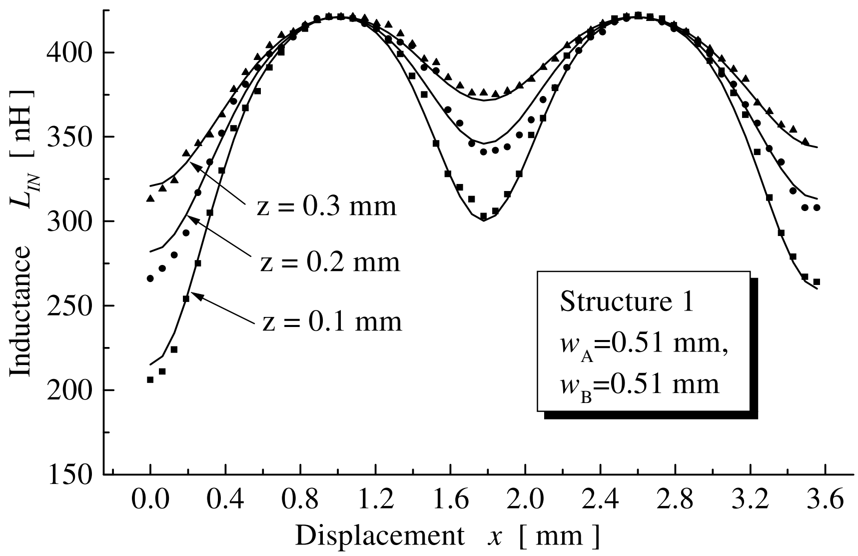

Fig. 6. *Computed and measured values of inductance L_{IN} versus displacement x, for three different distances between coils A and B. Meander coils are designed in structure 1 with two equal width coils, w_A=w_B = 0.51mm.*

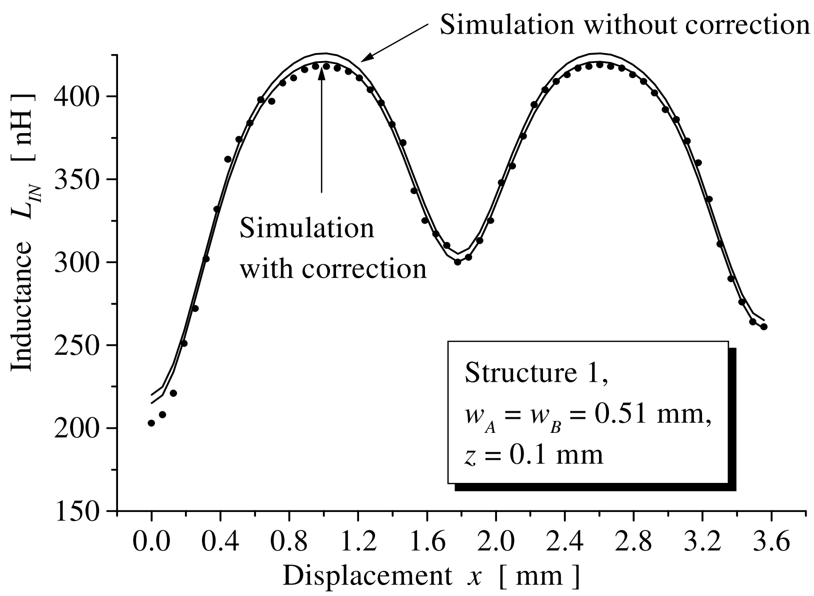

Fig. 7. *Comparison of measured and calculated values (with and without of correction of disagreement) of input inductance L_{IN}*

Table 2. *Measured values of inductance L_{IN} for three different structures of meander coils*

Structure	W_A+w_B [mm+mm]	L_{INmax} [nH]	L_{INmin} [nH]	ΔL_{IN} [nH]	δ [%]
1	0.51+.051	422	203	219	51.9
	1.52+0.51	166	93	73	44.0
2	0.51+.051	406	255	151	37.2
	1.52+0.51	174	117	57	32.8
3	0.51+.051	413	270	143	34.6
	1.52+0.51	172	97	75	43.6

As it can be seen in Fig. 6, if two meander coils are centered (i.e. x=0), their mutual inductance has its maximum, and the input inductance L_{IN} is minimal. All other local minima correspond to displacements of meander coil B in the direction of x-axis, which equals whole number of pitch p = 1.78 mm.

If the mutual inductance between meander coils A and B is equal to zero, then the input inductance L_{IN} has its maximum and it is equal to self-inductance of meander coil A. The inductance L_{IN} has its maximum at positions corresponding to displacement equals odd times half of the pitch p, i.e. $(2k\text{-}1)\cdot p/2$.

5. CONSTRUCTION OF SENSOR FOR SMALL DISPLACEMENTS IN *X - Z* PLANE

In order to detect small displacement in two direction, two pair of meander coils have been used [1]. On the basis of measurement results, shown in Table 2, it can be concluded that structure 2 of meander coils (w_A=1.51mm and w_B = 0.51 mm) have the least variation of inductance versus displacement in x-axis direction. Furthermore, in the vicinity of the zero position (i.e. x=0; meander coil B is exactly above meander coil A), the variation of the inductance L_{IN} is negligible, less than few nH (Fig. 8 and Fig. 9). Therefore, this sensor can be used to detect the gap between two meander coils, i.e. z-coordinate.

Other pair of meander coils has to be used to detect x-coordinate. To accomplish this task meander coils designed in structure 1 are chosen, with w_A=w_B=0.51mm, because this sensor has the largest inductance variation. If the coil B is arranged relative to coil A by one quarter of pitch, the slope of the inductance L_{IN} has its maximum (Fig. 9 and Fig. 10). In the vicinity of this position (i.e. x=0.44 mm) the inductance L_{IN} depends nearly linearly on displacement in the x-axis direction. This pair must be used combined with first pair of coils to determine the displacement x.

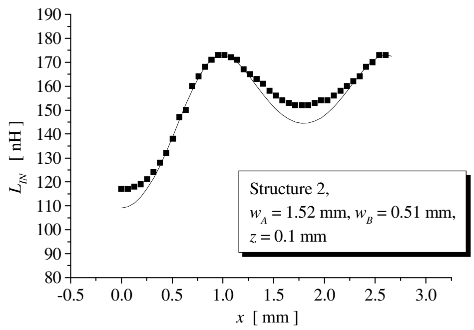

Fig. 8. *Calculated and measured values of inductance for structure 2, w_A = 1.52 mm, w_B = 0.51 mm, z = 0.1mm.*

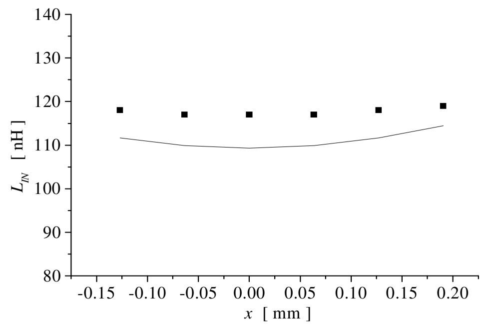

Fig. 9. *Enlarged part of curve from Fig. 8 for displacement in vicinity of x=0.*

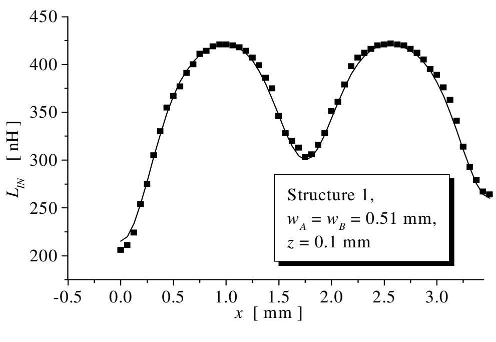

Fig. 10. *Calculated and measured values of inductance for structure 1, w_A = w_B = 0.51 mm, z = 0.1 mm*

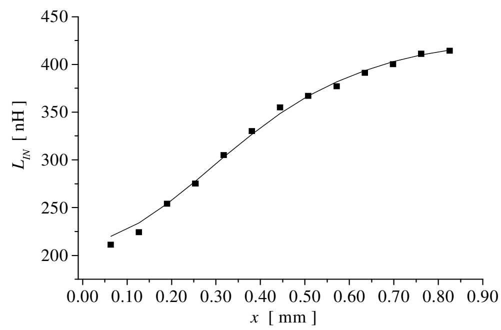

Fig. 11. *Enlarged part of curve from Fig. 10 for displacement in vicinity of x=0.4 mm.*

6. CONCLUSIONS

This work has investigated and developed a displacement inductive sensor. These sensors have been studied by the methods of mathematical modeling and simulation. Design methods for this type of inductive sensor have also been suggested.

Three sets of inductive sensor are considered: different width and thickness and composition of conductors. The same form of impedance-displacement characteristic was found for all conductor structures, width and thickness (as it is shown in Fig. 6). When the distance between two meander coils is smaller, the absolute variation of inductance is larger (caused by stronger coupling between the meander coils).

In order to detect small displacement in the plane (less than 0.5 mm), two pairs of meander coils must be used:

- *First pair of meander coils*, designed in structure 2, with w_A = 1.52 mm and w_B = 0.51 mm wide. When the coil *A* is exactly above coil *B*, inductance variation for small displacement in direction of x-axis is negligible, less than few nH. This pair of coils can be used for determination of gap between coils, i.e. *z*- coordinate.
- *Second pair*, consisting of two equal width coils, w_A=w_B = 0.51mm. If the coil *B* is arranged relative to coil A by one quarter of pitch, the slope of the inductance *LIN* has its maximum. This pair must be used combined with the first pair of coils to determine the displacement *x*.

A simple model of inductive sensor is proposed using the partial inductance method. The conductors of meander coil are divided into parallel segments having small, rectangular cross section. This model was upgraded with measured values of input inductance. A good agreement between measured and modeled inductances was found. Difference was less than 6 %. So, we can conclude that skin effect neglecting was justified.

The displacement (less than 0.5 mm) can be precisely detected by using two meander coils. The advantage of this sensor is that one of the coils is short-circuited (so the sensor has one port, only).

A possible application of such sensors is in robotics. Miniature version of such sensors could be incorporated into soft-covered fingertips of a robotic gripper. So, normal and tangential components of fingertips' deformation could be measured.

Taking into account the stiffness of the soft elastic material used, the value of forces acting on the fingertip could be calculated. So obtained results could be useful in performing precise peg-in-hole tasks by industrial robots.

7. REFERENCES

[1] M.Damnjanović, L.Nađ, Lj.Živanov, "Characteristics of meander type displacement inductive sensor", ETRAN'2001, 4-7. June2001, pp. 254-257.

[2] H. Wakiwaka, M. Nishizawa, S. Yanase: "Analysis of Impedance Characteristics of Meander Coil", IEEE Trans. on Magnetics, Vol.32, Sept. 1996, pp. 4332-4334.

[3] S.Yamada, M.Katou, M. Iwahara, F.P.Dawson: "Defect Images by Planar ECT Probe of Meander-Mesh Coils", IEEE Trans. on Magnetics. Vol.32, Sept.1996, pp.4956-4958.

[4] S.Yamada, H.Fujiki, M.Iwahara, S.C.Mukhopadhyay, F.P.Dawson: "Investigation of Printed Wiring Board Testing by Using Planar Coil Type ECT Probe", IEEE Trans. on Magnetics, Vol.33, Sept.1997, pp.3376-3378.

[5] Lj.D.Živanov, G.Stojanović, A.Vujanić, S.M.Jenei: "Determination of Optimal Parameters of Micromachined Inductive Sensor", ISEF'99, Pavia, Italia, 1999, pp.369-372.

[6] F.B.J.Leferink: "Inductance calculations; methods and equations", Proc. Inter. Sym. on EMC. IEEE '95. Atlanta, 1995, pp.16-22.

[7] A.E.Ruehli: "Inductance Calculations in a Complex Integrated Circuit Environment", IBM J. res. develop, Sept.1972, pp.470-482.

[8] A.Ruehli, C.Paul, J.Garret: "Inductance Calculations Using Partial Inductances and Macromodels" Proc. Inter. Sym. on EMC, Atlanta, 1995, pp.23-27.

[9] H.M.Greenhouse: "Design of Planar Rectangular Microelectronic Inductors", IEEE Trans. on parts, hyb. and pack., Vol.PHP10, June1974, pp.101-109.

[10] F.W.Grover, "*Inductance calculations*", D. Van Nostrand Company, New York, 1946.

MEASUREMENT OF NONSINUSOIDAL ELECTRICAL POWER AND ENERGY

Velibor Pjevalica, Vladimir Vujicic
The Hong Kong Polytechnic University, The University of Novi Sad-Faculty of technical sciences

Abstract: - *This paper describes novel method for measuring nonsinusoidal electrical power and energy. By adding high frequency noise signal with uniform distribution of amplitudes to measured analog signal, measurement accuracy can be significantly improved. Accuracy improvement is due to property of dithering method that measurement error decrease with number of samples taken. However, this feature also can be used to increase accuracy of measuring integral of product two analog signals. Now, stochastic adding analog-to-digital conversion together with additional digital signal processing can be used for accurate electrical power and energy measurement.*
Key Words: DFT, stochastic, power measurement, energy measurement, reactive energy measurement, *analog-to*-digital conversion, RMS.

INTRODUCTION

Stochastic adding analog-to-digital conversion is [1] method for measuring RMS, power and energy of the signals in wide frequency range. Block scheme of instrument based on stochastic adding analog-to-digital converter is displayed in Fig. 1:

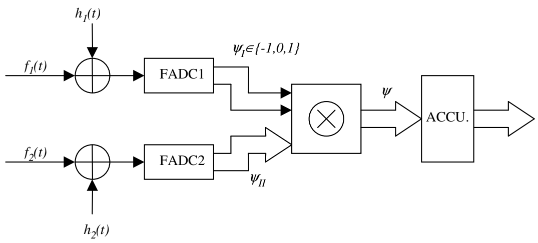

Fig. 1. Generalized instrument based on stochastic adding analog-to-digital converter

Flash AD converter FADC1 is two-bit resolution converter, and Flash AD converter FADC2 is multi-bit resolution flash converter. Now multiplying of samples is simplified because output from FADC1 is restricted to set of values {-1,0,1}, so there are no carry bits in multiplying.

After time interval $T = t_2 - t_1$, accumulator (marked on Fig. 1 as ACCU.) contains value, which is:

$$N\overline{\psi} = \sum_{i=1}^{N} \psi_i \qquad (1)$$

where: $\psi_i = \psi_I \cdot \psi_{II}$, N is number of samples sampled during time interval T, $\overline{\psi} = \frac{1}{T}\int_{T1}^{T2} f_1(t)\cdot f_2(t)dt$, and h_1 and h_2 are stochastic, mutually non correlated signals with uniform distributions of amplitudes, where probability of each amplitude is $p(h_i) = \frac{1}{a}$. Signals h_1 and h_2 fulfill Widrow condition $|h_i| \le \frac{a}{2}$, where a is quantum level of flash A/D converters (marked on Fig. 1 as FADC). According to central limit theorem, average value is:

$$\overline{\psi} = \frac{1}{T}\int_{t1}^{t2} f_1(t)\cdot f_2(t)dt = \frac{1}{N}\sum_{i=1}^{N}\psi_i \qquad (2)$$

and standard deviation is:

$$\sigma_{\overline{\psi}} = \frac{\sigma_\psi}{\sqrt{N}} \qquad (3)$$

where:

$$\sigma_\psi^2 = \frac{R^2}{T}\int_0^T |f_1(t)f_2(t)|dt - \left[\frac{1}{T}\int_0^T f_1(t)f_2(t)dt\right]^2 \qquad (4)$$

If $f_i(t)$ is basis function from set of orthonormal functions and this set of orthonormal functions defines signal transformation, then $\overline{\psi}$ is corresponding coefficient of this transform. More over, for particular transformation, Fourier for example, functions $f_i(t)$ are known, so analog-digital part for summing and digitalization signal function $f_i(t)$ and noise $h_2(t)$ can be replaced with memory block which contains sum samples of signal and noise, as it is shown in Fig. 2

:

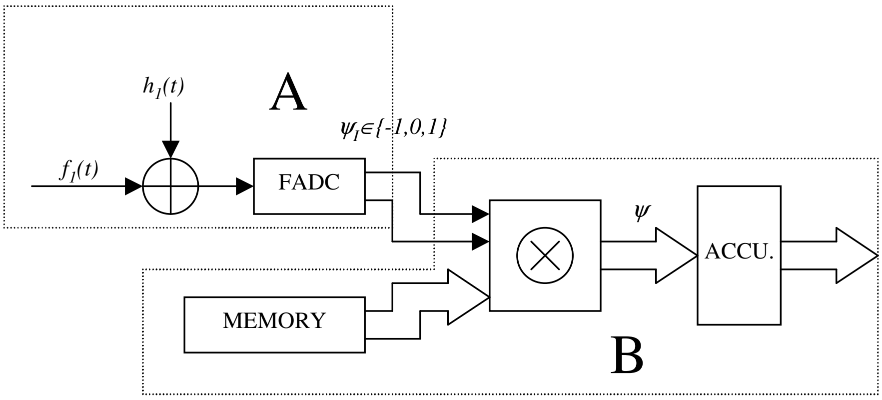

Fig. 2. Instrument for measurement of only one coefficient of otrhonormal transformation

DITHERED DFT PROCESSOR

In figure 2, there are clearly two functionally different segments: analog-digital part marked as 'A' and exclusively digital part marked as 'B'. With such simplified hardware [1], completely parallel measurement of M coefficients is possible. Instrument is shown in Fig. 3.

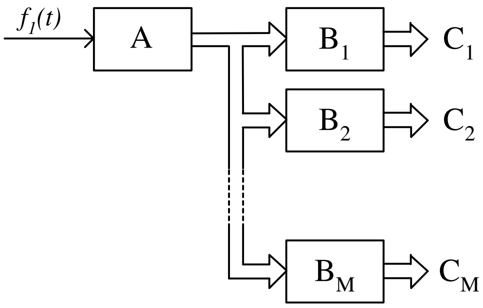

Fig. 3. Parallel measurement of M coefficients for orthogonal transformation of signal $f_1(t)$

Blocks B_i are the same for hardware point of view; only memory contest is different for each block. Digital part of the instrument, however can work with clock pulse up to 100 MHz , while combined analog-digital part due to sampling rate and dither generation can't work with clock pulse over 1 MHz. This means that speed of digital part is 100 times higher, so that up to 100 coefficients can be calculated is series and in such case digital block B_g looks like in Fig. 4.

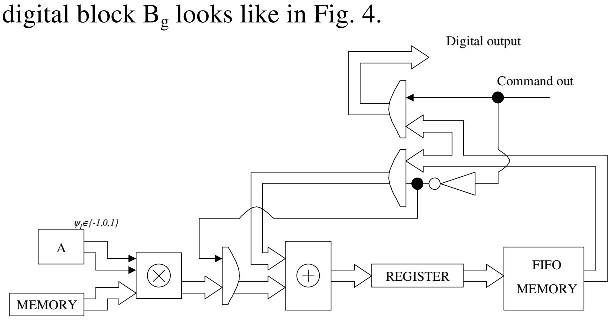

Fig. 4. Generalized digital block Bg for measurement of 100 coefficients of orthogonal transformation

[1] If there is more than 100 coefficients to measure, we can use the same approach, and in that case block diagram of instrument looks like it is shown in Fig. 5.

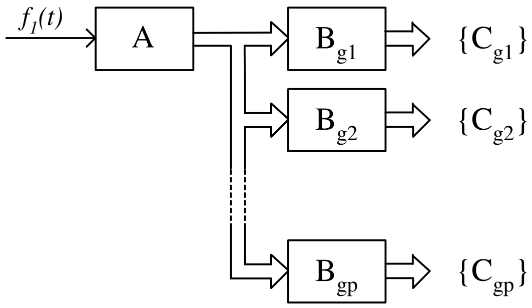

Fig. 5. Block diagram of generalized DFT processor

In Fig. 5, $\{C_{g1}\},\{C_{g2}\},\ldots,\{C_{gn}\}$, are sets with 100 of coefficients each. With such processor structure it is possible to achieve high speed and accuracy in coefficients measurement.

In real distributive 50 Hz /60 Hz power network is no harmonics higher than 100 order, because network itself is a low pass filter. It means that for complete analysis of network signals is enough to take P=2, i.e. 200 Fourier coefficients

ACCURACY

In the case of Fourier transform, basis functions are sinus and cosines with different frequencies:

$$f_{2ia}(t) = R\cos i\omega t; f_{2ib}(t) = R\sin i\omega t \qquad (5)$$

and adequate coefficients are:

$$a_{ia} = R\frac{1}{T}\int_0^T f_1(t)\cos(i\omega t)dt = Ra_i \qquad (6)$$

and analog $b_{ia} = Rb_i$. According (6), coefficients are numerically amplified 'R' times, where +/- R is range of flash analog-to-digital converter (FADC). Measurement accuracy of numerically amplified coefficients for 50 Hz sinus signal with small distortion for 2-bit resolution of FADC, R=5V, sampling frequency of 1 MHz and for measurement duration of 100 ms (i.e. N=100000) is:

$$2 \cdot \frac{\frac{R}{\sqrt{12} \cdot 2^{m-1} - 1}}{R} = \frac{R\sqrt{\frac{R^2}{2}}}{\sqrt{N} \cdot R^2} \qquad (7)$$

So, Benneth resolution is:

$$2^m = 103 \Rightarrow m \approx 10 bits \qquad (8)$$

i.e. resolution is between 13 and 14 bits. If measurement lasts for only one signal period, resolution is one bit less. It is easy to proof that accuracy of real Fourier coefficients and those numerically amplified by instrument are virtually the same:

$$\left|\frac{\Delta C_{ia}}{C_{ia}}\right| = \left|\frac{\Delta R}{R}\right| + \left|\frac{\Delta C_i}{C_i}\right| \approx \left|\frac{\Delta C_i}{C_i}\right| \qquad (9)$$

because R is known with high accuracy, i.e. $|R| >> |\Delta R|$.

THEORETICAL BACKGROUND

Voltage and current signals in distributed power network are non-interruptible functions of time, and according to Berstajn theorem, on finite time interval can be represented with finite trigonometrically polynomial with advance given accuracy. It means for example, that in every successive 20 ms or 100 ms time interval there is the trigonometrically polynomial, which approximate voltage (or current) signal with given accuracy. Of course, this trigonometrically polynomial is defined for infinite $(-\infty, +\infty)$ time interval, but it fit voltage (or current) signal during given time interval only. For different time interval, there different trigonometrically polynomial in generalized case

ADAPTABILITY

Assuming that the shortest sequence of dithered basis function is 20 periods, then maximum accuracy is between 10 and 11 bits, and duration of measurement is 0.4 s for 50 Hz signals. Such accuracy is quite acceptable even for measurement in stationary regime. Another good feature of this instrument is adaptability, i.e. possibility for adjusting speed/accuracy. Due to practical reasons, measurement can last from one up to twenty periods, and accuracy for 6-bit resolution of flesh analog-to-digital converters is from 8 up to 11 bits. Functional dependency of accuracy vs. duration of measurement is given in Fig. 6.

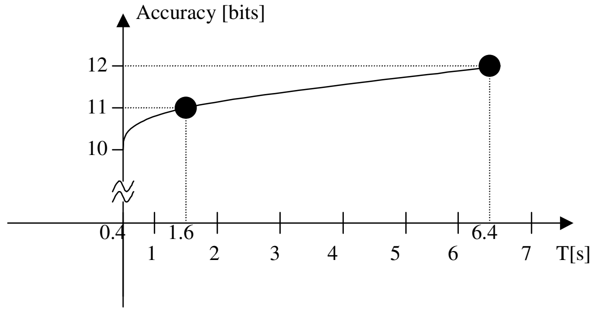

Fig. 6. Functional dependency accuracy vs. measurement duration

REACTIVE POWER/ENERGY MEASUREMENT

Phase shift of voltage is given by (10):

$$\begin{aligned} u(t) &= u(t + \frac{T}{4}) = U_0 + \\ &+ \sum_{i=1}^{N} \left[U_{ci} \cos(i\omega(t + \frac{T}{4})) + U_{si} \sin(i\omega(t + \frac{T}{4})) \right] \end{aligned} \qquad (10)$$

Relation between shifted and non-shifted harmonics is given in table T1:

Harmonic order	***Original harmonics*** (a_n, b_n)	***Shifted harmonics*** $(a_n^{'}, b_n^{'})$
$n = 4k + 0$	a_n, b_n	a_n, b_n
$n = 4k + 1$	a_n, b_n	$b_n, -a_n$
$n = 4k + 2$	a_n, b_n	$-a_n, -b_n$
$n = 4k + 3$	a_n, b_n	$-b_n, a_n$

Now, reactive power/energy can easily calculated by applying formula (11):

$$Q = \sum_{n=1}^{100} (u_{cn}^{'} i_{cn} + u_{sn}^{'} i_{sn}) \qquad (11)$$

It means that only one processor is enough for complete analysis of real signals in power network.

CONCLUSION

Proposed method for design of DFT processor use all advantages of stochastic adding analog-to-digital conversion [1] that is improved technique of dithering [2]. With additional FIFO memory, it is possible to directly measure both orthogonal components of each coefficient of DFT spectrum analysis. Difference in speed between analog and digital part allow using only one hardware structure for simultaneously measurement of 100 coefficients of DFT in real time. Adaptability, accuracy and reliability are main advantages of novel processor proposed.

REFERENCES

[1] Vladimir V. Vujicic, Slobodan S. Milovancev, Mile D. Pesaljevic, Dragan V Pejic and Ivan Zupunski, “Low-Frequency Stochastic True RMS Istrument” IEEE Trans. Instr. Meas. , Vol. 48, No 2, April, 1999.

[2] M.F Wagdy, and W.Ng. “Validiti of Uniform Quantization Error Model for Sinusoidal Signals Without and With Dither”, IEEE Trans. Instr. Meas, Vol38, pp 718-722, June 1989

IMPORTANT ASPECTS OF POWER QUALITY IN A DEREGULATED POWER SYSTEM

Jordan Shikoski, Vladimir Katić, Ustijana Rechkoska***
A.D.EMO-Ohrid, Electrical Industry & Engineering, Ohrid, Macedonia, jordans@mt.net.mk
** University of Novi Sad, Faculty of Technical Sciences, Novi Sad, Yugoslavia, katav@uns.ns.ac.yu*
*** Faculty of Electrical Engineering, Skopje, Macedonia, reckoice@unetoh.com.mk*

Abstract: *In this paper will be presented some of the important aspects of power quality in a deregulation power system: 1.Importance of power quality grows in a deregulated power system; 2.Power quality contracts in a deregulated system; 3.Power quality problems from cogeneration; 4.Attributing the power quality deterioration between customers and utilities; 5.Attributing harmonics in private power production; 6.Power quality monitoring under deregulation; 7.Power value rather than price only*

Key Words: ***Power Quality, Deregulation, Harmonics.***

1. INTRODUCTION

As deregulation and competition become a reality, power quality problems should be recognized from new perspectives. Power quality is a term often used today in describing an aspect of the electricity supply. A power quality problem is any occurrence manifested in voltage, current, or frequency deviation that results in failure of misoperation of electronic equipment. The terms used to describe power disturbances often have different meanings to different users.

Decades ago, power quality was not a worry, because it had no effect on most loads connected to electric distribution systems. Beginning in the late 1970s, power quality became important features to many companies as electronics pervaded each and every industry. Electric power utilities prodused electricity using synchronous generaters until recent times. Consequently, power quality deterioration has usually been viewed as a load side problem. The permissible norms and power quality mitigation have been studied in great detail from such a point view.

2. IMPORTANCE OF POWER QUALITY GROWS IN A DEREGULATED POWER SYSTEM

Deregulation is resulting in important structure changes in the utility industry. In a deregulated environment, people give power quality more concerns than before. Power quality becomes more important to both energy manufactures and energy consumers. Electric utilities are awakening to the fact that power quality deserves more to customers. Manufactures who begin to analyze power use patterns and understand how power quality issues impact their operations will be able to take advantages of these opportunities and of the frontier for reducing costs. Plants acquainted with their energy profile will be able to negotiate better rates for the type and amount of power they acquire. A company that can control the energy use can negotiate better rates by participating in power interrupting programs. In an open and competitive energy market, users who want to negotiate the best rates and guard against reliability and quality problems must understand their energy requirements. They must know if their operations can tolerate an occasional interruption.

Table 1. S*ummery of services of power quality concerns*

Facility electrical equipment	Power quality concerns
Computer/ /data system	Noise corruption of signal reference Harmonics interaction/overheating
Service feeders and apparatus	Lightening protection Switching transient interference
Facility lighting systems	Ballast efficiency selection Harmonics contamination
Engine generator systems	Non linear sizing Transfer and synchronization
Elevator systems	Control interactions Harmonics demands
HVAC/Air handling systems	Drive harmonic demands False operating sequences
Power factor requirements	Resonance conditions High frequency protection
Uninterruptable services	Line harmonics demand Load Interaction/corruption

Table 1 lists an overview of the "special" power quality services that have to be provided outside the rate-based power from the utility suppliers. This table is excerpted from reference [3]. It is a short summery of areas that have become critical for examination in terms of power quality implications.

3. POWER QUALITY CONTRACTS IN A DEREGULATED POWER SYSTEM

As far as power quality problems are concerned, there are many questions remained to be addressed. What are power quality requirements between the transmission company and the distribution company? What levels of the power quality must be and can be supplied by the distribution company to the end customers? Power quality contracts need to be established between different entities to address the above questions in a deregulated environment. As deregulation takes over the power industry, the level of the service and investments in the system obviously will deteriorate. The basic power quality requirements must be regulated to some extent. As defined in IEEE 1159, indices have been defined for categories of instantaneous, momentary, and temporary voltage sags. Other indices are defined for steady state voltage regulation, unbalance, flicker levels, harmonic distortion, and transient disturbance performance. Many utilities have already installed monitoring systems to help characterize the system performance with respect to the power quality levels. Some utilities also installed the monitoring systems to monitor the power quality performance to specific customers as required by the contracts. The concrete requirements of a power quality contract may depends on the parties involved and the characteristics of the system. However, the most typical parts need to be addressed in the contracts are: reliability and power quality concerns to be evaluated; performance indices to be used; expected level of performance; penalty for performance outside the expected level or incentives for performance better than be expected level (financial penalties, performance based rates, shared savings); measurement and calculation methods to verify performance; responsibilities for each party in achieving the desired performance; responsibilities of the parties for resolving the problems.

Figure 1 shows deregulated utility industry structure with the power quality contracts included. TRANSCOs are the transmission network operators. DISCOs are the distribution companies. ESCOs are the energy service companies. RETAILCOs are retail energy marketers. IPP is independent power producers.

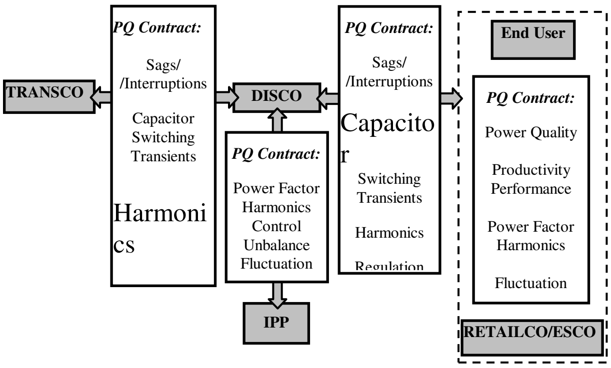

Fig. 1. *Power contracts in a deregulated power system*

4. POWER QUALITY PROBLEMS FROM COGENERATION

Cogeneration will be an important selection of many customers in the future. But it should be considered that load devices might create negative interaction when running on this smaller source of energy. Certainly, there are many instances where cogeneration power sources are very large (into the thousands of kVA). However, even a large power generation unit may be a smaller source of impedance that the system that supplies user facility from the utility power gird. By virtue of this size difference, the impedance of the two types of systems will be orders of magnitude different. The utility power grid looks very "strong" as a very "stiff" power source with very low impedance, possibly 3% to 4% as viewed from the load. The cogeneration unit, considerably smaller than the utility power grid, appears to be a soft power source, with higher impedance as seen by the load, possibly two to three times the impedance of grid. The combination of smaller size and higher impedance may make any harmonic currents from the load cause significantly higher voltage distortion at the terminals of the cogeneration unit. If these levels of voltage distortion are high enough to disturb the utility grid, there may be operating restrictions placed by the utility on the paralleling of the two systems. Effective solution is to install harmonic filters at the source of the harmonic current for demanding loads "clean up" the current wave shape to the point where the on-site generator handles sine waves for both current and voltage. People should examine all factors affecting the way their facility interfaces with the power source as well as include the issue of "power interaction" on the list of questions as apparatus are added or changed. It is general that everything is worked well until a new energy-saving device. Ultimately, some characteristics of the new piece of equipment cause either the existing equipment and/or this new device to malfunction.

5. ATTRIBUTING THE POWER QUALITY DETERIORATION BETWEEN CUSTOMERS AND UTILITIES

Customers have the ability to make choice in purchasing electricity considering power quality. Therefore, it has obvious significance to attributing the power quality deterioration between an individual customer and the network delivering the power.

Reference [12] proposes an approach to attribute steady quality deterioration to the load and supply side using a new concept of conforming and non-conforming current. The steady state power quality deterioration includes phase unbalance, cyclic fluctuations of rms values, harmonic distortion of waveform. Measurement of this type of quality deterioration at any point is reasonably independent of the time period of observation. This type of quality deterioration originates simultaneously at several points in a network. Thus the measured value at any point is the combined effect of the numerous deforming devices at different places. The current at every instant of time drawn by the load is the sum of two theoretical currents. It is reasonable to define a portion of the current with the same graphical pattern as the voltage as conforming current. It is a scaled version of the voltage, with appropriate phase difference. In addition, the conforming current accounts for 100% of the steady fundamental frequency positive sequence power. The balance of the current is called the non-conforming or balanced current.

Unbalances occur in three-phase system due to single-phase devices, unsymmetrical transmission and distribution. The conforming current is the portion of current, which retains the same level of unbalance as the voltage, while at the same time accounts for all of the positive sequence current. A balanced impedance load will account for all of the positive sequence active and reactive power. Thus the positive sequence of conforming current I_{cc} will equal the positive sequence of total current. The negative and zero sequence of conforming current (I_{cn} and I_{cz}) will be in the same proportion as their counterparts in the voltage. Let V_p, V_n, V_z, I_p, I_n, I_z, denote the total voltage and current symmetrical components for fundamental frequency (*p, n* and *z* denote positive, negative and zero sequence respectively). The following equations express this concept.

$$I_{cc} = I_p; \quad I_{cn} = I_p (V_n / V_p); I_{cz} = I_p (V_z / V_p) \tag{1}$$

The non-conforming current is the balance of current. It is attributable to the load. It is expressed in symmetrical components *(I_{ncc}, I_{ncn}, I_{ncz},)* as follows.

$$I_{ncc} = 0; I_{ncn} = I_n - I_{cn}; I_{ncz} = I_z - I_{cz} \quad (2)$$

Steady deviation of a signal from its purely sinusoidal form is harmonic distortion. With Fourier transformation, it is possible to study the effect of each individual sinusoidal voltage of a different frequency on the network and add them up in most cases.

The conforming current will account for all of the fundamental frequency active and reactive power. Thus the fundamental frequency component of the conforming current I_{c1} will equal the fundamental frequency of the total current I_1. All the other frequency components of the conforming current $I_c(t)$ will be in the same proportion as their counterparts in the voltage. The following equations express this concept.

$$I_c(t) = \sum_{k=1}^{n} (I_1 / V_1) V_k \sin(k\omega t + \theta_k + k(\phi_1 - \theta_1)) \quad (3)$$

where V_k and θ_k are the magnitude and phase angle of kth component of the voltage respectively, I_1 and ϕ_1 are the magnitude and phase angle of fundamental component of the current respectively.

The non-conforming current is the balance of current. It contains no fundamental frequency component. It is attribute to the load. It is expressed as follows.

$$I_{nc}(t) = I(t) - I_c(t) \quad (4)$$

The advantage of the approach of using conforming and non-conforming current is that similar customers receive similar treatment, irrespective of their individual differences in utility connection characteristics.

6. ATTRIBUTING HARMONICS IN PRIVATE POWER PRODUCTION

As deregulation dawns, possible private generation and delivery power to the transmission network may contaminate the utility grid and bring problems of power quality. One of applicable approaches is to attribute harmonics in private power production. The attribution is founded solely on measurements during operation and at the point of connection to the network. There is no need to switch the private production on and off. The true energy is the integrated value of the product of the instantaneous voltage and instantaneous current over a full cycle. The true power is the average of the true energy flowing. Digital instruments can measure these values exactly according to the definition. The true power is the sum of powers at all frequencies. It is the sum of fundamental power and harmonic powers.

$$\begin{aligned} &True\ \ Power = \sum_{k=1}^{n} V_k I_k \cos(\theta_k - \phi_k); \\ &Fundamenta\ l\ \ Power = V_k I_k \cos(\theta_1 - \phi_1); \\ &Harmonic\ \ Power = \sum_{k=2}^{n} V_k I_k \cos(\theta_k - \phi_k); \end{aligned} \quad (5)$$

where: V_k, θ_k, I_k, ϕ_k are the values for the fundamental frequency.

When the waveform is distorted, the notion of pricing for true power or true kWh implicitly results in the following. Producers of quality deterioration, who pump harmonic power into the network, will register higher true power. Those bearing damages as a result of consuming those harmonics will pay, in addition, for the harmonic power. Thus it is seen that true power is of questionable value. The types of private production from the point of view of power quality are the following:

a) Three phase synchronous generation: Typical hydro and thermal generation use synchronous machines, which normally produce pure sinusoidal current. When they are subjected to a distorted system voltage, they will consume the harmonics as heat. This will lead to reduction of their lifetime. At the network connection point the fundamental power will flow towards the network. The harmonic powers will flow towards the synchronous generators and dissipated as heat by the synchronous generators. The angular relationship can be represented as follows.

$$90^0 \geq (\theta_1 - \phi_1) \geq -90^0;\ 270^0 \geq (\theta_h - \phi_h) \geq 90^0 \quad (6)$$

b) Three phase synchronous generation serving local linear/non-linear loads and pumping the excess power, if any, into the transmission and distribution network: at the network connection point, the fundamental power can flow either way. The harmonic powers can also flow either way, depending on the non-lineary of the local loads. The angular relationship can be represented as follows.

$$360^0 \geq (\theta_1 - \phi_1) \geq 0^0;\ 360^0 \geq (\theta_h - \phi_h) \geq 0^0 \quad (7)$$

c) Non-synchronous generation: They may or may not serve local loads. The non-conventional source like wind and solar power usually us dc generators with inverters to gain in efficiency. The process of dc to ac conversion leads to harmonic generation. At the network connection point, the fundamental power as well as harmonic powers will flow towards the network. The angular relationship can be represented as follows.

$$90^0 \geq (\theta_1 - \phi_1) \geq -90^0;\ 90^0 \geq (\theta_h - \phi_h) \geq -90^0 \quad (8)$$

A pure resistive load will draw 100% conforming current and 0% non-conforming current, under all conditions of operation and for any value of the source impedance. This situation is valid even when the supply voltage is distorted, since the waveform of total current will look similar to that of the voltage. The conforming current thus becomes identical to the total current. A load/private production that amplifies attenuates or produces quality deterioration will draw/supply partly conforming current and partly non-conforming current. The non-conforming current should be attributed to the load/private production. A pseudo-resistive load (a resistive type load, but with any possible phase difference) is proposed as the reference load, to which all real-life loads are compared. Similarly, a private production, which generates a current identical to the voltage waveform, displaced by any phase angle, is proposed as reference, to which all real-life private production may be compared. A private producer has the right to produce the same proportion of harmonics, as is present in the voltage already. Anything beyond will be considered undesirable. Anything less shows that the private producer is absorbing harmonics.

7. POWER QUALITY MONITORING UNDER DEREGULATION

The objectives of power quality monitoring can be identified as three categories: ***The first one*** is to characterize system performance. This is based on the need to understand the system performance and be able to match the system performance with the needs of the customers. With the knowledge of the normal power quality performance of the system, customers can be notified with the problems quickly. The substantiate power quality baseline information can also help the customers to match the performance of their equipment with the power quality characteristics. ***The second*** category is to characterize specific problems. In this category, monitoring is used to help identify the problem, which then give the solutions to the problem. ***The third*** category is applied as part of an enhanced power quality service. Many utilities are developing enhanced power delivery services that can be offered to customers. One example will be for the utility to offer service with various levels of power quality to match the needs of specific customers. In this case, monitoring is needed to establish the different levels of service and to verify the promised levels of power quality provided.

Power quality includes a wide range of conditions on the power system. It is expensive and not necessary to monitor all types of power quality variations at many locations. Normally, the priorities of monitoring should be determined based on the objectives of the project. The methods to characterize the power quality are very important as the power quality variation rang from high frequency impulses to long term over voltages.

Various types of monitoring equipment can be used for power quality monitoring. They include complicated multifunction instruments for outdoor environment to basic designs for indoor applications. Table 2 gives a good summery for the major categories of the available monitoring equipment.

For power quality data analysis, the software needed should be able to integrate with the monitoring equipment. The storage of tremendous quantities of both steady state and disturbance measurement data requires an efficient and well-suited database. Data management tools should load and characterize the power quality data very quickly. And these tools must be well integrated with the database. The software design should support the automatic data management and report generation.

As power quality problems are closely related with customers, customers should be included into the power quality monitoring efforts. It is shown that Internet can be a practical tool to provide a direct link between the monitoring system and the customers. For example, by continuously monitoring individual instruments, personnel can be notified, when a disturbance exceeds the threshold, by email or fax. On the other hand, after a notification is received, both the customers and the utility should be able to check the associated database by getting access to the database via World Wide Web.

Table 2. *Equipment requirements for various types of PQ disturbances*

Concern	Measurement and Control	Analysis and Display
Harmonic levels	Voltage and current 3 phase waveform configurable periodically synchronized sampling	FFT capability Waveform/spectra plots
Long term voltage variations	3 phase voltage rms sampling configurable threshold level	Magnitude and duration plots
Short term voltage variations, interruptions	3 phase voltage rms sampling configurable threshold level 1 cycle rms resolution	Magnitude vs duration plots
Low frequency transients (switching)	3 phase voltage and current waveform sampling frequency response (5 kHz) configurable threshold level	Waveform plots showing prevent and recovery
High frequency transients (lightening)	3 phase voltage and current frequency response (1 MHz) impulse peak and width detection configurable threshold level	Waveform plots showing position of impulse on power frequency sinusoid

8. POWER VALUE INCLUDING POWER QUALITY RATHER THAN PRICE ONLY

The products that help correct power quality problems are part of a growing, billion-dollar industry. Power quality has an entire magazine dedicated to the subject, several IEEE sub-committees are engaged in setting standards, several governmental agencies are active in research and at least a dozen annual conferences world-wide bring together experts to discuss ways to improve the overall quality of power. No other deregulated industry comes to matching this emphasis on quality. This raises the question as to why the only emphasis so far to deregulation is on price. *Are the government agencies that are behind deregulation just merely following the pattern set by their previous successes? Are the large consumers pressing for change, unaware of the importance of power quality? Or do they just think that power quality and reliability will come along for free along with low price?* Obviously, no one can predict the future, but as the product of electricity unbundled, quality and reliability will become every bit as important as price. Currently, quality and reliability are part of a regulated game. Consumers receive a certain level based on regional conditions (e.g. population density, industrial density, age and length of the distribution network), current standards and the attitude of the local utility. If that level is insufficient for proper operation of the end-use, the consumer can purchase additional products to enhance the power quality. In the power quality market, the objective of equipment manufacturers is to compete against the local utility level of power quality. Good markets for UPS systems exit where the utility has a history of outages, and conversely, the markets are not as good where there is a highly redundant distribution loop as might be found in downtown grids. Surge protector sales are many betters in parts of the utility company have a poorly developed power quality program. But in all cases, the power quality is selling against the local utility's power quality. In the future, the electric market will evolve into a more competitive arena where quality is an option with several grades that can be purchased from a variety of sources, not just the local distribution company. At that time, the product being bought and sold will forever change from a regulated commodity to a versatile product with several differentiating factors. At that time power will be sold on its value to the end-user. Although the product and its price determined almost exclusively from the viewpoint of the utility industry, significant change will occur once deregulation gives customers a choice. Customer choice will dictate that energy providers must look at power from the customer viewpoint, and when they do, they will see that customer want value, and those who can provide the best power value will be positioned the best. Power value will be determined by the same four parameters that determine the value of electric power selling price, availability, quality and usefulness. It will also be customer dependent, unlike today market. Currently, price, reliability and quality are global attributes. Everyone within a class has the same price. Everyone within a local geographic area is subject to the same design for reliability and quality. In deregulated and competitive electricity market, the different opinions from different people as to what is the worth of the power they can be indicated by the power value.

9. CONLUSION

The deregulation of the power system affects power quality at two major aspects. Firstly, deregulation brings more power quality problems. For example, under deregulation, distribution generation will contaminates the power grid as a whole. A large amount of FACTS (Flexible AC Transmission Systems) equipment applied to facilitate or realize the deregulation process may greatly deteriorate power quality. Secondly, in a deregulated and competitive power system, power quality becomes more important to both the energy supplier and the energy consumer. The end users must know the energy requirement of their facilities to ask for energy with appropriate levels of power quality. To survive in the competitive environment, utilities need to provide energy with enhanced power quality. New services with power quality concerns emerge. The rate of the power supplied may be negotiated based on the level of the power quality. At the mean time, both the utilities and the end users are responsible to the power quality. The responsibility should be distributed fairly. Effects of deregulation on the power quality described above are investigated in some details based on a literature review. In order to better understand power quality problem, improve the power quality and, the most important, for the utilities and consumers to know the level of the power quality provided and obtained, power quality should be monitored along the circuits, especially to the principal customers of an utility. To meet the needs of power quality monitoring, the market for power quality monitoring equipment is going to be prosperous and more efforts will be made in designing meters embedded with power quality features. Power quality contracts must be developed carefully to define the power quality requirements and responsibilities at the interfaces between different entries in a deregulated power system.

10. REFERENCES

[1] K.Srinivasan, *"Attributing harmonics in private power production"*, IEEE Transactions on Industry Applications, Vol.34, No.5, pp.887-92, Sep.-Oct.1998.

[2] R. Waggoner, *"Deregulation and power quality: What to expect–part 1"*, EC&M, pp.16-18, May 1997.

[3] R. Waggoner, *"Deregulation and power quality: What to expect – part 2"*, EC&M, pp.16-20, June 1997.

[4] R. Waggoner, *"Deregulation and power quality: What to expect – part 3"*, EC&M, pp.16-18, July 1997.

[5] D.D.Sabin, A. Sundaram, *"Quality enhances reliability"*, IEEE Spectrum, pp.34-41, Feb. 1996.

[6] M. McGranagham, B. W. Kennedy, *"Power quality contracts in a competitive electric utility industry"*, 8th International Conference on Harmonics and Quality of Power. Proceedings. IEEE, Piscataway, NJ, USA, Vol.1, pp.170-175, 1998.

[7] S.Tonkin, *"Utilities deregulation instigates new services"*, InTech, pp. 40-44, March 1999.

[8] G.B.Rauch, D. D. Sabin, M .McGranagham, A. Sundaram, *"Implementing system-wide power quality monitoring plans"*, Proceedings of the 1996 IEEE Power Engineering Society Transmission and Distribution Conference, New York, NY, USA, pp.37-44, 1996.

[9] H.Saari, P. Koponen, E. Tahvanainen, *"Remote reading and data managment system for kWh meters with power quality monitoring"*, Metering and Tariffs for Energy Supply, pp.11-15, July 1996.

[10] P.Tedsko, *"Managment side of engineering"*, Plant engineering, pp.108-109, August 1997.

[11] Power Quality Assurance Staff, *"Power value in a deregulated environment - New lines in the sand"*, Power Quality, 1999.

[12] K.Srinivasan, "Conforming and non-conforming current for a attributing steady state power quality problems", IEEE Transactions on Industry Applications, 1997.

INSTRUCTION FOR AUTHORS

Name of the author/s, Institution/s

Abstract: *Short instruction for authors is presented in this paper. Works that are to be printed in the review "Electronics" should be typed according to this instruction.*

Keywords: *Review Electronics, Faculty of Electrical Engineering Banjaluka, Instruction for authors.*

1. INTRODUCTION

In the review "Electronics", we publish the scientific and professional works from different fields of electronics in the broadest sense like: automatics, telecommunications, computer techniques, power engineering, nuclear and medical electronics, analysis and synthesis of electronic circuits and systems, new technologies and materials in electronics etc. In addition to the scientific and professional works, we present new products, new books, B .Sc., M. Sc. and Ph.D. theses.

In order to enable the unification of the technical arrangement of the works, to simplify the printing of the review "ELECTRONICS", we are giving this instruction for the authors of the works to be published in this professional paper.

2. TECHNICAL DETAILS

2.1. Submitting the papers

The works are to be delivered to the editor of the review by the E-mail (elektronika@etf-bl.rstel.net) or on floppy (or CD) by post mail to the address of the Electrical Engineering Faculty (Elektrotehnicki fakultet, Patre 5, 78000 Banja Luka, Republic of Srpska, Bosnia and Herzegovina).

2.2. Typing details

The work has to be typed on the paper A4 format, 8.27" width and 11.69" height (21.0x29.7 cm), upper and lower margins of 1"(2.54 cm), left and right margins of 1" (2.54 cm) and the header and footer are 0,5" (1.27cm). The work has to be written in English language. Our suggestion to the authors is to make their works on a PC using the word processor MS WORD 97/2000, and for the figures to use the graphic program CorelDraw, if the graphs are not going from the original programs, i.e., from the programs received (like MATLAB).

The title of the work shall be written on the first page, in bold and 12 pt. size. Also, on the first page, moved for one line spacing from title, the author's name together with the name of his institution shall be printed in the letter size. The remaining parts of the manuscript shall be done in two columns with 0.5" (1.27cm) distance. The work shall be typed with line spacing 1 (Single) and size not less than 10 pt.(As like as this instruction). After the title of the work and the name of the author, a short content in English language follows, written in italics. The subtitles in the text shall be written in bold, capital letters of the size as in the text (not less than 10 pt.). Each work shall, at the beginning, comprise a subtitle INTRODUCTION, and, at the end, the subtitles CONCLUSION and BIBLIOGRAPHY / REFERENCES.

The operators and size marks that do not use numerical values, shall be written in common letters. The size marks that can use numerical values shall be written in italics. The equations shall be written in one column with right edge numeration. If the breaking of equations or figures is desired, those may be placed over both columns.

Illustrations (tables, figures, graphs etc.) may be wider than one column if necessary. Above a table there shall be a title, for instance: Table 2. *The experimental measuring results.* The same applies to figures and graphs but the accompanying text comes underneath the figure of graphs, for instance: Fig.3: *Equivalent circuit diagram...*

The work should not be finished at the beginning of a page. If the last manuscript page is not full, the columns on that page should be made even. Number of pages should not go over 6.

3. CONCLUSION

This short instruction is presented in order to enable the unification of technical arrangement of the works.

4. REFERENCES

At the end of work, the used literature shall be listed in order as used in the text. The literature in the text, shall be enclosed in square brackets, for instance: ...in [2] is shown ...